Thermal Management of the Silicon Tracking System of the CBM Experiment at FAIR

Kshitij Agarwal

2024

Thermal Management of the Silicon Tracking System of the CBM Experiment at FAIR

Dissertation
der Mathematisch-Naturwissenschaftlichen Fakultät
der Eberhard Karls Universität Tübingen
zur Erlangung des Grades eines
Doktors der Naturwissenschaften
(Dr. rer. nat.)

vorgelegt von
Kshitij Agarwal
aus Rishikesh, Indien

Tübingen
— 2024 —

Gedruckt mit Genehmigung der Mathematisch-Naturwissenschaftlichen Fakultät der Eberhard Karls Universität Tübingen.

Tag der mündlichen Qualifikation:	19.12.2024
Dekan:	Prof. Dr. Thilo Stehle
1. Berichterstatter/-in:	Prof. Dr. Hans Rudolf Schmidt
2. Berichterstatter/-in:	Prof. Dr. Peter Senger
3. Berichterstatter/-in:	Prof. Dr. Marc Weber

"It is not you who defends the thesis,
but the thesis that defends you..."

Abstract

The ever-growing miniaturisation of silicon microelectronics, coupled with detector signal processing requirements, has established silicon detectors as a cornerstone in modern high-energy physics experiments. These detectors are pivotal for experiments focused on a deeper understanding of the Standard Model in hadron collisions and the study of Quantum Chromodynamics (QCD) in extreme conditions with heavy-ion collisions. This research is focused on the Silicon Tracking System (STS) of the Compressed Baryonic Matter (CBM) experiment at the Facility for Antiproton and Ion Research (FAIR), designed to explore the high-density regime of the QCD phase diagram and a potential phase transition to the Quark-Gluon Plasma (QGP).

This project is focused on a critical aspect that has recently become central to the design and sustained operation of modern silicon trackers in high-energy physics experiments - Thermal Management. The CBM-STS, a forward spectrometer using silicon microstrip sensors specialised in tracking of low-momentum particles produced in heavy-ion collisions, presents a distinctive challenge. The highly irradiated STS silicon sensors must be cooled by introducing minimal material, while the nearby front-end electronics dissipate up to 40 kW of power within a 3.5 m^3 detector volume. Through theoretical calculations and simulations, a novel cooling concept - Liquid-Assisted Air Cooling - was developed. This concept integrates air cooling for the silicon sensors and liquid cooling for the front-end electronics to balance thermal management needs while minimising material budget.

The cooling concept was experimentally verified under realistic operational conditions using the CBM-STS Thermal Demonstrator, jointly designed and built at the University of Tübingen and GSI Helmholtz Centre for Heavy Ion Research in Darmstadt. This has provided critical insights into the operating parameters for STS cooling, and assessed the suitability of prototype and pre-production detector components, along with their integration methods in STS-like boundary conditions. The findings are essential for ensuring the long-term reliability of the CBM-STS as it approached its series production phase, with system integration scheduled for 2024-25 and data-taking with high-intensity heavy-ion beams at FAIR expected in 2028-29.

Zusammenfassung

Die zunehmende Miniaturisierung von Siliziumbasierter Mikroelektronik in Verbindung mit gestiegenen Anforderungen an die Signalverarbeitung der Detektoren hat dazu geführt, dass Siliziumdetektoren zu einem Eckpfeiler moderner Hochenergiephysikexperimente geworden sind. Solche Detektoren sind von zentraler Bedeutung für Experimente, die sich auf ein tieferes Verständnis des Standardmodells bei Hadronenkollisionen und die Untersuchung der Quantenchromodynamik (QCD) unter extremen Bedingungen bei Schwerionenkollisionen konzentrieren. Die vorliegende Forschungsarbeit bezieht sich auf das Silicon Tracking System (STS) des Compressed Baryonic Matter (CBM) Experiments an der Beschleunigeranlage Facility for Antiproton and Ion Research (FAIR), mit dem der Bereich hoher Dichte des QCD-Phasendiagramms und ein möglicher Phasenübergang zum Quark-Gluon Plasma (QGP) erforscht werden soll.

Das Projekt untersucht einen kritischen Aspekt, der in letzter Zeit für die Entwicklung und den dauerhaften Betrieb moderner Silizium-Tracker in Experimenten der Hochenergiephysik von zentraler Bedeutung geworden ist: das Wärmemanagement. Das CBM-STS ist ein Vorwärtsspektrometer, welches Silizium-Mikrostreifensensoren verwendet, die auf die besonders herausfordernde Vermessung von Zerfallsteilchen mit geringem Impuls in Schwerionenkollisionen spezialisiert sind. Die stark bestrahlten STS-Siliziumsensoren müssen mit minimalem Materialeinsatz gekühlt werden, während die Front-End-Elektronik bis zu 40 kW Leistung in dem 3.5 m^3 großen Detektorvolumen verbraucht. Durch theoretische Berechnungen und Simulationen wurde ein neuartiges Kühlungskonzept - die flüssigkeitsunterstützte Luftkühlung - entwickelt. Dieses Konzept integriert die Luftkühlung für die Siliziumsensoren und die Flüssigkeitskühlung für die Front-End-Elektronik, um die Anforderungen an das Wärmemanagement auszugleichen und gleichzeitig das Materialbudget zu minimieren.

Das Kühlkonzept wurde experimentell unter realistischen Betriebsbedingungen mit dem CBM-STS Thermal Demonstrator verifiziert, der gemeinsam an der Universität Tübingen und dem GSI Helmholtzzentrum für Schwerionenforschung in Darmstadt entwickelt und gebaut wurde. Dies hat entscheidende Erkenntnisse über die Betriebsparameter für die STS-Kühlung geliefert und die Eignung von Prototyp- und Vorserien-Detektorkomponenten sowie deren Integrationsmethoden unter STS-ähnlichen Randbedingungen bewertet. Die Ergebnisse sind von entscheidender Bedeutung zur Ermöglichung der Serienproduktion der Detektorkomponenten, um die langfristige Zuverlässigkeit des CBM-STS zu gewährleisten. Die Systemintegration ist für 2024-25 geplant und die Datennahme mit hochintensiven Schwerionenstrahlen bei FAIR wird für 2028-29 erwartet.

Contents

1. Introduction

Understanding the fundamental building blocks of matter and the forces that govern their interactions has been a central theme in nuclear and particle physics, and has led to the development of the Standard Model of Particle Physics. Over the years, rigorous exploration, utilising advanced detectors, has probed nuclear matter under extreme conditions at high-energy accelerators and space, ground and underground-based experiments [1–9]. In this pursuit, semiconductor detectors, particularly silicon detectors, have emerged to be a fundamental part of high-energy physics experiments since the 1960s. Silicon detectors depleted under reverse-bias configurations are, effectively, solid-state ionisation chambers. Initially used for the improved energy resolution, advancements in micro-scale segmentation since the 1980s have allowed the silicon detectors, in combination with strong B-fields, to be used for enhanced momentum resolution, and recently for timing resolution. Collectively, this has made silicon detectors indispensable to particle identification strategies in high-energy physics experiments [10–16]. This is manifested by a four-orders-of-magnitude increase in both the number of readout channels and area of silicon strip detectors in the particle physics experiments over the past 40 years (see Fig. 1.1) [17].

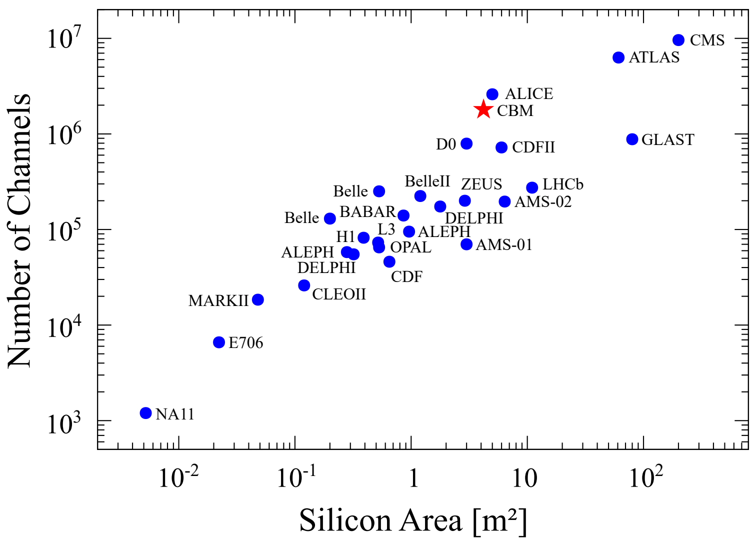

Figure 1.1.: Evolution of silicon strip detectors in accelerators and space-based particle physics experiments, correlating the number of readout channels with silicon area. The red star indicates the CBM experiment, the focus of this thesis (figure from [17]).

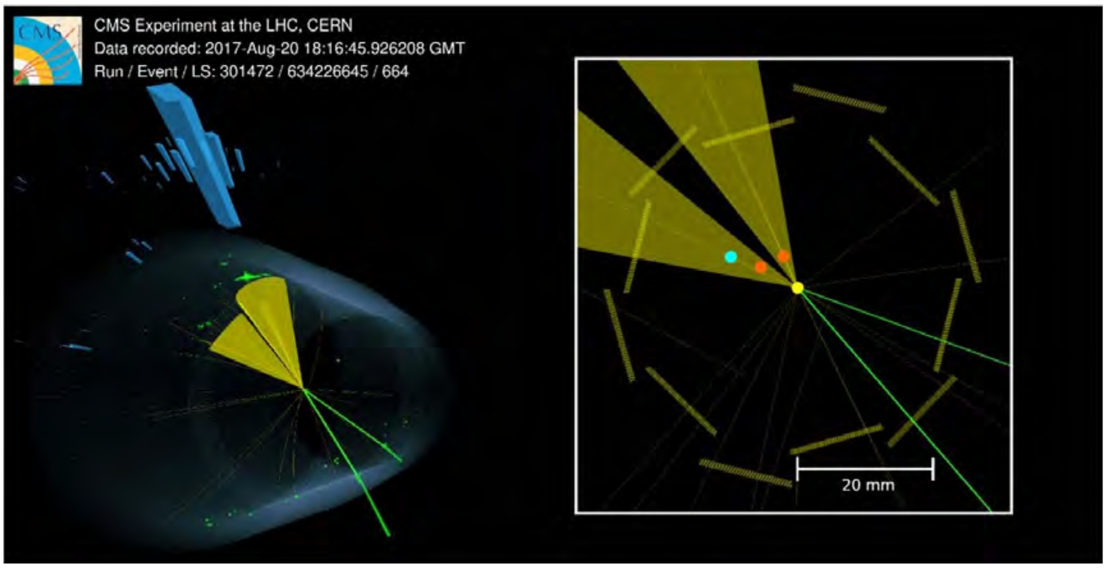

Figure 1.2.: CMS event display of an H $\rightarrow$ bb event in pp collisions at $\sqrt{s_{NN}} = 13$ TeV. The charged-particle tracks reconstructed in the inner tracker (yellow), electron tracks and electromagnetic calorimeter (ECAL) energy (green), hadron calorimeter (HCAL) energy (blue), muon tracks (red), and reconstructed jets (yellow cones) are depicted. Zoomed view into the collision region with the silicon pixel detector (yellow vertex and planes), displaying the reconstructed secondary vertices (red vertices) of two b quark, with one bottom hadron further decaying into a charm hadron ($b \rightarrow c \rightarrow X$; cyan vertex) (figure adapted from [18]).

Silicon detectors are typically deployed in multiple layers around the interaction point (IP) to reconstruct the primary and secondary vertices, thereby determining the lifetime of the decayed particles. This has been extensively used to track the decays of heavy-flavour particles, especially to tag b quarks within particle jets [19]. This has been instrumental in the observation of $B^0 - \overline{B}^0$ oscillations at the CERN Large Electron and Positron (LEP) Collider by the Apparatus for LEP PHysics (ALEPH) [20, 21] and DEtector with Lepton, Photon and Hadron Identification (DELPHI) collaborations [22]. This was also used in the discovery of the top quark at the Fermilab Tevatron by the DZero (DØ) [23] and Collider Detector at Fermilab (CDF) Collaboration [24]. The experiences gained from these experiments served as a springboard for even larger and precise silicon detectors critical to the discovery of the Higgs Boson at the CERN Large Hadron Collider (LHC) by the A Toroidal LHC Apparatus (ATLAS) [25,26] and Compact Muon Solenoid (CMS) collaborations [18, 27] (see Fig. 1.2). This substantiates the role of silicon detectors in the experimental verification of the Standard Model and further providing access to distinguishing signals from potential new physics beyond the the Standard Model.

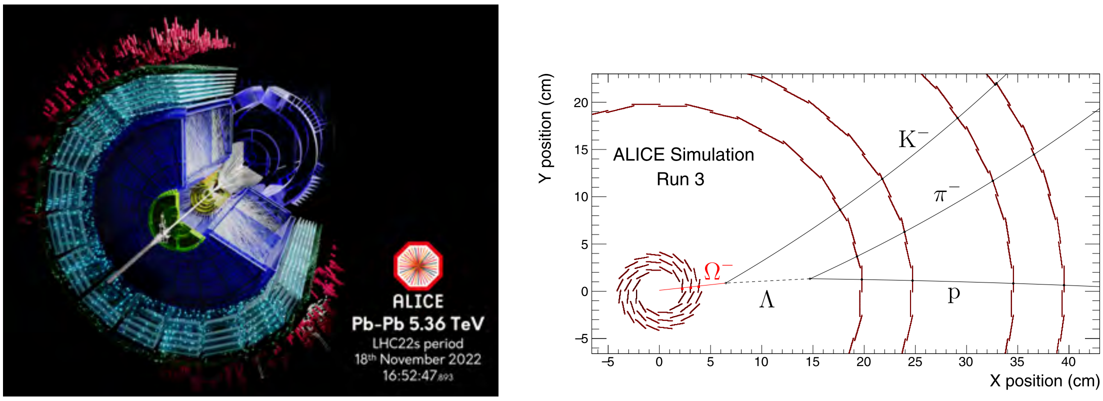

(a) (b)

Figure 1.3.: (a) Event display of the first Pb-Pb collisions recorded during Run-3 at $\sqrt{s_{NN}}$ = 5.36 TeV by the ALICE experiment (figure credit: 2022 CERN, for the benefit of the ALICE Collaboration ALICE-PHO-GEN-2022-009-2). (b) Simulation of Ω^- hyperon decay reconstruction by tracking the hits of prior to its decay in the inner layers of the upgraded ALICE Inner Tracking System (ALICE ITS2) (figure from [28]).

Silicon detectors, besides contributing to the understanding of the Standard Model in *pp* collisions, play a crucial role in investigating high-density nuclear matter governed by Quantum Chromodynamics (QCD) for Quark-Gluon Plasma (QGP) formation in heavy-ion collisions. This was initially pioneered at BNL Relativistic Heavy Ion Collider (RHIC) by the Solenoidal Tracker at RHIC (STAR) collaboration [29, 30], and later substantiated at the CERN LHC by the A Large Ion Collider Experiment (ALICE) collaboration [31]. Reconstruction of short-lived particles with heavy c and b quarks allows probing the micro-structure of QGP, exploring its thermodynamic, hydrodynamic, and transport properties (see Fig. 1.3). This facilitates the examination of QGP formation thresholds and quark/gluon deconfinement by systematically scanning the high-temperature regime of the QCD phase diagram.

Consequently, the Compressed Baryonic Matter (CBM) experiment at Facility for Antiproton and Ion Research (FAIR) will use all-silicon vertex and tracking detectors to scan the high-density regime of the QCD phase diagram at densities as in the core of neutron stars [32–34]. Its CBM Silicon Tracking System (CBM-STS) [35, 36], which is the subject of this thesis, is crucial for efficiently tracking low-multiplicity 'rare probes', including multi-strange hyperons and hypernuclei, at unprecedentedly high beam-target interaction rates up to 10 MHz. The subsequent sections will delve deeper into the design and operational challenges associated with modern silicon detectors, with a particular focus on the significance of employing lightweight thermal management strategies. This will be specifically addressed within the context of CBM-STS.

1.1. Motivation for Silicon Detectors' Lightweight Thermal Management

While there are shared technological choices and parameters for silicon detectors across various accelerator-based experiments, optimising these detectors presents a multifaceted challenge due to distinct collision conditions of hadron, lepton and heavy-ion colliders (see Fig. 1.4) [37]. The high-occupancy environment of hadron colliders (e.g., LHC and future FCC-hh experiments) necessitate detectors to have a high hit-rate, radiation tolerance and timing resolution to resolve multiple interactions within a bunch crossing and minimise pileup. Achieving physics goals in experiments at heavy-ion (e.g., ALICE and CBM) and lepton colliders (e.g., Belle II and ePIC) calls for tracking precision and efficiency at low momentum. This requires excellent position resolution, as well as low mass and power to minimise material near the interaction point.

This section will describe the design and operational challenges associated with silicon detectors used for tracking/vertexing applications in modern high-energy physics experiments. The specific focus will be on addressing these challenges within the demanding context of the harsh irradiation environment and the stringent requirements on tracking/vertexing performance. Additionally, it will underscore the pivotal role played by effective thermal management and mechanics in solving these challenges and ensuring optimal detector performance.

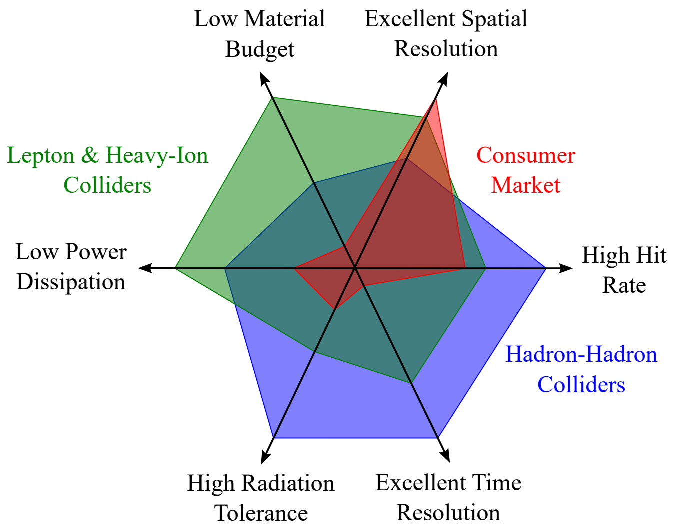

Figure 1.4.: Spider chart illustrating qualitative optimisation considerations for silicon sensors in the context of modern high-energy physics experiments, encompassing three distinct use cases: high-luminosity proton-proton collisions (e.g., ATLAS and CMS experiments), e^+e^- or heavy-ion collisions (e.g., Belle II and ALICE, CBM experiments), and applications in the consumer-driven market (figure from J. Baudot (IPHC, Strasbourg) and adapted from [38]).

1.1.1. Temperature and Radiation Damage

Micro-segmented silicon detectors ($\sim$ 10 µm) with miniaturised readout electronics permits higher on-detector segmentation, increased channel density, and superior position resolution[1]. Furthermore, the low ionisation threshold of silicon allows for a thin active layer of $\sim$ 100 µm resulting in large and fast signals[2]. Collectively, these factors make silicon detectors particularly suitable for being located closest to the particle interaction points where the irradiation environment is harshest, and consequently, the produced particles traverse at highest rates and densities. The accompanying radiation damage resulting from non-ionising energy loss (NIEL)[3] induces the displacement of atoms from their lattice sites, giving rise to point-like and cluster-like defects. These displacements and impurities introduce new energy levels within the forbidden energy gap of silicon, resulting in changes to the macroscopic electrical properties of the silicon sensor. Such changes include variations in leakage current, full-depletion voltage, and charge collection efficiency, as illustrated in Fig. 1.5. The basics of radiation damage in silicon detectors are detailed in [39–41]. Subsequent paragraphs briefly describe the effects of this damage on macroscopic electrical properties.

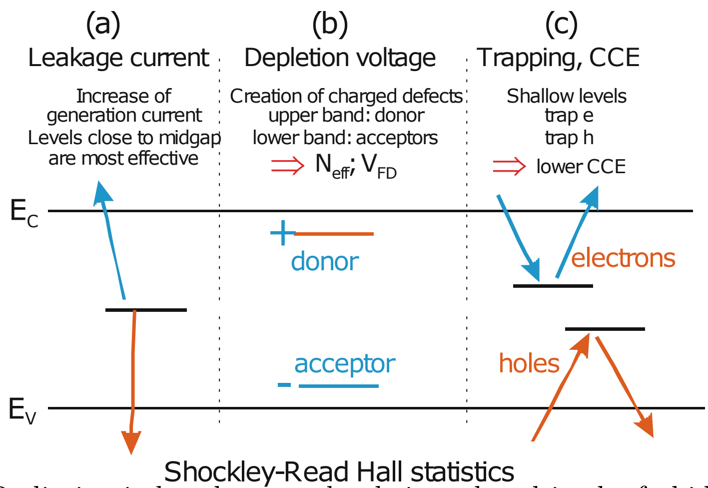

Figure 1.5.: Radiation-induced energy levels introduced in the forbidden energy gap and the respective changes in sensor's electrical properties (figure adapted from [14,15]).

1. For strip-like segmentation (pitch, p, and thickness, d), position resolution is $\sigma_x \approx p/\sqrt{12}$, providing a typical resolution of $\sim$ 10 µm for silicon strip detectors.
2. The ionisation energy, i.e., minimum energy required to form an electron-hole ($e-h$) pair is 3.65 eV for silicon as compared to $\approx$ 30 eV for gases. The silicon ionisation energy is much higher than the band gap of 1.12 eV as part of the deposited energy is used for phonon creation. For a minimum ionising particle (MIP) traversing silicon bulk, 108 $e-h$/µm are produced on average, while 76 $e-h$/µm are most probably produced (considering Landau fluctuations; $0.7 \cdot 108$ $e-h$/µm).
3. Conventionally, NIEL from different particle species is normalised to damage caused by 1 MeV neutrons and specified as neutron-equivalent fluence (Φ_{eq}; unit n_{eq}(1 MeV)/cm^2)

(a) Leakage Current: The mid-gap levels produced during irradiation (Φ_{eq}) in the forbidden energy gap of silicon are efficient electron-hole pair generators (see Fig. 1.5(a)). This is cause due to a two-step process of *Hole and Electron emission.* The former is equivalent of promoting an electron from the valence band to the defect's mid-gap level, whereas the latter includes the further transition of this electron to the conduction band and contribute to reverse bias leakage current ($I_{Leakage}$). This results in a linear increase of $I_{Leakage}$ with Φ_{eq}. This relationship is shown in Eq. 1.1a, where α is the current-related damage coefficient ($\alpha = 4 \ldots 7 \times 10^{-17}$ A/cm) for a given silicon sensor volume V (with surface area (A) and thickness (d)) [39]. This has further consequences on the shot noise ($\propto \sqrt{I_{Leakage}}$) and the power dissipation ($\propto I_{Leakage}$) of the silicon sensor. Moreover, $I_{Leakage}$ and the resulting sensor power dissipation and ENC_{IL} exhibit an exponential dependence on sensor temperature (T_{Sensor}) [42] (see Eq. 1.1b).

$$\frac{\Delta I_{Leakage}}{V} = \frac{\Delta I_{Leakage}}{A \cdot d} = \alpha \cdot \Phi_{eq} \tag{1.1a}$$

$$I_{Leakage} \propto T_{Sensor}^2 \cdot e^{-\frac{E_{gap}}{2 \cdot T_{Sensor} \cdot k_B}} \tag{1.1b}$$

This temperature-dependent relationship introduces a self-feeding cycle between temperature, $I_{Leakage}$, and power dissipation. This can, potentially, lead the sensors to go into an uncontrolled positive feedback loop, resulting in a state known as *Thermal Runaway* (see Fig. 1.6). Therefore, it's imperative that the sensor power dissipation must be neutralised by effective cooling to minimise the $I_{Leakage}$ and thereby ENC_{IL}. Operating the sensors down to 0°C typically reduces $I_{Leakage}$ and power dissipation to 1/6 of its value at room temperature. Consequently, this enhances the detector's signal-to-noise ratio (S/N) which is crucial to track reconstruction performance.

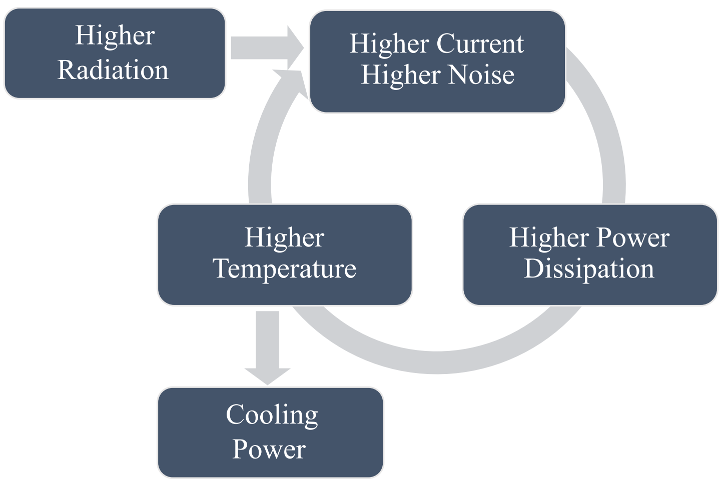

Figure 1.6.: Illustration showing the role of sensor cooling in neutralising the positive feedback loop of thermal runaway caused by irradiation.

(b) Full Depletion Voltage: Irradiation causes a creation of more defects in the silicon lattice by creating additional acceptor-like levels in the forbidden energy gap (see Fig. 1.5(b)). This changes the effective doping concentration of the bulk (N_{eff} by ΔN_{eff}) from its initial state (N_d). This appears as a change of doping level by making the silicon bulk to be *p*-type[4]. In practice, the bias voltage must be raised proportionally to the increase in space charge to transport the charge through the sensor thickness (d) and achieve full depletion (V_{dep}) (see Eq. 1.2a and Eq. 1.2b).

$$V_{dep} = \frac{e}{2\varepsilon} |N_{eff}| \, d^2 \tag{1.2a}$$

$$N_{eff} = N_d - \Delta N_{eff} \left(\Phi_{eq}, t, T\right) \tag{1.2b}$$

The diffusion of radiation-induced defects, therefore, N_{eff} or V_{dep} is highly temperature and time dependent. This is described by the *Hamburg Model* [39] which parameterises the change in space charge due to donor removal plus acceptor creation with fluence and subsequent diffusion with the *stable damage* (ΔN_C), *short-term annealing* (ΔN_A) and *long-term annealing* (ΔN_Y) (cumulatively expressed in Eq. 1.3).

$$\Delta N_{eff} \left(\Phi_{eq}, t, T\right) = \Delta N_C \left(\Phi_{eq}\right) + \Delta N_A \left(\Phi_{eq}, t, T\right) + \Delta N_Y \left(\Phi_{eq}, t, T\right) \tag{1.3}$$

The short-term annealing is beneficial in nature as it reduces the V_{dep}, whereas the long-term annealing is detrimental as it increases at later times. This can be problematic if the resulting V_{dep} at later times is above the maximum applicable bias voltage. Since the underlying annealing time constants are heavily temperature dependent (see Tab. 1.1). Therefore, a two-pronged strategy is common where the silicon sensors are maintained at sub-zero temperatures during operational periods (with beam) to suppress reverse annealing, whereas they are shortly kept at room temperatures or higher during the maintenance periods (without beam) to utilise beneficial annealing. Collectively, this strategy ensures V_{dep} remains safely below the maximum design voltage within the operational lifetime of the experiment both during operational and maintenance periods.

Annealing Temperature [°C]	-10	0	+10	+20	+40	+60	+80
Beneficial Annealing (τ_A)	306 d	53 d	10 d	55 h	4 h	19 m	2 m
Reverse Annealing (τ_Y)	516 y	61 y	8 y	475 d	17 d	21 h	92 m

Table 1.1.: Beneficial and reverse annealing time constants at different temperatures [39]. The time constants of the damage contributions are defined in detail in App. C and Eq. C.1.

4. For an initially donor-rich *n*-type doped silicon under constant irradiation, donor-like states are removed, whereas acceptor-like are created. Therefore, the effective space charge (doping type) is inverted from positive (*n*-type) to negative (*p*-type) at higher fluences ($\Phi_{eq} \sim 10^{13}$ n_{eq}(1 MeV)/cm^2). Operationally, this means that the full depletion voltage initially decreases and then increases with accumulated fluence

(c) Charge Collection Efficiency: Increasing irradiation (Φ_{eq}) proportionally creates shallow mid-gap levels in silicon's forbidden energy gap, which act as *trapping centres* for the produced free charge carriers (see Fig. 1.5(c)). This reduces the effective lifetime of the free carriers in the silicon bulk before they are trapped (τ_{eff}) (see Eq. 1.4a, where β is the effective trapping damage constant[5]). Therefore, τ_{eff} shorter than the integration time of the read-out electronics results in the loss of the Charge Collection Efficiency (CCE; see Eq. 1.4b, where Q_0 and $Q(t)$ are the charge collected before and after irradiation, respectively).

$$\tau_{eff} \approx \beta\,(t, T)\,/\Phi_{eq} \propto 1/N_{defects} \tag{1.4a}$$

$$\text{CCE} \ = Q(t)/Q_0 = \exp\left(-t/\tau_{eff}\right) \tag{1.4b}$$

However, it should be noted that trapping becomes a limiting factor only at $\Phi_{eq} \sim 10^{15}$ $n_{eq}(1\text{ MeV})/\text{cm}^2$, as the charges are no longer collected for 300 µm thick sensors due to low carrier lifetimes or travel distances[6]. Additionally, β shows only a weak dependency on temperature [44–46], therefore, thermal management of silicon detectors does not directly affect the CCE.

Extensive studies carried out within the CERN-RD48 [47–49] and CERN-RD50 [50–52] collaborations have played a pivotal role in understanding radiation-induced defects, both microscopically and macroscopically. This enables the engineering of HL-LHC-resistant[7] detector materials through techniques like oxygenating silicon sensors and using p-type silicon bulk with n^+ electrodes.

To summarise, thermal management of silicon detectors is crucial to mitigate the radiation-induced deficiencies which are reflected in deteriorating electrical properties of sensors. These effects are mentioned as follows:

- The exponentially increasing leakage current and power dissipation with temperature mandates that an efficient cooling concept is required to avoid the sensors to go into a positive feedback loop (thermal runaway).
- The rising leakage current with fluence also increases detector shot noise, which in turn deteriorates S/N. Therefore, operating the detector at optimal temperatures can help maintain the desired S/N.
- The radiation-induced change to the effective space charge, i.e., full depletion voltage, is temperature dependent and can undergo accelerated reverse annealing at higher temperature. So, optimal operating temperatures are needed to effectively "freeze" this effect and maintain the full depletion voltage below the maximum allowable bias voltage.

5. β is different for electrons ($\beta_{e,0}$) and holes ($\beta_{h,0}$) due to their different mobilities. For proton irradiation, $\beta_{e,0}$ and $\beta_{h,0}$ are 4.97×10^{-16} and 5.25×10^{-16} cm^2/ns, respectively. For neutron irradiation, $\beta_{e,0}$ and $\beta_{h,0}$ are 3.53×10^{-16} and 5.10×10^{-16} cm^2/ns, respectively [43].
6. For $\Phi_{eq} = 10^{15}$ $n_{eq}(1\text{ MeV})/\text{cm}^2$: $\tau_{eff} = 2$ ns $\Rightarrow$ Travel Distance $x = 200$ µm
   For $\Phi_{eq} = 10^{16}$ $n_{eq}(1\text{ MeV})/\text{cm}^2$: $\tau_{eff} = 0.2$ ns $\Rightarrow$ Travel Distance $x = 20$ µm
7. $\Phi_{eq} \gtrsim 10^{15}$ $n_{eq}(1\text{ MeV})/\text{cm}^2$ at High Luminosity Large Hadron Collider (HL-LHC)

1.1.2. Material Budget and Track Reconstruction

Most modern accelerator-based high-energy physics experiments are designed to identify the produced (charged) particles by determining their momenta and velocities. The former is measured by accurate reconstruction of the curvature of particle trajectories in the magnetic field, as the traversing charged particles ionise the detector material to generate the space points or *hits*.

The particle interaction with the detector material not only causes ionisation, but also results in the traversing particle undergoing Coulomb interaction, deviating its trajectory (see Fig. 1.7). The resulting angular dispersion θ_{plane} of the incident particle (standard deviation of the distribution of the projected scattering angle) can be calculated by the Highland formula [53, 54] (see Eq. 1.5),

$$\theta_{plane} = \frac{13.6\ \mathrm{MeV}}{\beta c \cdot p} \cdot |z| \cdot \sqrt{\frac{x}{X_0}} \left[1 + 0.038 \cdot \ln \frac{x}{X_0}\right] \propto \frac{1}{p} \cdot \sqrt{\frac{x}{X_0}}\ (\text{for } \beta \approx 1)\ , \quad (1.5)$$

where p, βc and z are the momentum, speed, and charge of the incident particle, respectively, while traversing a medium of thickness x and path length or material budget x/X_0 (in units of radiation length X_0). X_0 is the detector material property defined as the distance over which the traversing electron loses energy by $1/e$ through Bremsstrahlung [55] (see Eq. 1.6),

$$X_0 = \frac{716.4 \cdot A}{Z \cdot (Z+1) \cdot \ln \frac{287}{\sqrt{Z}} \cdot \rho}\ , \quad (1.6)$$

where A, Z and ρ are the atomic number, mass number, and density of the detector material. Altogether, it can be concluded from Eqs. 1.5-1.6 that thin and lightweight materials are crucial to minimise the multiple scattering of the traversing particles. The role of multiple scattering on the track reconstruction performance, in terms of momentum and impact parameter resolution, is summarised as follows with details in [8].

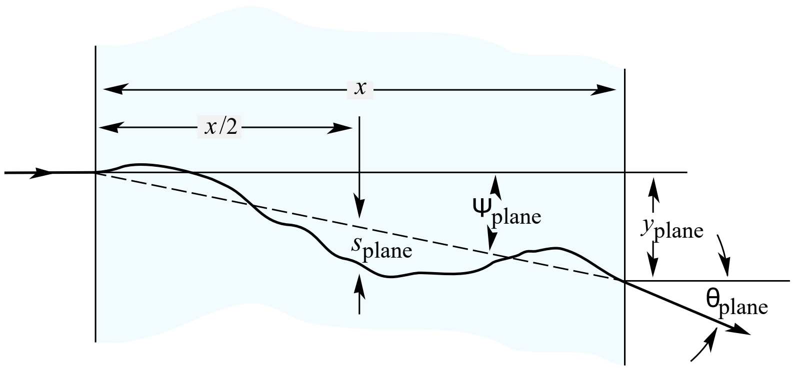

Figure 1.7.: Illustration showing dispersion of incident particle by θ_{plane} due to Coulomb scattering whilst traversing through a medium of thickness x (figure from [55]).

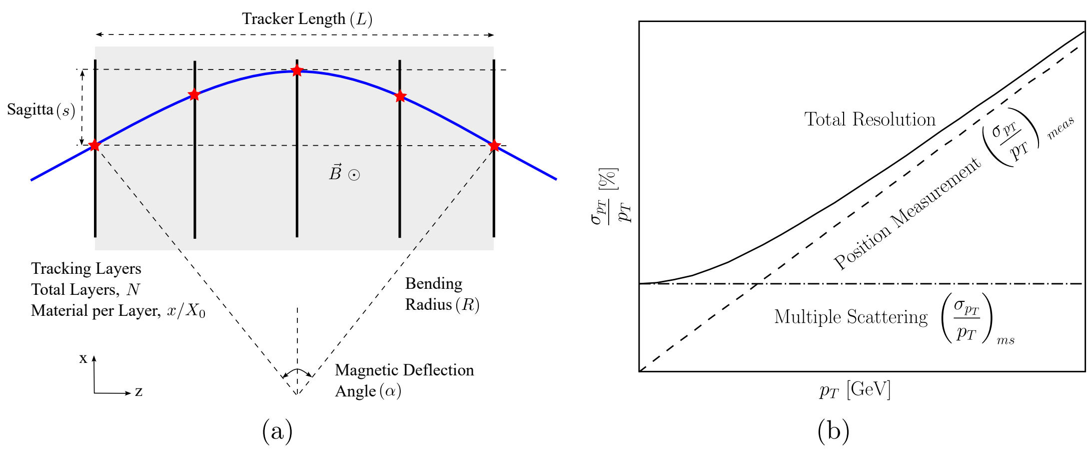

Figure 1.8.: (a) Particle trajectory in a forward spectrometer shown perpendicular to the magnetic field (x-z plane; beam along z-axis). (b) Sketch showing the variation of transverse momentum resolution with transverse momentum. The contributing components are based on Eqs. 1.7 and are parameterised as $\sigma_{p_T}/p_T \equiv \sqrt{(a \cdot p_T)^2 + b^2}$ (for $\beta \approx 1$), with coefficients a and b corresponding to errors from position measurement and multiple scattering, respectively (figures adapted from [8]).

(a) Momentum Resolution: Gluckstern formalism [56, 57] defines the momentum resolution (σ_{p_T}/p_T) of charged particles by accurately determining their trajectories' curvatures in the magnetic field $\overrightarrow{B}$. The curvature is measured over N equally spaced detector planes along the length L, each with material budget x/X_0 (see Fig. 1.8(a) and Eq. 1.7)[8]. The underlying components of p_T resolution in Eq. 1.7a are the errors associated with the measured detector resolution σ_{meas} (see Eq. 1.7b) and multiple scattering over all detector planes (see Eq. 1.7c).

$$\frac{\sigma_{p_T}}{p_T} = \sqrt{\left(\frac{\sigma_{p_T}}{p_T}\right)^2_{meas} + \left(\frac{\sigma_{p_T}}{p_T}\right)^2_{ms}} \tag{1.7a}$$

$$\text{where,} \left(\frac{\sigma_{p_T}}{p_T}\right)_{meas} \approx \frac{p_T}{0.3|z|} \cdot \frac{\sigma_{meas}}{BL^2} \cdot \sqrt{\frac{720}{N+4}} \tag{1.7b}$$

$$\text{and,} \left(\frac{\sigma_{p_T}}{p_T}\right)_{ms} \approx \frac{0.0136 \text{ GeV/c}}{0.3\beta} \cdot \frac{1}{BL} \cdot \sqrt{(N-1) \cdot \frac{x/\sin\theta}{X_0}} \,. \tag{1.7c}$$

As shown in Fig. 1.8(b), the p_T resolution saturates (for $\beta \approx 1$) at smaller p_T as multiple scattering is the limiting factor. Therefore, the material budget of the detector planes (along with its auxiliary services) must be carefully optimised to effectively increase the contribution of σ_{meas}, especially at low p_T.

8. Momentum resolution here is defined for the transverse component, i.e, momentum component perpendicular to the direction of the magnetic field ($p_T = \overrightarrow{p} \cdot \sin\theta$, where θ is the angle between the track of momentum $\overrightarrow{p}$ and the magnetic field $\overrightarrow{B}$).

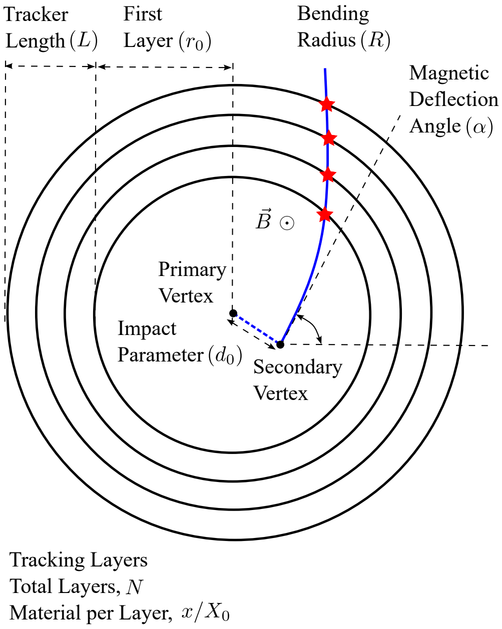

Figure 1.9.: Sketch showing secondary vertex reconstruction by detector layers oriented in a solenoid spectrometer (figure adapted from [8, 57]).

(b) Impact Parameter Resolution: Vertex detectors, located closest to the interaction point, are primarily tasked with reconstructing the secondary decay vertices of weakly decaying heavy quarks and leptons with $c\tau \sim 100$ µm. The impact parameter (d_0) is defined as the shortest perpendicular distance of a interpolated secondary particle track to the primary vertex (interaction point). Therefore, the primary performance parameter of any vertex detector is the impact parameter resolution (Δd_0), which determines if the interpolated secondary track is well separated from the primary vertex (see Fig. 1.9). Δd_0 is determined by the error due to position measurements ($\Delta d_0|_{meas}$) and the multiple scattering ($\Delta d_0|_{ms}$) (see Eq. 1.8). The extension of Gluckstern formalism [57] calculates Δd_0 for N number of evenly spaced detector layers over the length L, each with material budget x/X_0 and first layer r_0 away from the primary vertex.

$$\Delta d_0 = \sqrt{(\Delta d_0)^2_{meas} + (\Delta d_0)^2_{ms}} \tag{1.8a}$$

$$\text{where,}\ \ (\Delta d_0)_{meas} \approx \frac{3\sigma_{meas}}{\sqrt{N+4}} \cdot \sqrt{1 + 8\left(\frac{r_0}{L}\right) + 28\left(\frac{r_0}{L}\right)^2 + 40\left(\frac{r_0}{L}\right)^3 + 20\left(\frac{r_0}{L}\right)^4} \tag{1.8b}$$

$$\text{and,}\ \ (\Delta d_0)_{ms} \approx \frac{0.0136\ \text{GeV/c}}{\beta \cdot p_T} \cdot r_0 \cdot \sqrt{\left(1 + \frac{1}{2}\left(\frac{r_0}{L}\right) + \frac{N-1}{4}\left(\frac{r_0}{L}\right)^2\right) \cdot \frac{x/\sin\theta}{X_0}} \tag{1.8c}$$

Given that $\Delta d_0|_{ms}$ and p_T are inversely proportional to each other, the contribution of multiple scattering due to the material budget x/X_0 within the detector planes becomes more dominant at lower p_T.

In summary, the inhibiting factors determining the track reconstruction performance, i.e., momentum (σ_{p_T}/p_T) and impact parameter resolution (Δd_0), are the uncertainties associated with intrinsic detector resolution (σ_{meas}) and multiple scattering within the detector planes (x/X_0). The deterioration of the track reconstruction at low p_T is driven by x/X_0, therefore, the detector design, including cooling and mechanics, must be optimised to minimise x/X_0.

1.2. General Thermal Management Strategies for Silicon Detectors

The increasing adoption and challenging operational conditions (in terms of radiation tolerance and track reconstruction goals) of silicon trackers in high-energy physics experiments have made their mechanics aspects, especially thermal management, central to their design and lasting operation (see reports from various R&D programmes [37, 58, 59]). Hence, the suitable thermal management solution for any experiment requires adhering to the following constraints:

- Power density dissipated by the silicon sensors and electronics
- Silicon sensor operational temperature and acceptable uniformity
- Minimum allowed temperature of the heat sink or coolant
- Requirements on track reconstruction performance, which determines the additional material budget of the solution (x/X_0)
- Available space and location of the power dissipating elements
- Operational environment (magnetic field, accumulated radiation, vacuum)
- Coefficient of Thermal Expansion (CTE) of the underlying materials to minimise the thermal stresses caused by operational cycling
- Environmental impact, lifetime and cost of the experiment

Based on the aforementioned constraints, special thermal management solutions are needed for silicon detectors, despite the fact that their volumetric power density is comparable to commercial electronics such as high-power computing chips (~ 0.1 W/cm^3) [60]. The thermal efficiency of the thermal management strategy implemented is quantified as *Thermal Figure of Merit* (TFM), which is the inverse of thermal impedance (see Eq. 1.9) [61]. Since the goal of any thermal management solution is to minimise the temperature difference between the coolant and the silicon sensor, the chosen solution must minimise the TFM.

$$\text{TFM} = \frac{\Delta T_{\text{sensor - coolant}}}{\text{Surface Power Density}} \left[\frac{\text{K}}{\text{W/cm}^2}\right] \tag{1.9}$$

Although the TFM can be minimised by bringing the heat sink and the connecting thermal interfaces closer to the silicon sensor and electronics, this introduces additional material, which would deteriorate the track reconstruction parameters. Therefore, the optimal thermal management strategy for any silicon detector is to simultaneously minimise the TFM (i.e., temperature gradient) by introducing minimum x/X_0 (i.e., mass of the thermal bridge to the heat sink). This sections aims to summarise the state-of-the-art thermal management strategies which are integrated and planned for various experiments. Detailed overviews of these methods are discussed in [61–66] and R&D updates from various experiments are reported annually in *Forum on Tracking Detector Mechanics* [67].

1.2.1. Gas Cooling

Silicon detector cooling by using gas as the coolant is the ideal choice for experiments focusing on low-momentum observables due to negligible additional material budget required to integrate gas cooling. The heat transfer between the gas and heat-producing elements (sensors and electronics) is achieved by channelling the gas directly onto these elements by using the detector support structures as ducts and/or introducing lightweight profiles (such as nozzles, perforated tubes, etc.) (see Fig. 1.10). However, gas cooling methods are inherently limited to remove low power dissipation (~ 50 mW/cm^2) due to the low specific heat capacity of gases (see Tab. 1.2). Moreover, these methods can lead to large temperature gradients without proper channelling of the air flow onto the sensor, and they carry the risk of introducing dynamical structural fluctuations, such as vibrations, at higher flow rates. Collectively, this results in a large TFM (~ 100 K·cm^2/W), albeit without adding substantially extra material budget.

Based on these considerations, thermal management strategies based on gas cooling have been deployed in silicon detectors of precision physics experiments at lepton colliders, such as the Belle II PXD [68, 69] and the Mu3e Vertex Detector [70, 71]. Moreover, gas cooling has also been used in silicon detectors of heavy-ion experiments, such as the STAR PXL-HFT [72, 73] and will be used for the ALICE ITS3 [74–76] (see Fig. 1.11). Notably, the Mu3e Vertex Detector has used gaseous helium cooling which has almost five times higher specific heat capacity and 17 times lower radiation length than air (see Tab. 1.2). This has paved the way to use gas cooling of silicon detectors with much higher power dissipation of up to 400 mW/cm^2, while simultaneously lowering the material budget and TFM.

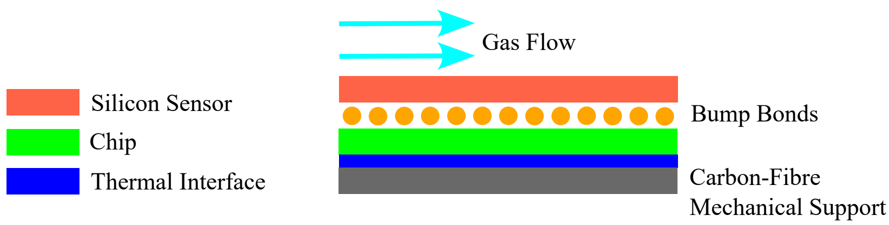

Figure 1.10.: Illustration of the thermo-mechanical layout for gas cooling of silicon detectors (figure not to scale; adapted from [77]).

Coolant	Density [kg/m^3]	Radiation Length [m]	Material Budget [% X_0; for 1 m]	Thermal Conductivity [W/m·K]	Specific Heat Capacity [J/kg·K]
Air	1.205	304	0.329	0.026	1006.1
Nitrogen	1.165	326	0.307	0.026	1041.3
Helium	0.166	5671	0.018	0.154	5193.2

Table 1.2.: Properties of gases commonly used for cooling silicon detectors (values at NTP conditions of 20°C and 1 atm; compiled from [55, 78]).

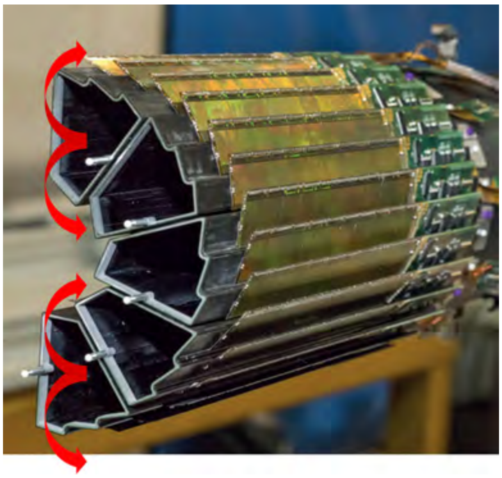

(a) STAR PXL-HFT

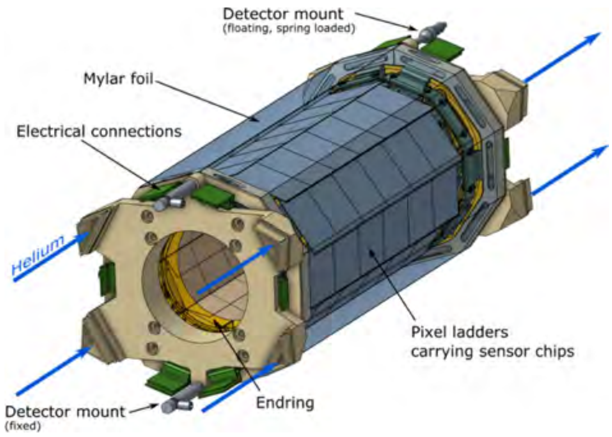

(b) Mu3e Vertex Detector

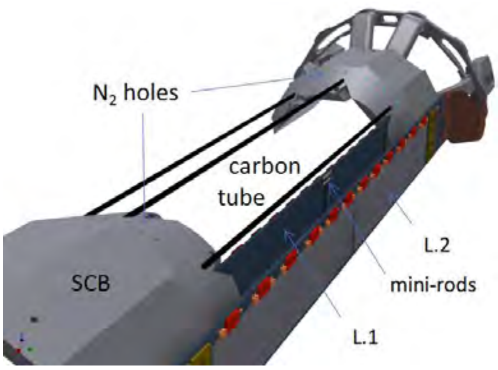

(c) Belle II PXD

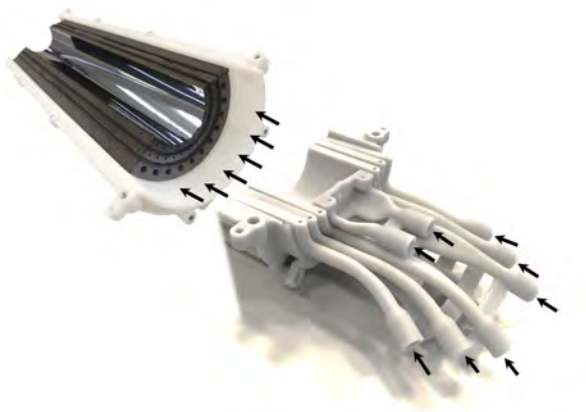

(d) ALICE ITS3

Figure 1.11.: (a) Assembled STAR PXL detector showing silicon sensors assembled on carbon-fibre *sector tubes*. These tubes act as air ducts guiding the air flow (shown as red arrows) along both the inside and outside surfaces of the sector (figure from [79]). (b) Schematic of the Mu3e vertex detector, where the ladder support structure *endrings* also contain helium inlets and outlets (blue arrows) to provide helium flow between the inner layers (figure from [70]). (c) Mechanical design of the Belle II PXD, where sensor holding ladders are mounted on peripherally located *Support and Cooling Blocks* (SCBs), which also contain open channels to provide forced nitrogen flow. Moreover, perforated carbon tubes are also running along the ladders to directly channel nitrogen onto the sensors to provide additional local cooling. Note that the peripherally located chips on the sensor are cooled with biphase CO_2 through the channels engraved in the SCBs (figure from [68]). (d) Engineering model of the ALICE ITS3 showing half barrel assembly and the air-cooling-ducts for the 3 layers (air flow flowing parallel to the sensor surface illustrated as black arrows) (figure from [75]).

1.2.2. Liquid Cooling

The silicon detectors exposed to high radiation damage in environments like hadron-hadron colliders (e.g., LHC; $\sim$ 100 MGy/10 years) dissipate power of $\sim$ 1 W/cm^2. Therefore, liquid coolant-based heat sinks are attached to the heat-producing elements (sensors and electronics) to enhance the heat transfer coefficient between them, thus reducing TFM but also increasing x/X_0. Various optimisation strategies, both for thermal path topologies in the thermo-mechanical structures and coolant configurations, are discussed below.

(a) Thermo-Mechanical Structures:
Earlier generations of silicon detectors ($<$ 2013) were cooled by gluing the heat producing elements to the peripherally located heat sink/cooling pipe via a thermally conducting ledge (see Fig. 1.12(a)) [62]. The thermal efficiency of this method is primarily limited by the thermal resistance introduced by multiple thermal interfaces of different CTE, leading to a non-uniform temperature distribution, large thermal stresses, TFM ($\sim$ 20 K·cm^2/W), and material budget (2% X_0 per layer) (see Tab. 1.3(a)). Subsequent generations of silicon detectors have undergone significant optimisation to simultaneously reduce TFM and x/X_0 (see Tab. 1.3(b,c)). This has been achieved by: (i) eliminating multiple thermal interfaces by integrating the cooling pipe/channel into detector support structure to form so called cold plate, and, (ii) using lightweight, rigid and thermally conductive components as cold plate materials. The approaches here mainly include the use of a cold plate with embedded cooling pipe in lightweight carbon core (see Fig. 1.12(b)) and distributed microchannels in silicon substrate (see Fig. 1.12(c)) [80]. Moreover, these approaches have also resulted in significant reduction of thermal stresses caused by CTE mismatches.

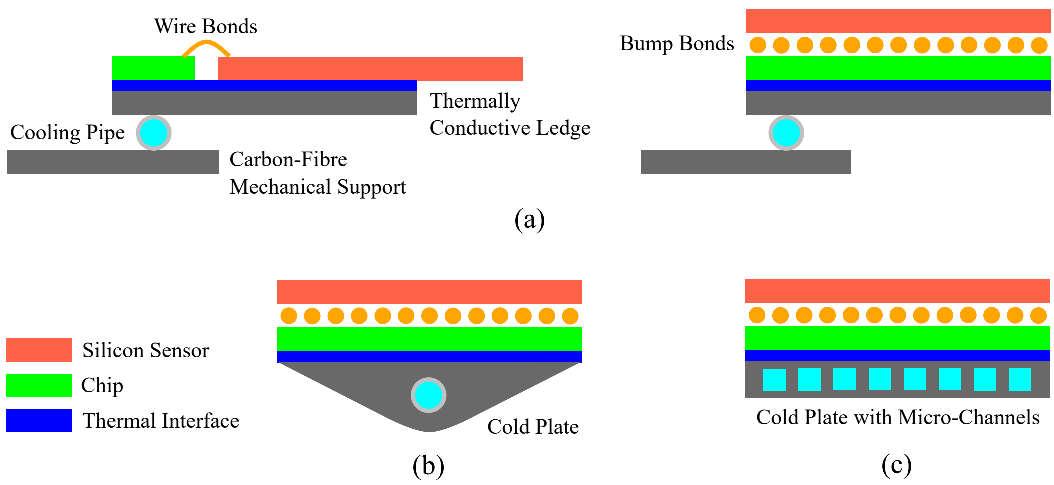

Figure 1.12.: Illustration of different thermo-mechanical structures and the underlying cooling topologies (figure not to scale; adapted from [77]).

Thermo-mechanical Structure Type	Material Budget [% X_0 per layer]	TFM [K·cm^2/W]	Example Use Cases
(a) Cooling pipe with thermally conductive ledge	~ 2	~ 20	ATLAS SCT [96,97] LHCb VELO [98–100]
(b) Embedded-pipe cooling plate	~ 1	~ 12	ATLAS IBL [101] ALICE ITS-2 [102,103] ATLAS ITk [104–106]
(c) Microchannel cooling plate	~ 0.5	~ 3	NA62 GTK [92,107] LHCb VELO Upgrade I [108,109]

Table 1.3.: Properties of thermo-mechanical structures commonly used in tandem with liquid cooling for silicon detectors (values indicative only; compilation from [60,77]).

(b) Coolant Configurations:

Mono-phase Cooling: Systems using liquids without state change have a simple design, operate under low pressure, and lack complex regulation loops. However, they are limited to remove power dissipation of ~ 0.1 W/cm^2 in cold plates with embedded cooling pipe to minimise the temperature gradient over the detector, while minimising the pressure drop due to high viscosity (see Tab. 1.4). Nevertheless, combining mono-phase liquid cooling with optimised thermo-mechanical structures like microchannels, has resulted in an overall higher thermal efficiency (see Fig. 1.13). Water-based cooling is prevalent in room temperature silicon detectors and is preferably operated in *leakless mode* (i.e., water pressure below the atmospheric pressure) [81–83]. This mode is standard for LHC-based detectors, such as the ALICE-ITS using it with thermally conductive lightweight carbon-based cold plates with embedded polyimide cooling pipes [84–86]. Sub-zero temperature silicon detectors utilise coolants like water-glycol mixtures and fluorocarbons like C_6F_{14}, used in CDF SVX-II [87,88] and CMS Phase-I SST [89,90], respectively. Notably, the NA62 GTK [91,92] pioneered silicon micro-fabrication with C_6F_{14} to neutralise power dissipation of up to 2 W/cm^2 at sensor temperatures < -10°C. Moreover, spur-oxygenated fluoroketones ($C_nF_{2n}O$) like 3M™ NOVEC™ 649, have recently gained popularity due to low Global Warming Potential (GWP) and thermodynamic similarities to C_6F_{14} [93]. However, being a per- and poly-fluoroalkyl (PFAS) raises concerns about toxicity, prolonged degradation and potential discontinuation [94,95].

Coolant	Density [kg/m^3]	Radiation Length [m]	Thermal Cond. [W/m·K]	Specific Heat Capacity [J/kg·K]	Kin. Viscosity [$\times 10^{-6}$ m^2/s]	Min. Temp. [°C]	GWP [-]
Water	998.2	0.362	0.598	4184.1	1.003	0	-
Ethylene glycol (52% v/v)	1082	0.347	0.402	3260	4.5	-40	-
C_6F_{14}	1690.7	0.205	0.066	1038.9	0.425	-90	7910
3M™ NOVEC™ 649	1617.5	0.215	0.059	1099.2	0.415	-108	1

Table 1.4.: Properties of mono-phase liquids commonly used for cooling silicon detectors (values at NTP conditions of 20°C and 1 atm; compiled from [55,78,110,111]).

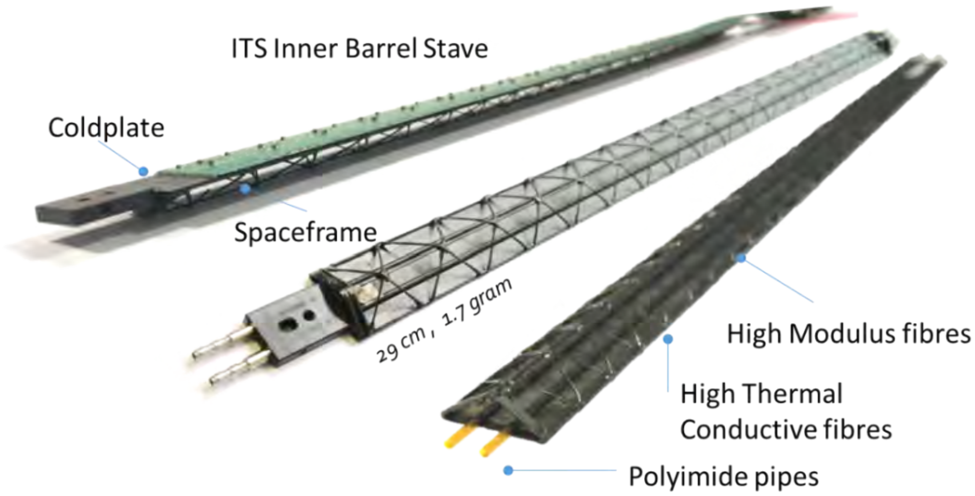

(a) ALICE ITS-2

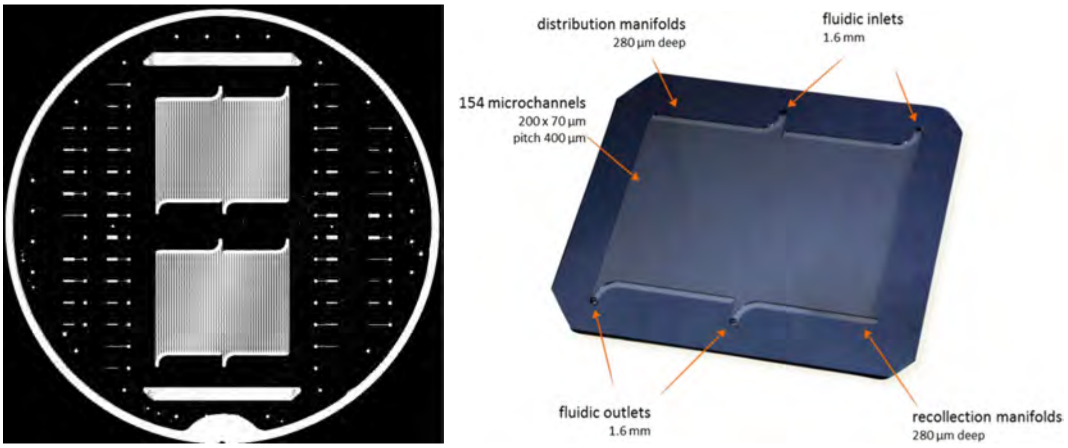

(b) NA62 GTK

Figure 1.13.: (a) Assembled inner barrel (IB) stave of ALICE ITS-2, where the thermo-mechanical structure comprises of the cold plate stiffened by the carbon-filament-wound *Spaceframe* with a triangular cross section. The cold plate is made of several layers of thermal conductive carbon plies with embedded polyimide cooling pipes (inner diameter 1.024 mm) carrying water in “leakless” mode. The mean material budget of the assembled stave is 0.3% X_0, which primarily includes the coldplate, sensors, flexible printed circuit and water (figure from [112]). (b) Silicon microchannel cooling plate for the NA62 GTK cooled with mono-phase C_6F_{14}. Left: Scanning Acoustic Microscopy image of the wafer hosting two cold plates (figure from [107]). Right: Silicon microchannel cooler (outer dimensions 80 × 70 mm) comprising two parallel fluidic circuits. The central part of the silicon microchannel cooler is thinned down to 210 µm and contains 154 microchannels. Each microchannel has a cross-sectional dimension of 200×70 µm^2, a length of 50 mm and a pitch of 400 µm. The material budget of the assembled station is 0.5% X_0, with the cooler contributing to only 0.22% X_0 (figure from [92]).

Evaporative or Bi-phase Cooling: Bi-phase cooling uses isothermal evaporation to effectively extract cooling capacity per unit volume by utilising the latent heat of evaporation. Compared to mono-phase cooling, bi-phase cooling offers advantages, including: (i) reduced coolant flow rates, enabling smaller pipe diameters and reduced material budget; (ii) uniform temperature along the cooling pipe and the detector surface; (iii) a wide range of achievable temperatures. However, bi-phase cooling requires complex multi-branch evaporative compression cycles and control loops. Nevertheless, its higher volumetric heat transfer coefficient along with reduced material budget has established bi-phase cooling circuits as the primary solution for most silicon detectors at hadron colliders [60].

The first generation of most silicon detectors at the LHC used saturated n-type fluorocarbon refrigerants $C_nF_{(2n+2)}$ [113, 114], such as C_3F_8 and C_4F_{10} were used at the ATLAS ID [115–117] and ALICE SSD [118], respectively. The newer generation of silicon detectors at LHC are increasingly using CO_2 due to: (i) high latent heat of evaporation and the low viscosity, further reducing pipe diameter and material budget; (ii) carbon-neutral nature with a GWP = 1; (iii) long term availability and cheaper refilling; (iv) radiation-tolerant, nonflammable and non-toxic characteristics (see Tab. 1.5). Pioneered for high-energy physics experiments by the LHCb VELO, the 2-Phase Accumulator Controlled Loop (2PACL) method deploys CO_2 as a liquid-pumped, oil-free system with precise temperature control via pressure regulation in the CO_2 accumulator tank [119–121]. This concept has been further implemented in several upgrades, such as the ATLAS IBL [101], CMS Phase-1 Pixel Detector Upgrade [122, 123], and the LHCb VELO Upgrade-I [109] (see Fig. 1.14). Notably, bi-phase CO_2 cooling in silicon microchannels at the LHCb VELO Upgrade-I achieved a TFM of 1.5 - 3.5 K·cm^2/W, neutralising a power dissipation of 0.88 W/cm^2 at a coolant temperature of -30°C. Consequently, future upgrades for silicon detectors of ATLAS and CMS at HL-LHC with bi-phase CO_2 cooling are also underway [124–129]. Moreover, R&D on Krypton-based cooling systems is also underway to enable even lower evaporation temperatures than CO_2 (triple point -56.6°C) to negate the future requirements of ever increasing radiation tolerance [37, 130–134].

Coolant	Boiling Temp. at 1 atm [°C]	Evaporation Pressure at 20°C [bar]	Critical Point		Latent Heat at 20°C [kJ/kg]	Liquefied Gas Properties at 20°C and boiling pressure or 1 atm*			GWP [-]
			Temp. [°C]	Pressure [bar]		Density [kg/m^3]	Specific Heat Capacity [kJ/kg·K]	Kin. Viscosity [$\times 10^{-6}$ m^2/s]	
C_3F_8	-36.8	7.56	71.9	26.4	79.1	1352	1.15	0.131	8900
C_4F_{10}	-2.2	2.29	113.2	23.2	88.9	1515	1.14	0.185	9200
CO_2	-78.4	57.29	30.97	73.8	152	773	4.3	0.086	1
N_2O	-88.5	50.53	36.4	71.5	169.9	785	3.2	0.087	265
Krypton*	-153.42	-	-63.7	55.3	- Supercritical -				0

Table 1.5.: Properties of bi-phase liquids commonly used for cooling silicon detectors (compiled from [78, 131]).

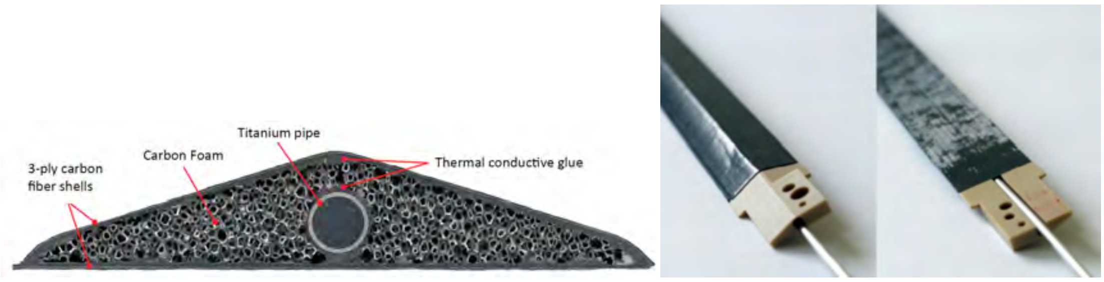

(a) ATLAS IBL

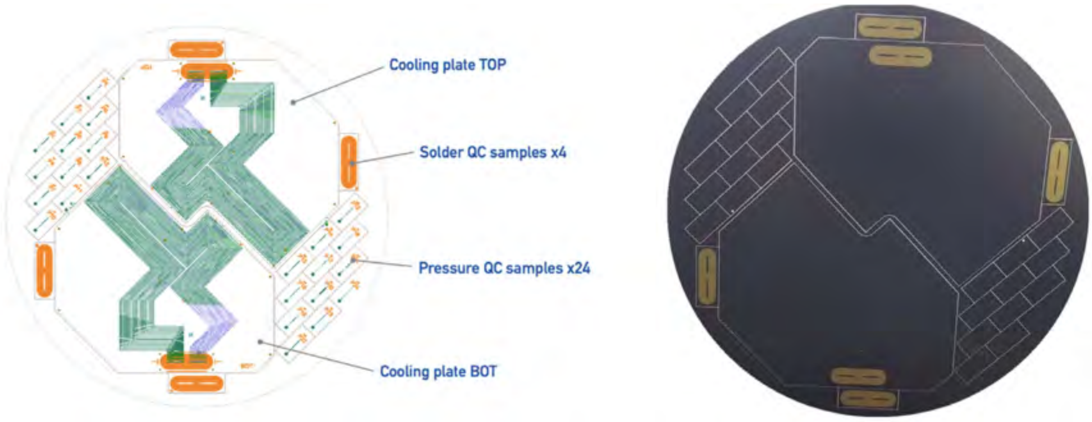

(b) LHCb VELO Upgrade

Figure 1.14.: (a) Left: The transverse section of a bare ATLAS IBL stave. It primarily comprises of four components, namely titanium cooling tube with bi-phase CO_2 (1.7 mm external diameter), thermally-conducting carbon foam, carbon-fiber reinforcement shells and further plastic fixation structures (not shown in the figure). All components are glued together with a thermally conducting epoxy (figure from [101]). Right: Photographs of an end of the bare ATLAS IBL stave, with the plastic fixation structure also shown. Each bare stave is 724 mm long, 18.8 mm wide and has a material budget of 0.62% X_0, while the assembled stave totals to 1.88% X_0 (figure from [135]). (b) Left: Wafer layout of the LHCb silicon microchannel cooler with bi-phase CO_2 coolant. Each wafer is eight-inch-wide, 500 µm thick and hosts two coolers. Each cooler comprises 19 channels, each with a cross-sectional dimension of 120×200 µm^2, a length ranging from 231 to 292 mm, and a pitch of 700 µm. Each cooler also consists of a metallised footprint for bonding an input-output connector block. Other peripheral features on the wafer include four additional connector footprints for metallisation and adhesion tests, and 24 pressure control samples. Right: Photograph of the processed and diced wafer of silicon microchannel cooler. The material budget of the bare wafer corresponds to 0.53% X_0, while the per layer contribution totals to $\approx$ 3% X_0 (figure from [109]).

1.3. The Compressed Baryonic Matter Experiment at FAIR

The Facility for Antiproton and Ion Research (FAIR) is an international flagship accelerator facility in Darmstadt (Germany), which aims to decipher the property of matter as created under astrophysical conditions [136–138]. The physics programme of FAIR is focused on nuclear and hadron physics, and on applied research, and is addressed by its four scientific pillars:

(i) Atomic, Plasma Physics and Applications (APPA)
(ii) Compressed Baryonic Matter (CBM)
(iii) Nuclear Structure, Astrophysics and Reactions (NUSTAR)
(iv) AntiProton Annihilation at Darmstadt (PANDA)

FAIR is currently under construction adjacent to the GSI Helmholtz Centre for Heavy Ion Research. FAIR's physics goals are centred around a 1,100-metre-long and 100 T·m ring accelerator named Schwerionensynchrotron-100 (SIS-100), which will use GSI's SIS-18 synchrotron as an injector. These primary high-intensity beams of protons and heavy ions can be converted into intense secondary beams of antiprotons and rare isotopes, and stored into a network of storage rings enabling FAIR to conduct its extensive physics programme (see Fig. 1.15).

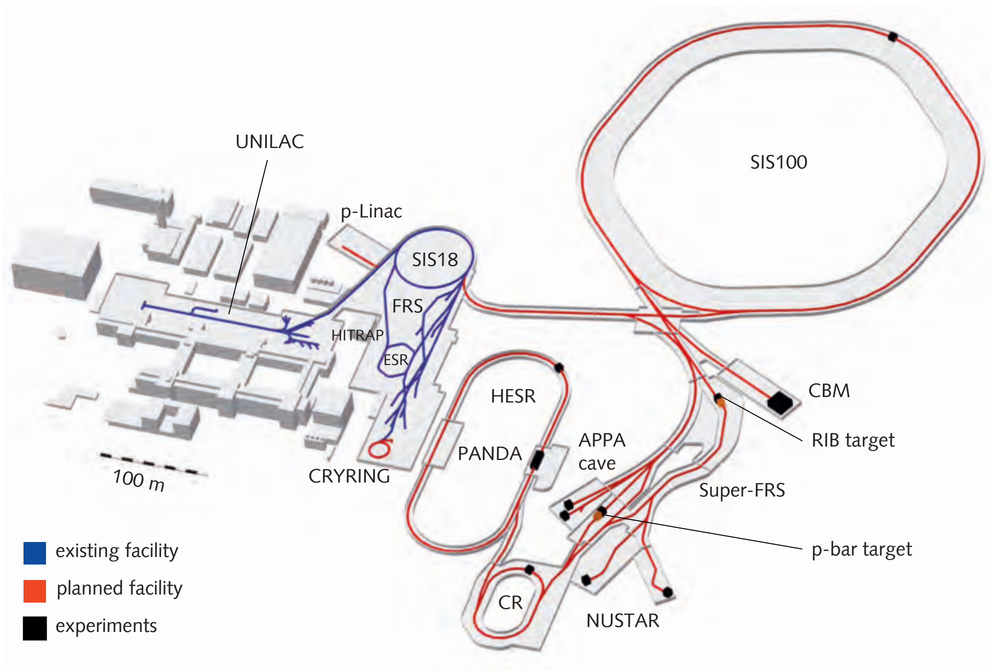

Figure 1.15.: Layout of GSI-FAIR with the existing and planned beamlines are shown in blue and red, respectively. The experimental sites are marked in black (figure from GSI/FAIR Darmstadt).

The CBM experiment at FAIR explores heavy-ion collisions in the SIS-100 energy range (Au+Au, $\sqrt{s_{NN}} = 2.9 - 4.9$ GeV), probing the high-density region of the Quantum Chromodynamics (QCD) phase diagram (see Fig. 1.16). This uniquely positions CBM to answer the fundamental questions for QCD at supra-saturation densities ($\gtrsim 3\rho_0$). Additionally, the achieved densities at SIS-100 energy range are comparable to astrophysical events like binary neutron-star mergers, offering CBM a distinctive role in the growing field of multi-messenger inference of neutron star properties [139–141]. More details on CBM's physics goals and experimental observables are reviewed in [32–34].

- Equation of State (EOS) of symmetric nuclear (and asymmetric neutron) matter at neutron star core densities
- Phase structure of QCD matter and the conjectured first-order phase transition between Hadron Gas and Quark Gluon Plasma (QGP)
- Chiral phase transition and symmetry restoration at high densities
- Strange matter, including hypernuclei and bound states with strangeness
- Charmonium production and properties in cold-dense matter

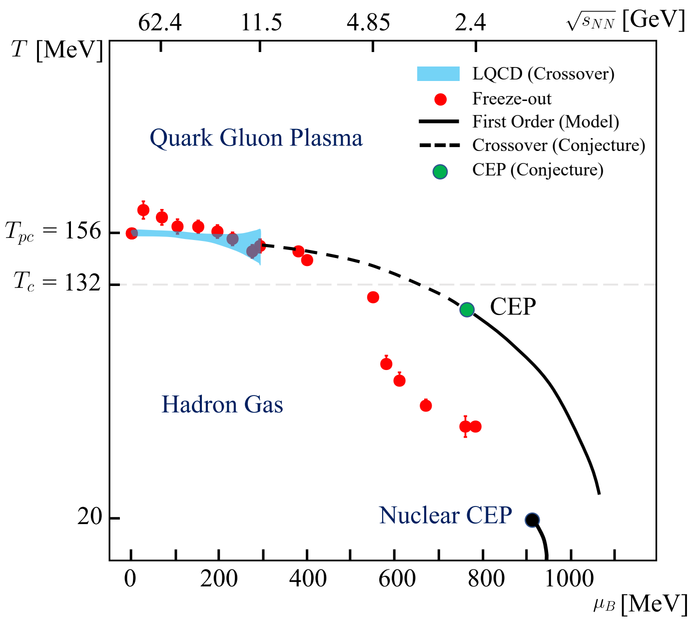

Figure 1.16.: QCD Phase Diagram shown as a variation of temperature (T) with baryon chemical potential (μ_B) and centre-of-mass energy of heavy-ion collisions ($\sqrt{s_{NN}}$). It highlights two main QCD matter phases: Hadron Gas and Quark-Gluon Plasma (QGP). The red symbols correspond to the chemical freeze-out parameters determined from the experimental hadron yields [142, 143]. The blue band corresponds to Lattice QCD (LQCD) calculations of the chiral phase boundary [144, 145]. Moreover, the nuclear liquid-gas phase boundary [146] and the conjectured line of the first-order phase transition with a critical end point (CEP) are also shown (figure from [147]).

CBM is designed as a fixed-target experiment (depicted in Fig. 1.17) with an angular acceptance of $2.5° < \theta < 25°$ allowing sufficient rapidity coverage over the entire energy range. The standout feature of CBM compared to other experiments in a similar energy range is the unprecedented beam-target interaction rates of up to 10 MHz. This enables CBM to perform precision multi-differential analyses with low-multiplicity 'rare probes', such as dileptons, multi-strange hyperons, and hypernuclei, sensitive to the previously listed physics goals. Therefore, all detector subsystems are equipped with novel free-streaming and radiation-hard readout electronics for online event selection and reconstruction [148–150]. A brief description of all detector subsystems is listed below:

1. Beam Monitor and Start (BMON) Detectors for beam diagnostics and to provide precise T_0 information for time-of-flight measurements [151].
2. Micro Vertex Detector (MVD) and the Silicon Tracking System (STS) tasked to resolve the secondary vertex of short-lived open-charm mesons and provide momentum determination of charged particles, respectively [35, 152].
3. Superconducting dipole magnet which houses the silicon detectors (MVD and STS) and provides a field integral of 1 T·m [153].
4. Muon Chambers (MuCh) for dimuon identification with Gas Electron Multipliers and Resistive Plate Chambers between hadron absorbers [154].
5. Ring Imaging Cherenkov (RICH) detector for dielectron identification with UV detector planes of multi-anode photomultiplier tubes [155].
6. Transition Radiation Detector (TRD) for pion suppression, particle tracking, and light-nuclei identification by using Multi-Wire Proportional Counters (MWPCs) with PE-foam radiators [156].
7. Time-of-Flight (TOF) wall for charged hadrons detection from Multi-Gap Resistive Plate Chambers (MRPCs) located about 7 m downstream [157].
8. Forward Spectator Detector (FSD) is used to determine the collision centrality and reaction plane orientation [158].

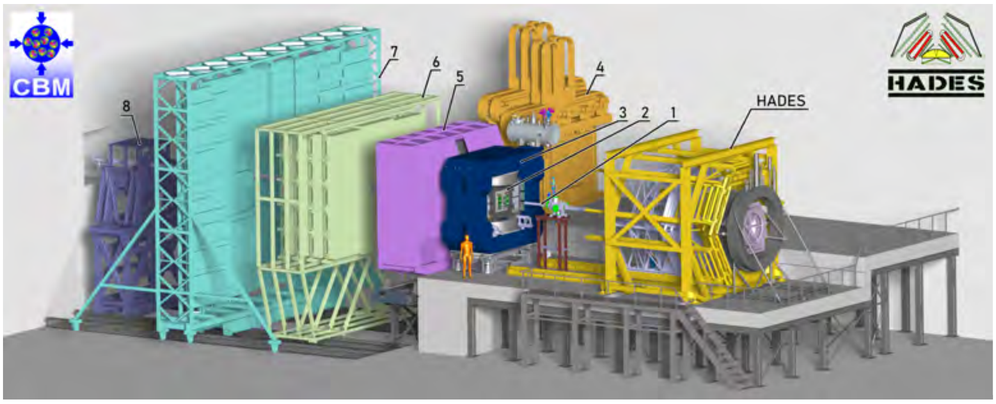

Figure 1.17.: Experimental setup of CBM (left) and HADES (right), with SIS-100 beam coming from right to left. Detector subsystem callouts are described in the text.

1.4. The Silicon Tracking System

The Silicon Tracking System (STS) [35, 36], located inside the 1 T·m superconducting dipole magnet, is the core tracking detector subsystem of the CBM experiment (see Fig. 1.18(a)). STS is primarily tasked with performing accurate track reconstruction ($> 95\%$) and momentum determination with high resolution ($< 2\%$) of emitted charged particles. It comprises eight equidistant tracking layers ($z = 0.3 - 1.0$ m), hereby referred to as *stations*, and has a polar angle coverage of $2.5° - 25°$ (see Fig. 1.18(b)). This allows STS to reconstruct both stable/long-lived particles[9] and short-lived particles[10] with sufficient rapidity coverage which is crucial for the CBM physics programme. The former can be tracked directly as they traverse the STS, whereas the latter decay before or shortly within the STS and are indirectly reconstructed by their decay products.

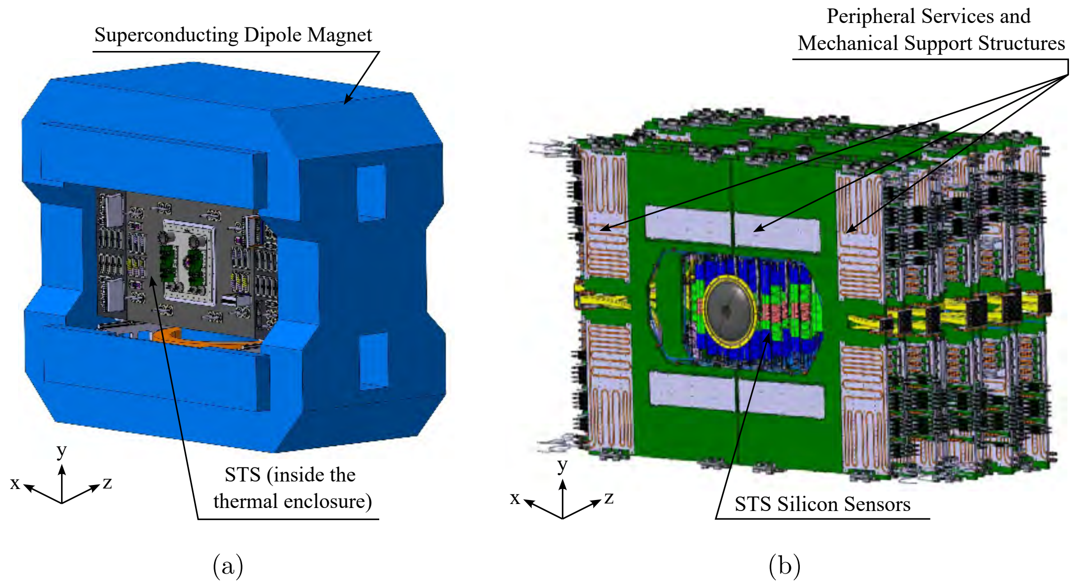

Figure 1.18.: (a) CAD rendering of STS, along with its thermal enclosure positioned inside the superconducting dipole magnet. (b) CAD rendering of the eight STS tracking stations. The silicon sensors are shown in bright red, green and blue colours, whereas the services are located at the periphery on C-shaped mechanical support structures (figures from O. Vasylyev (GSI Darmstadt)).

9. Decay length ($c\tau$) of some relevant long-lived particles
$\mu^{\pm} = 660$ m; $K^{\pm} = 3.7$ m; $\pi^{\pm} = 7.8$ m
10. Decay length ($c\tau$) of some relevant short-lived particles
Hyperons: $K_s^0 = 2.7$ cm; $\Lambda = 7.9$ cm
Multi-Strange Hyperons: $\Sigma^{+/-} = 2.4$ cm; $\Xi^0 = 8.7$ cm; $\Xi^- = 4.9$ cm; $\Omega^{+/-} = 2.5$ cm
Hypernuclei: ${}^3_\Lambda H = 5.5$ cm; ${}^4_\Lambda H = 5.4$ cm; ${}^4_\Lambda He = 4.5$ cm; ${}^5_\Lambda He = 4.2$ cm

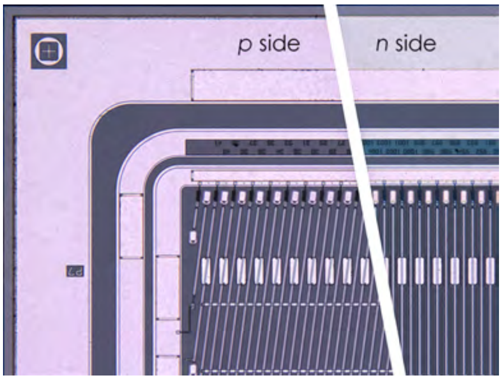

(a)

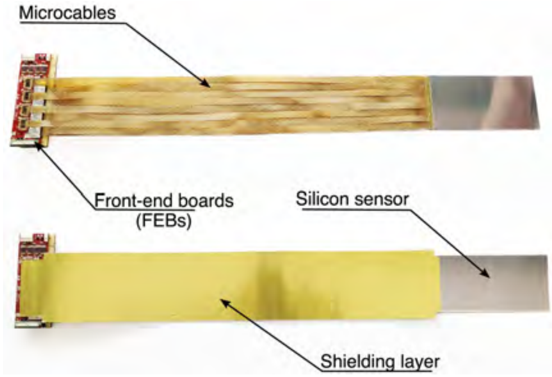

(b)

Figure 1.19.: (a) STS double-sided silicon microstrip sensor with both p and n side shown split (figure from [17]). (b) STS module with all its components, before and after connecting the shielding layers of the microcables (figure from [159]).

The STS utilises double-sided silicon microstrip sensors from Hamamatsu Photonics K.K. [160] for two-coordinate space-point measurement (see Fig. 1.19(a)). These sensors feature 1024 implanted p^+ and n^+ strips with a 58 µm pitch on either sides of an n-type bulk, wherein the p side is oriented at a 7.5° stereo angle relative to the n side. The sensors are 320 µm thick to provide sufficient signal-to-noise (S/N) ratio for efficient track reconstruction. The material budget contribution per sensor is $0.34\%X_0$. The sensors, with a width of 6.2 cm, come in four strip-length variants (2.2 cm, 4.2 cm, 6.2 cm, 12.4 cm) to cover different STS regions, providing high granularity, minimising hit occupancy, and reducing number of readout channels. In total, the STS comprises 876 sensors resulting in approximately 1.8 million channels. This extensive and granular sensing area allows to reconstruct the decay trajectories of about 700 charged particles emitted per Au+Au collision at 10 MHz interaction rate. Further details on sensor design, manufacturing, and quality assurance are available in Ref. [17, 35, 161, 162].

The functional block of the STS is called a *module* and it comprises a sensor connected to a pair of front-end boards (FEBs) via a stack of 32 ultra-thin aluminium-polyimide microcables (see Fig. 1.19(b)). Designed to minimise the material budget within the detector's physics acceptance, the FEBs are positioned outside this region, and the connecting microcables, up to 500 mm in length, contribute approximately $\approx 0.124\%X_0$ per module [163]. Each sensor side is read out by eight custom-designed self-triggering SMX2 ASICs[11]with 128 channels each, providing a simultaneous measurement of the signal amplitude (dynamic range < 15 fC; 5-bit) and time (resolution ≈ 5 ns; 14-bit) [164]. Therefore, this allows the STS to perform *5D tracking* by performing space (x, y and z co-ordinates), time, and energy (dE/dx) measurements [165].

11. Application Specific Integrated Circuit (ASIC) named STS/MuCh-XYTER2 (SMX2; Silicon Tracking System / Muon Chamber - X-Y-Time-Energy Read-out)

The structural unit following the STS modules, called *ladder*, can host up to 10 modules and spans up to 970 mm [166]. Herein, the silicon sensors are precisely and stably held by carbon-fibre space frames, and the corresponding FEBs are collectively housed in a FEB box outside the physics aperture (see Fig. 1.20(a)). The lightweight space frame construction locally adds a maximum of $0.60\%X_0$ material budget, averaging only $0.047\%X_0$ across the sensor area. In total, the STS comprises 106 ladders, each with a material budget of 0.3 ... $1.4\%X_0$. Subsequently, up to four ladders are arranged on either side of a C-shaped aluminium support structure, called *C-Frame* (see Fig. 1.20(b)). The C-Frame also accommodates GBT-based[12] readout boards (ROBs) [167, 168], FEASTMP-based[13] power boards (POBs) [169], and the cooling elements of electronics and silicon sensors. Overall, the STS is composed of 20 such C-frames housed in a CF-foam thermal enclosure, with a section for the vacuum beam pipe in the center (see Fig. 1.18).

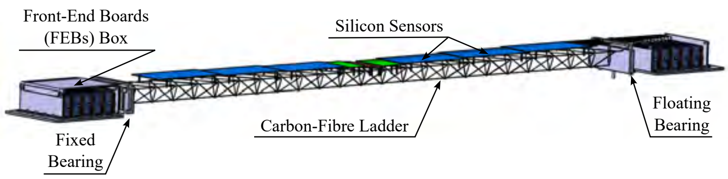

(a)

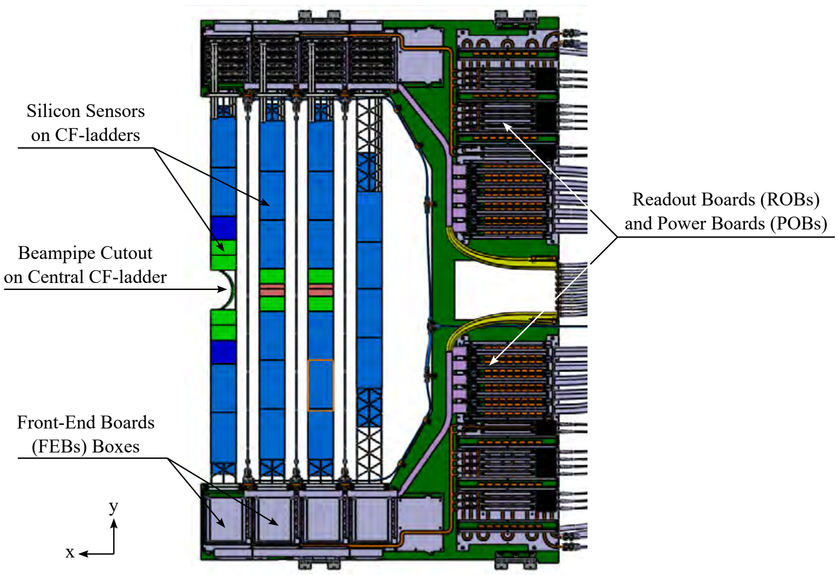

(b)

Figure 1.20.: CAD renderings of an assembled (a) STS ladder, (b) C-frame, with the underlying components (figures from O. Vasylyev (GSI Darmstadt)).

12. GigaBit Transceiver (GBT) architecture that aggregate the e-link data streams on to optical link to the central high-performance computing farm
13. FEASTMP is a radiation-hard DC/DC converter module

1.5. Motivation and Requirements for CBM-STS Thermal Management

The primary motivation for efficient thermal management of the CBM-STS is to negate the adverse effects of radiation damage on the silicon bulk and consequently on the sensor performance (see Sec. 1.1.1 for general theory about the role of temperature in silicon sensor performance). The STS is designed to withstand a non-ionising fluence (Φ_{eq}) of up to 10^{14}n$_{eq}$(1 MeV)/cm^2 during its lifetime [35], and is hereby referred as end-of-lifetime fluence (EOL Φ_{eq}). This has been verified by studying the full-depletion voltage and charge collection efficiency behaviour of smaller prototype STS sensors in a series of irradiation campaigns in 2014-15 [170] and 2018-19 [171, 172] (see App. C and App. D for details). It's worth noting that the updated FLUKA[14]calculations for the foreseen CBM operating scenario suggests that the accumulated Φ_{eq} over the expected duration of CBM operation, i.e., 10 years, will sum up to 0.24×10^{14}n$_{eq}$(1 MeV)/cm^2 (see Fig. 1.21 and App. A for more details). Therefore, the EOL Φ_{eq} will only be accumulated after 40 years of CBM operation, consequently providing substantial safety margin in determining the STS's operating parameters.

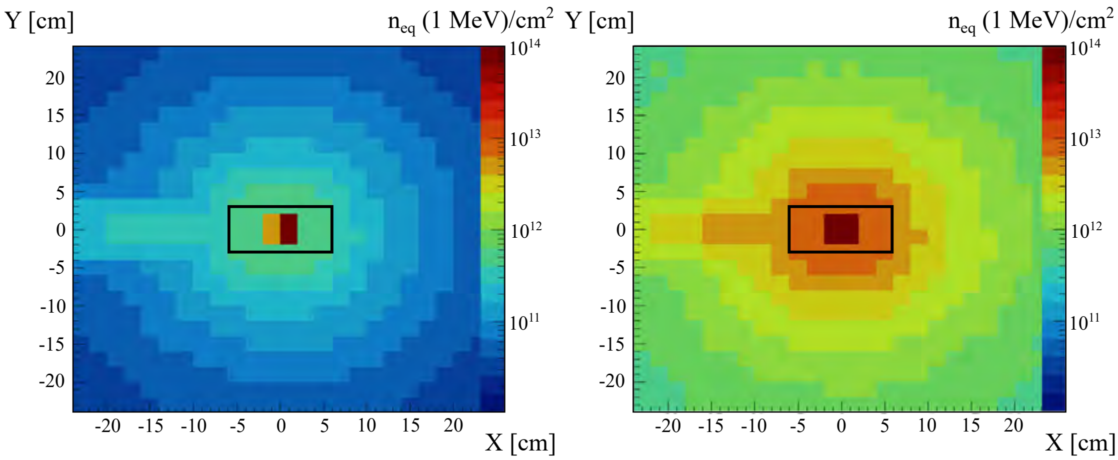

(a) Baseline Beam Intensity (b) Maximum Beam Intensity

Figure 1.21.: FLUKA simulations showing the fluence distribution for the first STS station located 30 cm downstream from the target. Calculations are for the 3-year running scenario foreseen at (a) baseline, and (b) highest beam intensities (see App. A for more details). Please note that the black rectangle represents the beam opening, and the and the highest on-sensor value corresponds to 0.01×10^{14}n$_{eq}$(1 MeV)/cm^2 and 0.1×10^{14}n$_{eq}$(1 MeV)/cm^2, respectively (figure from [174]).

14. "FLUKA" stands for FLUktuierende KAskade (German for "fluctuating cascade") and is a general-purpose particle physics Monte Carlo simulation code used for the simulation of the interaction and transport of particles and radiation in matter [173].

The role of temperature in mitigating the adverse affects at EOL Φ_{eq} on the electrical performance of STS is discussed in the following points.

(a) Leakage Current and Signal-to-Noise (S/N): The track reconstruction and momentum resolution requirements mandates that S/N $\geq$ 10 must be maintained for the STS [175]. Extensive experimental studies carried out with prototype and pre-production components have resulted in reliable modelling of both signal and noise of the STS detector modules (see App. B for more details). These models, in tandem with Eq. 1.1 introduced in Sec. 1.1.1, allows to estimate the S/N behaviour of STS modules with fluence and temperature (see Fig. 1.22(a)). Therefore, STS sensors could be operated at temperatures as high as $+14^{+4.7}_{-6.1}$°C at EOL Φ_{eq}, and still fulfill the criteria to obtain S/N $\gtrsim$ 10.

(b) (Reverse) Annealing of Full Depletion Voltage: The STS has been designed to operate at maximum 500 V to fully collect the deposited charge in the silicon [171, 172]. Therefore, the temperature-dependent reverse annealing must be controlled to keep the full depletion voltage V_{dep} safely below 500 V. The evolution of V_{dep} for smaller STS-type prototype sensors has been experimentally studied [170] to parameterise the annealing time constants using the Hamburg Model [39] (see Sec. 1.1.1 for introduction and App. C for more details). These parameters can be used to calculate the variation of V_{dep} with annealing time at EOL Φ_{eq} for different temperatures (see Fig. 1.22(b)). Therefore, V_{dep} for the STS sensors after accumulating EOL Φ_{eq} will safely remain below 500 V for temperatures as high as +10°C even after 10 years of annealing.

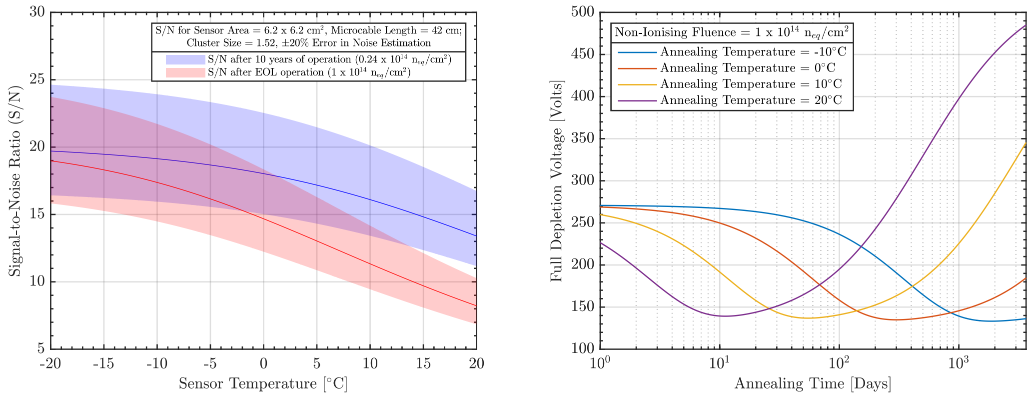

(a) (b)

Figure 1.22.: (a) Variation of module S/N with sensor temperature after 10 years and EOL fluence. The shaded bands indicate 20% modelling error. The results are for the longest and innermost STS sensor module (located on the ladder #1008), by assuming all charge is collected and mean cluster size of 1.52 (taken from [175]]). (b) Variation of Full Depletion Voltage of STS sensors with annealing time of up to 10 years after EOL fluence and being annealed at different temperatures (-10 ... +20°C).

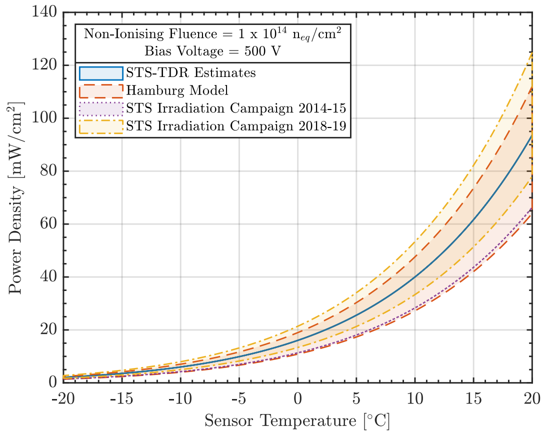

Figure 1.23.: Variation of STS sensor power density with temperature at the end-of-lifetime conditions for different estimates. More details in App. D.

Sources	Values [W]
Front-End Boards (FEBs)	25756
Readout Boards (ROBs)	2817
Power Boards (POBs)	6770
Powering Cables	2938
Thermal Enclosure	943

Table 1.6.: Different power dissipation sources inside STS (maximum values used for designing the cooling plant). More details in Ref. [176, 177].

Therefore, STS sensors can deliver S/N $\gtrsim$ 10 and have V_{dep} safely below 500 V at temperatures ≈+10°C after accumulating EOL Φ_{eq} over 10 years of STS operational lifetime. This imposes the following conditions on both silicon sensor and electronics cooling.

(a) Silicon Sensor Cooling: The STS sensor cooling concept has to be efficient enough to compensate for the rising sensor power dissipation ($T^2 \cdot e^{-1/T}$; maximum of ≈ 53.4 mW/cm^2 at +10°C at EOL Φ_{eq}) and preventing it from going into a state of thermal runaway (see Fig. 1.23) [178]. Moreover, this must be achieved by minimal introduction of additional material budget within the detector's physics acceptance. This is specially crucial for the innermost silicon sensors of every tracking station in the vicinity of the beampipe, as they will accumulate the highest fluence and will consequently dissipate the highest power (Δx = Δy $\leq \pm$ 10 cm; see Fig. 1.21).

(b) Electronics Cooling: The power dissipation caused due to STS electronics and powering cables total up to ∼ 40 kW (see Tab. 1.6) in the detector volume of 3.5 m^3 [176,177]. Since the FEB boxes hosting these electronics are only 25 ... 50 cm away from the innermost silicon sensors (see Fig. 1.20(b)), the temperature gradient between the two must be minimal and FEE power dissipation should be completely neutralised. Therefore, the target electronics temperature is also ≈+10°C. Given the high power density, a thermally conducting path is required to efficiently carry the power dissipated by the electronics to the heat sink. Moreover, the underlying coolant must be radiation hard (up to 10 kGy), have a high volumetric heat transfer coefficient and should be environmentally friendly (Global Warming Potential = 1).

1.6. Thesis Scope

This thesis focuses on the thermal management of the CBM-STS, both for silicon sensors and front-end electronics. It systematically addresses crucial aspects spanning from thermal simulations to detector integration and mechanical considerations, culminating in rigorous experimental validation.

Initially in Chap. 2, the thesis concentrates on theoretical calculations and numerical simulations to model the cooling behaviour of silicon sensors and front-end electronics. Through these simulations, the aim is to establish a viable cooling concept and provide a theoretical foundation for the subsequent experimental investigations.

Building on the insights obtained from simulations, the thesis delves into the practical implementation of thermal management strategies in Chap. 3. This involves the design and construction of an experimental setup, hereby referred as the *Thermal Demonstrator*, that mirrors the conditions encountered by CBM-STS. Chap. 4 aims to validate the proposed thermal management strategies with the Thermal Demonstrator. Chap. 5 will summarise the contributions of the STS Thermal Demonstrator in context of the ongoing CBM-STS detector production and assembly.

Finally, this thesis concludes with a summary and an outlook in Chap. 6. The summary encapsulates the key findings and insights gained throughout the research process. Additionally, the outlook section discusses potential avenues for future research, extending the discussion beyond the immediate scope of the thesis.

2. CBM-STS Cooling Concept - Calculations and Simulations

The ever-growing silicon microelectronics miniaturisation coupled with detector signal processing requirements has resulted in a roughly common scheme for silicon detector modules where the sensitive silicon bulk is either bonded directly to the front-end electronics in its vicinity or both are implanted on the same monolithic silicon structure. Depending on the specific use case, the underlying thermal management strategy is broadly based on either "heavier" liquid cooling (for detectors at hadron colliders) or "lighter" air cooling (for detectors at heavy-ion and lepton colliders) (see Sec. 1.2 for general thermal management strategies). The design of the CBM-STS module, although utilising state-of-the-art silicon fabrication, has a unique design where the sensing and readout elements are connected via long microcables, ensuring minimal material budget (see Fig. 1.19). Consequently, the CBM-STS cooling concept is challenging yet fascinating due to this unique design, wherein the dedicated cooling concepts are needed for both highly-irradiated silicon sensors inside and power-intensive front-end electronics outside the detector's physics acceptance. The STS cooling concept uses *Liquid Assisted Air Cooling* (term coined by P. Petagna (CERN) and M. Voss (IFIC) [179]), where silicon sensors are air cooled to minimise the material budget, while peripherally located front-end electronics are cooled by liquid cooling, thereby combining the two most commonly used thermal management approaches. In this chapter, theoretical calculations and numerical simulations are used to gain an individual understanding about air-cooling for silicon sensors (Sec. 2.1) and liquid-cooling for front-end electronics cooling (Sec. 2.2). The collective understanding of the CBM-STS cooling concept are then summarised in Sec. 2.3.

2.1. Silicon Sensor Cooling

The primary objective of STS silicon sensor cooling is to provide sufficient "Cooling Power" to neutralise the exponential self-heating of sensors - "Heating Power" inhibit *Thermal Runaway*, while minimising the material budget of the cooling elements to maintain a stable operating temperature of ≈ 10°C (see Sec. 1.1.1 and Eq. 1.1b for further introduction). As illustrated in Fig. 2.1, effective cooling ensures that the stable temperature (T_{Stable}) is below the critical temperature ($T_{Critical}$) where the runaway occurs and system goes into an uncontrolled pos-

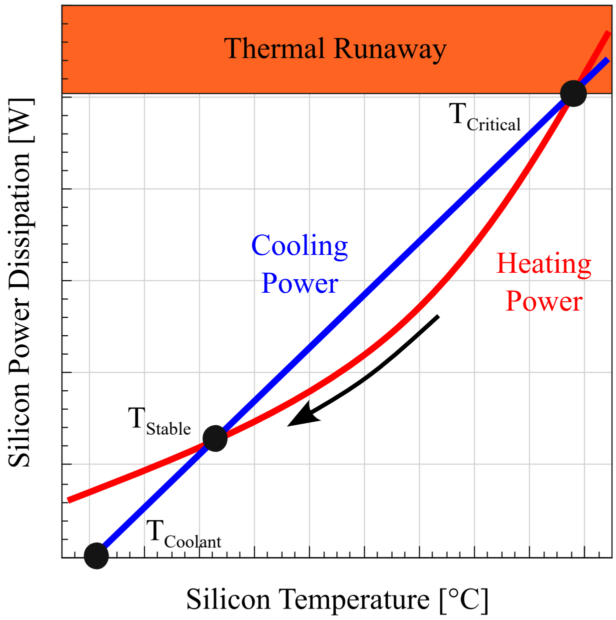

Figure 2.1.: Illustration of thermal runaway in silicon sensors shown as a variation of sensor's power dissipation with its temperature. The silicon sensor is in thermal runaway above the critical temperature ($T_{sensor} \geq T_{critical}$), while the silicon sensor stables below the critical temperature to a stable value ($T_{sensor} = T_{stable}$ at $T_{sensor} < T_{critical}$) (figure adapted from [15]).

itive feedback. Given the stringent material budget requirements of CBM-STS, air cooling is the most viable cooling concept for STS sensor cooling. This section aims to investigate the feasibility of sensor air cooling in terms of its capability to avoid thermal runaway within STS boundary conditions both by theoretical calculations (Sec. 2.1.1) and numerical simulations (Sec. 2.1.2). The heating power of a given silicon sensor will be calculated based on the expected accumulated fluence from FLUKA simulations, while the cooling power will be calculated by using widely-used empirical formulations and computational tools, such as Computational Fluid Dynamics (CFD) analysis.

2.1.1. Theoretical Calculations

Theoretically, STS sensor air cooling is described by *Convective Heat Transfer*, wherein the heat transfer rate ($\dot{q}$) is proportional to the temperature difference between the heat producing sensor surface (at T_s) and the surrounding moving air (at T_∞), as described by *Newton's Law of Cooling* (see Eq. 2.1):

$$\dot{q} = h \cdot (T_s - T_\infty) \tag{2.1}$$

where, the proportionality constant is the heat transfer coefficient (h). h is dependent on several factors such as the air velocity, air thermal properties (such as specific heat capacity (C_p) and thermal conductivity (k)), and the geometry of the heat-producing surface with characteristic length (L). Microscopically, the interaction between the sensor surface and surrounding air is dependent on the temperature and velocity gradients, resulting in the formation of a *boundary layer*. h combines both the random molecular motion near the surface (*diffusion* or *conduction*) and the bulk motion of air within the boundary layer (*advection*). The Nusselt number (Nu) is a dimensionless parameter that indicates the efficiency of convection relative to conduction (see Eq. 2.2), and is crucial for understanding the impact of boundary layer behaviour and flow conditions on convection.

$$Nu = \frac{h}{k/L} = \frac{\dot{q}}{(T_s - T_\infty)} \cdot \frac{1}{k/L} \tag{2.2}$$

In the case of *Natural Convection* (see Fig. 2.2(a)), the buoyancy forces caused by temperature differences creates a thicker boundary layer with laminar flow along the surface where the gradient of fluid velocity is gradual, resulting in a lower Nu and less effective heat transfer. In *Forced Convection* (see Fig. 2.2(b)), external forces drive the bulk air motion within the boundary layer, creating more turbulence, thinner boundary layer, and steeper gradients, leading to a higher Nu and more effective heat transfer.

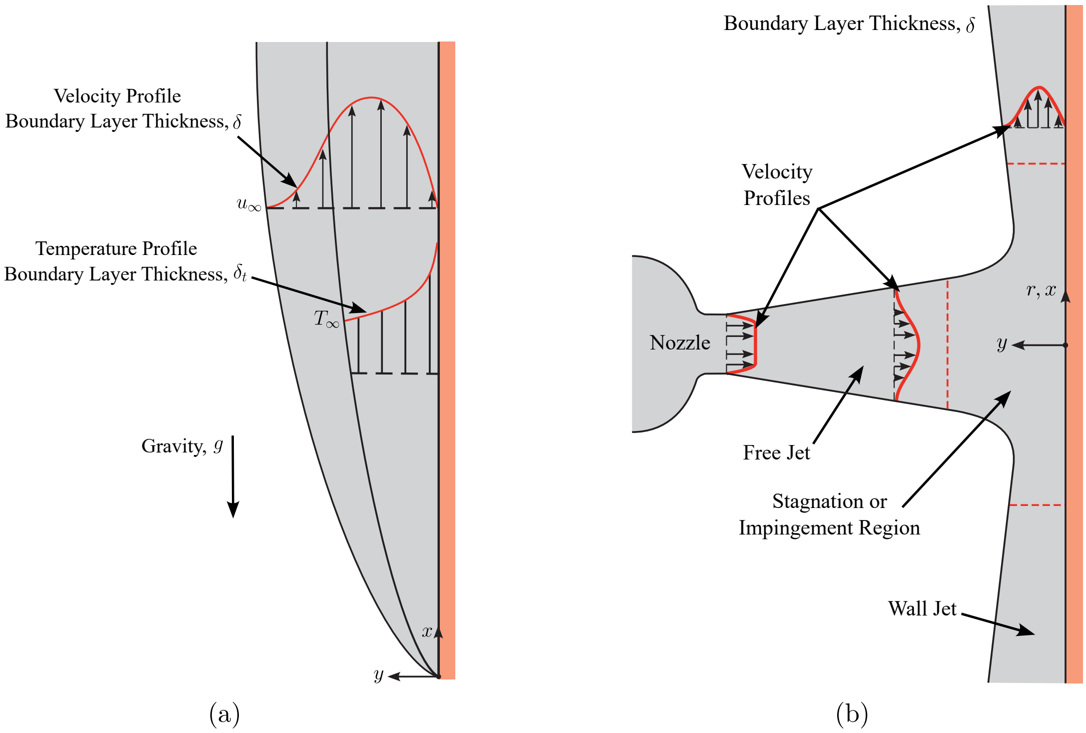

Figure 2.2.: Illustration showing the difference between the boundary layer thickness (δ) on a vertical surface for (a) natural and (b) forced convection via impinging air jet (figures adapted from [180]).

In this section, commonly-used empirical correlations, expressed as average Nusselt number ($\overline{Nu}$), will be used to evaluate the "back-of-the-envelope" applicability of both natural (Sec. 2.1.1.1) and forced convection (Sec. 2.1.1.2) for STS sensor cooling application within the STS boundary conditions.

2.1.1.1. Case for Natural Air Convection

Sensor cooling by natural air convection represents the best-case scenario to remove the sensor power dissipation as it does not introduce any additional material budget within the STS physics aperture. The feasibility of using natural convection for sensor cooling can be theoretically done with commonly used empirical formulation from Churchill and Chu [181]. Temperature of a silicon sensor (T_s) can be theoretically calculated by equating it as a vertical plate (length L) dissipating a constant power dissipation per unit area ($\dot{q}$) in an ambient temperature (T_∞) (see Fig. 2.3). The corresponding Nusselt number ($\overline{Nu}$) is described as:

$$\overline{Nu} = \left\{0.825 + \frac{0.387 Ra_L^{1/6}}{[1 + (0.492/Pr)^{9/16}]^{8/27}}\right\}^2 , \tag{2.3}$$

for $Ra_L < 10^{12}$ and where,

$$Ra_L = Gr_L Pr , \tag{2.4a}$$

$$Gr_L = \frac{g\beta(T_s - T_\infty)L^3}{\nu^2} , \tag{2.4b}$$

where air properties are described in terms of thermal conductivity (k), kinematic viscosity (ν) and Prandt Number (Pr); Ra_L and Gr_L are dimensionless parameters Rayleigh number and Grashof number respectively; β is coefficient of volume expansion ($\beta = 1/T_\infty$ for ideal gases). T_s can be determined by solving Eq. 2.2 and Eq. 2.3 iteratively so that the respective Nu match for the temperature dependent $\dot{q}$ (Eq. 1.1b). This has been done for all sensor length variants (2.2, 4.2, 6.2, 12.4 cm) to determine the margins from the thermal runaway (see Fig. 2.4 and Tab. 2.1), with the following conclusions:

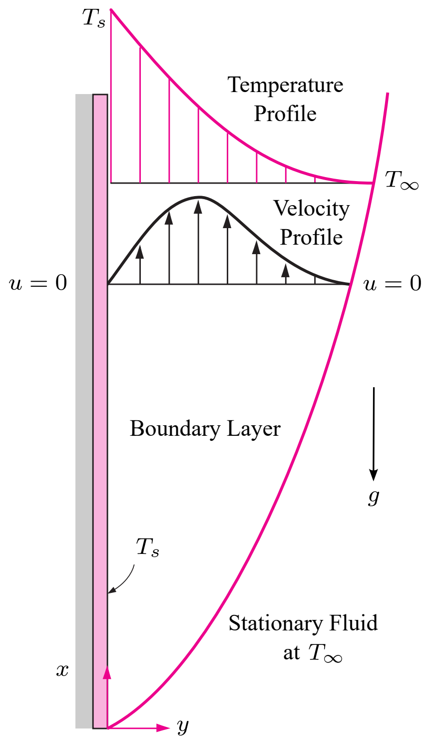

Figure 2.3.: Typical velocity and temperature profiles for natural convection flow over a hot vertical plate at temperature T_s inserted in a fluid at temperature T_∞ (figure adapted from [182]).

- Innermost STS sensors (Δx = Δy $\leq \pm$ 10 cm) with the end-of-lifetime accumulated fluence (10^{14}n$_{eq}$(1 MeV)/cm^2) can only be cooled by natural convection for ambient air temperature of $\lesssim -25$°C to avoid thermal runaway (see Fig. 2.4(a)). Since this will be technically difficult to achieve, active air cooling will be needed for innermost sensors.
- Peripheral STS sensors (Δx = Δy $\geq \pm$ 10 cm) with fluence foreseen at the end-of-lifetime operation (0.1×10^{14}n$_{eq}$(1 MeV)/cm^2) can be cooled down by natural convection for ambient air temperature of $\lesssim$ 0°C to avoid thermal runaway (see Fig. 2.4(b)). Therefore, natural convection is technically feasible for peripheral sensors.

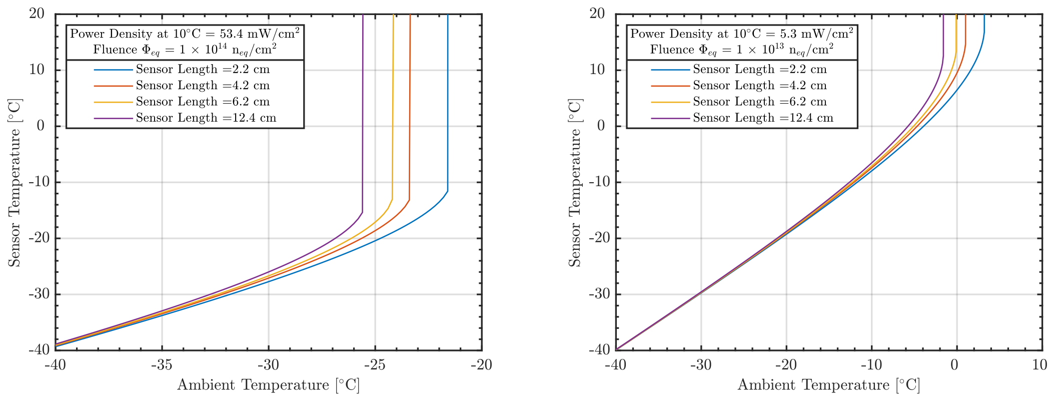

(a) After End-of-Lifetime Operation Innermost Sensors

(b) After End-of-Lifetime Operation Peripheral Sensors

Figure 2.4.: Stable sensor temperature variation with ambient temperature for different sensor lengths cooled by natural air convection at end-of-lifetime sensor power densities (a) 53.4 mW/cm^2 (innermost sensors) and (b) 5.3 mW/cm^2 (peripheral sensors) at 10°C. Critical ambient air temperatures for thermal runaway are in Tab. 2.1. Calculations assume air properties at STP (0°C, 1 atm).

Sensor Length (L) [cm]	Critical Air Temperature [°C] After End-of-Lifetime Operation	
	Innermost Sensors	Peripheral Sensors
2.2	-21.6	3.2
4.2	-23.4	1.0
6.2	-24.2	-0.1
12.4	-25.6	-1.6

Table 2.1.: Critical ambient temperatures at which (a) innermost, and (b) peripheral silicon sensors cooled by natural air convection undergo thermal runaway for different sensor length variants. The underlying distributions are plotted in Fig. 2.4.

2.1.1.2. Case for Forced Air Convection via Impinging Jets

As concluded in Sec. 2.1.1.1, the innermost and most power-intensive sensors of each station ((Δx = Δy $\leq \pm$ 10 cm)) require active air cooling. Sensor cooling using perforated carbon-fibre tubes, which direct cold air onto the exposed sensor surface, actively cools the innermost silicon sensors while minimising the introduced material budget (see Fig. 2.5). Therefore, the impinging air jets from the perforations penetrate the stationary insulating boundary layer over the flat surface, reducing the effective thickness of the insulating layer and increasing the local heat transfer coefficient (see Fig. 2.6) [183, 184].

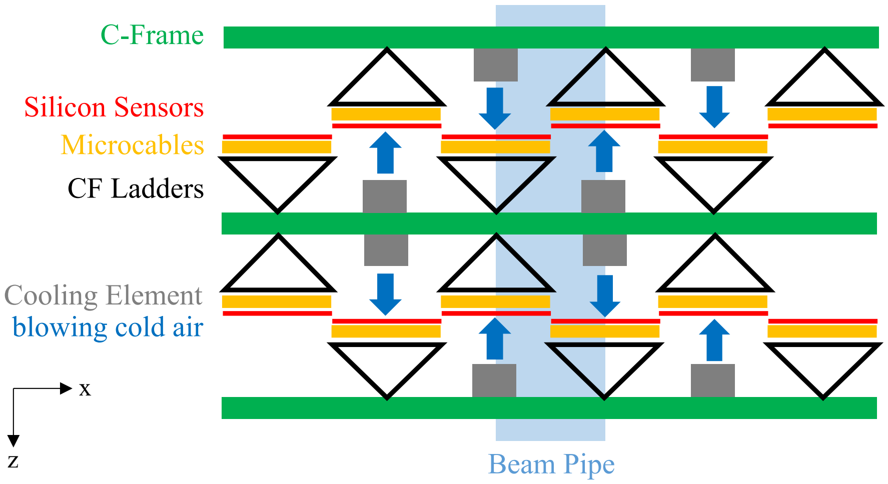

Figure 2.5.: Top-view illustration of STS showing the ladders to be actively cooled with cooling elements placed on adjacent C-Frames to blow cold air on sensor surface.

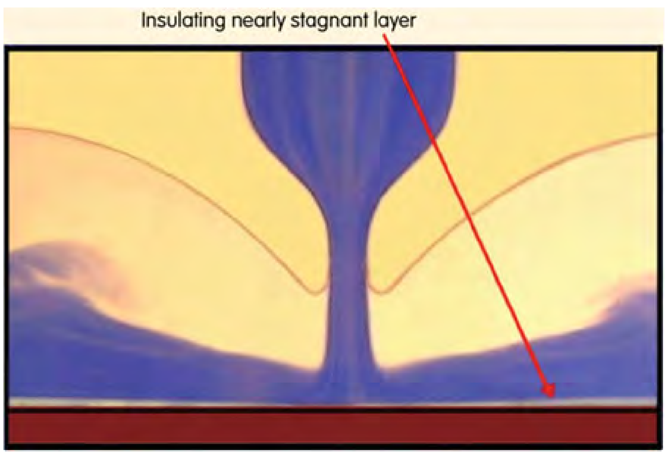

Figure 2.6.: Flow visualisation of an impinging jet on a flat surface with thin stationary insulating boundary layer (figure from [184]).

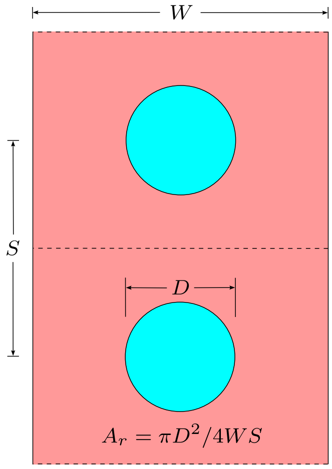

Figure 2.7.: Illustration showing the pertinent geometrical features of the perforated tube arrangement for STS sensor cooling (figure adapted from [180]).

The design of the perforated tube is optimised to enhance the heat transfer caused by impinging air jets within the geometrical boundary conditions of the STS. Theoretical estimations of the underlying optimal geometrical parameters has been made by using the correlation by Martin [185], which is an extensive review of available convection coefficient data for impinging gas jets of various geometries and configurations. An exhaustive summary of the several correlations and numerical modeling methods are described in [186, 187]. Geometrically, a perforated tube held in front of the sensor is analogous to an array of round sharp-edged orifices (see Fig. 2.7). The corresponding correlation from Martin [185] to determine the average Nusselt number ($\overline{Nu}$) is described as Eq. 2.5:

$$\frac{\overline{Nu}\sqrt{\epsilon}}{Pr^{0.42}} = G\left(A_r, \frac{H}{D}\right) \cdot \left(\frac{Re}{\sqrt{\epsilon}}\right)^{2/3} \cdot K\left(A_r, \frac{H}{D}\right) \tag{2.5}$$

which comprises of,

- *Geometric function* (G) dependent on the pertinent geometrical features, namely hole diameter (D), height from the surface (H), hole pitch (S), sensor width ($W = 6.2$ cm) and the relative nozzle area (A_r) (see Eq. 2.6a). Herein, A_r is defined as the ratio of the nozzle exit cross-sectional area to the surface area of the cooled surface (see Fig. 2.7 and Eq. 2.6b).

$$G = (\epsilon A_r)^{1/2} \frac{1 - 2.2(\epsilon A_r)^{1/2}}{1 + 0.2(H/D\sqrt{\epsilon} - 6)(\epsilon A_r)^{1/2}} \tag{2.6a}$$

$$A_r = \frac{\pi D^2}{4WS} \tag{2.6b}$$

- *Jet Contraction Coefficient* (ϵ) to account for the jet contraction observed in jets from sharp-edged orifices, such as perforated tubes. It is defined as the ratio of the narrowest jet cross-sectional area (D') to the geometric orifice exit cross-sectional area (D) (see Eq. 2.7) [188].

$$\epsilon = \frac{\pi D'^2/4}{\pi D^2/4} = 0.611 \tag{2.7}$$

- *Array Correction Function* (K) to consider the interaction of adjoining wall jets for an array. This is to account for the more rapid decay of Nu with increasing H/D in an array that for a single jet for a limiting distance $H/D \gtrsim 0.6/A_r^{1/2}$ (see Eq. 2.8).

$$K = \left[1 + \left(\frac{H/D}{0.6/A_r^{1/2}}\right)^6\right]^{-0.05} \tag{2.8}$$

- *Flow Conditions* which is quantified as the Reynolds number (Re) (see Eq. 2.9) of air with kinematic viscosity ν exiting through the hole diameter D at flow velocity v_e.

$$Re = \frac{v_e D}{\nu} \tag{2.9}$$

This correlation (Eq. 2.5) is valid within the following range

$$\begin{bmatrix} 2000 & \leqslant & Re & \leqslant & 400{,}000 \\ 2 & \leqslant & H/D & \leqslant & 12 \\ 0.004 & \leqslant & A_r & \leqslant & 0.04 \\ 4 & \leqslant & S & \leqslant & 14 \end{bmatrix}$$

Based on the correlation validity range and STS boundary conditions, the parameters for perforated tube design can be narrowed down to the following (resulting tube properties summarised in Tab. 2.2):

- *Height* (H) between the holes and the innermost sensors must account for the staggered structure of the ladder (up to 7.5 mm) and distance required to safely mount the tube (4...5 mm) (see Fig. 2.8). Therefore, the chosen H is 12 mm (10.5 mm for central ladders with eight sensors).

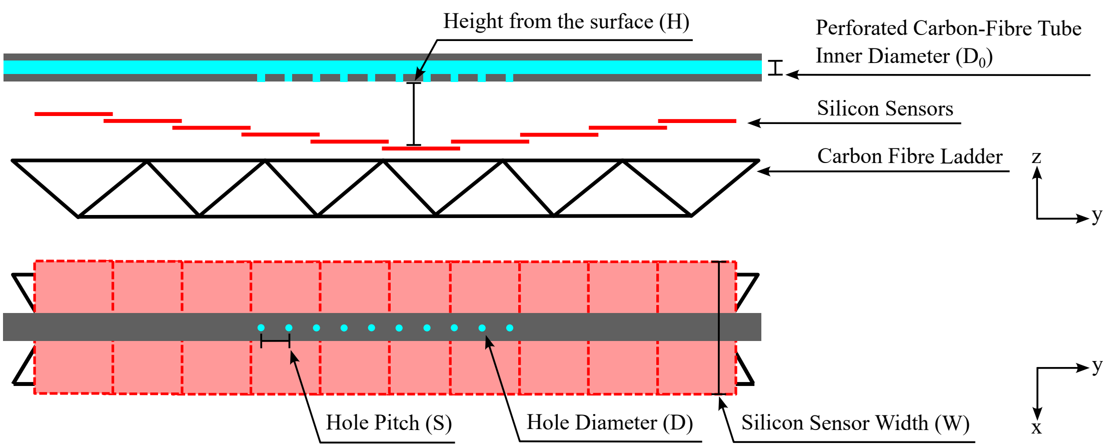

Figure 2.8.: Illustrations of perforated carbon-fibre tube on an assembled STS ladder.

- *Length* (L) is effectively the part where perforations are present on the tube, which is only the inner 20 cm part of the tube as the only the innermost silicon sensors require active cooling from the impinging air jets.
- *Tube inner diameter (D_0)* must be optimised such that the tube diameter, i.e., material budget is minimal, while ensuring equal flow distribution amongst all the holes. Since this is governed by the ratio (α) of tube and sum of all hole areas, it can be represented as follows:

$$\frac{\pi D_0^2}{4} = \alpha N \frac{\pi D^2}{4} = \alpha \left(\frac{L}{S} + 1 \right) \frac{\pi D^2}{4} \tag{2.10}$$

where N are the number of holes spread equidistantly over the length (L) with a pitch (S). Eq. 2.10 can be arranged to solve for tube diameter D_0 in terms of the S/D and H/D, i.e., parameters which are used in the Martin correlations [185] as shown below:

$$D_0 = \sqrt{\alpha H^2 \left(\frac{L}{H} + \frac{\frac{S}{D}}{\frac{H}{D}} \right) \frac{1}{\frac{S}{D}} \frac{1}{\frac{H}{D}}} \tag{2.11a}$$

$$D_0 \approx \sqrt{\alpha H L} \sqrt{\frac{1}{\frac{S}{D}} \frac{1}{\frac{H}{D}}}, \text{ if } N \gg 1 \tag{2.11b}$$

Based on Eq. 2.11, the tube diameter D_0 can be minimised if:

- H/D and S/D are maximised, i.e., $H/D = 12$ and $S/D = 14$ based on [185] (see Fig. 2.9).
- L is minimised - This can be achieved if the gas flow in the perforated tube comes from both sides, as it will effectively half the tube length from 200 to 100 mm (see Fig. 2.9(a)-2.9(b)).
- α is minimised - This leads to more uneven flow distribution among holes (Fig. 2.9(c)-2.9(d)).
- H is minimised - This is limited by STS mechanics and minimum possible value is 12 mm.

Therefore, D_0 is dependent effectively only on α. Computational Fluid Dynamics (CFD) simulations are used to simulate tubes with varying α (or D_0) to quantify the air flow distribution amongst all holes. The results plotted in Fig. 2.10 clearly shows that increasing α (or D_0) leads to a more evenly distributed flow, but would also lead to an increase in the added material budget. So, as a trade-off, $\alpha = 1.5$ ($D_0 = 3.5$ mm) is chosen to be the tube inner diameter due to an acceptable flow distribution ($< \pm 5\%$) and lower material budget addition.

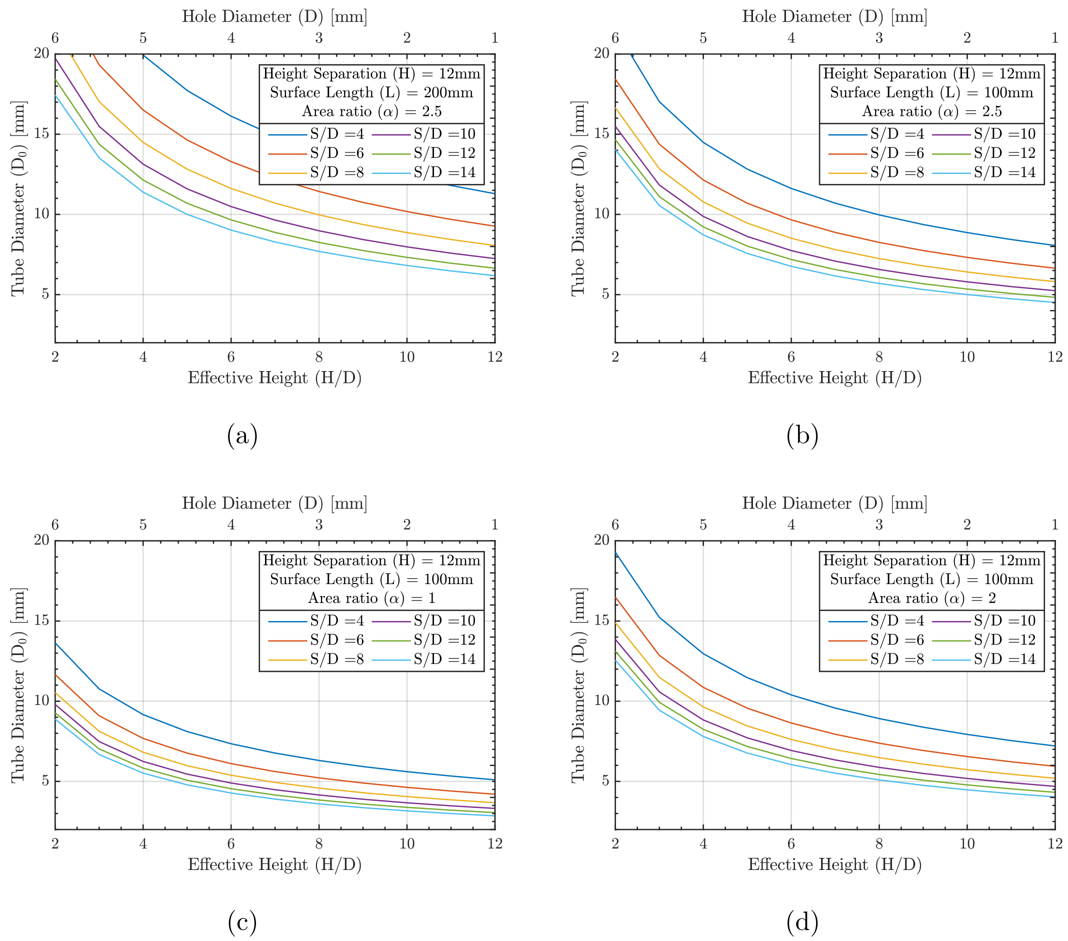

Figure 2.9.: Variation of perforated tube's inner diameter (D_0) with hole diameter (D) for various hole pitch (S/D) for given values of height (H), length (L) and area ratio (α). (a, b) Dependency on surface length L of 200 mm and 100 mm, respectively. (c, d) Dependency on area ratio α of 1 and 2, respectively.

Parameter	Value
Inner Diameter (D_0)	3.50 mm
Shell Thickness	0.75 mm
Material Budget (local; max. trajectory length = 3.57 cm)	1.25% x/X_0
Material Budget (averaged over sensor area)	0.06% x/X_0
Length over which holes distributed ($2L$)	200 mm
Hole Pitch (S)	14 mm
Hole Diameter (D)	1 mm
Total Number of Holes ($2N$)	16
Relative Nozzle Area (A_r)	0.001
Distance between the tube and the innermost sensor of a normal ladder (H_{Normal})	12 mm
Distance between the tube and the innermost sensor of a central ladder ($N_{Central}$)	10.5 mm

Table 2.2.: Properties of the carbon-fibre based perforated tube.

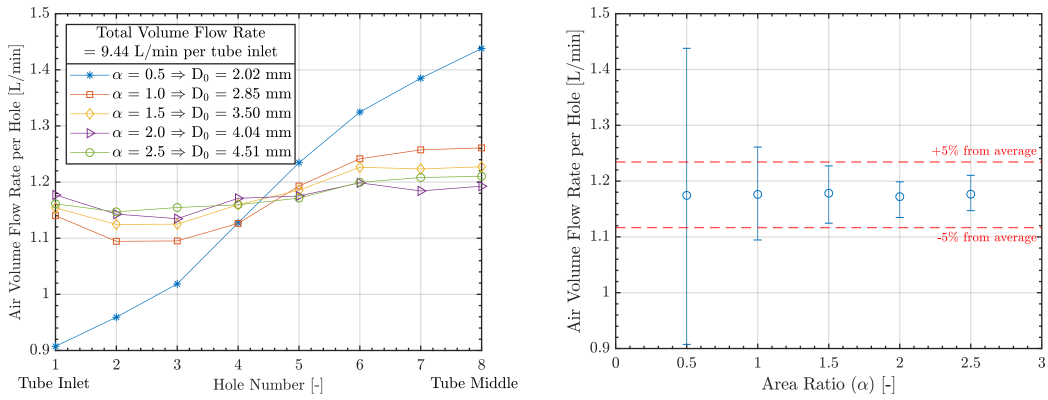

(a) (b)

Figure 2.10.: (a) Variation of the volumetric air flow rate from each hole for various tube diameters (D_0) or area ratios (α) from CFD simulations. The plot is only for half of the holes because the hole air flow distribution is expected to be symmetric when air inlet is from both ends of the tube. (b) Flow deviation distribution with reference to various tube diameters (D_0) or area ratios (α). The error bars denote the minimum and maximum deviation from the average in Fig. 2.10(a).

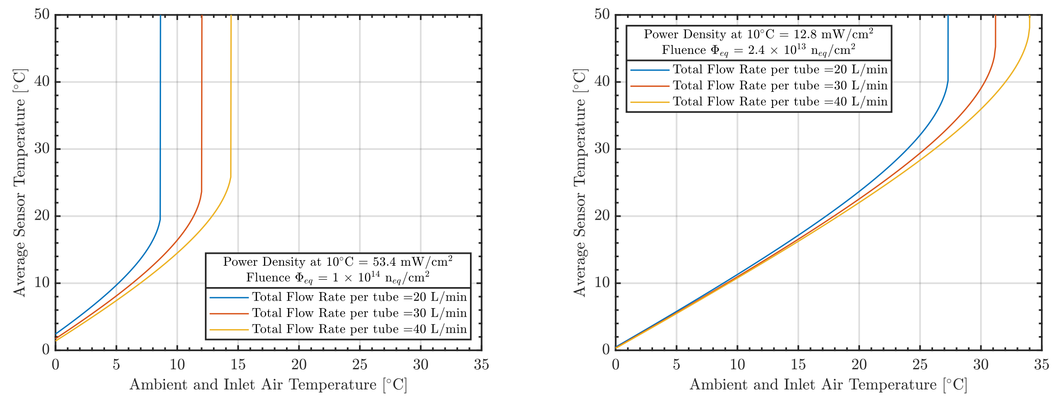

(a) After EOL Accumulated Fluence Innermost Sensors

(b) After 10 Years Accumulated Fluence Innermost Sensors

Figure 2.11.: Stable sensor temperature variation with ambient temperature for different flow rate per perforated tube (20 ... 40 L/min; tube parameters in Tab. 2.2) cooled by impinging air jets at sensor power densities for innermost sensors of (a) 53.4 mW/cm^2 (end-of-lifetime fluence; 1×10^{14}n$_{eq}$(1 MeV)/cm^2) and (b) 12.8 mW/cm^2 (10 year fluence; 0.24×10^{14}n$_{eq}$(1 MeV)/cm^2) at 10°C. Critical ambient air temperatures for thermal runaway are in Tab. 2.3. Calculations assume air properties at STP (0°C, 1 atm).

Total Flow Rate per Tube [L/min]	Reynolds Number per Hole [-]	Critical Air Temperature [°C]	
		After EOL Accumulated Fluence	After 10 Years Accumulated Fluence
20	$1997.5 \approx 2000$	8.6	27.3
30	$2996.2 \approx 3000$	12.0	31.2
40	$3994.9 \approx 4000$	14.4	34.0

Table 2.3.: Critical ambient temperatures at which the innermost sensors with accumulated fluence corresponding to (a) end-of-lifetime (1×10^{14}n$_{eq}$(1 MeV)/cm^2), and (b) 10 years of operation (0.24×10^{14}n$_{eq}$(1 MeV)/cm^2) cooled by impinging air jets undergo thermal runaway for different flow rates per tube. The underlying distributions are plotted in Fig. 2.11.

The thermal runaway behaviour for the designed perforated tube (see Tab. 2.2) with different flow rates per perforated tube (20 ... 40 L/min) has been studied in terms of the variation of stable sensor temperature with air temperature (see Fig. 2.11 and Tab. 2.3) by using the Martin correlations [185] (see Eqs. 2.5-2.9). The studied scenarios correspond to the end-of-lifetime and 10-year fluence of detector operation. The conclusions from this study are as follows:

- Sensor power dissipation can be neutralised for all studied flow rates by having an air temperature of $\approx$ 0°C while maintaining sufficient margin from thermal runaway (see Fig. 2.11(a)).
- For up to 10 years of detector operation, air temperature of $\approx$ 20°C are deemed sufficient to ensure a stable operation and safe margin from thermal runaway (see Fig. 2.11(b)).

To summarise, sensor cooling performance by using theoretical calculations for two different air convection types, natural convection and forced convection via impinging jets suggest that:

- Natural convection at ambient air temperature of $\approx$ 0°C is sufficient to cool the peripheral STS sensors ($\Delta x = \Delta y \geq \pm$ 10 cm) and avoid thermal runaway after the end-of-lifetime operation ($< 0.1 \times 10^{14}$n$_{eq}$(1 MeV)/cm^2).
- Forced air convection via impinging jets from custom-designed perforated tubes with air temperature of $\approx$ 0°C can effectively neutralise the irradiation-caused power dissipation from the innermost STS sensors ($\Delta x = \Delta y \leq \pm$ 10 cm) after the end-of-lifetime operation (10^{14}n$_{eq}$(1 MeV)/cm^2).

This hybrid solution is not only technically feasible, but also optimises the additional material budget which will be added within the STS's physics acceptance, while safely keeping the sensors away from thermal runaway through the STS operational lifetime.

2.1.2. Numerical Simulations

Numerical simulations, particularly Computational Fluid Dynamics (CFD), are vital for modeling the complex nature of STS sensor cooling. They enable precise simulation of heat transfer, fluid flow, and thermal interactions, which is essential for optimising air cooling by predicting airflow patterns and sensor temperature distributions. This section tests the sensor cooling hypothesis (presented in Sec. 2.1.1) by using the CFD simulations package from SolidWorks® at the ladder level. Specific ladder types were chosen to address certain aspects and worst-case scenarios of interest for both, central and peripheral ladders. These simulations assume a homogeneous ambient temperature and do not account for residual heat transfer to the ladder from the peripheral sources such as electronics or thermal enclosure. Moreover, the resulting temperature distributions are compared to the sensor temperatures by using theoretical formulations as described in Sec. 2.1.1.

2.1.2.1. Case for Natural Air Convection

The cooling performance of natural air convection for vertical surfaces, as is representative of silicon sensors mounted on ladders, worsens with higher power dissipation and longer surface lengths. Therefore, two peripheral ladders, *Ladder Type 1109_102* and *Ladder Type 1022_811*, were chosen to simulate the respective worst case scenarios (see Tab. 2.4 and Fig. 2.12 for their properties). Their sensor cooling performance was evaluated in terms of thermal runaway performance of the comprising sensors using both CFD simulations and theoretical calculations for ambient temperatures of -10, 5, 20°C. This is exemplified in Fig. 2.13 which shows thermal runaway behaviour for the longest and most power-intensive sensor cooled by natural air convection (module type 1109_102-3T) for the considered ladders after EOL operation of STS. Based on the resulting ladder temperature distributions shown in Fig. 2.14, it can be concluded that:

- Natural convection at an ambient air temperature of ≈ 0°C is sufficient to cool the considered ladders while avoiding thermal runaway.
- Ladder CFD simulations and theoretical calculations for comprising sensors agree reasonably well.

Unit ID	Ladder ID	x [cm]	± y [cm]	z [cm]	Remarks
Unit01R_3	LadderType1109_102	-14.875	15.83	≈ 30	Highest sensor power dissipation
Unit08L_18	LadderType1022_811	14.875	39.33	≈ 100	Longest sensor length

Table 2.4.: STS ladders used for CFD simulations of natural air convection cooling for silicon sensors, based on STS geometry version v21b. Coordinates reference the beam-target interaction point (primary vertex).

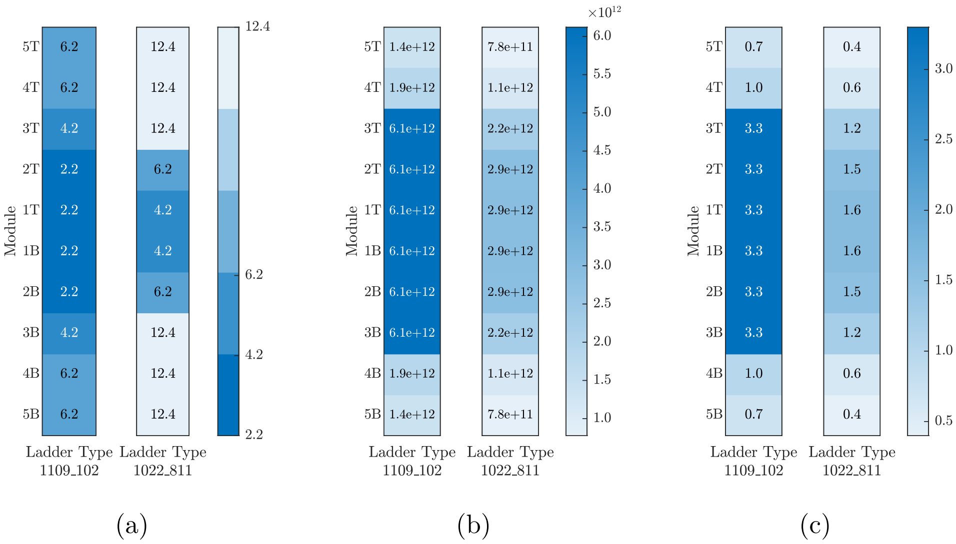

Figure 2.12.: (a) Sensor size [cm], (b) accumulated non-ionising fluence [n_{eq}(1 MeV)/cm^2] after end-of-lifetime operation, and (c) corresponding sensor power dissipation [mW/cm^2] at 10°C for the two ladders for which CFD simulations have been performed for natural air convection. The fluence values are derived for STS geometry version v21b and scaled to the respective fluence from the initial irradiation case of 11*A*GeV Au+Au at 10 MHz after 1 month. The end-of-lifetime operation corresponds to an accumulated fluence of $10^{14} n_{eq}$(1 MeV)/cm^2 and power dissipation of 53.4 mW/cm^2 at 10°C for the sensors closest to the beampipe.

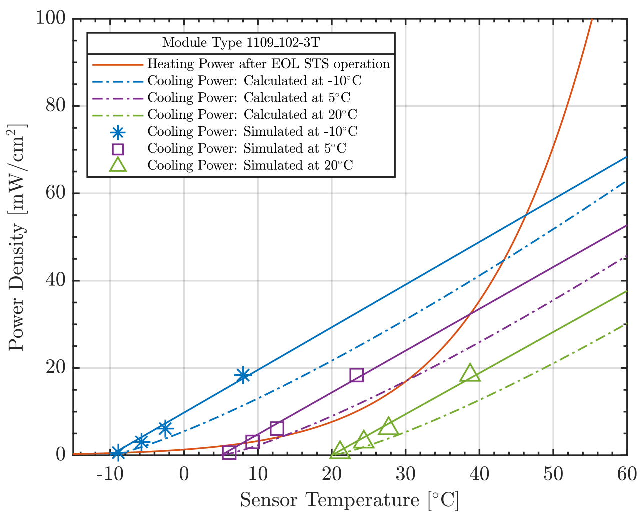

Figure 2.13.: Thermal runaway behavior of Module Type 1109_102-3T, shown as a variation of sensor's power density with its temperature. The heating power curve (shown in red) is for the accumulated fluence after EOL operation, while the cooling power curves are shown for theoretical calculations (dashed curve) and CFD simulations (solid curve) at ambient temperatures of -10, 5, 20°C.

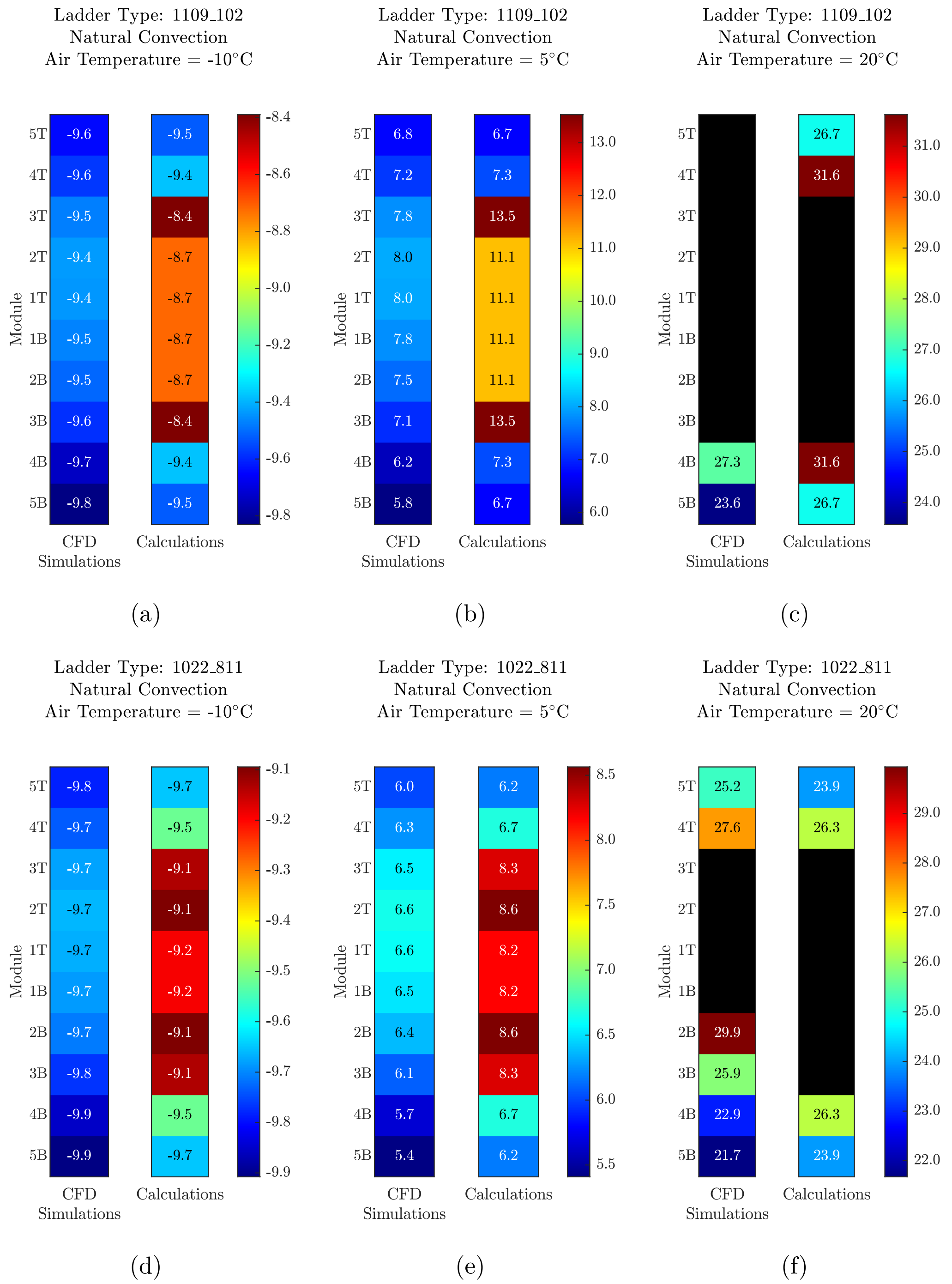

Figure 2.14.: Ladder temperature distributions after EOL operation for ladder type 1109_102 (top row) and 1022_811 (bottom row) as obtained for theoretical calculations (right sub-figure) and CFD simulations (left sub-figure) at ambient temperatures of −10°C (left figure), 5°C (middle figure), 20°C (left figure). The black bins comprise sensors where no stable temperature was achieved after EOL operation, i.e., the sensors are in thermal runaway.

2.1.2.2. Case for Forced Air Convection via Impinging Jets

For the staggered sensor arrangement as is the case of silicon sensors mounted on ladders and given perforated tube geometry (summarised in Tab. 2.2), the cooling performance of forced air convection via impinging jets is worst for sensors with higher power dissipation and maximum height between the perforations and sensor surface. Therefore, two central ladders, *Ladder Type 1101_104* and *Ladder Type 1107_708*, were chosen to simulate the respective worst case scenarios (see Tab. 2.5 and Fig. 2.15 for their properties).

Unit ID	Ladder ID	x [cm]	± y [cm]	z [cm]	Remarks
01R_3	1101_104	-2.975	17.035	≈ 30	Highest sensor power dissipation for innermost sensor
07R_15	1107_708	-2.975	35.97	≈ 90	Longest sensor-tube separation for innermost sensor

Table 2.5.: Central STS ladders used for CFD simulations of forced air convection cooling for silicon sensors via impinging air jets, based on STS geometry version v21b. Coordinates reference the beam-target interaction point (primary vertex).

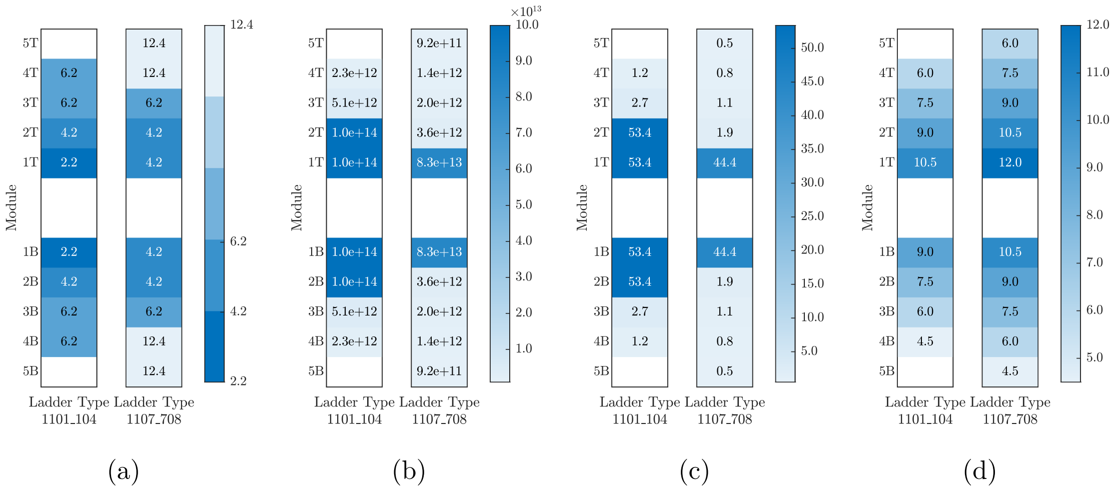

Figure 2.15.: (a) Sensor size [cm], (b) accumulated non-ionising fluence [n_{eq}(1 MeV)/cm^2] after end-of-lifetime operation, (c) corresponding sensor power dissipation [mW/cm^2] at 10°C, and (d) height between the perforations and sensors [mm] for the two ladders for which CFD simulations have been performed for forced air convection. The fluence values are for STS geometry version v21b and scaled to the respective fluence from the initial irradiation case of 11*A*GeV Au+Au at 10 MHz after 1 month. The end-of-lifetime operation corresponds to an accumulated fluence of $10^{14} n_{eq}$(1 MeV)/cm^2 and power dissipation of 53.4 mW/cm^2 at 10°C for the sensors closest to the beampipe. The central white bins correspond to the beampipe opening, while the peripheral white bins correspond to the locations without silicon sensors.

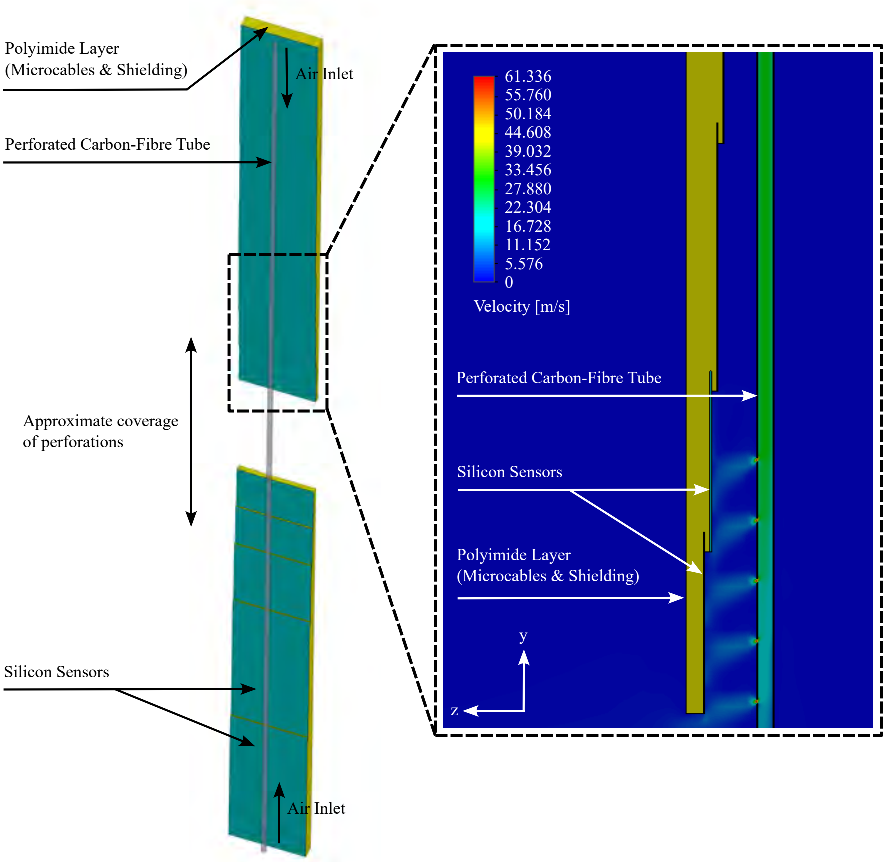

Figure 2.16.: CAD rendering of the CFD simulation setup of Ladder Type 1107_708 being cooled by air jets from the perforated carbon-fibre tube in front (total air flow rate of 30 L/min). The call-out on the right shows the zoomed-in view of the resulting air velocity profile of jets on the innermost silicon sensors.

The sensor cooling performance of the chosen ladders was evaluated in terms of thermal runaway performance using CFD simulations[1](see Fig. 2.16) to study dependencies on: (a) air temperature (-10, 5, 20°C), (b) air flow rate (20, 30, 40 L/min). Theoretical formulations to predict thermal performance of impinging air jets (introduced in Sec. 2.1.1.2) were concurrently used to compute and compare the sensor temperatures. This is exemplified in Fig. 2.17 which shows the air temperature and flow rate behaviour of thermal runaway for the most power-intensive silicon sensor in STS (module type 1101_104-1T). Moreover, since only the innermost silicon sensors are cooled by impinging air jets, formulations pertaining to natural convection (see Sec. 2.1.1.1) were used to calculate the temperatures of peripheral silicon sensors. Based on the resulting ladder temperature distributions shown in Figs. 2.18-2.19, it can be concluded that:

1. k-omega ($k - \omega$) turbulence model was used to simulate turbulence at the perforated tube inlet in terms of the turbulent kinetic energy (k) and specific dissipation rate (ω).

- CFD simulations and theoretical calculations of the silicon sensors cooled by impinging air jets do not align, with theoretical predictions showing better cooling performance (see also Fig. 2.17). This significant discrepancy in cooling performance can be attributed to several factors, such as simplified geometry and meshing assumptions, turbulence modeling, boundary conditions, material property inaccuracies, external influences, differences in heat source representation, and simplified geometry assumptions.
- Assuming that calculations for impinging air jets are correct, air inlet for varying flow rates (20-40 L/min) at 5°C is sufficient to neutralise the radiation induced sensor power dissipation and avoid their thermal runaway with a stable temperature of ≈ 10°C at end-of-lifetime.
- Conversely, as observed in Sec. 2.1.2.1, ladder CFD simulations and theoretical calculations for comprising sensors agree reasonably well for the peripherally located sensors cooled by natural convection.

In conclusion, there is a notable disagreement between simulations and calculations for silicon sensors cooled by forced convection, while there is agreement for those cooled by natural convection. Addressing these discrepancies involves careful validation of CFD models with experimental data, refining mesh and numerical methods, and ensuring that both theoretical and simulation models account for similar assumptions and conditions.

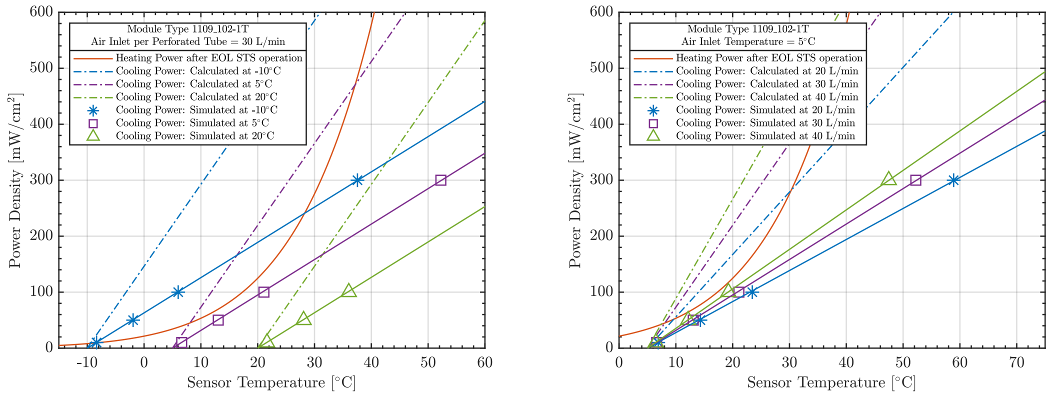

(a) Inlet Air Temperature Dependency (b) Inlet Air Flow Rate Dependency

Figure 2.17.: Thermal runaway behavior of Module Type 1101_104-1T (most power-intensive silicon sensor in STS; cooled by impinging air jets), shown as a variation of sensor's power density with its temperature. The heating power curve (shown in red) is for the accumulated fluence after EOL operation, while the cooling power curves are shown for theoretical calculations (dashed curve) and CFD simulations (solid curve) at: (a) varying air temperatures of -10, 5, 20°C, and (b) varying air flow rate per tube of 20, 30, 40 L/min.

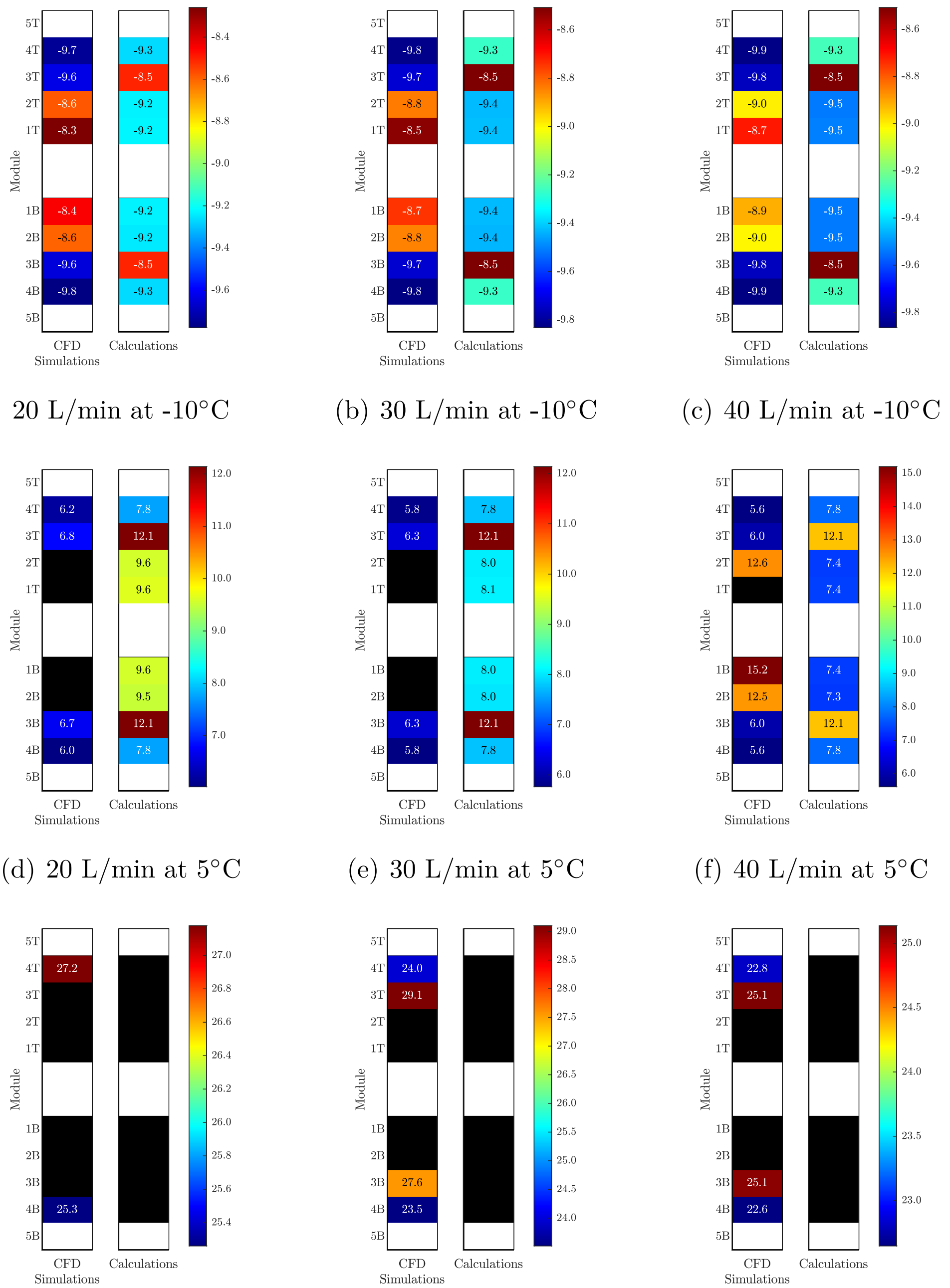

(a) 20 L/min at -10°C (b) 30 L/min at -10°C (c) 40 L/min at -10°C

(d) 20 L/min at 5°C (e) 30 L/min at 5°C (f) 40 L/min at 5°C

(g) 20 L/min at 20°C (h) 30 L/min at 20°C (i) 40 L/min at 20°C

Figure 2.18.: Ladder temperature distributions after EOL operation for ladder type 1101_104 as obtained for theoretical calculations (right sub-figure) and CFD simulations (left sub-figure) at air temperatures of -10°C (top row), 5°C (middle row), 20°C (bottom row) and air flow rates of 20 L/min (left column), 30 L/min (left column) and 40 L/min (right column). The white bins represent locations without silicon sensors (beampipe opening and peripheral locations), whereas the black bins comprise sensors in thermal runaway after EOL operation.

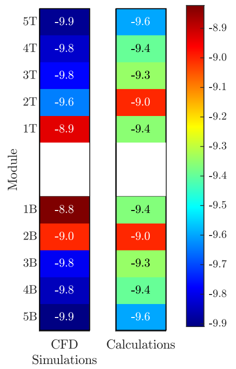

(a) 20 L/min at -10°C

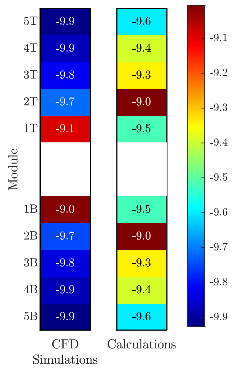

(b) 30 L/min at -10°C

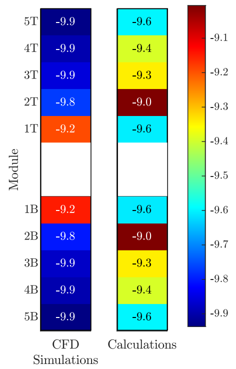

(c) 40 L/min at -10°C

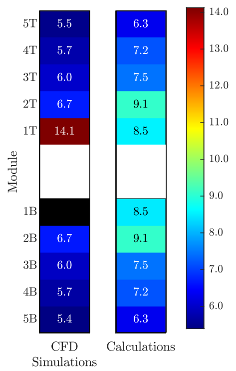

(d) 20 L/min at 5°C

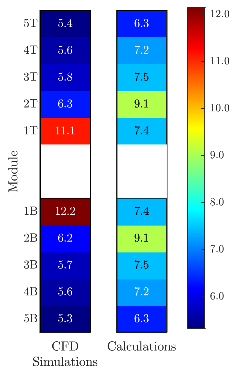

(e) 30 L/min at 5°C

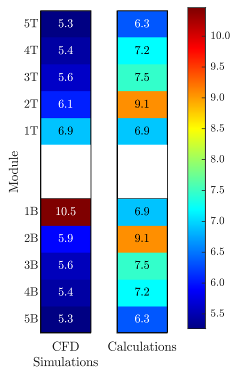

(f) 40 L/min at 5°C

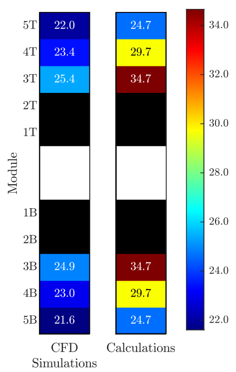

(g) 20 L/min at 20°C

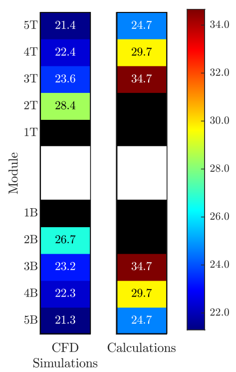

(h) 30 L/min at 20°C

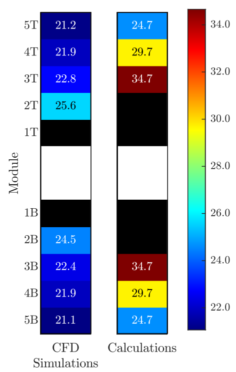

(i) 40 L/min at 20°C

Figure 2.19.: Ladder temperature distributions after EOL operation for ladder type 1107_708 as obtained for theoretical calculations (right sub-figure) and CFD simulations (left sub-figure) at air temperatures of -10°C (top row), 5°C (middle row), 20°C (bottom row) and air flow rates of 20 L/min (left column), 30 L/min (left column) and 40 L/min (right column). The white bins represent locations without silicon sensors (beampipe opening and peripheral locations), whereas the black bins comprise sensors in thermal runaway after EOL operation.

2.2. Front-End Electronics Cooling

The STS front-end electronics (FEE) dissipate up to 26 kW of the total 40 kW electronics power dissipation (roughly 66%; see Tab. 1.6 for breakdown of the power dissipation sources). Therefore, their effective cooling is crucial to prevent residual heat transfer from raising the temperature of nearby silicon sensors (located only 25 ... 50 cm away), thus preventing their thermal runaway. This is aimed by maintaining the FEE temperature at ≈10°C, similar to that of silicon sensors. The cooling efficiency of the FEE cooling concept depends primarily on its thermal path (see Fig. 2.20) which is influenced by:

(a) Thermal impedance of the conductive path from the heat-dissipating readout ASICs and LDO regulators into the heat sink.

(b) Cooling capacity of the underlying heat sink and coolant quantified in terms of the heat transfer coefficient.

This section aims to describe the use of numerical simulations to optimise the aforementioned aspects in Sec. 2.2.1 and Sec. 2.2.2, respectively, to obtain the maximum temperature on FEE of ≈10°C.

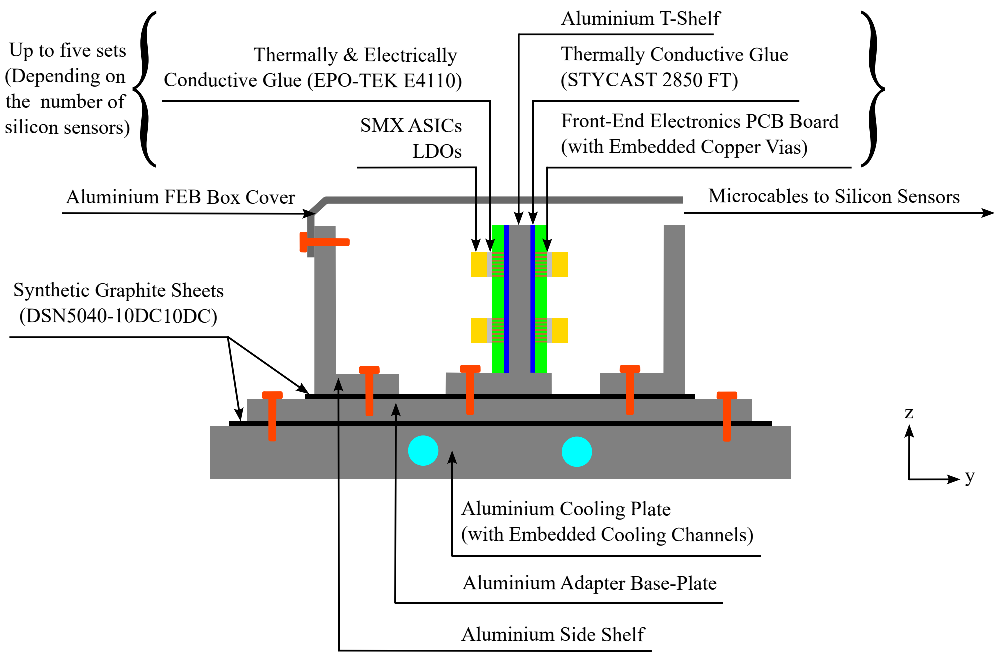

Figure 2.20.: Thermal path illustration of front-end electronics cooling comprising FEB box and underlying cooling plate. This illustration corresponds to one silicon sensor and up to five assembled T-shelves can be accommodated in a FEB box. Drawing is not to scale.

2.2.1. Front-End Electronics Board (FEB) Box

As introduced in Sec. 1.4, the primary functional block of the STS is the *Module*, consisting of a double-sided silicon microstrip STS sensor connected to a pair of front-end boards (FEBs) via ultra-thin aluminium-polyimide microcables (see Fig. 1.19(b)). Structurally, up to 10 STS modules are hosted on a low-mass space frame called a *Ladder*, with the modules stacked starting from the middle of the ladder. Consequently, up to 10 FEBs (corresponding to 5 STS modules) are collectively housed in a *FEB Box* outside the physics aperture at either end of the ladder, mechanically detached for separate attachment to the heat sink (see Fig. 1.20). The FEB box is primarily designed to provide a thermally conducting path to the heat sink with minimum impedance and enclose the residual heat within, preventing heat transfer to the STS ambient conditions (see Fig. 2.20). The various elements comprising the thermal path within a FEB box are:

Readout ASICs and LDO Regulators: These are the primary power generation sources in the FEE thermal path. The analog signals from 1024 strips on each side of the STS sensor are digitised by eight SMX2 ASICs, each with 128 channels and a design power consumption of <10 mW/channel [164]. Furthermore, four LDO voltage regulators stabilise the input low voltages required for ASIC functionality. Typically, the eight ASICs and four LDOs on an FEB dissipate 7.08 W and 4.34 W, respectively, with power dissipation varying based on input FEB currents and DC-DC converter efficiencies (see App. E.2). For thermal evaluation of the FEBs, the *Maximum Scenario* is used as the baseline, where all ASICs and LDOs dissipate 8.16 W and 4.77 W, respectively.

Front-End Electronics (FEE) PCB: This 12-layer, 1.6 mm thick board hosts the readout SMX2 ASICs, LDO regulators, and interfaces for silicon sensor powering and readout. In the FEE thermal path, it provides a thermally conducting path from the heat-producing ASICs and LDOs, which are glued over arrays of thermal vias using silver-filled epoxy paste (EPO-TEK® E4110) (see Fig. 2.21). The thermal resistance of these thermal vias[2]is 2.2 K/W for ASICs and 4.3 K/W for LDOs. For comparison, using an Aluminium Nitride interface instead, as was considered in initial designs [161, 189], would provide a thermal resistance of 0.07 K/W and 0.15 K/W, respectively.

Aluminium T-Shelf and Adapter Base Plate: They are the final elements in the conductive FEE thermal path and bridge the power dissipating sources to the heat sink. Their thicknesses, 2.7 mm and 3 mm respectively, are optimised to provide sufficient cold mass within the spatial boundary conditions [161]. A T-shelf is glued to a pair of FEBs of the same module by STYCAST 2850FT/Catalyst 23LV, with the dispensed glue pattern optimised to achieve the targeted glue

2. The thermal resistance of one thermal via with 0.3 mm diameter in 1.6 mm thick FR4 material is about 210 K/W. This equates to total thermal resistance of 2.2 K/W for ASICs and 4.3 K/W for LDOs (calculation credits: R.M. Kapell (GSI Darmstadt)).

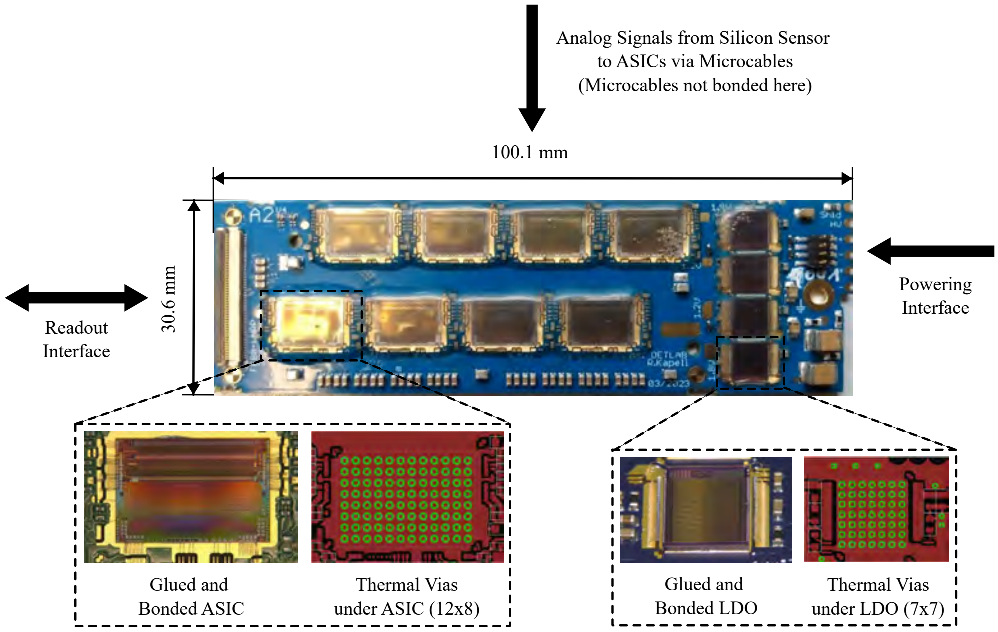

Figure 2.21.: An assembled FEB with all ASICs and LDOs glued and bonded on the FEB PCB. The callouts zoom into respective heat producing elements with the underlying array of thermal vias (figures from R.M. Kapell (GSI Darmstadt)).

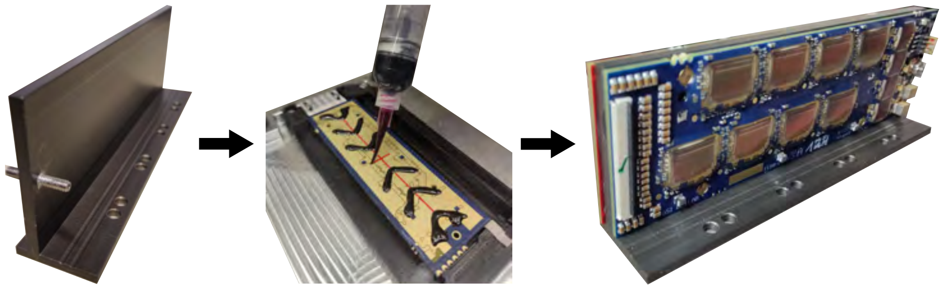

Figure 2.22.: Gluing process of a pair of assembled FEBs to an aluminium T-shelf, exercised on prototypes without microcables, while the final gluing process is carried out microcables attached to the ASICs (figure from S. Mehta (EKU Tübingen)).

thickness of 150 µm over the entire surface by using capillary dispersion (see Fig. 2.22). Further details about the gluing process are summarised in Sec. 3.2 and detailed in [190–192]. The assembled T-shelves are further interfaced with the heat sink by screwing them to the adapter base plate, which can host up to five T-shelves (corresponding to five modules on either ladder end). The aluminium base plate is sandwiched between thermally conducting synthetic graphite sheets (40 µm thick; DSN5040-10DC10DC).

Aluminium FEB Box Cover and Side Shelves: While not directly contributing to the conductive thermal path, they crucially enclose the residual heat emitted by the FEBs, preventing it from heating the STS ambient conditions.

Element in the FEE Thermal Path	Thermal Conductivity (out-of-plane) [W/m·K]	Remarks
	Heat Producing Elements	
ASIC	124	200 µm thick silicon dissipating 1.02 W
LDO	124	200 µm thick silicon dissipating 1.19 W
	Thermal Interface Materials	
Thermally & Electrically Conductive Glue (EPO-TEK® E4110; TIM-4)	1.37	100 µm thick; simulated as contact resistance of 7.3×10^{-5} K·m^2/W
Thermally Conductive Glue (STYCAST 2850FT/Catalyst 23LV; TIM-3)	1.02	150 µm thick; simulated as contact resistance of 1.5×10^{-4} K·m^2/W
Synthetic Graphite Sheet (DSN5040-10DC10DC; TIM-1 & TIM-2)	20	40 µm thick; simulated as contact resistance of 2×10^{-6} K·m^2/W
	FEB PCB	
Thermal Vias - ASIC	$\gtrsim 10.4$	Effective properties corresponding to 1.6 mm thickness, 10×6.5 mm^2 and 2.2 K/W thermal resistance
Thermal Vias - LDO	$\gtrsim 10.4$	Effective properties corresponding to 1.6 mm thickness, 5.8×6.15 mm^2 and 4.3 K/W thermal resistance
PCB	0.45	Simulated as FR4
	Miscellaneous	
T-Shelf	200	Aluminium material (1060 Alloy)
Adapter Base Plate	200	Aluminium material (1060 Alloy)
Side Shelf	200	Aluminium material (1060 Alloy)
FEB Box Cover	200	Aluminium material (1060 Alloy)

Table 2.6.: Thermal properties of various elements comprising the thermal path within a FEB box used in the FEA thermal simulation. Only thermal conductivity values are necessary for steady state thermal simulations in SolidWorks®.

Thermal Finite Element Analysis (FEA) in SolidWorks® has been used to model heat transfer within the FEB box. This involves meshing the FEB box into smaller elements, allowing for detailed analysis of heat distribution. The thermal properties of the elements used in the simulation are listed in Tab. 2.6. Since the FEB box is composed of elements of varying sizes ($\sim 10\mu\text{m} - 1$ mm), this can result in very small element size leading to computationally intensive calculations due to unnecessarily large number of elements. Therefore, several assumptions and simplification methods have been used to minimise computation time. Thermal interface materials were modeled with surface-to-surface contact conditions and corresponding thermal contact resistance[3]. Thermal vias under the ASICs and LDOs were simplified using effective properties based on their thermal resistances. Only conductive thermal transfer was considered, excluding convection with surrounding air and assuming a constant surface temperature between the FEB box and cooling plate. Based on the resulting FEB box temperature distributions shown in Fig. 2.23, it can be concluded that:

3. Thermal contact resistance (R_T) of a layer with thermal conductivity (k) and thickness (d) across area (A) is defined as: $R_T = d/k \cdot A$ [K/W]. The distributed thermal resistance is defined as $R_{T,dist} = d/k$ [K·m^2/W]

- Target FEE temp. of 10°C can be achieved with a cooling plate temp. of -15°C, as the total temp. rise across the FEB box is ≈ 25°C.
- Significant temperature gradients are observed across all elements in an assembled T-shelf, particularly across the thermal interface materials.
- The FEB box cover temperature remains unaffected, allowing for higher FEE temperature without increasing the silicon sensor temperature.

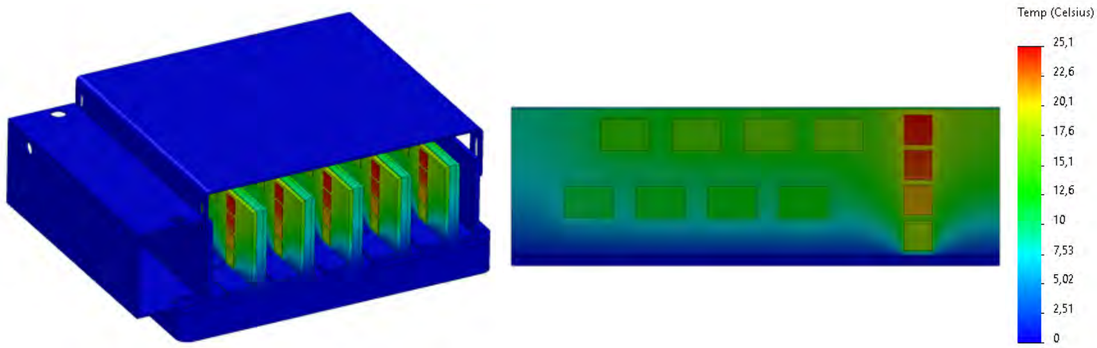

(a)

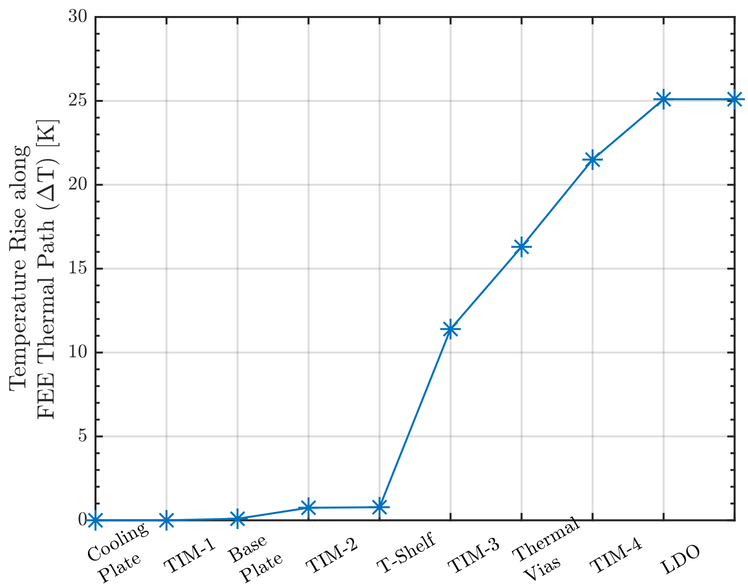

(b)

Figure 2.23.: (a) Temperature distribution of an assembled STS FEB box with total FEE power dissipation of 129.3 W (*Maximum Scenario*) and constant surface temperature between the FEB box and cooling plate of 0°C. (b) Temperature rise (ΔT) across the various elements comprising the thermal path within a FEB box from Fig. 2.23(a). The thermal properties of the comprising elements are in Tab. 2.6.

2.2.2. Front-End Electronics Cooling Plate and Coolant

The cooling efficiency of the FEE thermal path (see Fig. 2.20) depends significantly on the coupling between the cooling plate and coolant, i.e., the heat-transfer coefficient, which is determined by cooling plate geometry (channel diameter, geometry and length) and coolant's properties (input flow conditions). Moreover, the choice of coolant directly affects the choice of cooling plate technology (see Sec.1.2 for an overview of general strategies deployed for cooling silicon detectors). The requirements for STS FEE cooling include:

- *Wide Operating Temperature Range:* As concluded in Sec. 2.2.1, a cooling plate temperature of ≈-15°C is required to ensure a maximum FEE temperature of 10°C. Considering the inefficient heat transfer between the coolant and cooling plate, and temperature gain from the cooling plant to the cooling plate (due to imperfect transfer line insulation), the coolant should ideally be capable of reaching temperatures as low as -40°C. However, even lower temperatures necessitate a dryer detector environment, more expensive components, and higher thermal stress. Furthermore, room temperature operation is also necessary for in-lab detector commissioning and testing. Therefore, the desired operating range for the coolant is -40 ... 20°C.

- *Radiation Hardness:* Radiation in high-energy physics experiments can cause chemical breakdown of coolant molecules, leading to potential degradation of the fluid's thermal and physical properties, and formation of reactive species and particulates that may clog or damage system components [193, 194]. Additionally, other elements in the cooling loop, such as tube materials and the efficiency of filtering and purification elements, are crucial. Therefore, the STS FEE coolant must exhibit radiation hardness up to ∼10 kGy to ensure reliable cooling.

- *High Volumetric Heat Transfer Coefficient:* The available "cold mass", primarily the cooling plate volume, must neutralise the STS FEE power density of ≈1 W/cm^3 within the geometrical constraints. Therefore, it's imperative to extract the maximum cooling from the coolant within an optimised cooling plate geometry, quantified in terms of the system's volumetric heat transfer coefficient.

- *Commercial Manufacturability and Minimal Regulatory Constraints:* The use of climate-friendly coolants in commercial systems in the EU is essential to reduce greenhouse gas emissions and carbon-footprint, comply with environmental regulations [195–197] and ensure reliable long-term operation of the STS FEE cooling system (beyond 2040). Moreover, the coolants should be inert, non-flammable, and have ultra-high electrical resistivity for safe operation.

The aforementioned requirements substantially narrow down the choice of coolants deemed suitable for STS FEE cooling. Over the past decade of STS cooling R&D, the choice of coolant, cooling plate technology, and underlying geometrical conditions has changed dynamically and substantially. This includes:

- *Choice of Coolant:* Initially, bi-phase CO_2 was chosen for the FEE coolant as it met all the aforementioned requirements. This R&D was detailed in the CBM-STS Conceptual[4] and Core Preliminary Design Reviews[5]. However, after further scrutiny during the CBM-STS Cooling Conceptual Design Review[6], mono-phase 3M™ NOVEC™ 649 was chosen as the primary choice of coolant due to its easier implementation compared to the high-pressure and complex bi-phase systems, as well as relaxed temperature uniformity and material budget requirements for the STS FEE.
- *Cooling Plate Thickness:* Initially, the spacing between STS stations was 100 mm wherein the cooling plate thickness was 15 mm. However, this design could not accommodate the thermal expansion of the micro-cable, an updated design of the FEB boxes, and mechanical tolerances of the assembly. Therefore, the inter-station spacing was increased to 105 mm and cooling plate thickness was decreased to 12 mm as part of STS Design Change Request - 2020 [198].
- *Nominal FEE Temperature:* Initially, lower silicon sensor and FEE temperatures (<-5°C) were assumed for STS operation that required a cooling plate temperature of ≈-30°C. But after further study of the role of operating sensor temperature on the electrical performance of STS in mitigating the adverse radiation effects, these requirements were relaxed to a sensor and FEE temperature of 10°C (see Sec. 1.5 and Fig. 1.22), resulting in a cooling plate temperature of ≈-15°C.

This section aims to provide a coherent and systematic comparison between bi-phase CO_2 (Sec. 2.2.2.1) and mono-phase 3M™ NOVEC™ 649 (Sec. 2.2.2.2) in their respective cooling plates technologies using numerical simulations under comparable boundary conditions to obtain a maximum cooling plate temperature of ≈-15°C. The use case considered is a 12 mm thick *FEB Cooling Block 4* that can host up to eight FEB Boxes (four per side) and dissipate 1040 W (12.93 W per FEB, with one FEB box holding up to 10 FEBs; see App. E.2 for powering scenarios). Additionally, the channel geometry within the cooling plate will be optimised to have a Swagelok®-compatible end-connection of 1/4 in. or 6 mm.

4. CBM-STS Conceptual Design Review (October 17-18, 2012) `https://indico.gsi.de/event/1814/`
5. CBM-STS Core Preliminary Design Review (November 30, 2018) `https://indico.gsi.de/event/7929/`
6. CBM-STS Cooling Conceptual Design Review (December 10, 2019) `https://indico.gsi.de/event/9671/`

2.2.2.1. Biphase CO_2

Over the past two decades, bi-phase CO_2 cooling has emerged as a standard to cool silicon detectors at sub-zero temperatures (usable coolant temperature range between the triple point (-56.6°C, 5.2 bar) and critical point (31°C, 73.8 bar); see Fig. 2.24(a)). CO_2 offers, in comparison with other coolants, a high volumetric heat transfer coefficient[7]as well as low viscosity at high pressure (see Fig. 2.24(b)). This allows long tubes of small diameter, which is of great advantage given the strict geometrical and material budget constraints. In addition to optimal thermal properties, it is also a practical choice as it is radiation-tolerant, nonflammable, nontoxic, inexpensive and carbon-neutral (see Sec.1.2.2 and Tab. 1.5 for an overview of bi-phase cooling in silicon detectors).

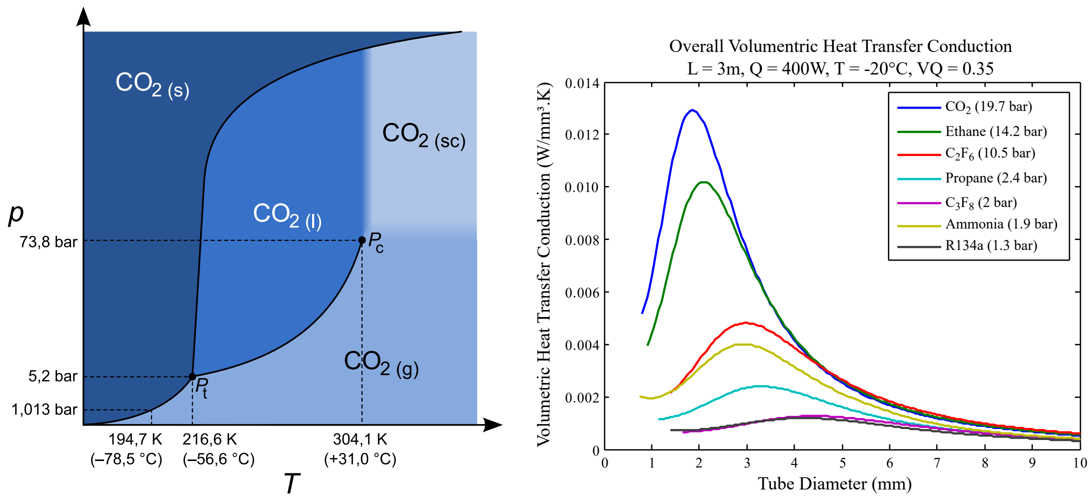

(a) (b)

Figure 2.24.: (a) CO_2 phase diagram shown as a variation of pressure with temperature. The triple and critical points are marked as P_t and P_c, respectively (figure from Sponk, Public domain, via Wikimedia Commons). (b) Variation of the volumetric heat transfer coefficient with tube diameter for different fluids. The specific use case considered here represents a typical silicon detector cooling application with a 400 W heat load along the cooling pipe of 3 m length, inlet temperature is -20°C and the outlet vapour quality 0.35. The thermal performance for CO_2 is better than other fluids while having a small tube diameter. The pressure drop and heat transfer coefficient are calculated with the Friedel [199] and Kandlikar correlations [200], respectively (figure from B. Verlaat (CERN, Geneva)) [119–121].

7. Volumetric heat transfer coefficient (HTC_{vol}) is defined as: $HTC_{vol} = \dot{q}/\Delta T_{Total}$ [60]. Here, $\dot{q}$ is the total power density across the cooling tube and ΔT_{Total} is the total temperature gradient caused due to the sum of: (a) the maximum temperature difference between the fluid and tube wall, and (b) the temperature difference of the fluid between inlet and outlet of the cooling tube due to the pressure drop.

Cooling Plant:

Traditionally, evaporative cooling is provided by a conventional *Vapour Compression System* (see Fig. 2.25). It primarily comprises of four active components: an evaporator (i.e., the heat-producing detector subsystem), compressor, condenser, and expansion valve, with only the compressor being accessible and placed away from the detector. This setup has the advantage of warm transfer lines, negating the need for insulation and saving space. However, limitations include having active components within the inaccessible detector area and using an admixture of oil in the coolant needed for compressor operation, which can be problematic in high-radiation environments due to possible polymerisation of the oil. Although cooling plants with oil-free compressors are commercially available (used in the ATLAS ID [115]), they use coolants other than CO_2.

To mitigate the applicability of vapour compression system for CO_2, the *2-Phase Accumulator Controlled Loop (2PACL) method* [119] deploys CO_2 as a liquid-pumped, oil-free system. It primarily comprises of: an evaporator (i.e., the heat-producing detector subsystem), expansion valve or capillaries, pump, chiller, and accumulator, with the latter three accessible and placed away from the detector (see Fig. 2.25). As the name suggests, the two-phase temperature is passively, yet precisely, controlled only via pressure regulation in the accessible CO_2 accumulator tank by heating or cooling the liquid/vapour pool. This ensures a stable evaporator temperature that is largely independent of the heat load, with all active components stationed in accessible areas. Moreover, the large liquid overflow through the evaporator ensures that only a fraction of the liquid is evaporated, avoiding dry-out (i.e., only vapour and no liquid), thus providing a higher heat transfer coefficient between the fluid and tube surface. However, the drawback is that concentric transfer lines (with input liquid lines enclosed

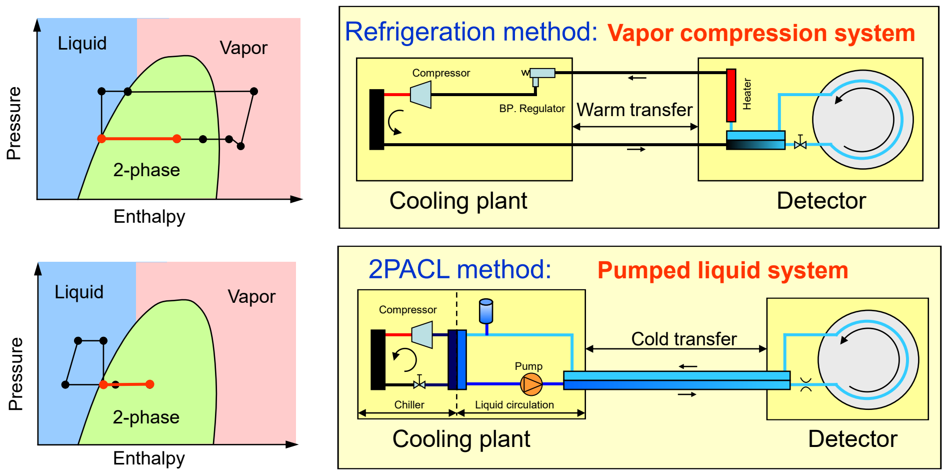

Figure 2.25.: Schematic representation of different cooling cycles with their pressure-enthalpy diagrams. Top: Conventional Vapour Compression System. Bottom: 2PACL Liquid Circulation System (figure from B. Verlaat (CERN, Geneva)).

inside the output bi-phase lines) are cold and require space-consuming insulation. This method was first used at the AMS02 Tracker Temperature Control System (TTCS) deployed at the International Space Station (ISS) in 2011 [201] and was subsequently pioneered for high-energy physics experiments by the LHCb VELO [120,121]. Since then, the 2PACL concept has been implemented in several silicon tracker upgrades of LHC experiments, such as the ATLAS IBL [101], CMS Phase-1 Pixel Detector Upgrade [122, 123], LHCb VELO Upgrade-I [109], and future upgrades for silicon detectors of ATLAS and CMS at HL-LHC [124–129].

Inspired by the 2PACL laboratory refrigeration unit developed at CERN, the *Transportable Refrigeration Apparatus for CO_2 Investigation (TRACI)*, STS developed a 1 kW closed-loop bi-phase CO_2 cooling plant, TRACI-XL [202, 203]. Moreover, the commercial manufacturability of a larger 50 kW cooling plant was accessed with potential industrial partners[8] [204, 205]. This chain of R&D was discontinued in 2019 in favour of 3M™ NOVEC™ 649 (see Sec. 2.2.2.2).

Cooling Plate:

The FEE cooling plates are designed to maximise the heat transfer coefficient between the coolant and the plate while withstanding high pressures up to 120 bar to comply with the Pressure Equipment Directive[9]. A commercially available solution fulfilling these requirements is provided by Cool Tec[10], where copper tube (inner and outer diameter of 4 mm and 6 mm, with 3.6 mm length) are press fitted into an aluminium base to ensure direct metal-to-metal contact (equivalent inner diameter of 3.6 mm; see Fig. 2.26). The first prototypes were successfully tested up to 100 bar. However, the main disadvantage of this design is the limitation in the length of the cooling pipe due to finite bending radius of the copper tube (9 mm for the considered tube diameter).

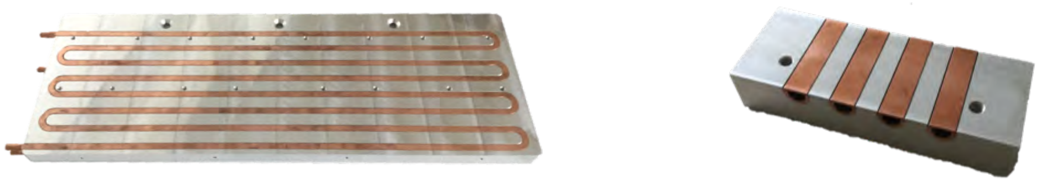

(a) (b)

Figure 2.26.: (a) First prototype of the FEE cooling with press-fitted tube channels by Cool Tec Electronic GmbH. (b) Cross-sectional view of the press-fitted tube channels.

8. compact Kältetechnik GmbH - www.compact-kaeltetechnik.de
Hafner-Muschler Kälte- und Klimatechnik GmbH - www.konzmann.de/kontakt/konzmann-hafner-muschler
9. Pressure Equipment Directive (PED) 97/23/EC sets out the standards for the design and fabrication of pressure equipment, such as the FEE cooling plate, based on the stored energy (product of maximum pressure and the volume). The stored energy for the FEE cooling plate with tube of 4 mm inner diameter under 100 bar pressure is 125.7 J·m.
10. Cool Tec Electronic GmbH, Germany, www.cooltec.de

Calculations and Numerical Simulations:

Two-phase flow boiling heat-transfer mechanism is dependent on the complex interaction of concurrent gas and liquid flows represented by various flow patterns which are dependent on the physical and geometrical structures. This makes it significantly challenging to use Computational Fluid Dynamics (CFD) software packages to accurately model phase transitions and liquid-vapour dynamics, while ensuring numerical stability and convergence in the presence of steep temperature and pressure gradients. To overcome these difficulties, a hybrid approach is taken wherein the empirical correlations are used to theoretically calculate the heat transfer properties of bi-phase CO_2 for a simplified geometrical setup, which are then inputted to the thermal Finite Element Analysis (FEA) to obtain realistic temperature distribution over the entire cooling plate. Subsequent paragraphs will briefly describe the approach and comprising steps.

Flow Pattern Map: Various flow patterns emerge during the transition of a liquid into a vapour phase as it is heated along its flow path. Initially, the fluid enters as a single-phase liquid, and heat transfer occurs through forced convection. As heating continues, vapour bubbles start to form and coalesce creating turbulence that enhances heat transfer. The emerging bi-phase flow patterns are also affected by gravity separating the liquid at the bottom and vapour at the top of the tube. The primary patterns include (see Fig. 2.27(a)):

(i) bubbly flow, where vapour bubbles are concentrated in the upper half of the liquid

(ii) stratified flow, where liquid and vapour form separate layers with a flat interface at low velocities

(iii) stratified-wavy flow, where increased vapour velocity creates waves on the liquid-vapour interface

(iv) intermittent flow occurs at higher vapour velocities, where large waves of liquid intermittently reach the top of the tube, including plug flow (with small elongated bubbles and liquid plugs) and slug flow (with bubbles nearly as large as the tube diameter)

(v) annular flow, seen at even higher flow rates, forms a continuous liquid film around the tube's interior and exhibits the highest heat transfer coefficient

(vi) dry-out flow, where no liquid is in contact with the tube wall, which results in a sharp drop of heat transfer coefficient

(vii) mist flow, when all liquid dries out and only a small amount of dispersed liquid droplets

Therefore, the tube geometry and operational parameters have to optimised such that the boiling process in the tube remains in the intermittent and annular regime, while being safely away from the dry-out regime (see Fig. 2.27(b)).

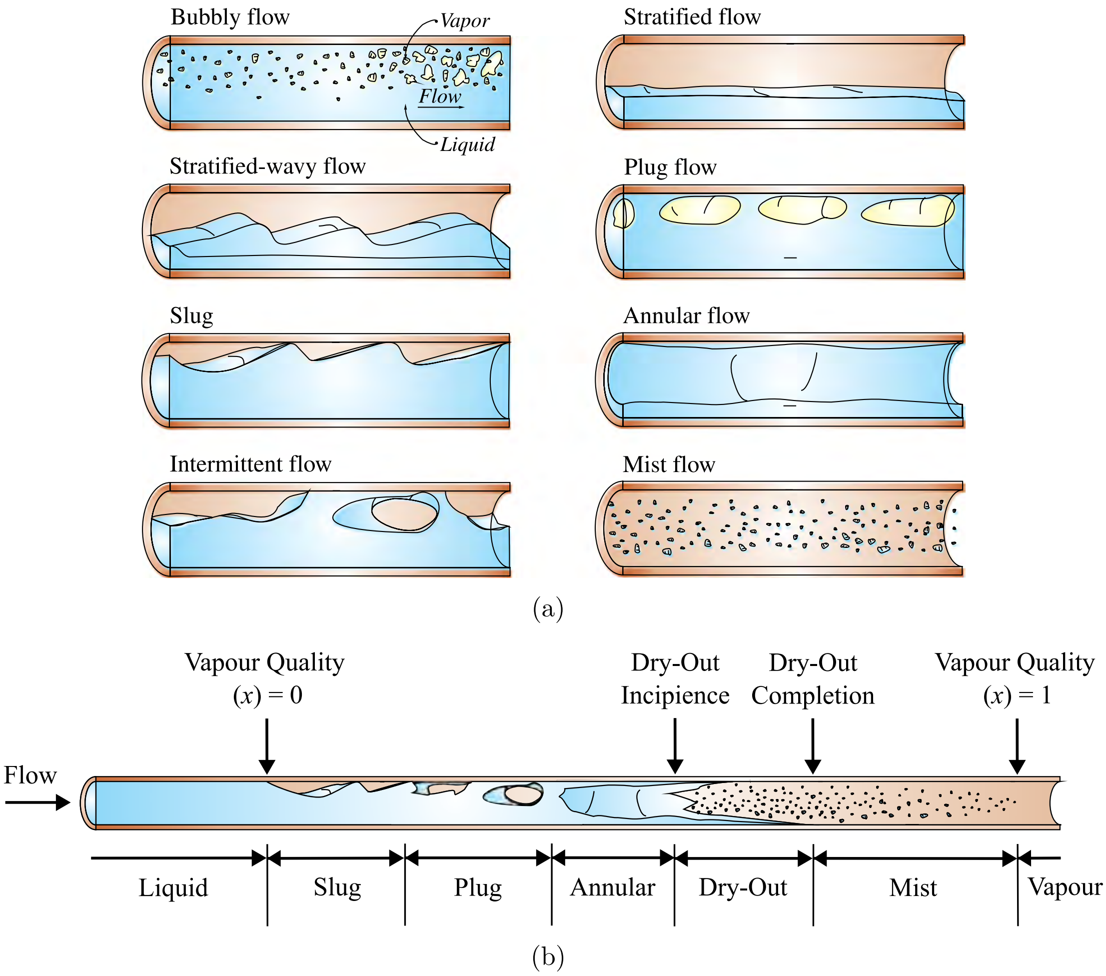

Figure 2.27.: (a) Liquid-vapour flow patterns and (b) their progression during boiling in a horizontal tube (figures adapted from [206]).

These various flow regimes or patterns are graphically described on a Flow Pattern Map, shown typically as the variation of Mass Velocity (G) with Vapour Quality (x) for a given channel orientation (equivalent diameter (D_{eq}) and length (L)), thus predicting the flow pattern to calculate the heat transfer and pressure drop. The CO_2 flow pattern map used in this work are based on the semi-emperical correlations by Cheng-Ribatski-Wojtan-Thome [207,208]. The resulting map for the press-fitted channel cooling plate described previously ($D_{eq} = 3.6$ mm and $L = 3.6$ m) with inlet CO_2 temperature T_{sat} = -20°C and heat load of 1040 W (corresponding to eight fully populated FEB boxes) with various mass flow rates (5 ...15 g/s) is shown in Fig. 2.28. It can observed that higher flow rates tend to increase the margin from dry-out, wherein the lowest considered flow rate (5 g/s) results in the system finishing in the dry-out regime. Consequently, flow rate of 10 g/s is the baseline flow rate as it provides sufficient dry-out margin (31.7%) while leaving enough possibility for higher flow rates.

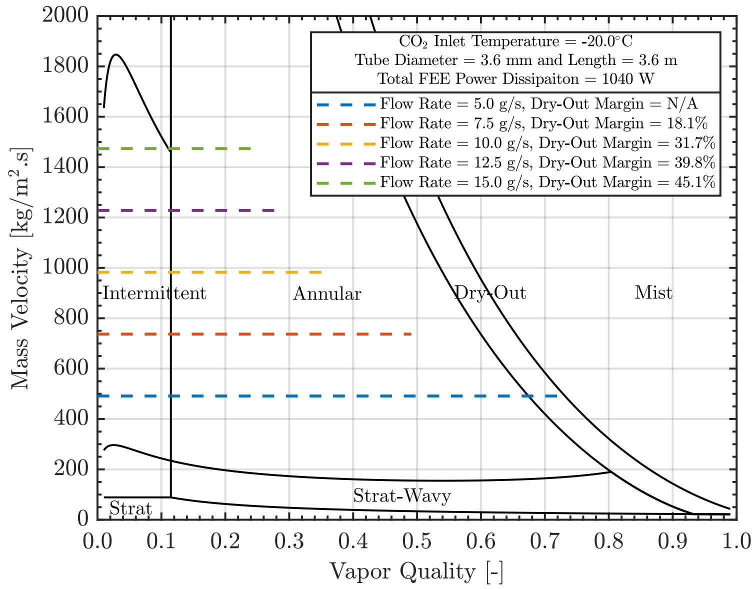

Figure 2.28.: Flow pattern map for press-fitted channel cooling plate, corresponding to the specifications of *FEB Cooling Block 4*, with process path depicted for various flow rates (5 ...15 g/s) along with the respective dry-out margins.

Calculations: CO_2 flow pattern maps by Cheng-Ribatski-Wojtan-Thome [207, 208], described previously, enable to model the heat exchange process during steady-state flow of rate $\dot{m}$ inside a horizontal tube of length L with a total FEE heat input of $\dot{Q}$. This is done by dividing the tube into N equal elements, each labeled i, with a corresponding FEE heat input of $\dot{Q}(i)$. Initial conditions at the entry node of the first element are manually set to saturation conditions (temperature, pressure, and enthalpy). For each ending node of the element, energy conservation is applied to calculate the enthalpy $H(j)$ and pressure $P(j)$ at the node by calculating the pressure drop across the element. Furthermore, this allows to further estimate the local heat transfer coefficient, CO_2 temperature and vapour quality. The process iterates along the subsequent elements of the entire cooling tube length, updating CO_2 thermal properties from the NIST REFPROP database [209] via MATLAB. This entire process is illustrated in Fig. 2.29. Please note that detector temperature in the 2PACL scheme is controlled by the accumulator pressure (see Fig. 2.25). Therefore, outlet node conditions ($j = N + 1$) are iteratively calculated to match the desired saturation values while adjusting the initial pressure until convergence. This results in CO_2 entering the tube in a sub-cooled state, albeit for only short lengths, thus correlations to treat liquid CO_2 are also included. The work presented here was motivated from the CoBra (CO2 BRAnch Calculator) tool [210, 211], extensively used in designing CERN CO_2 cooling systems like the ATLAS Inner Alpine Detector [212]. However, the presented work was done independently for CBM-STS FEE cooling application.

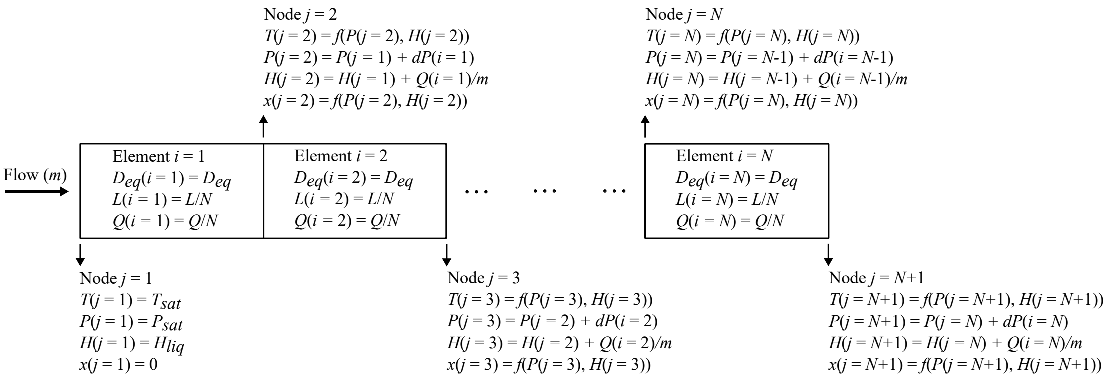

Figure 2.29.: Illustration of the calculation procedure used for model the bi-phase CO_2 heat exchange process inside a horizontal tube (figure adapted from [212]).

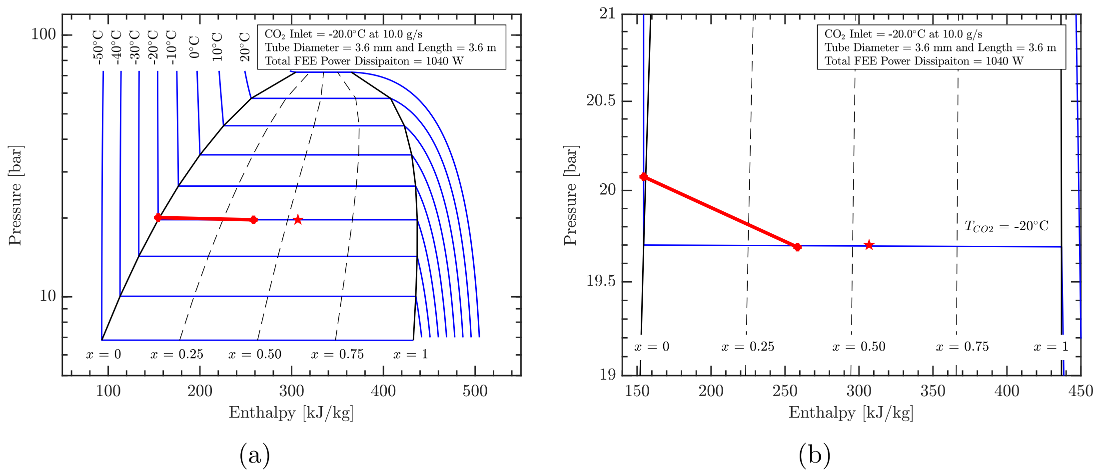

Figure 2.30.: (a) Zoomed-out, and (b) zoomed-in CO_2 pressure-enthalpy diagrams showing the heat exchange process (solid-red line) and the dry-out incipience point (red star marker) for the baseline parameters of *FEB Cooling Block 4*. The isotherms, phase boundaries and vapour quality markings are shown as solid-blue, solid-black and dashed-black lines, respectively.

Calculations for the *FEB Cooling Block 4* are shown in Figs. 2.30-2.31, based on which the following can be concluded:

- CO_2 enters the cooling tube in a sub-cooled liquid state and starts boiling after 50 mm. The resulting sudden rise of tube temperature is not concerning for the STS FEE, as they are located at detector periphery with relaxed temperature uniformity requirements.
- The maximum temperature gradient between bi-phase CO_2 and tube wall (ΔT_{HTC}^{Max}) of 1.6 K. This is due to local variation of heat transfer co-efficient, as the bi-phase regime shifts from intermittent to annular flow regime.

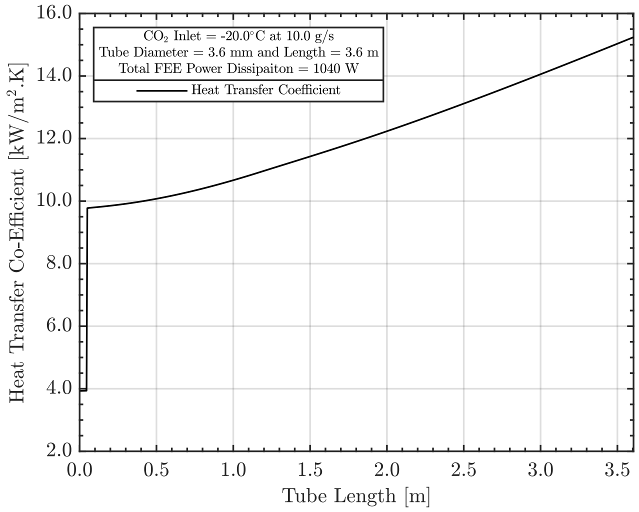

(a)

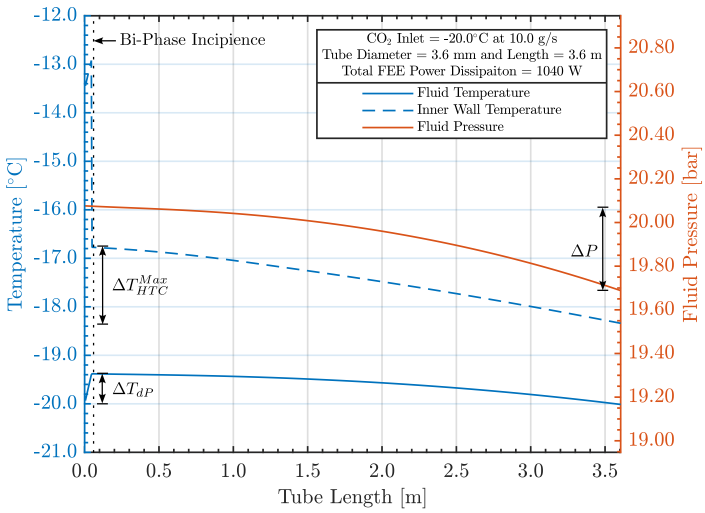

(b)

Figure 2.31.: (a) Variation of heat-transfer coefficient between CO_2 and cooling tube's inner-wall along the tube length. (b) Variation of CO_2 temperature (solid-blue), cooling tube's inner-wall temperature (dashed-blue) and pressure (solid-orange) with the tube length. Calculations are for the baseline parameters of *FEB Cooling Block 4*.

- CO_2 undergoes a low pressure drop of 0.39 bar resulting in largely constant fluid temperature with a maximum temperature difference at inlet and outlet of the cooling tube (ΔT_{dP}) of 0.6 K.
- The total temperature gradient ($\Delta T_{Total} = \Delta T_{HTC}^{Max} + \Delta T_{dP}$) is 2.2 K, resulting in a high volumetric heat transfer coefficient of 1.3 kW/cm^3·K.

Numerical Simulations: Thermal Finite Element Analysis (FEA) from SolidWorks® is used to obtain realistic temperature distributions across the entire cooling plate surface. This is achieved by defining a forced convection environment within the press-fitted channels, with the average local heat transfer coefficient (≈12 kW/m^2·K; see Fig. 2.31(a)) and fluid temperature (≈-19.6°C; see Fig. 2.31(b)) extracted from the aforementioned calculations. Moreover, the total power dissipation of 1040 W is distributed based on the FEB box locations. The resulting temperature distribution across the cooling plate is shown in Fig. 2.32(a), where the maximum cooling plate temperature is below the target value of ≈-15°C and would result in maximum FEE temperature of ≈10°C (see Fig. 2.32(b)).

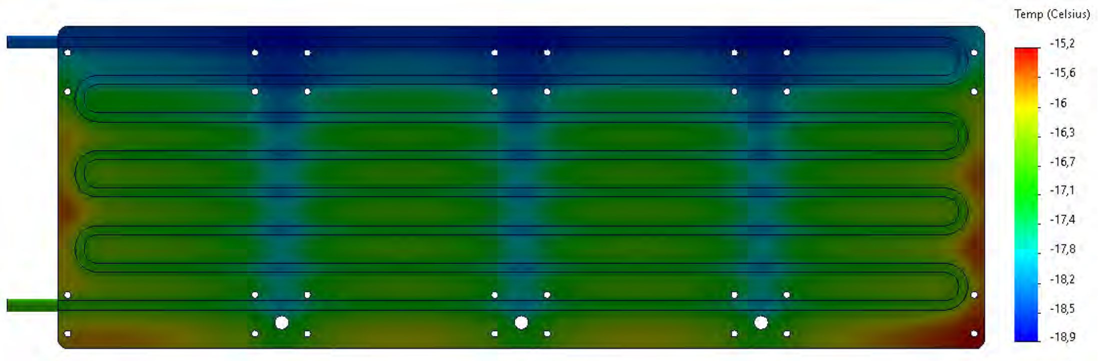

(a)

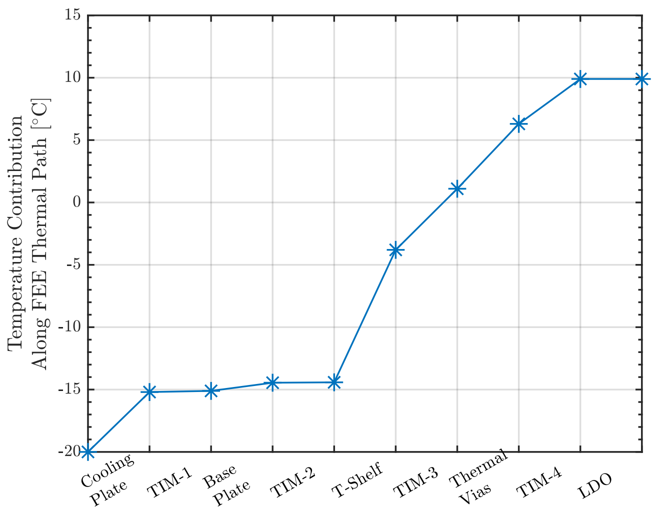

(b)

Figure 2.32.: (a) Thermal FEA temperature distribution of *FEB Cooling Block 4* under baseline operational parameters. (b) Temperature contribution along FEE thermal path by combining the FEB box (see Fig. 2.23(b)) and cooling plate temperature distribution (see Fig. 2.32(a)).

2.2.2.2. Monophase 3M™ NOVEC™ 649

Despite the growing use of bi-phase CO_2 for silicon detector cooling at sub-zero temperatures, mono-phase cooling remains relevant for applications with less stringent requirements on temperature uniformity, pressure drop, and material budget. This offers great advantages in terms of relatively simple design, low operational pressure, and lack of complex regulation loops (see Sec. 1.2.2 for a brief review). In recent years, engineered fluids like 3M™ NOVEC™ 649 ($C_6F_{12}O$; spur-oxygenated fluoroketone) have shown commercially viability in evaporative immersion cooling of electronics because of their low boiling point. Moreover, it has emerged as an environmentally friendly alternative to the commonly used perfluorocarbon (PFC) - C_6F_{14} for liquid cooling of particle detectors. Its suitability for detector cooling applications has been accessed under the framework of the LHCb Scintillating Fibre (SciFi) tracker cooling and discussed in detail in [65, 93, 213, 214]. Based on these reports, its feasibility for use in STS-FEE cooling is reasoned as follows:

Operating Range: The boiling and freezing points of 3M™ NOVEC™ 649 are 49°C and -108°C, respectively, making it usable for liquid cooling across a broad operating range.

Thermal Properties: Liquid 3M™ NOVEC™ 649 is easier to pump at sub-zero temperatures due to its low kinematic viscosity of 1.1 ... 0.4 cSt at -40 ... 20°C. Moreover, it exhibits comparable thermal properties (thermal conductivity, kinematic viscosity, and specific heat capacity) to liquid C_6F_{14} (see Tab. 1.4). This makes it a suitable drop-in replacement of liquid C_6F_{14}, allowing the use of commercially available products.

Radiation Hardness: 3M™ NOVEC™ 649 shows radiation resistance with gamma doses of up to 100 kGy due to the absence of hydrogen atoms, which reduces the likelihood of radiolysis and formation of hydrofluoric acid, thereby preventing corrosion of pipes in radiation environments.

Environmental Friendliness: 3M™ NOVEC™ 649 has a Global Warming Potential (GWP) of 1, which is substantially lower than other conventional coolants such as C_6F_{14} (GWP = 9300).

Handling and Safety: 3M™ NOVEC™ 649 is non-flammable, non-toxic, chemically inert, and electrically resistive. However, the cooling system must consider its high thermal expansion coefficient, potential cavitation due to low fluid-to-vapour-density ratio, reactivity with water, and limited material compatibility.

Collectively, these arguments make 3M™ NOVEC™ 649 an optimal choice for use as the STS-FEE coolant. Subsequent paragraphs will further explore practical on- and off-detector aspects, such as the cooling plant and plate technology, to use 3M™ NOVEC™ 649 in the STS-FEE cooling system.

Cooling Plant:

The mono-phase nature of 3M™ NOVEC™ 649 coolant within the STS FEE cooling circuit simplifies the cooling cycle design compared to bi-phase CO_2, allowing for the use of more conventional and industrial solutions. A mono-phase pumped liquid cooling system with 3M™ NOVEC™ 649 (*secondary loop*), cooled by a conventional vapour compression system with bi-phase CO_2 (*primary loop*), offers an optimal solution for STS FEE cooling. The secondary loop mainly comprises of: an evaporator (i.e., the heat-producing detector subsystem), pump, heater, chiller, and accumulator, with the latter four accessible and placed away from the detector (see Fig. 2.33). Liquid 3M™ NOVEC™ 649 is circulated through a closed loop via a pump, absorbing the power from the STS FEE. The heated liquid is subsequently cooled by evaporating CO_2 in a vapour compression cycle via a heat exchanger. This effectively cools the liquid 3M™ NOVEC™ 649, which is then recirculated back to the STS FEE cooling circuit. The extra heater in the secondary loop allows to extend the usable temperature range of the cooling circuit and compensates for any mismatches between the partial cooling capacity of the plant and detector power dissipation.

This integrated system offers low overall global warming potential, low operating pressure and non-toxicity in the secondary loop with 3M™ NOVEC™ 649, along with high volumetric heat-transfer coefficient in the primary loop with biphase CO_2. Additionally, it benefits from the growing commercial market of CO_2 vapour compression systems, providing a robust solution with established technology. However, the cold transfer lines carrying the liquid between the cooling plant and detector are require space-consuming insulation. Furthermore, high viscosity of 3M™ NOVEC™ 649 results in large pressure drops along the transfer lines, which must be mitigated by carefully dimensioning the secondary loop. The material compatibility issues of 3M™ NOVEC™ 649 also considerably narrows down the range of products usable in the secondary loop. The details of the pilot cooling plant with aforementioned scheme and steps to mitigate the challenges are discussed in Sec. 3.5.

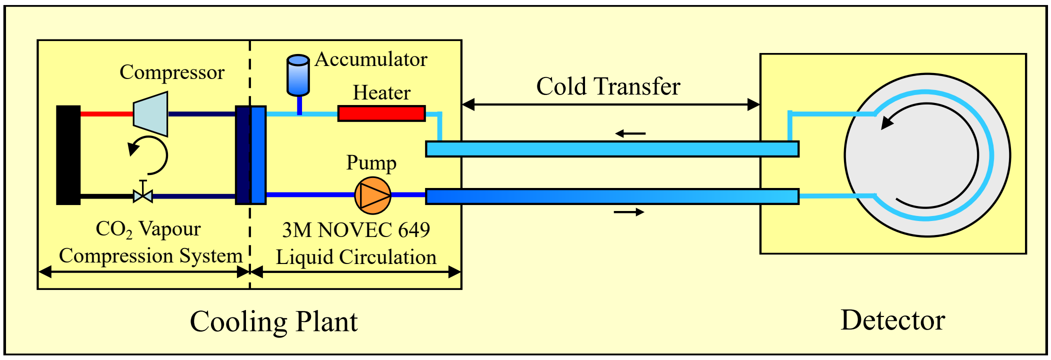

Figure 2.33.: Schematic representation of liquid-pumped 3M™ NOVEC™ 649 cooling plant cooled with bi-phase CO_2 in a vapour-compression cycle.

Cooling Plate:

The design of the STS-FEE cooling plate using 3M™ NOVEC™ 649 coolant presents several challenges: (i) low specific heat capacity and high viscosity of the coolant; (ii) the high FEE power density; (iii) the limited cooling plate thickness, i.e., cold mass. Moreover, cooling plates with press-fitted channels, previously introduced for bi-phase CO_2 (see Sec. 2.2.2.1), are not optimal for this application. This is due to the limited tube length and the need for flow rates higher than the erosional limit of 5.6 L/min [215, 216] to reach the desired cooling plate temperature [217]. To address these issues, cooling plate manufactured using 'Friction Stir Welding' technology for aluminium (AlMg3) was explored in collaboration with Cool Tec[11]. This technology allows milling fluid channels within the cooling plate, enhancing heat transfer between the 3M™ NOVEC™ 649 coolant and the cooling plate, while ensuring lower flow rates and reduced pressure drop. The process involves milling parallel channels on a thicker base-plate, which is then sealed by friction stir-welding a cover-plate on top (see Fig. 2.34). Moreover, this technology also allows to use threaded connections for inlet and outlet. However, welded joints are susceptible to leakage under higher pressure, limiting the operational pressure of the cooling plate. This issue is addressed through detailed mechanical characterisation of the prototype cooling plates, validating their suitability for the STS-FEE cooling application (discussed later in Sec. 3.1).

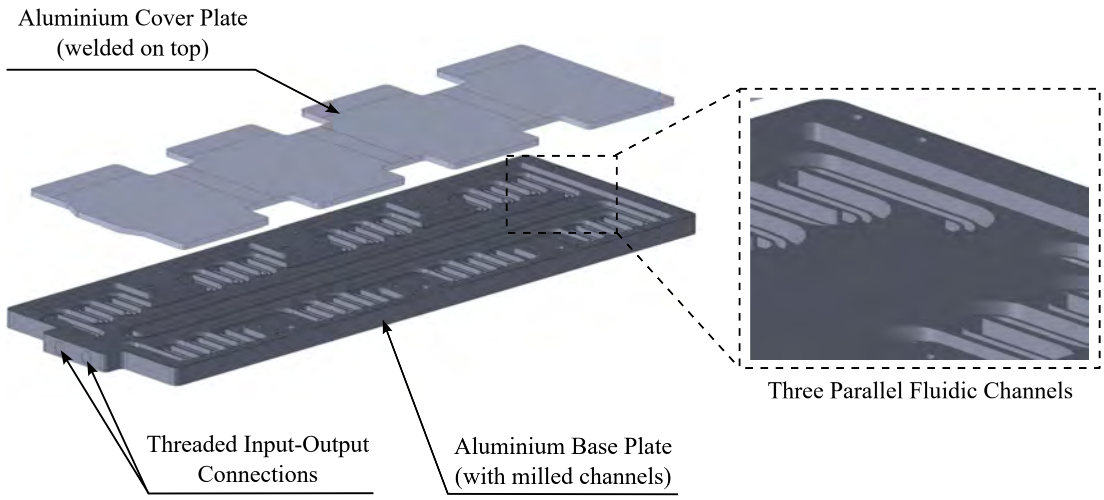

Figure 2.34.: CAD rendering of the 3M™ NOVEC™ 649 cooling plate manufactured with the 'Friction Stir Welding' technology. The exploded view on the left shows the comprising base- and cover-plate. The call-out on the right shows the zoomed-in view of the three parallel channels milled inside the base-plate (CAD drawings provided by Cool Tec Electronics GmbH).

11. Cool Tec Electronic GmbH, Germany, `www.cooltec.de`

Numerical Simulations:

The mono-phase nature of 3M™ NOVEC™ 649 heat-transfer for STS FEE cooling application enables to conveniently use the Computational Fluid Dynamics (CFD) package from SolidWorks® to obtain realistic temperature distributions across the entire cooling plate surface. The boundary conditions[12]involved in these simulations are inlet fluid temperature of -30°C at volumetric flow rate of 3 L/min (safely below the erosional limit) to remove total power dissipation of 1040 W which is distributed based on the FEB box locations.

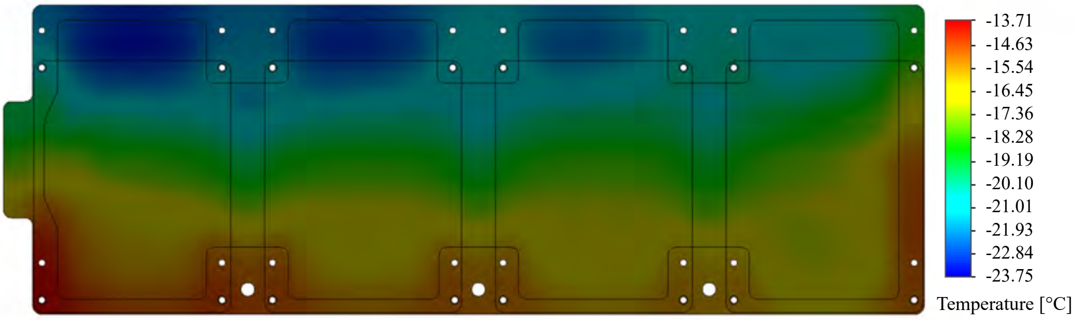

(a)

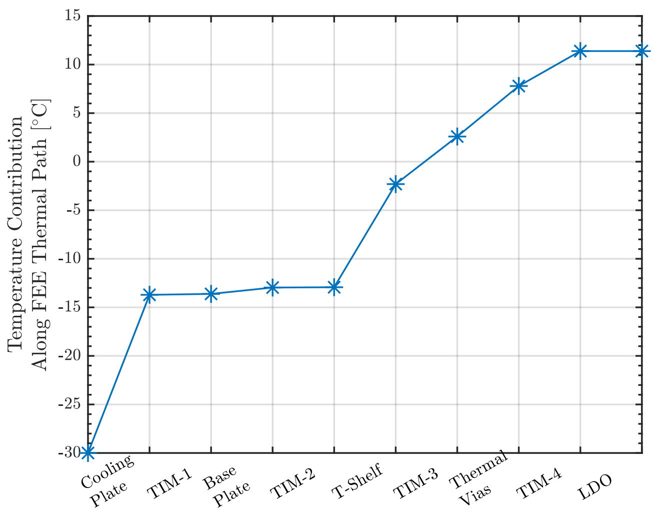

(b)

Figure 2.35.: (a) CFD temperature distribution of *FEB Cooling Block 4* under baseline operational parameters with mono-phase 3M™ NOVEC™ 649. (b) Temperature contribution along FEE thermal path by combining the FEB box (see Fig. 2.23(b)) and cooling plate temperature distribution (see Fig. 2.35(a)).

12. k-omega ($k-\omega$) turbulence model was used to simulate turbulence at the cooling plate inlet in terms of the turbulent kinetic energy (k) and specific dissipation rate (ω).

The resulting temperature distribution across the cooling plate is shown in Fig. 2.35(a), where the maximum cooling plate temperature is below the target value of ≈-13.7°C and would result in maximum FEE temperature of ≈11°C (see Fig. 2.35(b)). 3M™ NOVEC™ 649 undergoes a gradual temperature rise of ≈10 K (see Fig. 2.36(a)) and pressure drop of 1.17 bar (see Fig. 2.36(b)). Please note that the flow rate is primarily chosen to avoid the erosional velocity[13]of ≈ 3 m/s for long-term continuous use (see Fig. 2.36(c)).

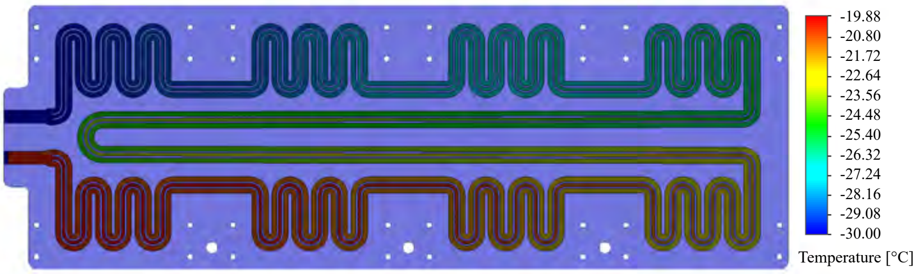

(a) 3M™ NOVEC™ 649 Temperature Distribution

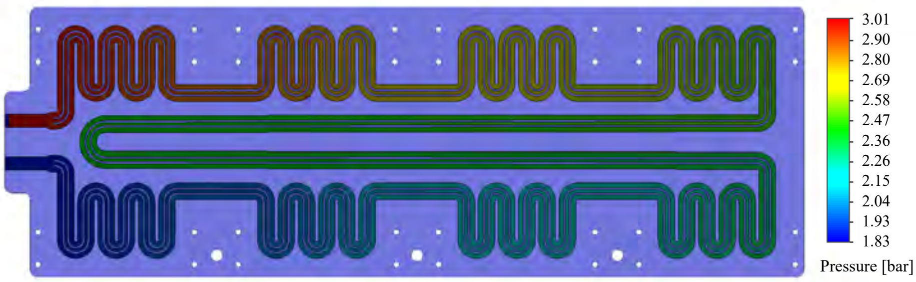

(b) 3M™ NOVEC™ 649 Pressure Distribution

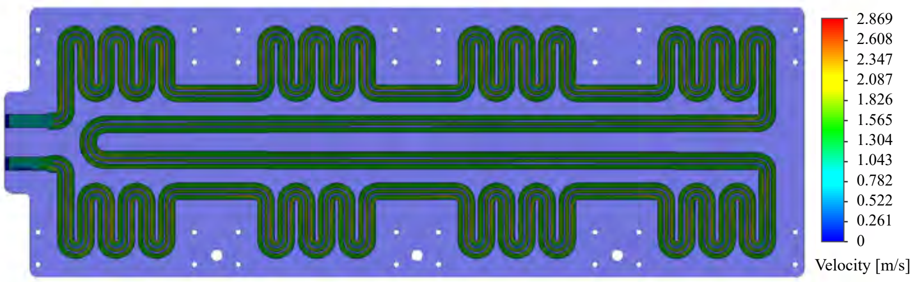

(c) 3M™ NOVEC™ 649 Velocity Distribution

Figure 2.36.: 3M™ NOVEC™ 649 (a) temperature, (b) pressure, and (c) velocity distribution of *FEB Cooling Block 4* under baseline operational parameters.

13. Erosional velocity for continuous operation is defined as: $v_{erosional}[\text{ft/s}] = 100/\sqrt{\rho[\text{lb/ft}^3]}$ [215, 216]. For 3M™ NOVEC™ 649 at -30°C, $v_{erosional} = 2.91$ m/s.

2.3. CBM-STS Cooling Concept

Based on the calculations and simulations shown in this chapter both for silicon sensor (Sec. 2.1) and front-end electronics cooling (Sec. 2.2), the following can be concluded as the CBM-STS cooling concept:

Silicon Sensor Cooling: Air cooling is the chosen cooling concept to inhibit thermal runaway and minimise material budget within the detector's physics acceptance. Forced air convection using impinging jets via perforated carbon-fibre tubes is needed to neutralise the power dissipation in the innermost sensors of all STS stations ($\Delta x = \Delta y \leq \pm$ 10 cm), while natural air convection is sufficient to cool the peripheral sensors.

Front-End Electronics Cooling: The power dissipation for STS-FEE can be effectively neutralised by housing the FEBs in a FEB box which provides a conductive path with minimal thermal impedance from the heat-dissipating read-out ASICs and LDO regulators into the friction-stir welded cooling plate carrying mono-phase liquid 3M™ NOVEC™ 649.

The aforementioned concept, also illustrated in Fig. 2.37, will serve as the baseline to design and produce pre-production components for CBM-STS cooling mechanics, and experimentally verify the cooling concept with a *Thermal Demonstrator* under realistic STS boundary conditions.

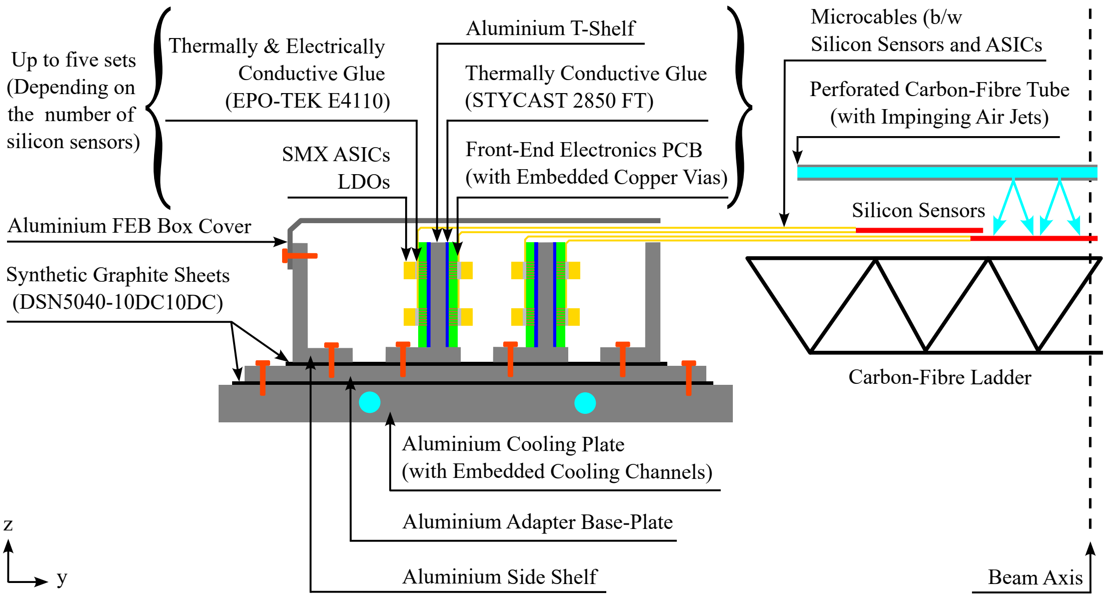

Figure 2.37.: Illustration showing the thermal path of STS sensor and FEE cooling. Drawing is not to scale.

3. The CBM-STS Thermal Demonstrator

The CBM-STS *Thermal Demonstrator* aims to experimentally investigate the STS thermal operational conditions and to verify the cooling concepts under realistic boundary conditions. The Thermal Demonstrator consists of three STS-like half-stations examining the "active" layer's thermal behaviour of sensor and electronics heat dissipation, sandwiched between two mechanically "passive" layers (see Fig. 3.1). This setup also represents the possibility to establish the concepts of STS cooling mechanics, such as the cooling elements and peripheral services, such as feedthroughs etc. Insights gained play a pivotal role in shaping component choices and integration processes for the final STS, currently in series procurement and production. Therefore, this chapter summarises the efforts presented in the CBM-STS Mechanics[1] and Cooling Engineering Design Review[2] .

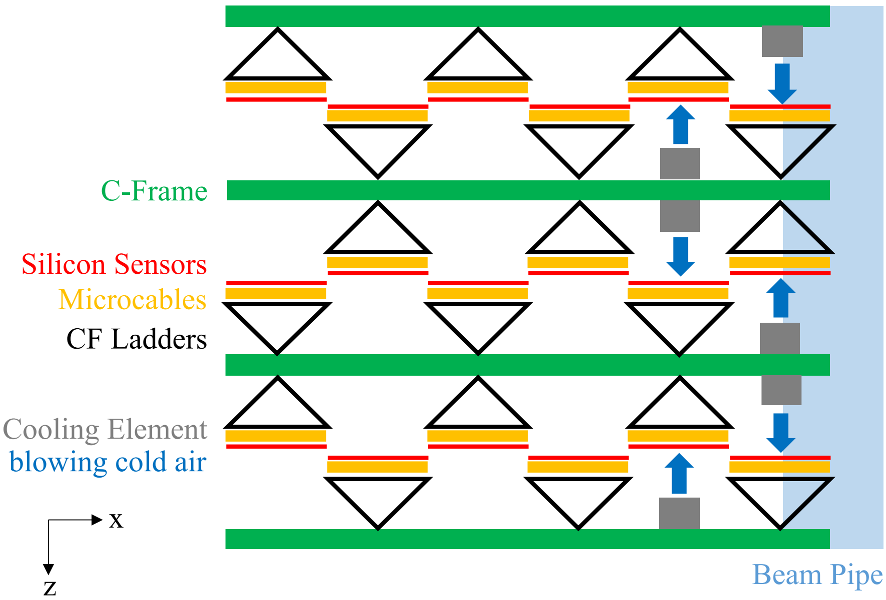

Figure 3.1.: Conceptual illustration of the three half-stations of the Thermal Demonstrator (top view). The red shaded area encloses the thermally "active" half-layer.

1. CBM-STS Mechanics Engineering Design Review (November 05, 2021) `https://indico.gsi.de/event/13250/`
2. CBM-STS Cooling Engineering Design Review (July 07, 2023) `https://indico.gsi.de/event/17904/`

3.1. Cooling Elements: Mechanical Design

3.1.1. Silicon Sensor Cooling

Perforated carbon-fibre (CF) tubes are the cooling elements designed to neutralise the power dissipation from the most irradiated silicon sensors. These tubes are mounted on the C-frame opposite to the ladder to be cooled (see Fig. 3.1 for the illustration). They serve a twofold benefit: (i) focused airflow onto the exposed surface of the innermost sensors of the innermost ladders ($\Delta x = \Delta y \leq \pm$ 10 cm) of every STS station; (ii) minimal additional material budget in the STS's physics acceptance. The typical values of CF-tube's important geometric parameters used in the Thermal Demonstrator are listed in Tab. 2.2 (see Sec. 2.1 for the design rationale based on calculations and numerical simulations). Commercially available CF tubes[3] were used with the perforations drilled in house.

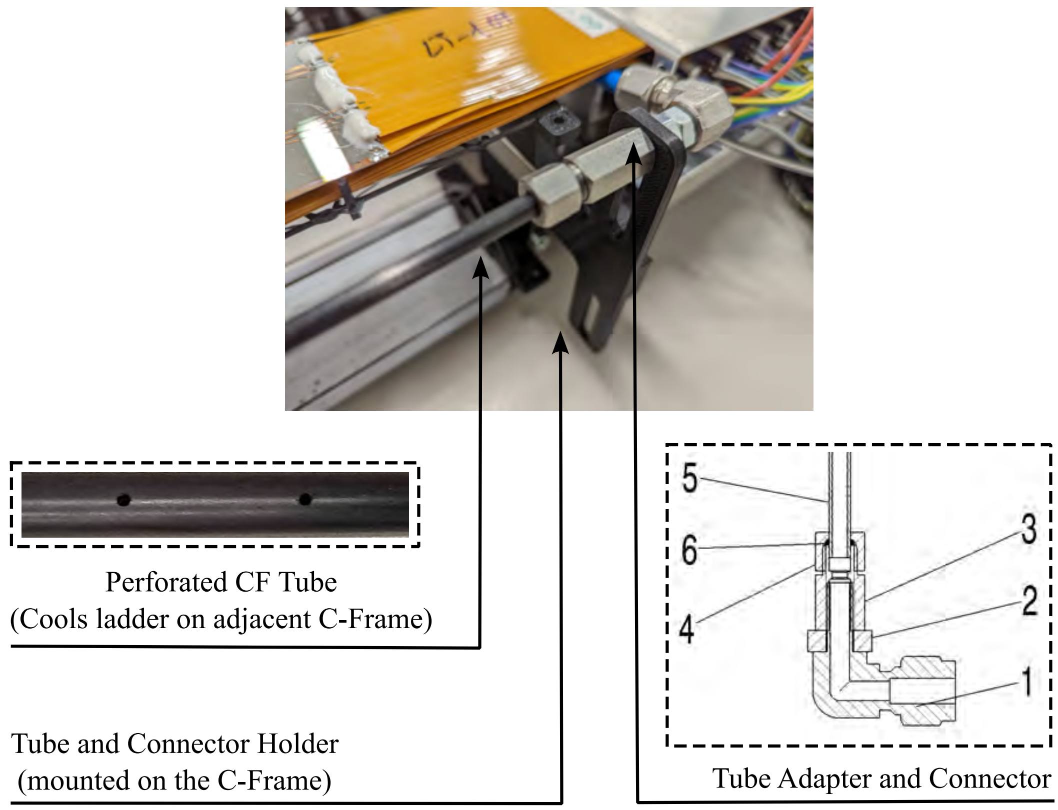

Figure 3.2.: Perforated CF-tube assembled on the Thermal Demonstrator's C-Frame with a 3D-printed plastic holder (in black). The call-out on the left shows the zoomed-in view of the perforations on the CF-tube. The call-out on the right shows the sectional view of the tube adapter and connector, with the details of comprising individual items given in the text (figures from J. Thaufelder (GSI Darmstadt)).

3. Carbon Composite GbR; Article Number - PCT05035-1

Given the non-standard dimensions of the CF-tube and the lack of integration space on the C-frame, customised holders and connectors have been produced (see Fig. 3.2 for an overview of the assembled CF-tube on the C-Frame). For the mounting of carbon tubes, 3D-printed holders were produced that allow the distance between the tubes and the sensor surface to be adjusted. To further connect the CF-tube to the global air distribution system, a commercially available angle connector[4] was modified and screwed to a hexagon adapter that was customised to the tube's geometry (see Fig. 3.2: right call-out). The hexagon adapter consists of two parts: the lower part (item 3) is used for fastening to the C-frame mounting holder (item 2), while the upper cap nut (item 4) and the O-ring (item 6) are used for fastening and sealing the carbon tube (item 5). When mounting, it is important to ensure that the perforations are correctly aligned.

These manufacturing and integration feasibility of these concepts have been experimentally tested in the Thermal Demonstrator. Furthermore, this also allowed to test the airflow distribution amongst several C-frames by using a distribution box based on dedicated rotameters[5]. This distribution box also contains a dedicated supply line to provide dry nitrogen to the thermal enclosure of the Thermal Demonstrator to maintain a low-humidity environment. This is achieved by further distributing the supply line into several perforated pneumatic hoses[6] throughout the enclosure's volume.

3.1.2. Front-End Electronics Cooling

The cooling plates for STS front-end electronics (FEE), using liquid 3M™ NOVEC™ 649 coolant, is designed to enhance the heat transfer coefficient between the coolant and electronics, while limiting the cooling plate thickness to 12 mm. The FEE cooling plates are developed in collaboration with Cool Tec[7], which uses 'Friction Stir Welding' technology for aluminium (AlMg3). This solid-state joining process utilises a non-consumable tool to join facing workpieces without melting the material. The process involves milling parallel channels on a thicker base-plate, which is then sealed by friction stir-welding a cover-plate on top (see Fig. 2.34). Moreover, this technology also allows to use threaded connections for inlet and outlet. Details about the thermal performance of these plates by using Computational Fluid Dynamics (CFD) simulations are described in Sec. 2.2.2.2.

However, the high fluidic channel density required to effectively cool the FEE power dissipation limits the distribution of welding joints, limiting the operational pressure of the cooling plate. This makes these plates prone to bulging under high pressure and, in worse case scenario, even leakage at welding joints. Therefore, bulging of the sample pre-production cooling plate under various pressures was

4. Swagelok Part Number - SS-6M0-2R-6M
5. Yokogawa Rotameter Type RAGL41
6. Festo 6mm Pneumatic Tube
7. Cool Tec Electronic GmbH, Germany, www.cooltec.de

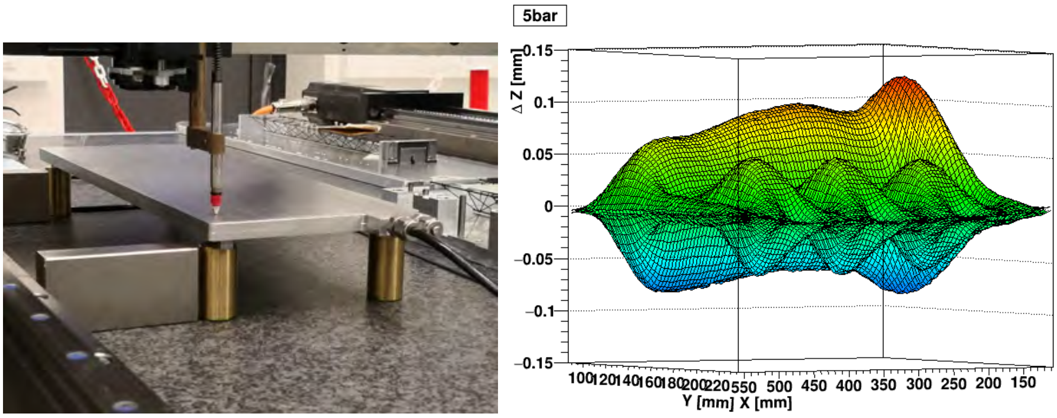

(a) (b)

Figure 3.3.: (a) Metrology setup to measure cooling plate's bulging when kept under pressure. (b) Bulging measured across the top and bottom of the cooling plate's surface under pressure of 5 bar(g) (figures from U. Frankenfeld (GSI Darmstadt)).

Class of Materials	Substrates[8]	Compatibility
Metals and Alloys	Aluminium, Copper, Stainless Steel, ...	OK
Rigid Polymers	PE, PP, PMMA, PC, GRP, PA, PEEK, ... PVC	OK Partially (plasticizers)
Flexible Polymers	Silicone, PTFE PUR, UHMWPE	Partially (swelling) OK
Elastomers	EPDM, Butyl, Nitril	Partially (plasticizers)
Adhesives	Epoxies Silicone PUR Acrylic Adhesives	OK Not compatible Partially Specific tests required

Table 3.1.: 3M™NOVEC™649 material compatibility [219, 220].

measured using the STS ladder metrology setup [218] (see Fig. 3.3(a)), indicating a maximum deformation of ≈ 100 µm at the maximum operational pressure of 5 bar(g) (see Fig. 3.3(b)). Considering the entire thermal pathway of the front-end cooling system, mounting procedure and underlying mechanical tolerances, these results were deemed satisfactory.

The crucial criterion for selecting components in the front-end electronics cooling circuit, including valves, connectors, hoses, and sealants, is their compatibility with 3M™ NOVEC™ 649 (see Tab. 3.1 for summary of prior research and oper-

8. PE = Polyethylene; PP = Polypropylene; PMMA = Poly(methyl methacrylate) ; PC = Polycarbonate; GRP = Glass Reinforced Plastic; PA = Polyamide; PEEK = Polyether ether ketone; PVC = Polyvinyl chloride ; PTFE = Polytetrafluoroethylene ; PUR = Polyurethane ; UHMWPE = Ultra-High Molecular Weight Polyethylene; EPDM = Ethylene propylene diene monomer

ational experiences [219, 220]). This along with the low viscosity and leak-prone nature of 3M™ NOVEC™ 649 narrowed down the preferred connector interface to Swagelok® VCR® connector[9] providing metal-to-metal sealing. To address limited options for threaded connections from Cool Tec, similar metal-to-metal sealing is achieved with Swagelok® RS-Fittings[10] using copper gaskets. Cooling plates for the Thermal Demonstrator are assembled based on these criteria and tested for leak tightness up to 7 bar(g) (see Fig. 3.4).

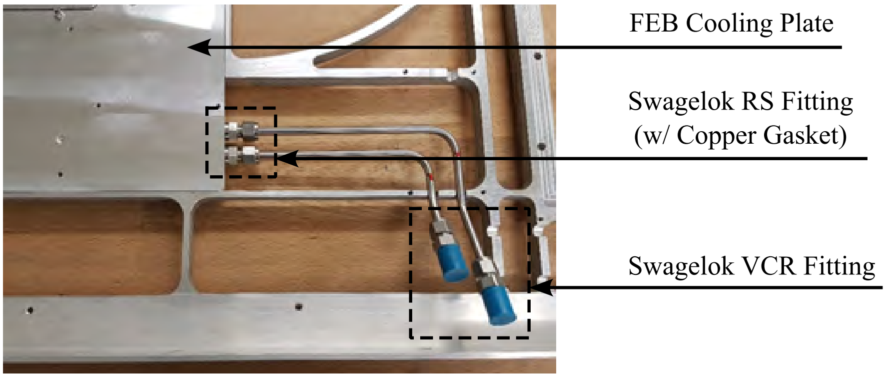

Figure 3.4.: FEB cooling plate assembled with metal-to-metal seal connectors (figure from J. Thaufelder (GSI, Darmstadt)).

The distribution manifold located inside the STS thermal enclosure is designed to passively distribute the desired flowrate from the cooling plant to a given set of cooling plates on the C-Frame. It comprises of the main distribution tube and individual branches along with their respective control valves on the return branches. Individual branches are made from 1/4 in. stainless steel flexible hoses, and can also help dampen the vibrations carried by the coolant from the cooling system's components. Swagelok® FJ-series metal hose[11] is the chosen option because of its high pressure rating, Swagelok® VCR end-connection availability, low bending radius (2.54 cm) and low weight (0.16 kg/m). The fine flow regulation is provided by the Swagelok® NR-series needle valve[12], where components are rated down to -53°C and are available with 3M™ NOVEC™ 649 compatible materials (UHMWPE, PEEK, Grafoil). Based on these concepts, two sample manifolds for the Thermal Demonstrator have been produced in cooperation with the local Swagelok subsidiary[13] (see Fig. 3.5(a), 3.5(b)). In addition, there are connec-

9. Swagelok® VCR® Catalogue - www.swagelok.com/downloads/webcatalogs/en/ms-01-24.pdf
10. Swagelok® Gaugeable Tube and Adapter Fittings Catalogue - www.swagelok.com/downloads/webcatalogs/en/MS-01-140.pdf
11. Swagelok® Hose and Flexible Tubing Catalogue - www.swagelok.com/downloads/webcatalogs/en/MS-01-180.pdf
12. Swagelok® Needle Valve Catalogue - www.swagelok.com/downloads/webcatalogs/en/MS-01-168.pdf
13. Swagelok® Stuttgart - B.E.S.T. Fluidsysteme GmbH, Germany - www.stuttgart.swagelok.solutions

tions for temperature and pressure measurement in the supply and return lines, a feature that won't be included in the final STS's manifolds because of their unsuitability in radiation and magnetic environment. The manifold has a total of six connections, four of which are used for FEB cooling, and another connection is for the side cooling plates, which serve as condensate traps. The last port is a spare and is not connected. The main ports are connected to the insulated hoses of the cooling system, which are routed through dedicated feedthroughs (more information on the condensate traps and feedthroughs in Sec. 3.3).

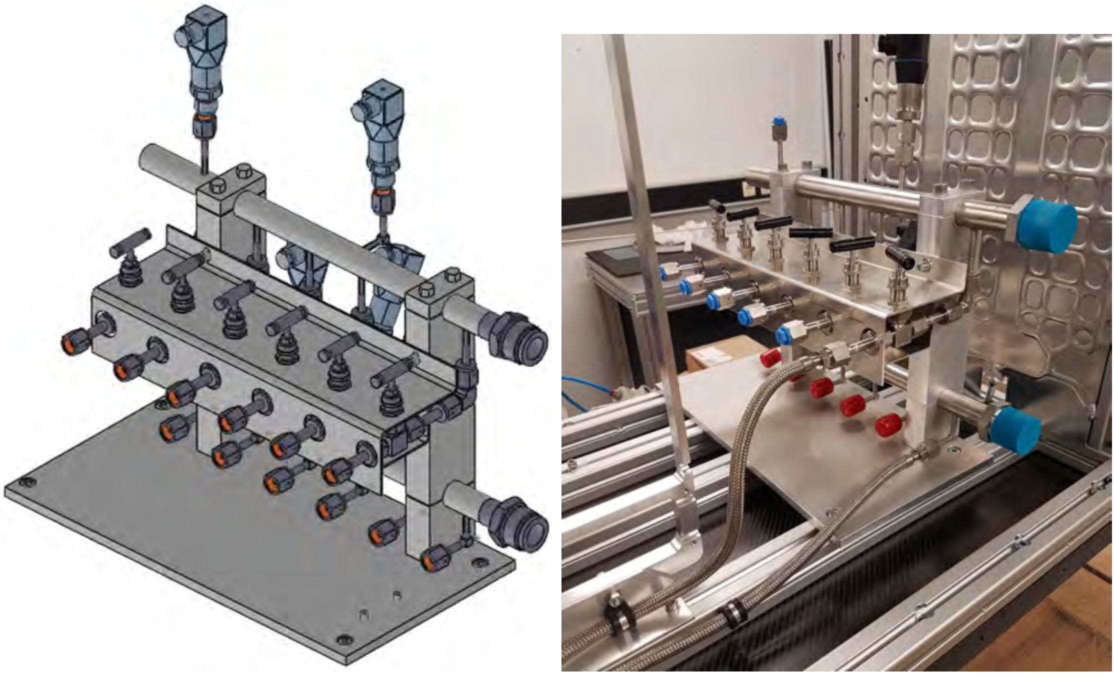

(a) (b)

Figure 3.5.: (a) CAD rendering, and (b) produced sample of the 3M™ NOVEC™ 649 distribution manifold for the Thermal Demonstrator (figures from J. Thaufelder (GSI, Darmstadt)).

3.2. Heating Elements

The thermally active half-layer of the Thermal Demonstrator comprises of 50 silicon sensor modules. In order to realistically mimic the heat production of the entire module within the STS-like boundary conditions, dummy heating elements for both silicon sensors and front-end electronics boards (FEBs) were manufactured. It must be noted that other heat sources, such as the read-out boards (ROBs) and the power boards (POBs) aren't simulated in this setup. Therefore, their effect on the entire cooling dynamics can't be demonstrated and will be addressed in future upgrades.

3.2.1. Silicon Sensors

Silicon power resistors are used to mimic the heat produced by STS silicon sensors, by producing joule heat across 180±20 nm thick Inconel® (nickel-chromium-based alloy) layer deposited on 300 ± 20 µm silicon bulk, with additional 2 µm thick copper stripes at the edges as electrodes. These power resistors were manufactured in different STS-sensor-like form factors[14] (see Fig. 3.6). This concept is directly inspired from the silicon power resistors used for the ATLAS Pixel Upgrade Project (with Alpine inclined staves) [221]. This allows to precisely control the sensor power dissipation across the half-station[15] and make it proportional to the expected anisotropic EOL radiation damage distribution (see Fig.1.21).

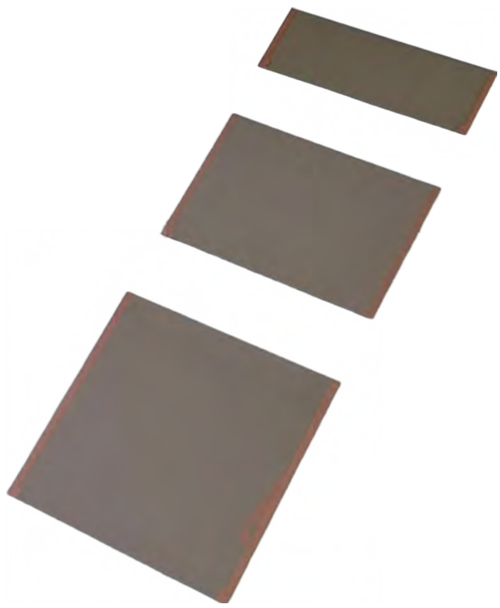

Figure 3.6.: Silicon power resistor in different form factors (6.2×(2.2, 4.2, 6.2 cm^2)).

3.2.2. Front-End Electronics Boards (FEBs)

Dummy front-end electronics boards (FEBs) were designed and manufactured[16] to realistically mimic the thermal behaviour of the real FEBs. This was done by depositing copper meanders on the PCBs as the heat producing chips (SMX2 ASICs and Low Drop-Out (LDO) Regulators), allowing to precisely mimic their different power densities[17] (see Fig. 3.7). It must be noted the rest of the PCB layout, most importantly the underlying thermal vias, is identical to the FEB PCB for final STS series production.

14. Manufactured by Sil'tronix Silicon Technologies, Archamps (France)
15. Powered by R&S®HMP4040
16. Manufactured by ILFA Feinstleitertechnik GmbH
17. Powered by TDK-Lambda GEN8-180

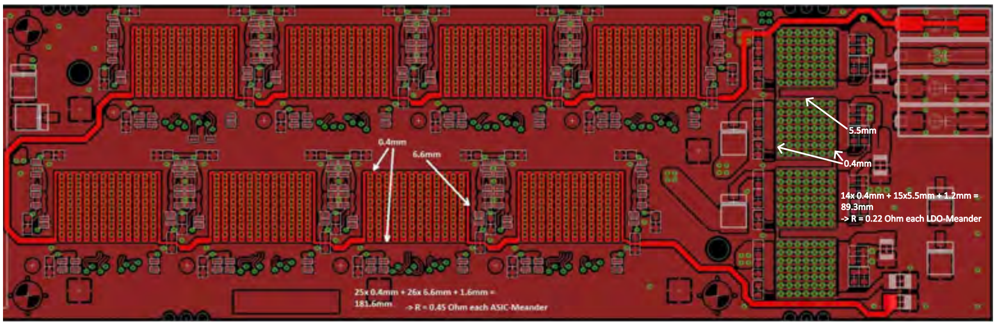

(a)

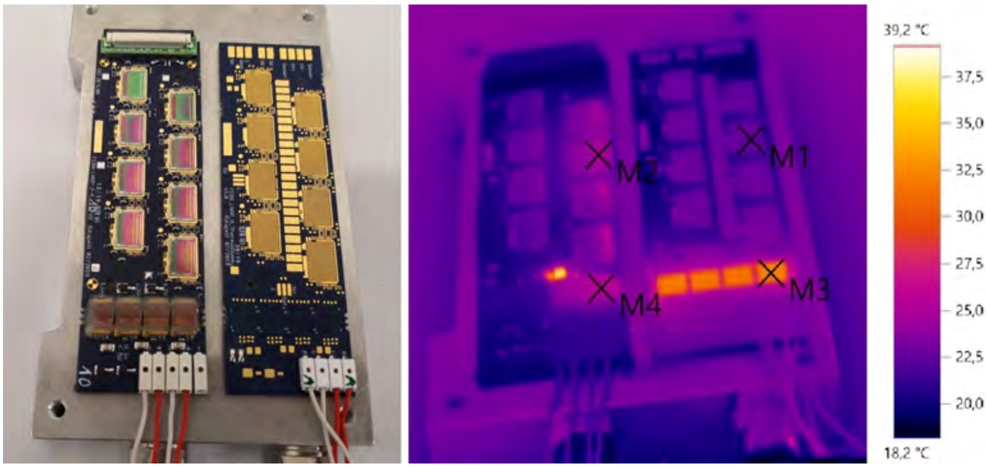

(b)

Figure 3.7.: (a) PCB layout of the FEB thermal dummy. Copper meanders (width 0.2 mm, thickness 0.35 µm) are deposited onto topmost PCB surface to mimic the power dissipation from ASICs and LDOs. Total resistance for the eight ASICs and four LDOs is 3.65 Ω and 0.9 Ω, respectively (figure from R.M. Kapell (GSI Darmstadt)). (b) Real & thermal dummy FEB (left and right of each image). Infrared images of the power objects show comparable temperature profiles.

3.2.3. Thermal Dummy Module

The thermal dummy module for the Thermal Demonstrator represents a thermal equivalent to the STS module. It is assembled by soldering the previously introduced silicon power resistor and pair of FEBs via a pair of Polyimide-cladded Multi-Wire Copper Flexible Cables[18]. These cables are intended to mimic the ultra-thin aluminium microcables. Moreover, they are also used to power and readout the temperature of the silicon power resistors. The temperature on the silicon power resistors and FEBs is measured by Pt-100 and 1-wire temperature sensors[19], respectively, via the FEBs (see Fig. 3.8(a)).

18. Manufactured by SUMIDA Flexible Connections GmbH
19. Maxim Integrated DS18B20 (1-wire® readout)

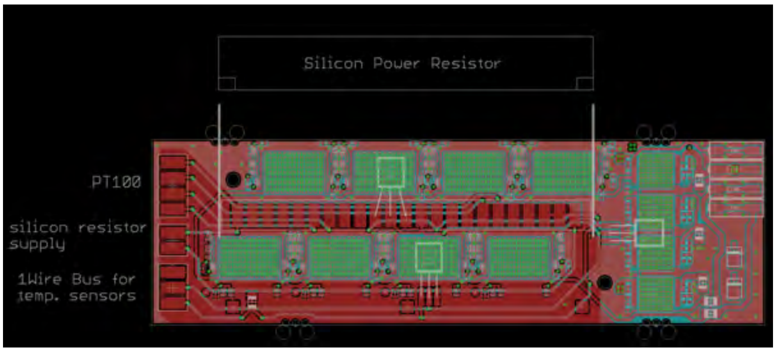

(a)

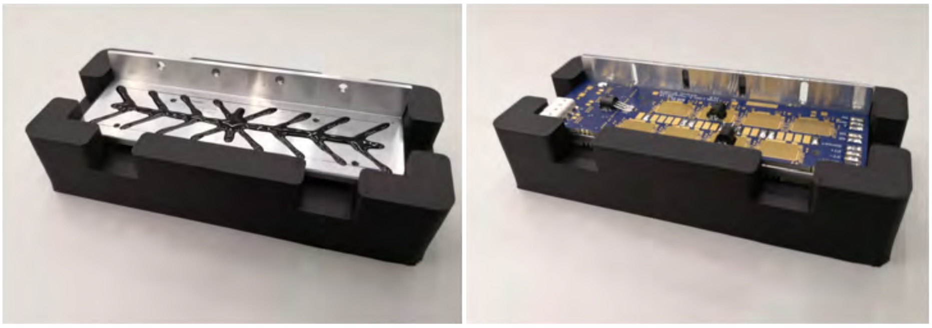

(b)

Figure 3.8.: (a) Layout of the thermal dummy module and comprising heat elements (silicon power resistor and FEB pair) connected via cables. The temperatures are readout by Pt100 sensors on either sides of the silicon power resistor and by three 1-wire temperature sensors (white rectangles) on the ASIC and LDO meanders (figure from R.M. Kapell (GSI Darmstadt)). (b) Gluing procedure between the cooling shelf and heat-producing thermal dummy FEBs. The objects are held on a 3D-printed gluing jig. Left: Glue pattern on the aluminium cooling shelf. Right: Overlayed thermal dummy FEB (right).

Figure 3.9.: Assembled thermal dummy module.

Furthermore, the pair of FEBs are thermally bridged to the cooling plate by gluing[20] them on a T-shaped aluminium *cooling shelf*. The dispensed pattern used has been optimised to achieve the targeted glue thickness of 150 µm over the entire surface by using capillary dispersion. Based on this, 50 such thermal dummy modules, in different form factors, were assembled for the Thermal Demonstrator (prototype shown in Fig. 3.9).

3.3. Thermal Enclosure and Services

3.3.1. General Requirements and Concept

The requirements on the detector enclosure are threefold: (i) thermal, (ii) electromagnetic, and (iii) mechanical. Due to operating conditions below room temperature of the STS, it will be hosted inside a thermal enclosure to avoid outside heat and humidity ingression in the STS environment. Moreover, the enclosure will also act as an electromagnetic shield to prevent noise being picked up by STS's electronics. Mechanically, the enclosure must be rigid enough to host ≈ 2000 kg of weight with minimum deformations, yet lightweight enough to not introduce minimal additional material budget. A more detailed list of general requirements for detector enclosure are as follows:

- Thermal insulation
- Thermal radiation shielding
- Gas tightness
- Mechanical stability and minimum bulging of the bottom panel
- Minimal material budget of the back panel
- Fixture for the beam pipe and the target box on the back and front panel, respectively
- Feedhthroughs in the front panel
- Cryo trap on the side panels
- Precise mounting options rail systems and support frames

Given the convoluted and complex nature of the detector enclosure, this thesis only addressed the possible solutions to the thermal aspects under realistic mechanical boundary conditions with the Thermal Demonstrator. The general concept of the detector enclosure's insulation panel fulfilling the aforementioned thermal requirements is illustrated in Fig. 3.10. Primarily, the insulation panel comprises of CF-foam sandwich which is further sandwiched in aluminised polyimide foils for thermal shielding. Additionally, the inner side of the enclosure's side panel includes thin cooling plates as the coldest spot in the enclosure to safely host any condensation outside the electronics area and provide additional cooling of the STS environment. Please note that other panels of the enclosure can't host similar cooling plates due to either material budget or space constraints.

20. STYCAST 2850FT/Catalyst 23LV

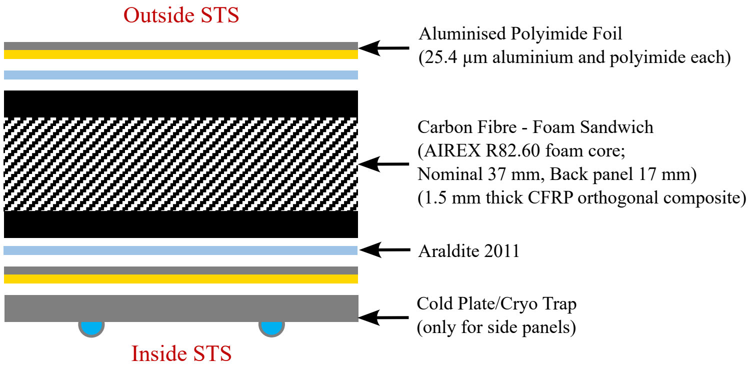

Figure 3.10.: Cross-sectional schematic of the insulation panel.

3.3.2. Insulation Panels and Mainframe

CarbonVision[21] manufactures CF-foam sandwich panels featuring AIREX® R82.60[22] core (37mm thick, 17mm for back panel to minimise material) sandwiched between 1.5 mm thick carbon cover sheets. AIREX® R82.60 is a polyetherimide structural foam which provides stiffness, formability, good adhesive bonding, thermal insulation ($k = 0.031 \ldots 0.039$ W/m·K), low density ($\rho = 60$ kg/m^3), radiation hard and has been successfully used by several trackers based at the CERN's LHC experiments [222, 223]. CF cover sheets consists of a fabric pre-preg on the outer layers and a unidirectional pre-preg on the inner layers. The orientation of the inner layers is rotated alternately by 90° and aligned parallel to the edge of the panel until a layer thickness per panel of 1.5 mm has been achieved. The mainframe, assembled from aluminium item© profiles, supports sandwich panels, C-frames and coolant manifolds. Flat countersinks drilled into frame profiles on two sides (see Fig. 3.11, 3.13(a) for drawings and details) allow flexibility in assembly stages and adaptation of test structures for the Thermal Demonstrator.

HELICOIL® threaded inserts with blind holes were used inside the sandwich panels to seal panels on the mainframe. Polyamide rims, a cost-effective solution, are embedded along the edges and cutouts to enhance stability of screw connections, maintaining thermal insulation (see Fig. 3.12). Initial assembly test on item© mainframe is illustrated in Fig. 3.13(b).

The sandwich insulation panels are subsequently glued with CGS[23] aluminised polyimide foils (25.4 μm + 25.4 μm) for thermal radiation and electrical shielding. Spray adhesive, coupled with light pressure, enhances foil contact with panels. Future assemblies, following LHC trackers' experiences [223–227], involve vacuum bagging with ARALDITE® 2011 for durable bonding. The proof-of-principle of the in-house vacuum bagging process is shown in Fig. 3.14. The aluminium-

21. CarbonVision GmbH, Germany - `www.carbonvision.de`
22. AIREX® R82.60 Technical Information - `https://www.3accorematerials.com/en/markets-and-products/airex-foam/airex-r82-resistant-dielectric-foam`
23. Creative Global Services (CGS), Canada - `www.cgstape.com`

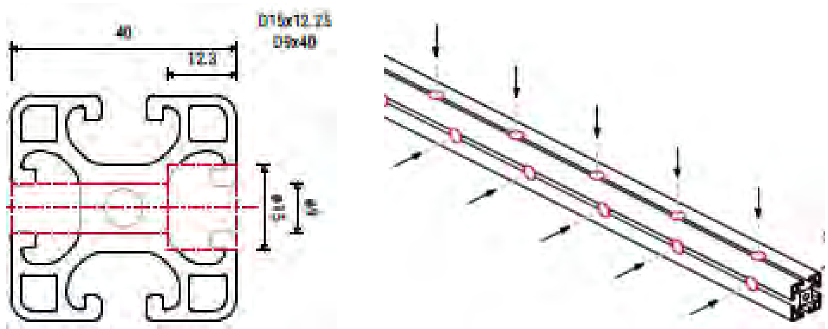

(a)

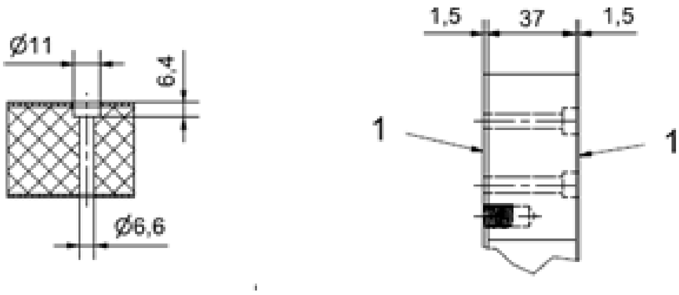

(b)

Figure 3.11.: (a) Drawing of the mechanical adjustment on the aluminium item© frame for mounting the eventual mainframe and carbon box. (b) Drawing section of the screw holes and threaded sets in the carbon plates for mounting and other connections (figures from J. Thaufelder (GSI, Darmstadt)).

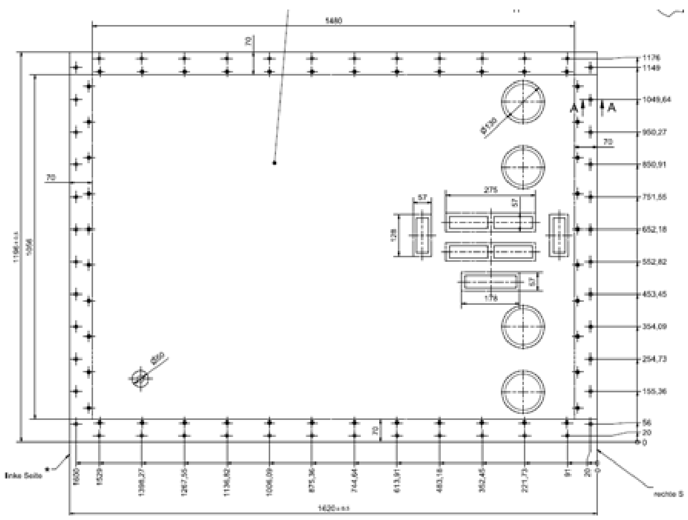

Figure 3.12.: Drawing of the front panel with the polyamide frames inserted around the perimeter to ensure the strength of the screw connection (figure from J. Thaufelder (GSI, Darmstadt)).

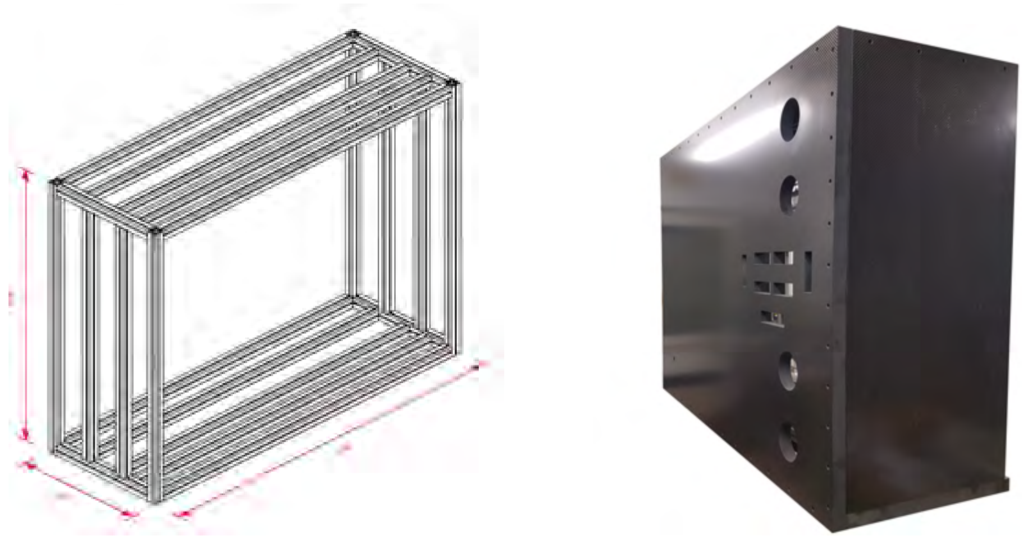

(a) (b)

Figure 3.13.: (a) Mainframe made of aluminium item© profiles for mounting the internal components and sandwich panels. (b) Thermal enclosure made from integrating CarbonVision sandwich panels onto item© mainframe (figures from J. Thaufelder (GSI, Darmstadt)).

polyimide glued sandwich panels integrate onto the mainframe using two parallel rows of 10×2 mm^2 EPDM sealing tape. The resulting enclosure and mainframe have a sealing gap of 1 mm (see Fig. 3.15(a)). Sealing gaskets can be applied during the assembly of items 1-4, leaving the rear wall (item 5) open for feedthrough and test part assembly (see Fig. 3.15(b)). Notably, a single EPDM sealing row is used for the back plate to prevent deformation due to its reduced thickness.

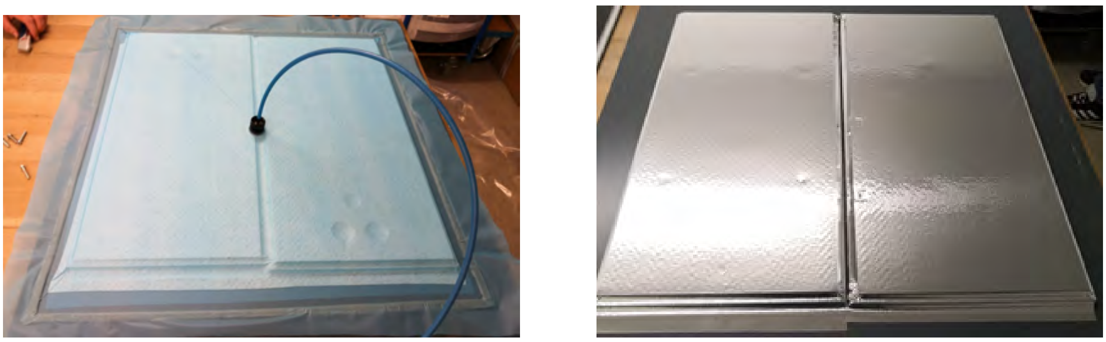

(a) (b)

Figure 3.14.: Vacuum bagging of aluminised polyimide foils to sandwich panels.

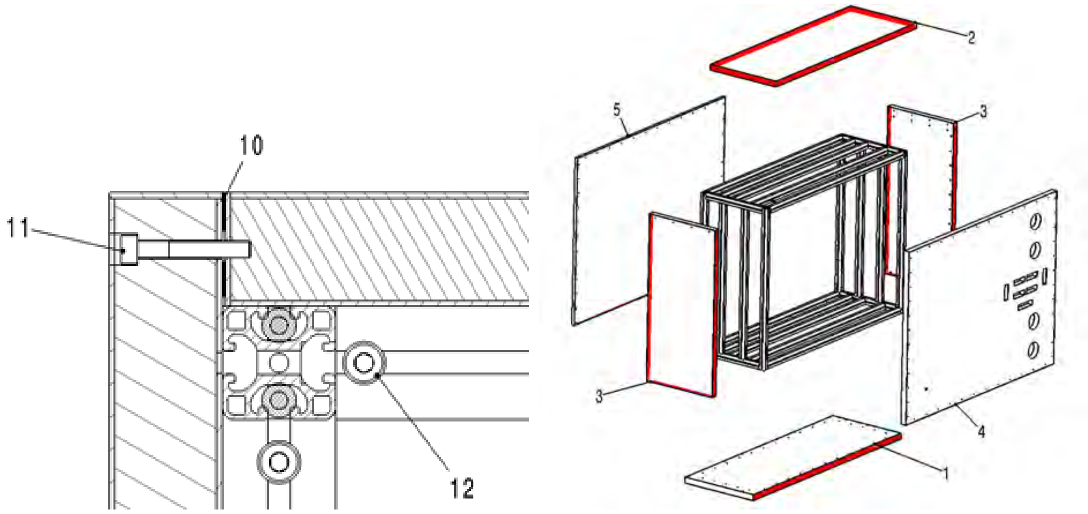

(a) (b)

Figure 3.15.: (a) Connection between sandwich plates, mainframe and EPDM sealing (pos. 10). (b) Exploded view of the box with the mainframe and the sealing surfaces (marked in red) (figures from J. Thaufelder (GSI, Darmstadt)).

3.3.3. Service Feedthroughs

The integration and testing procedure of STS, along with its operating conditions impose the following requirements on service feedthroughs. Based on the these requirements, feedthrough concepts have been developed and tested for both the cold-bulky 3M™ NOVEC™ 649 lines and numerous yet thinner cables.

- modular and reusable concept to ensure accessibility to all services
- minimise any moisture ingression inside STS enclosure's dry environment
- thermally isolating to minimise heat ingression into STS enclosure
- minimise the feedthrough area on the enclosure's front panel

(a) 3M™ NOVEC™ 649 Lines: Custom-designed feedthrough assembly connects transport lines for 3M™ NOVEC™ 649 and the manifold distribution. The assembly is thermally insulating, leak-tight, and removable, and is fastened to the front sandwich panel with counter-plates (concept shown in Fig. 3.16(a)). The feedthrough for the cooling line is initially screwed to the front panel with proper O-ring placement (item 15) to ensures gas tightness. After feeding through and connecting to the manifold, an O-ring (item 16) guarantees radial gas tightness, while the clamping ring (item 13) secures the cooling lines. EPDM foam insulates cavities and heat-conducting surfaces post-cooling line installation. The feedthrough is versatile, suitable for both Demaco Vacuum

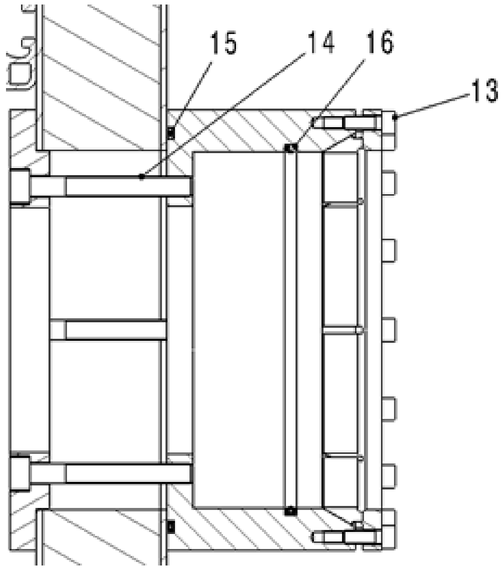

(a)

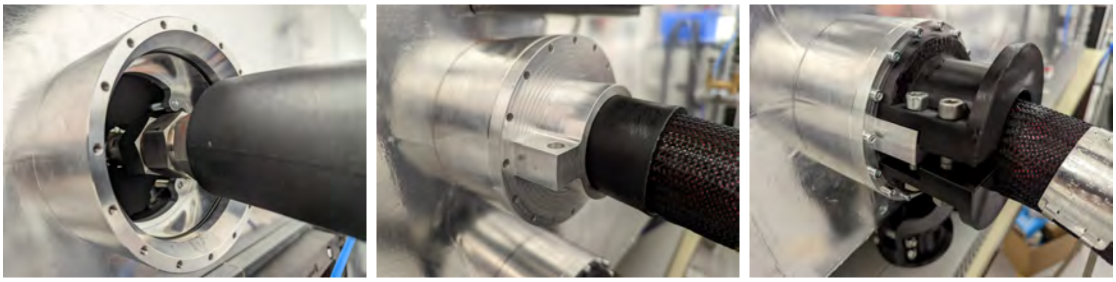

(b)

Figure 3.16.: (a) Sectional view of the feedthrough concept for the 3M™ NOVEC™ 649 lines (figure from J. Thaufelder (GSI, Darmstadt)). (b) The feedthrough assembly process with the JULABO Insulated Metal Tubing in the Thermal Demonstrator.

Insulated Transfer Lines[24] and JULABO Insulated Metal Tubing[25]. The subsequent assembly adapter for the JULABO lines in the Thermal Demonstrator is shown in Fig. 3.16(b).

(b) Cables and Gas Lines: Roxtec EzEntry™ cable entry seals[26] serve as a commercial feedthrough solution for cables and gas transfer lines (see Fig. 3.17(a)). The sealing glands provide IP 66/67 protection and are available to fit different cable/tube diameters. The assembled panels can either be directly mounted on the front panel or via an adapter and counter plates (as in the Thermal Demonstrator). Imperfect contact between some cable/tubes and sealing glands resulted in

24. Demaco Vacuum Insulated Transfer Lines (VIP) - `https://demaco-cryogenics.com/products/vacuum-insulated-transfer-lines/`
25. JULABO GmbH, Germany - `www.julabo.com`
26. Roxtec EzEntry™ - `www.roxtec.com/en/products/solutions/roxtec-ezentry`

observed leakages (see Fig. 3.17(b)), therefore the assembled sealing glands were further encapsulated with a removable sealant putty[27] (see Fig. 3.17(c)).

(a)

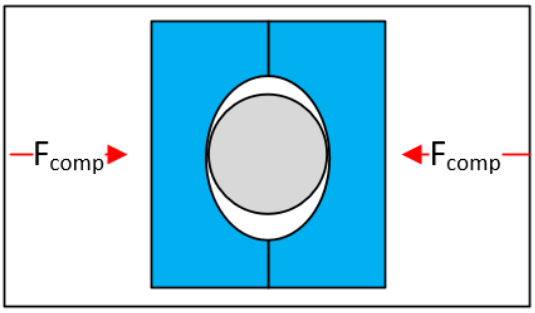

(b)

(c)

Figure 3.17.: (a) Feedthrough panel (Roxtec EzEntry™ 16) for cables and gas lines. (b) Gas leakage in installed state with undersized cable. The lateral compression of the blue rubber element creates a gap between the cable and the rubber element in the opposite direction (figure from J. Thaufelder (GSI, Darmstadt)). (c) Assembled feedthroughs with further transparent encapsulation to enhance their leak-tightness in the Thermal Demonstrator.

27. Sylmasta Pack & Seal Electrical Sealant Putty - `https://sylmasta.com/product/pack-seal/`

3.3.4. Cryo Trap/Side-Wall Cooling

The side panels of the enclosure feature cold plates (see Fig. 3.10), serving to: (i) compensate for thin insulation by minimising net heat influx, (ii) enhance environment cooling by removing residual power dissipation from peripheral cables, (iii) act as a cryo-trap to prevent condensation on critical electronics in case of an accidental event of dew point rise.

The first prototype of these cooling plates were manufactured by Rubanox[28] by using aluminium Roll-Bond technology, which allows to minimise the thickness down to 3 mm. The plates are mechanically mounted on the mainframe and hydraulically connected to the 3M™ NOVEC™ 649 distribution manifolds by using clamp connections and VCR adapter fittings (see Fig. 3.18). Care must be taken to ensure a damage-free surface at the cold plate connections so that a proper seal is achieved. First cooling tests without dry gas circulation have shown that in the event of condensation forming in the box, a large proportion of the condensation adheres to the side cooling plates. Please note that dedicated simulations were not done to optimise the channel geometry for these samples since they are foreseen as an initial proof-of-concept. Subsequent versions will be based on Thermal Demonstrator's experience and detailed thermal modelling.

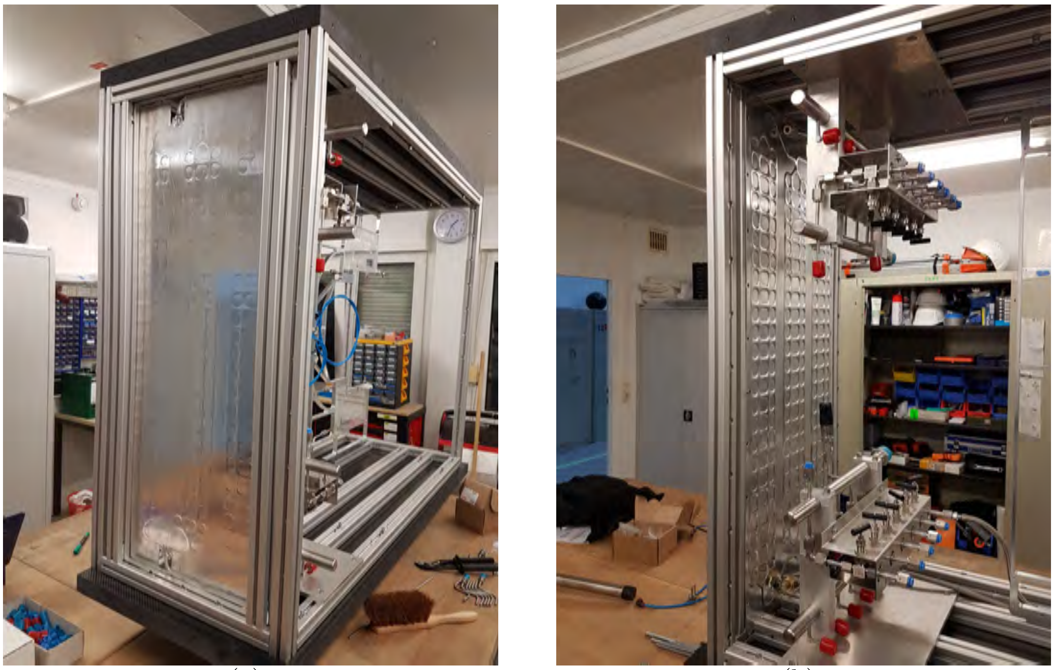

(a) (b)

Figure 3.18.: Side-wall cooling plate (a) mounted onto the Thermal Demonstrator's mainframe, and (b) connected to the 3M™ NOVEC™ 649 distribution manifold.

28. Rubanox Italia srl, Italy - `www.rubanox.com`

Based on the concept described in this section, the finally assembled enclosure for the Thermal Demonstrator is shown in Fig. 3.19.

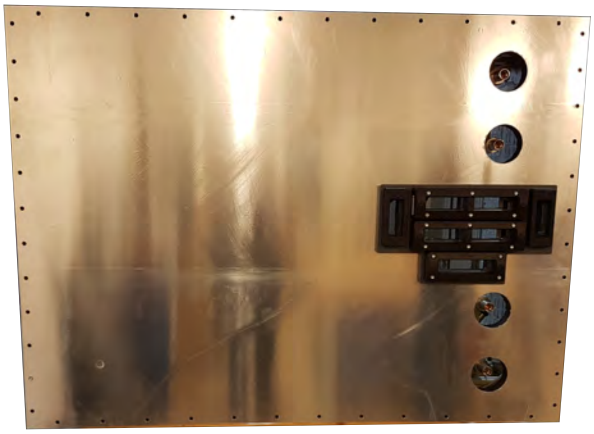

(a)

(b)

Figure 3.19.: Carbon fibre reinforced sandwich box with foam core and aluminium profile frame for C-Frame assembly. (a) Front side with feed-through for the supply lines. (b) Opened rear side with C-frames and manifold before mounting the sensor components and electronics (figures from J. Thaufelder (GSI, Darmstadt)).

3.4. Environmental Monitoring

The STS Thermal Demonstrator serves as the perfect test-bench to obtain operational experience with several temperature and dew point sensors in thermal conditions as foreseen in the final STS. Therefore, several such sensors have been implemented at various levels inside the Thermal Demonstrator, which are described below. Collectively, all these sensors are interfaced with a LabVIEW™-based data-acquisition (DAQ) system, instead of the EPICS[29]-based Detector Control System (DCS) to be used for final STS.

3.4.1. Temperature Monitoring

The temperature on the heat producing sources, i.e., silicon power resistors and FEBs is measured by Pt-100 and 1-wire temperature sensors[30], respectively (see Sec. 3.2). Therefore, these measurements were the primary observables for judging the thermal performance of the entire setup. The Pt-100 temperature sensors are readout in 4-wire configuration by resistance temperature detector (RTD) input modules from National Instruments™[31], while the 1-wire digital temperature sensors are readout by an Arduino® PRO[32]. Furthermore, the temperature of the exterior of the enclosure is also measured by several 1-wire temperature sensors to monitor the heat influx from the surrounding laboratory conditions into the Thermal Demonstrator's enclosure. These sensors are readout by a dedicated Arduino® UNO[33]. Lastly, the temperature sensors in the 3M™ NOVEC™ 649 manifold[34] are also read separately by data-acquisition module from National Instruments™[35].

3.4.2. Dew Point Monitoring

The sub-zero temperature of the 3M™ NOVEC™ 649 coolant (down to -40°C) further requires that the ambient dew point must be sufficiently lower to avoid condensation on any critical components. The ambient conditions inside the Thermal Demonstrator's enclosure are continuously measured primarily by a distributed network of commercially available humidity sensors[36] readout by a dedicated Arduino® UNO. Moreover, some critical places, in terms of humidity formation on sensitive components, are measured with further redundancy by using

29. Experimental Physics and Industrial Control System
30. Maxim Integrated DS18B20 (1-wire® readout)
31. NI-9216 RTD module hosted in NI cDAQ-9189 CompactDAQ Chassis
    NI-9217 RTD module hosted in NI cDAQ-9188 CompactDAQ Chassis
32. STM32H747-microcontroller based Arduino Pro Portenta H7, with 1 kΩ shunt resistance
33. ATmega328P-microcontroller based Arduino Uno, with 1 kΩ shunt resistance
34. WIKA TFT35 threaded thermometer
35. NI USB-6009 USB Multifunction Data Acquisition Card Module
36. IST HYT-221 (I^2C readout)

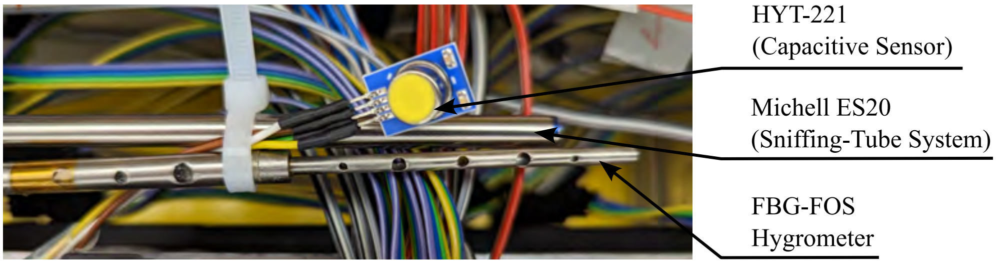

Figure 3.20.: Set of humidity sensors mounted on one of Thermal Demonstrator's C-frames providing a redundant humidity information.

Sniffing-Tube Systems[37] and custom-made Fibre-Optics Sensors[38] [228, 229] (see Fig. 3.20). It's worth mentioning that these two solutions are the baseline solution for dew point monitoring in most high-energy physics experiments due to radiation hardness and insensitivity to the magnetic field [230]. The former is readout by a dedicated data-acquisition module from National Instruments™[39], while the latter by an optical sensing instrument [40].

3.5. Cooling Plants

This section aims to summarise the crucial topic of pilot cooling plants for both silicon sensor and front-end electronics cooling. These systems have proven to be crucial to complete the STS Thermal Demonstrator programme, with the later system also planned to be used for STS in-lab assembly and commissioning. Experiences derived from these systems have been crucial to draft up the specifications for the final STS cooling plants. These systems are detailed further in [177,231].

3.5.1. Silicon Sensor Cooling

A custom-designed Air Handling System (AHS) was developed to supply cold and dry air to the Thermal Demonstrator [231]. It provides active cooling for the heat-producing dummy silicon sensor and dehumidifies the thermal enclosure for sub-zero operation. It mainly consists of a commercially available gas cryochiller[41] with adjustable output temperatures via a regulated heater (-15 ... +30°C). Additionally, an adsorption dryer[42] is installed at the inlet to absorb moisture, maintaining the air dew point at approximately -60°C at the outlet. Lastly, a

37. Michell Instruments ES20 Compact Sampling System
38. Hygrometers manufactured by Advanced Optics Solutions (AOS) GmbH; Temperature and Humidity Sensing Arrays manufactured by Technica Optical Components LLC and packaged by Advanced Optics Solutions (AOS) GmbH
39. NI USB-6009 USB Multifunction Data Acquisition Card Module
40. Luna Innovations (Micron Optics) HYPERION si255
41. Polycold® PGC-152 Gas Chiller
42. Parker Desiccant Compressed Air Dryer - PNEUDRI MiDAS DAS6

distribution box, equipped with back-pressure valves at the exhaust, rotameters[43], and regulating valves, is placed between the AHS and the Thermal Demonstrator to regulate and distribute the cold, dry airflow to individual C-frames.

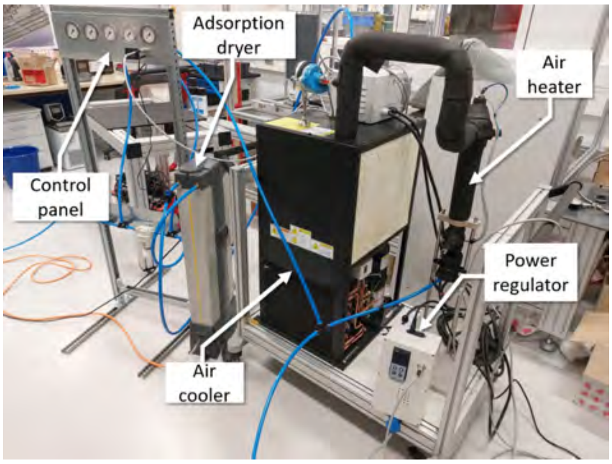

(a)

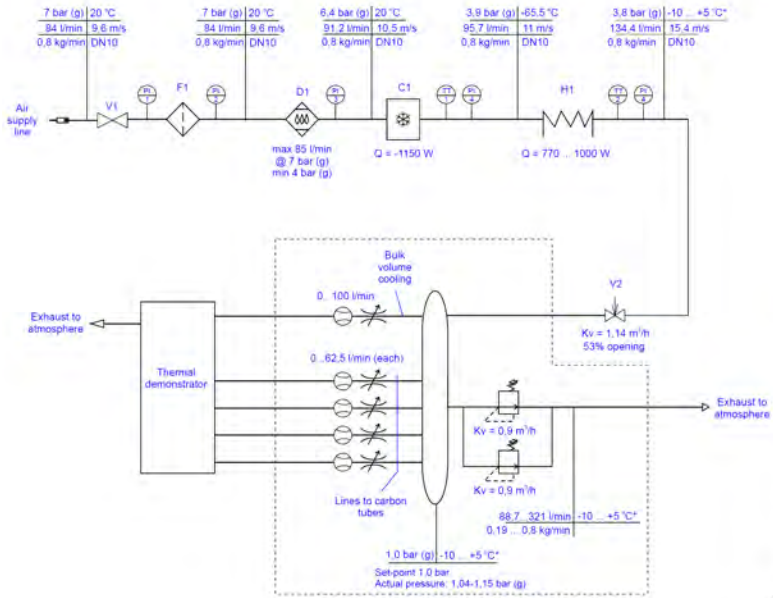

(b)

Figure 3.21.: (a) Photograph of the Air Handling System, highlighting major parts (figure from [231]). (b) Schematic of the Air Handling System along with the distribution box and various underlying parts. Various callouts in blue denote the air properties at a given location within the entire scheme (figure from I. Elizarov (GSI Darmstadt)).

43. Yukogawa RAGL41 Rotameter

3.5.2. Front-End Electronics Cooling

Monophase 3M™ NOVEC™ 649 (*secondary loop*) cooled by biphase CO_2 (*primary loop*) is chosen as cooling cycle for STS electronics cooling. This enables the STS to (i) use climatically friendly coolants in the entire cooling cycle (Global Warming Potential, GWP = 1); (ii) utilise the low operating pressure, non-toxicity and easy to use 3M™ NOVEC™ 649 for on-detector secondary loop; (iii) utilise the high volumetric heat-transfer coefficient, commercial availability, but high operating pressure of CO_2 on the primary loop.

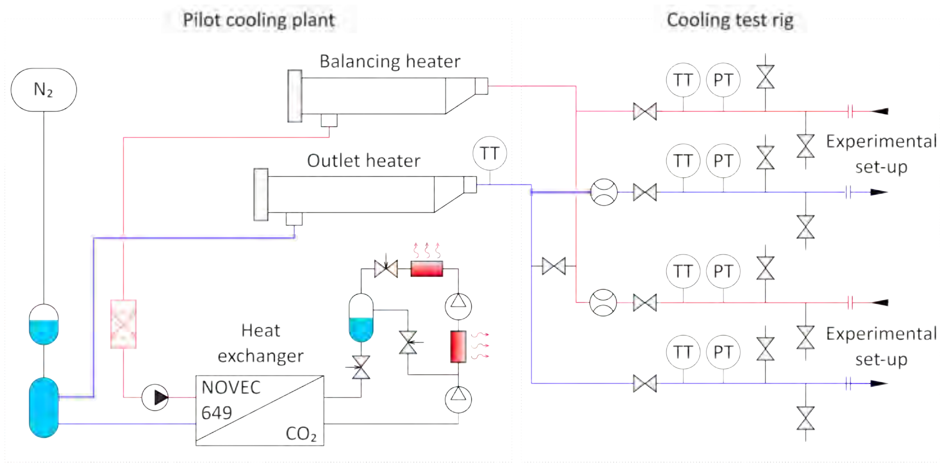

(a)

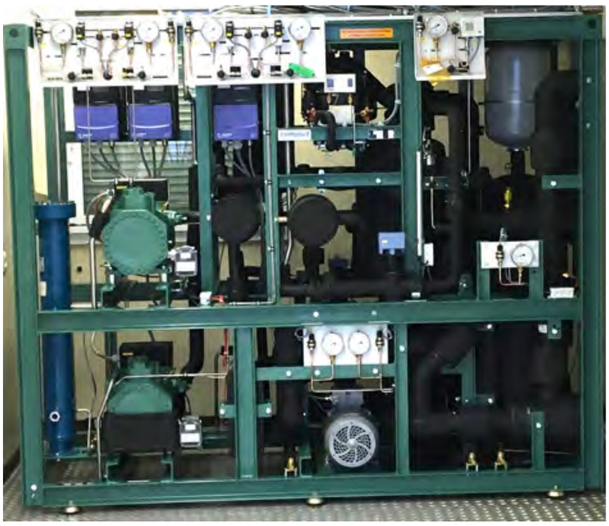

(b)

(c)

Figure 3.22.: (a) Process flow diagram of the 3M™ NOVEC™ 649 pilot cooling plant. Additionally, the corresponding distribution system, *Cooling Test Rig* is also shown. (b) Photograph of the pilot cooling plant (without the balancing and outlet heaters). (c) Photograph of the cooling test rig (figures from [177]).

Parameter	Value
Refrigerant - Primary Loop	CO_2 (R744)
Refrigerant - Secondary Loop	3M™ NOVEC™ 649
Cooling Capacity - Nominal	15 kW
Cooling Capacity - Partial	6.4 kW
Coolant Temperature - Nominal	-40 ... -30°C
Coolant Temperature - Outlet Heater	-30 ... +10°C
Flow Rate (at -40°C)	1.2 ... 2.8 m^3/h
Pressure Difference	0.5 ... 2.5 bar
Static Pressure (Secondary Loop) - Standby Mode	3.1 bar
Static Pressure (Secondary Loop) - Operation	3.4 bar
Electric Power Range - Balancing Heater	0 ... 11 kW
Electric Power Range - Outlet Heater	0 ... 24 kW
Refrigeration Cycle Coefficient Of Performance (COP)	2.05

Table 3.2.: Basic specifications of the 3M™ NOVEC™ 649 pilot cooling plant [177].

A custom-made pilot cooling plant was commissioned at GSI Darmstadt to validate this novel cooling concept with the Thermal Demonstrator and eventual use during the in-lab STS integration and commissioning (see Fig. 3.22). It has been manufactured in close cooperation with our industrial partners[44]. The primary loop consists a booster-type CO_2 refrigeration system which cools the 3M™ NOVEC™ 649 in the secondary loop via a heat exchanger (evaporator). 3M™ NOVEC™ 649 is circulated throughout the loop by a centrifugal pump. It flows through an *accumulator* allowing coolant storage and expansion under temperature change, while the accumulator is further connected to an *expansion tank* which is pressurised with gaseous nitrogen to maintain the static pressure within the acceptable range. The secondary loop also comprises a filter-dryer to absorb precipitated water from 3M™ NOVEC™ 649 and avoid acid formation. Further customisation includes adding an outlet heater to extend the upper limit of the usable temperature range from -30°C to +10°C, and a balancing heater to compensate for any mismatches between the partial cooling capacity of the plant and the requirements of experimental setups. Collectively, this enables to use 3M™ NOVEC™ 649 at varied temperature range (-40 ... +10°C) with control on the coolant flow rate and cooling capacity (6.4 ... 15 kW) (see Tab. 3.2). The coolant is further distributed to various experimental setups, including the Thermal Demonstrator, via the *Cooling Test Rig.* This enables to monitor the coolant parameters, such as flow rate, temperature and pressure via the data-acquisition module from National Instruments™[45], and supports connecting the drainage system.

44. compact Kältetechnik GmbH - `www.compact-kaeltetechnik.de`
KKR Klima-Kälte-Reinraumtechnik GmbH - `www.kkr-gmbh.info`
45. NI USB-6218 USB Multifunction Data Acquisition Card Module

3.6. Experimental Setup

The thermally active half-station of the Thermal Demonstrator aims to simulate the unwanted heat transfer between the silicon sensors and peripherally located front-end electronics. Since this effect worsens for the upstream stations of the final STS due to the closer vicinity between the sensors and electronics, the Thermal Demonstrator's active layer largely resembles the left-half of the STS Station-1[46](see Tab. 3.3 and Fig. 3.23).

Thermal Demonstrator Ladder ID	Equivalent Co-ordinates in STS_v21b			
	Unit ID	Ladder ID	x [cm]	z [cm]
LT201	Unit02L_6	LadderType1002_207	2.975	40.990
LT202	Unit01L_4	LadderType0109_208	8.925	39.935
LT203	Unit02L_6	LadderType1028_209	14.875	41.065
LT204	Unit01L_4	LadderType0110_210	20.825	39.935
LT205	-	-	-	-
LT206	Unit01L_4	LadderType0111_212	32.725	40.160

Table 3.3.: Thermal demonstrator ladders and their equivalent in the STS geometry version v21b. The x- and z- coordinates are with reference to the beam-target interaction point (primary vertex).

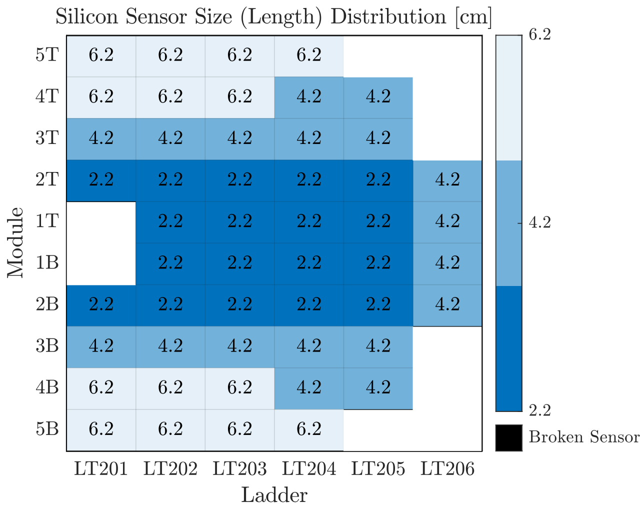

Figure 3.23.: The sensor size (length) distribution for the Thermal Demonstrator, with all sensors having equal width of 6.2 cm. The innermost area (LT201-1T/B) represents the beampipe opening.

46. The reference STS geometry used for the Thermal Demonstrator is STS_v21b. This geometry was also used for judging the sensor quality grades based on the accumulated fluence [232]. Note that ladder LT205 doesn't exist in the STS geometry version v21b and was introduced to introduce the maximum number of sensors and electronics in the given mechanical boundary conditions and number of available dummy heating elements.

All components, described in the previous sections, were brought together to form the Thermal Demonstrator. The heating and cooling elements were subsequently assembled onto ladders and C-frames, where they are cabled up to their respective power supplies via a network of distribution blocks[47].

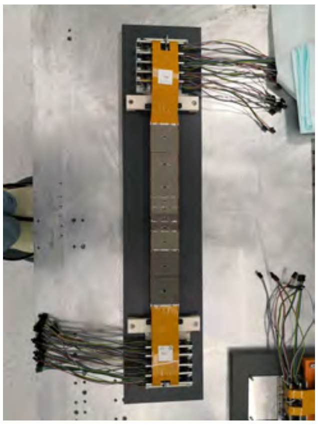

(a)

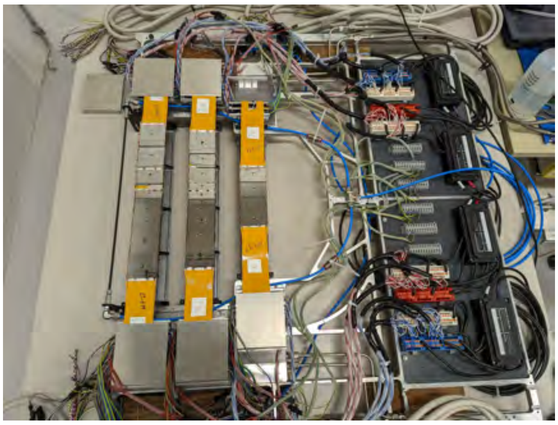

(b)

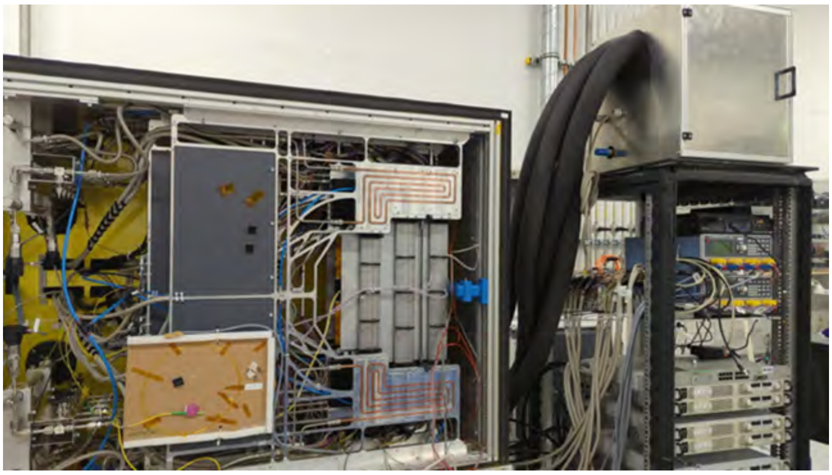

(c)

Figure 3.24.: (a) Assembled ladder with the thermal dummy heating elements. The cables out of the FEB boxes at the top and bottom end are for connecting it to the readout system. (b) Assembled C-frame comprising the ladder along with the cooling elements. The powering cables are patched up to the network of distribution blocks on the right. (c) Fully assembled Thermal Demonstrator inside its thermal enclosure along with its peripheral services, including the readout and power rack on the right.

47. WAGO 261-112 Terminal Block
Phoenix Contact PTFIX 6/12X2,5
T Tocas 100A BusBar Box

4. Experimental Verification of CBM-STS Cooling Concept

This chapter presents experimental results from the CBM-STS Thermal Demonstrator (introduced in Chap. 3) to verify the novel liquid-assisted gas cooling concept (detailed in Chap. 2). The investigation systematically evaluated the cooling of both silicon sensors and front-end electronics. The silicon sensor cooling concept was assessed based on its ability to prevent thermal runaway at the detector's end-of-lifetime fluence, while the front-end electronics cooling was judged on its effectiveness to neutralise the significantly higher power dissipation. Additionally, the interaction between the silicon sensors and front-end electronics was studied. Furthermore, comprehensive studies were conducted to understand the dependencies of the CBM-STS cooling concept on various operational parameters, providing a holistic understanding. As a result, these experiments helped to verify the baseline operational parameters and the underlying margins essential for maintaining long-term, reliable operation of the CBM-STS.

4.1. Silicon Sensor Cooling

The CBM-STS silicon sensor cooling concept is evaluated primarily on its ability to prevent thermal runaway and maintain a stable operating temperature (≈ 10°C) for optimal signal-to-noise ratio (S/N $\gtrsim 10$) and to avoid reverse annealing (full depletion voltage $V_{dep} < 500$ V) up to the detector's end-of-lifetime (EOL) fluence (1×10^{14}n$_{eq}$(1 MeV)/cm^2) (see Sec. 1.5). As introduced in Sec. 1.1.1, the temperature-dependent sensor leakage current ($I_{Leakage}$) creates a self-feeding cycle between temperature, $I_{Leakage}$, and power dissipation, potentially leading the sensors to go into an uncontrolled positive feedback loop leading to Thermal Runaway. This can be estimated by comparing the effectiveness of the cooling concept's linear[1] *Cooling Power* relative to the radiation-induced exponential *Heating Power* (see Fig. 4.1). Effective cooling ensures that the stable temperature (T_{stable}) is below the critical temperature ($T_{critical}$) where the runaway occurs, requiring a substantial safety margin between T_{stable} and $T_{critical}$.

1. The heat flux ($\dot{q}$) between the heat producing source (at T_{source}) and the surrounding fluid acting as heat sink (at T_{sink}) is given by: $\dot{q} = h \cdot (T_{sink} - T_{source})$, where h being the proportionality constant is also known as the heat transfer coefficient. Therefore, the cooling power is linear ($\dot{q} \propto T_{source}$).

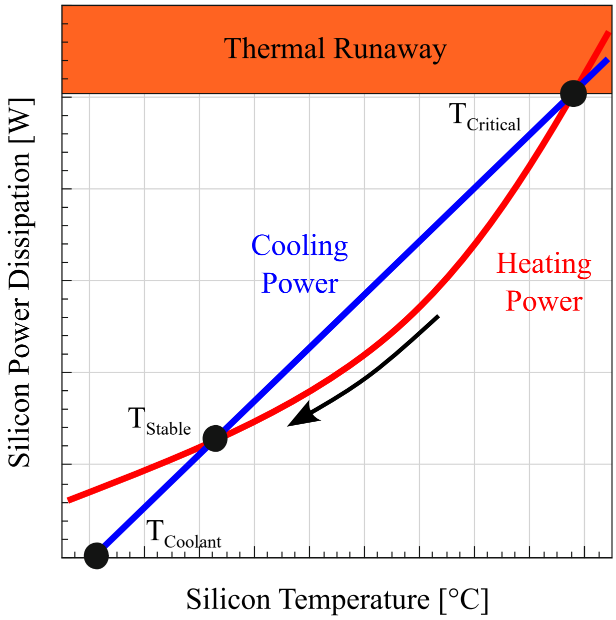

Figure 4.1.: Illustration of thermal runaway in silicon sensors shown as a variation of sensor's power dissipation with its temperature. The silicon sensor is in thermal runaway above the critical temperature ($T_{sensor} \geq T_{critical}$), while the silicon sensor stables below the critical temperature to a stable value ($T_{sensor} = T_{stable}$ at $T_{sensor} < T_{critical}$) (figure adapted from [15]).

The thermal runaway behavior of STS silicon sensors is investigated using the STS Thermal Demonstrator, focusing on comparing heating and cooling power.

Calculated Heating Power: The heating power for all silicon sensors is calculated based on their accumulated fluence and operational temperature. Two scenarios are considered: (i) when the maximum accumulated fluence on any given sensor reaches $0.24 \times 10^{14} n_{eq}(1\ \text{MeV})/\text{cm}^2$ (equivalent to 10 years of CBM operation), and (ii) when it reaches $1 \times 10^{14} n_{eq}(1\ \text{MeV})/\text{cm}^2$ (EOL for STS silicon sensors). Refer to Fig. 4.2 for the corresponding fluence distributions used for calculating the heating power of the comprising sensors in the Thermal Demonstrator for the two scenarios. Refer to App. A for the rationale behind these fluence values, and App. D for details on STS sensor power dissipation behavior with temperature and irradiation.

Measured Cooling Power: Pt-100 temperature sensors glued to all silicon sensors in the thermally active half-station of the Thermal Demonstrator allows extensive temperature distribution measurements and its variation with the applied power, i.e., the Cooling Power (see Sec. 3.2 for the thermal dummy module design and App. E.1 for the silicon sensor powering details). All sensors are powered proportionally to the non-ionising dose distribution simulated for STS Station-1, allowing realistic mapping of cooling power across the active half-station (see Fig. 4.2(b) for the EOL fluence distribution).

This section primarily discusses measured cooling power for a *Baseline Operational Scenario* and its dependencies on various operational parameters. Additionally, cooling performance during beam shutdown is addressed.

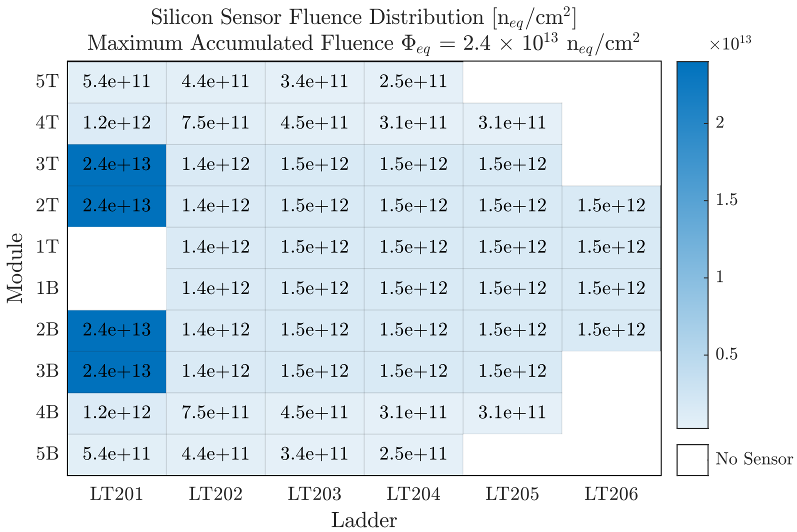

(a) Fluence Distribution after 10 years

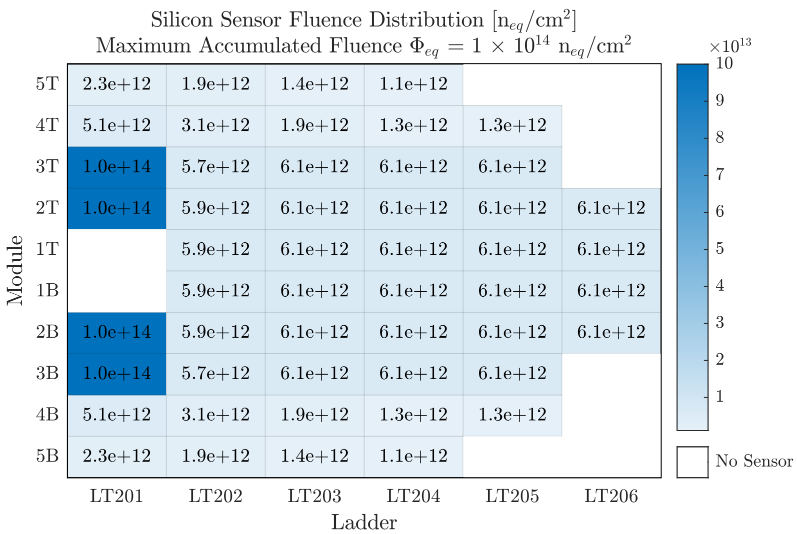

(b) Fluence Distribution after EOL

Figure 4.2.: Non-Ionising Dose distribution across the STS Thermal Demonstrator's active station after (a) 10 years ($0.24{\times}10^{14}$n$_{eq}$(1 MeV)/cm^2), and (b) at the EOL value ($1{\times}10^{14}$n$_{eq}$(1 MeV)/cm^2). This is derived for STS geometry version STS_v21b and scaled to the respective fluence from the initial irradiation case of 11*A*GeV Au+Au at 10 MHz after 1 month (see Fig. E.1(a) for initial values).

4.1.1. Baseline Operational Scenario

The baseline cooling parameters are determined by the survival properties of the STS components under extended cooling conditions. The decision-making factors for these parameters are summarised as follows:

Air Flow Rate = 30 L/min (inner ladders): Extensive measurements characterised the vibrational behavior of the assembled STS ladders under airflow from the carbon-fiber perforated tube [191, 233]. The airflow between 20 ... 40 L/min resulted in no excitation of the ladder's eigenfrequency, with z-plane displacement safely below 3.7 µm, (limit to minimise the degradation of STS's track reconstruction performance). Thus, an intermediate value of 30 L/min was chosen as the baseline. Please note that only the inner ladders (LT201 and LT202) are actively cooled with the impinging air jets from perforated tubes, while the remaining peripheral ladders are cooled by natural air convection, i.e., no air flow.

Air Temperature = -15° C: To maximise the cooling effect from cold air, the air handling system was set to -15°C for the Thermal Demonstrator's pilot cooling plant (see Sec. 3.5). Note that the temperature rise along the transfer lines results in an inlet temperature of ≈ -10°C at the Thermal Demonstrator.

3M™ NOVEC™ 649 Temperature = -20° C (FEB and Side-Wall Cooling): Thermal cycling studies on pre-production FEB prototypes, simulating a 10-year operational period, established a minimum operational limit of -25°C. Therefore, -20°C is designated as the safe operational temperature and serves as the baseline value for both FEB and side-wall cooling.

3M™ NOVEC™ 649 Flow Rate = 1.5 L/min: The nominal flow rate for the STS-FEB cooling plates is 3 L/min, providing sufficient cooling while avoiding erosional velocity (3 m/s) [215, 216]. Since the FEB boxes in the Thermal Demonstrator occupy only one side of the cooling plates, the baseline flow rate was half of the nominal flow, i.e., 1.5 L/min.

Power Dissipation per FEB = 12.93 W: FEB power dissipation is dependent on input FEB currents and efficiencies of the DC-DC converters (based on FEASTMP modules). Operating settings based on the LDO current limit and data-rate fluctuations based on beam-target interaction rate yield three scenarios: *Minimum* (8.63 W), *Typical* (11.42 W), and *Maximum* (12.93 W) (see App. E.2). Therefore, the *Maximum Scenario* is used as the baseline.

For the aforementioned baseline operational scenario, the cooling power of all silicon sensors in the thermally active half-station of the Thermal Demonstrator was measured. This is exemplified in Fig. 4.3(a) and Fig. 4.3(b) which shows examples of thermal runaway behaviour in sensors cooled by impinging air jets (module type LT201-3T) and natural air convection (module type LT204-3T), respectively. The cooling power was measured for the baseline operational parameters and compared to two heating power scenarios: 10-year equivalent of

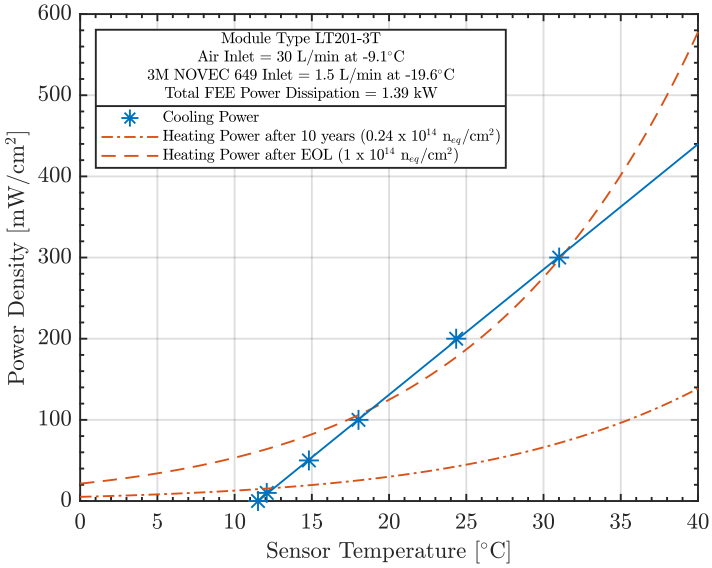

(a) Heating vs Cooling Power
Module LT201-3T: Cooled by impinging air jets

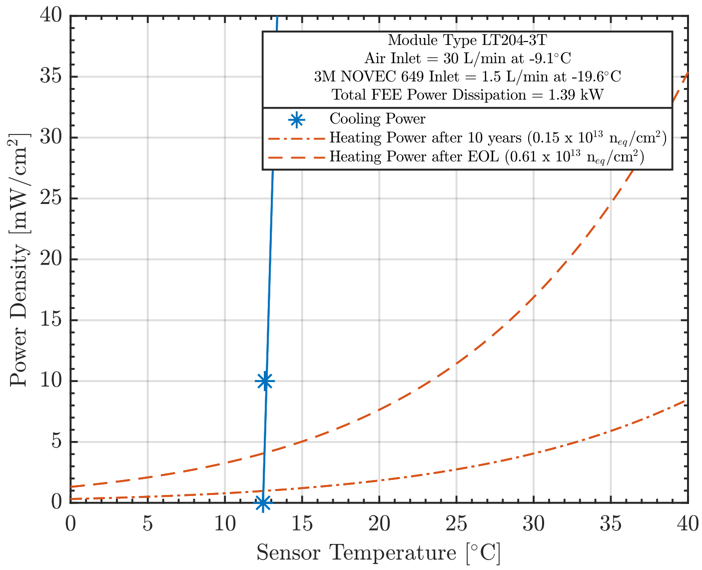

(b) Heating vs Cooling Power
Module LT204-3T: Cooled by natural air convection

Figure 4.3.: Thermal runaway behavior, shown as a variation of sensor's power density with its temperature, for module cooled by (a) impinging air jets and (b) natural air convection. The two heating power curves (shown in red) are for their respective accumulated fluence after 10 years and EOL operation (note the different power density scales of the sub-figures). The measured cooling power is denoted as blue star marker, with several measurements linearly fitted with a blue line.

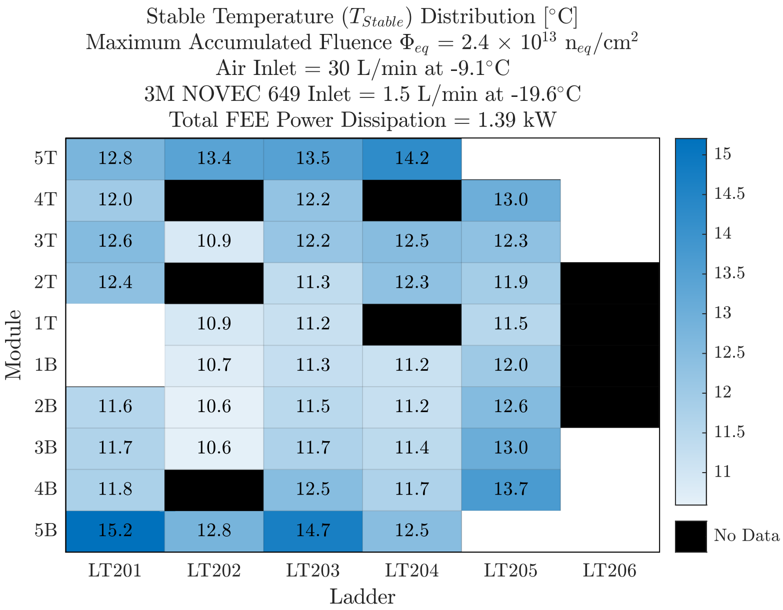

(a) Stable Temperature Distribution after 10 years

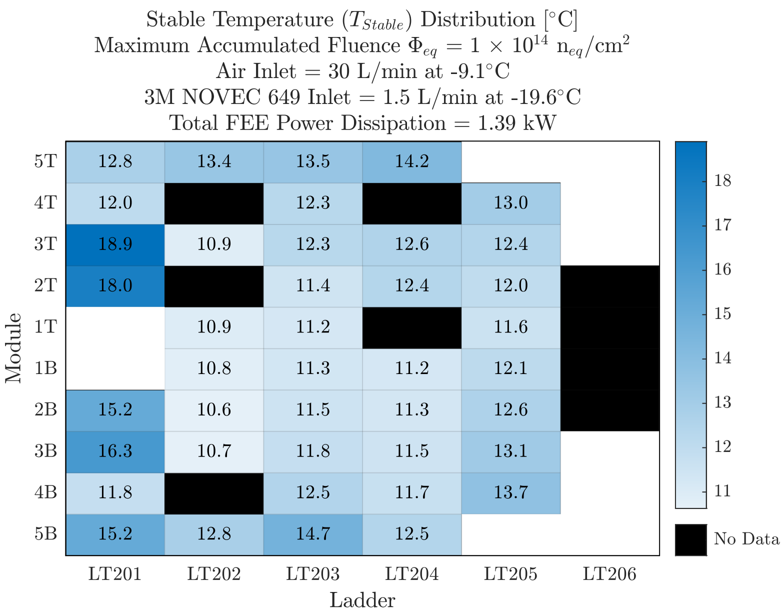

(b) Stable Temperature Distribution after EOL

Figure 4.4.: Stable Temperature (T_{Stable}) distributions across the thermally active half-station for the baseline operational scenario after an accumulated fluence of (a) $0.24\times10^{14}n_{eq}(1\ \text{MeV})/cm^2$ for 10 years of CBM operation, and (b) $1\times10^{14}n_{eq}(1\ \text{MeV})/cm^2$ for STS sensors EOL. The innermost area in all figures (LT201-1T/B) represents the beam pipe opening, whereas the black bins comprise sensors which are either physically broken or have faulty Pt-100 sensor.

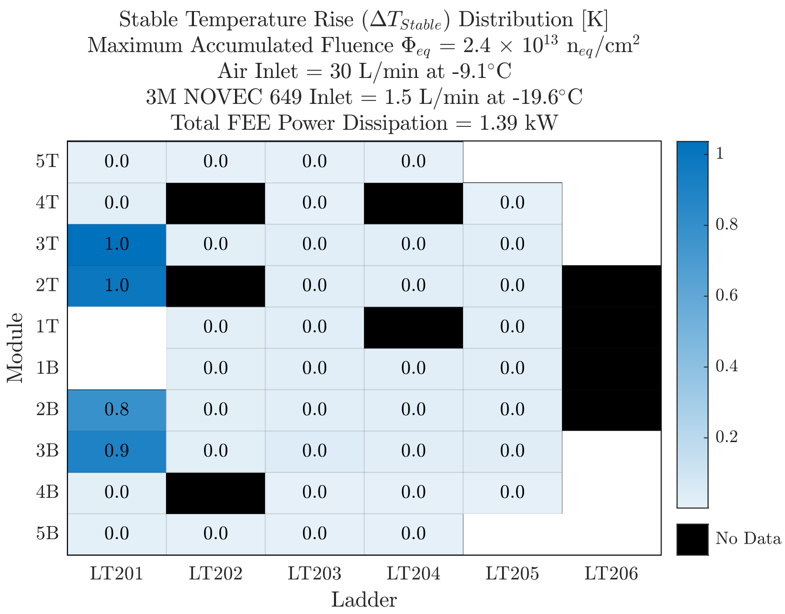

(a) Stable Temperature Rise Distribution after 10 years

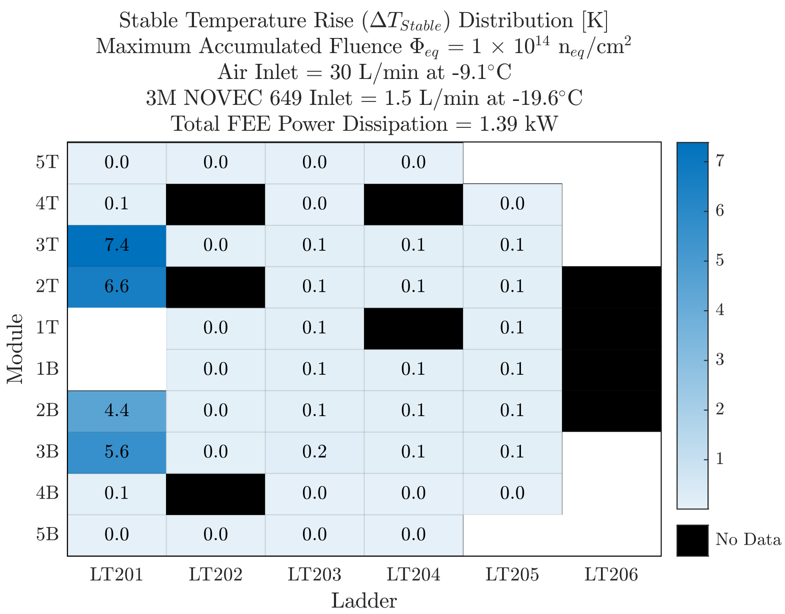

(b) Stable Temperature Rise Distribution after EOL

Figure 4.5.: Distributions showing the rise of Stable Temperature (ΔT_{Stable}) across the thermally active half-station for the baseline operational scenario after an accumulated fluence of (a) $0.24{\times}10^{14}n_{eq}(1\ \text{MeV})/cm^2$ for 10 years of CBM operation, and (b) $1{\times}10^{14}n_{eq}(1\ \text{MeV})/cm^2$ for STS sensors EOL. The innermost area in all figures (LT201-1T/B) represents the beam pipe opening, whereas the black bins comprise sensors which are either physically broken or have faulty Pt-100 sensor.

CBM operation and EOL for STS silicon sensors). This comparison enabled the experimental determination of the stable temperature (T_{stable}) and critical temperature $T_{critical}$, as initially illustrated in Fig. 4.1. The T_{stable} distribution for the half-station was mapped, resulting in a mean temperature of $12.2^{+3.0}_{-1.6}$°C after 10 years and of $12.7^{+6.2}_{-2.1}$°C at EOL (see Fig. 4.4). To negate the initial temperature inhomogeneity caused by various systematic effects, the rise in T_{stable} (ΔT_{stable}) was also mapped for the half-station (see Fig. 4.5). This mapping highlights the role of air cooling based on sensor fluence distribution, i.e., power dissipation. Based on these measurements, the following conclusions can be drawn:

- Temperature hotspots on the half-station correlate directly with the accumulated fluence distribution (see Fig. 4.5 and Fig. 4.2). This underscores the need of forced air convection via impinging jets for the innermost sensors around the beam pipe (on ladder LT201 and LT202).
- The negligible temperature rise on the remaining peripheral sensors (mostly on ladder LT203-LT206) indicates that they can be reliably cooled by natural air convection.
- The chosen baseline operational scenario ensures stable temperatures for all sensors, preventing thermal runaway for both 10-year and EOL fluence scenarios.

4.1.2. Exploring Margins and Dependencies

The cooling performance was further evaluated by exploring the margins relative to the baseline operational scenario. This subsection describes the dependencies studied on the following operational parameters:

- *Air flow rate on inner ladders*: 0 to 40 L/min
- *Air temperature*: -15 to 20 °C
- *3M™ NOVEC™ 649 flow rate*: 1 to 2 L/min
- *3M™ NOVEC™ 649 temperature*: -40 to -20 °C
- *Side-wall cooling configuration*: ON(-20°C) to OFF
- *FEE power dissipation*: 8.63 to 14.22 W per FEB (total 0.88 to 1.57 kW)

Tab. 4.1 summarises the dependencies evaluated in terms of T_{stable} and ΔT_{stable} for the two fluence scenarios, with the underlying temperature distributions provided in App. F. Additionally, Tab. 4.2 presents the cooling performance details of the most irradiated and hottest module, MT201-3T. This includes thermal runaway temperatures (T_{stable}, $T_{critical}$) and fitted cooling parameters (heat transfer coefficient and base temperature T_0). Further details about these dependencies are provided in the following Sec. 4.1.2.1-4.1.2.6[2].

2. The dependency curves therein only comprises of T_{stable} and ΔT_{stable} at parameter values for which thermal runaway behaviour was not observed. See App. F for sensors which in thermal runaway for any given parameter value.

Coolant Input Parameters						Total FEE Power Dissipation [kW]	Median Stable Temperature			
Air (per ladder)		3M™ NOVEC™ 649 (per cooling plate)		Environmental Cooling			After 10 Years ($0.24\times10^{14}\mathrm{n}_{eq}/\mathrm{cm}^2$)		After EOL ($1\times10^{14}\mathrm{n}_{eq}/\mathrm{cm}^2$)	
$\dot{V}_{Air}$ [L/min]	T_{Air} [°C]	$\dot{V}_{Novec}$ [L/min]	T_{Novec} [°C]	Air Flow Rate [L/min]	Side Wall Cooling Bath Temp. [°C]		T_{Stable} [°C]	ΔT_{Stable} [°C]	T_{Stable} [°C]	ΔT_{Stable} [°C]
(A) Baseline Scenario										
30	-15 (-9.1)	1.5	-20 (-19.6)	60	-20	1.39	$12.2^{+3.0}_{-1.6}$	$0.1^{+0.9}_{-0.1}$	$12.7^{+6.2}_{-2.1}$	$0.6^{+6.8}_{-0.6}$
(B) Dependency on Air Flow Rate										
0	-15 (-9.6)	1.5	-20 (-19.6)	60	-20	1.39	—	—	—	—
20	-15 (-9.5)		-20 (-19.6)				$13.5^{+3.9}_{-1.4}$	$0.2^{+1.5}_{-0.2}$	—	—
30	-15 (-9.1)		-20 (-19.6)				$12.2^{+3.0}_{-1.6}$	$0.1^{+0.9}_{-0.1}$	$12.7^{+6.2}_{-2.1}$	$0.6^{+6.8}_{-0.6}$
40	-15 (-8.8)		-20 (-19.6)				$11.3^{+2.7}_{-1.8}$	$0.1^{+0.7}_{-0.1}$	$11.6^{+3.8}_{-2.2}$	$0.4^{+4.2}_{-0.4}$
(C) Dependency on Air Temperature										
30	-15 (-9.1)	1.5	-20 (-19.6)	60	-20	1.39	$12.2^{+3.0}_{-1.6}$	$0.1^{+0.9}_{-0.1}$	$12.7^{+6.2}_{-2.1}$	$0.6^{+6.8}_{-0.6}$
	0 (4.1)		-20 (-19.6)				$14.3^{+3.0}_{-1.2}$	$0.2^{+1.3}_{-0.2}$	—	—
	20 (21.2)		-20 (-19.5)				$16.3^{+2.4}_{-1.2}$	$0.2^{+1.6}_{-0.2}$	—	—
(D) Dependency on 3M™ NOVEC™ 649 Flow Rate										
30	-15 (-8.7)	1.0	-20 (-18.9)	60	-20	1.39	$16.1^{+4.4}_{-2.6}$	$0.2^{+1.4}_{-0.2}$	—	—
	-15 (-9.1)	1.5	-20 (-19.6)				$12.2^{+3.0}_{-1.6}$	$0.1^{+0.9}_{-0.1}$	$12.7^{+6.2}_{-2.1}$	$0.6^{+6.8}_{-0.6}$
	-15 (-8.8)	2.0	-20 (-20.4)				$10.2^{+2.8}_{-1.4}$	$0.1^{+0.8}_{-0.1}$	$10.6^{+4.5}_{-1.8}$	$0.5^{+5.0}_{-0.5}$
(E) Dependency on 3M™ NOVEC™ 649 Temperature										
30	-15 (-9.1)	1.5	-20 (-19.6)	60	-20	1.39	$12.2^{+3.0}_{-1.6}$	$0.1^{+0.9}_{-0.1}$	$12.7^{+6.2}_{-2.1}$	$0.6^{+6.8}_{-0.6}$
	-15 (-9.3)		-30 (-30.0)		-30		$4.9^{+2.0}_{-1.1}$	$0.1^{+0.5}_{-0.1}$	$5.2^{+2.6}_{-1.3}$	$0.3^{+2.7}_{-0.3}$
	-15 (-9.3)		-40 (-36.6)		$-40(\lesssim$ -30)		$0.5^{+1.6}_{-1.2}$	$0.0^{+0.4}_{-0.0}$	$0.7^{+2.1}_{-1.3}$	$0.2^{+1.7}_{-0.2}$
(F) Dependency on Side-Wall Cooling										
30	-15 (-9.1)	1.5	-20 (-19.6)	60	ON (-20)	1.39	$12.2^{+3.0}_{-1.6}$	$0.1^{+0.9}_{-0.1}$	$12.7^{+6.2}_{-2.1}$	$0.6^{+6.8}_{-0.6}$
	-15 (-9.1)		-20 (-19.6)		OFF		$15.2^{+2.2}_{-1.6}$	$0.2^{+1.2}_{-0.2}$	—	—
(G) Dependency on FEE Power Dissipation										
30	-15 (-8.8)	1.5	-20 (-19.5)	60	20	0.88 (*Min*)	$5.3^{+1.2}_{-0.8}$	$0.1^{+0.6}_{-0.1}$	$5.6^{+3.0}_{-1.0}$	$0.3^{+2.9}_{-0.3}$
	-15 (-8.7)		-20 (-19.5)			1.21 (*Typical*)	$10.2^{+2.0}_{-1.4}$	$0.1^{+0.8}_{-0.1}$	$10.7^{+5.1}_{-1.9}$	$0.6^{+5.4}_{-0.6}$
	-15 (-9.1)		-20 (-19.6)			1.39 (*Max*)	$12.2^{+3.0}_{-1.6}$	$0.1^{+0.9}_{-0.1}$	$12.7^{+6.2}_{-2.1}$	$0.6^{+6.8}_{-0.6}$
	-15 (-8.8)		-20 (-19.6)			1.57 (*Max + 10%*)	$15.1^{+4.3}_{-2.4}$	$0.1^{+1.2}_{-0.1}$	—	—

Table 4.1.: Summary showing the dependencies of the mean stable temperature ($T_{Stable}\ {}^{+Max}_{-Min}$) and its rise ($\Delta T_{Stable}\ {}^{+Max}_{-Min}$) on the variation of various operational parameters (respective values highlighted in yellow; see text for more details). The coolant temperature values outside brackets are the set values at the respective cooling plants, whereas the values within brackets are the measured values at the distribution manifolds outside the Thermal Demonstrator's enclosure. The mean temperatures are filled with dash (—) in case there is a sensor in the half-station which doesn't have a stable temperature, i.e., is in thermal runaway. The underlying temperature distributions are shown in App. F.

Coolant Input Parameters						Total FEE Power Dissipation [kW]	Cooling Power Fit Parameters (Module LT201-3T)		Thermal Runaway Temp. (Module LT201-3T)			
Air (per ladder)		3M™ NOVEC™ 649 (per cooling plate)		Environmental Cooling					After 10 Years ($0.24\times10^{14} n_{eq}/cm^2$)		After EOL ($1\times10^{14} n_{eq}/cm^2$)	
$\dot{V}_{Air}$ [L/min]	T_{Air} [°C]	$\dot{V}_{Novec}$ [L/min]	T_{Novec} [°C]	Air Flow Rate [L/min]	Side Wall Cooling Bath Temp. [°C]		T_0 [°C]	HTC [mW/cm²·K]	T_{Stable} [°C]	$T_{Critical}$ [°C]	T_{Stable} [°C]	$T_{Critical}$ [°C]
(A) Baseline Scenario												
30	-15 (-9.1)	1.5	-20 (-19.6)	60	-20	1.39	11.5	15.4	12.6	68.2	18.9	31.4
(B) Dependency on Air Flow Rate												
0	-15 (-9.6)	1.5	-20 (-19.6)	60	-20	1.39	12.9	3.9	21.7	30.4	—	—
20	-15 (-9.5)		-20 (-19.6)				12.4	10.7	14.1	59.1	—	—
30	-15 (-9.1)		-20 (-19.6)				11.5	15.4	12.6	68.2	18.9	31.4
40	-15 (-8.8)		-20 (-19.6)				10.8	18.6	11.6	72.9	15.4	38.3
(C) Dependency on Air Temperature												
30	-15 (-9.1)	1.5	-20 (-19.6)	60	-20	1.39	11.5	15.4	12.6	68.2	18.9	31.4
	0 (4.1)		-20 (-19.6)				13.6	14.1	15.0	65.0	—	—
	20 (21.2)		-20 (-19.5)				15.8	13.8	17.5	63.5	—	—
(D) Dependency on 3M™ NOVEC™ 649 Flow Rate												
30	-15 (-8.7)	1.0	-20 (-18.9)	60	-20	1.39	15.1	14.7	16.7	65.3	—	—
	-15 (-9.1)	1.5	-20 (-19.6)				11.5	15.4	12.6	68.2	18.9	31.4
	-15 (-8.8)	2.0	-20 (-20.4)				10.6	90.5	10.8	> 100	11.3	76.7
(E) Dependency on 3M™ NOVEC™ 649 Temperature												
30	-15 (-9.1)	1.5	-20 (-19.6)	60	-20	1.39	11.5	15.4	12.6	68.2	18.9	31.4
	-15 (-9.3)		-30 (-30.0)		-30		4.8	14.5	5.4	69.3	7.8	37.2
	-15 (-9.3)		-40 (-36.6)		$-40(\lesssim -30)$		0.9	14.6	1.3	70.2	2.8	39.7
(F) Dependency on Side-Wall Cooling												
30	-15 (-9.1)	1.5	-20 (-19.6)	60	ON (-20)	1.39	11.5	15.4	12.6	68.2	18.9	31.4
	-15 (-9.1)		-20 (-19.6)		OFF		14.4	15.2	15.8	66.5	—	—
(G) Dependency on FEE Power Dissipation												
30	-15 (-8.8)	1.5	-20 (-19.5)	60	20	0.88 (*Min*)	5.4	14.6	6.0	69.2	8.6	36.8
	-15 (-8.7)		-20 (-19.5)			1.21 (*Typical*)	9.8	14.6	10.7	67.5	15.8	32.4
	-15 (-9.1)		-20 (-19.6)			1.39 (*Max*)	11.5	15.4	12.6	68.2	18.9	31.4
	-15 (-8.8)		-20 (-19.6)			1.57 (*Max + 10%*)	14.1	15.5	15.6	67.0	—	—

Table 4.2.: Summary showing the dependencies of the most crucial module (Module Type LT201-3T; most irradiated and highest temperature) on the variation of various operational parameters (respective values highlighted in yellow; see text for more details). The coolant temperature values outside brackets are the set values at the respective cooling plants, whereas the values within brackets are the measured values at the distribution manifolds outside the Thermal Demonstrator's enclosure. The thermal runaway temperatures filled with dash (—) have no stable operating conditions at the given fluence.

4.1.2.1. Dependency on Air Flow Rate

The dependency of the cooling power and thermal runaway behaviour for different air flow rates (0 ... 40 L/min) has been studied for the two fluence scenarios, i.e., after 10 years and EOL (see Fig. 4.6(a) to see an example of the LT201-3T module). The variation of the resulting mean stable temperature and its rise across the half-station with respect to the air flow rate is shown in Fig. 4.6(b) and Fig. 4.6(c), respectively. Based on this, the following can be concluded:

- The baseline air flow rate of 30 L/min safely neutralises the sensor power dissipation after 10 years and EOL fluence.
- Cooling the silicon sensors solely by natural convection (air flow rate of 0 L/min) leads to some sensors exhibiting thermal runaway behaviour.

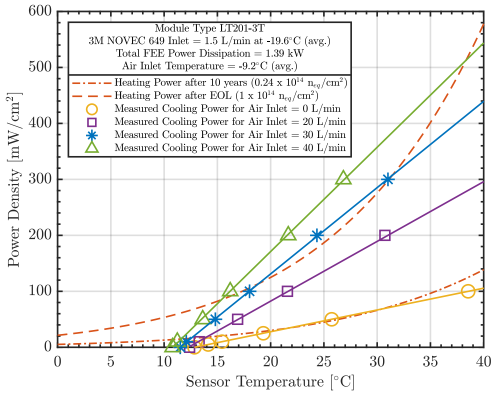

(a) Heating vs Cooling Power

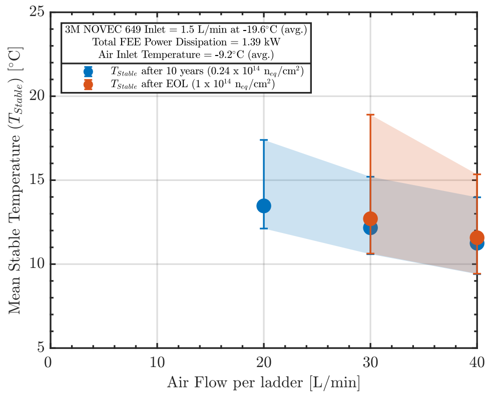

(b) Mean Stable Temp. ($T_{Stable}\ {}^{+Max}_{-Min}$)

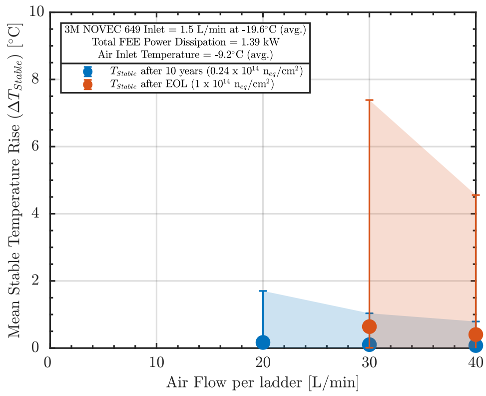

(c) Mean Stable Temp. Rise ($\Delta T_{Stable}\ {}^{+Max}_{-Min}$)

Figure 4.6.: The variation of thermal runaway behaviour with air flow rate per ladder (set value 0 ... 40 L/min; measured at the distribution manifold outside the Thermal Demonstrator's enclosure) for the two fluence scenarios (10 years and EOL). The underlying values are tabulated in Tab. 4.1-4.2 and Fig. F.5-F.8.

4.1.2.2. Dependency on Air Temperature

The dependency of the cooling power and thermal runaway behaviour for different air temperatures (-15 ... 20 °C) has been studied for the two fluence scenarios, i.e., after 10 years and EOL (see Fig. 4.7(a) to see an example of the LT201-3T module). The variation of the resulting mean stable temperature and its rise across the half-station with respect to the air temperature is shown in Fig. 4.7(b) and Fig. 4.7(c), respectively. Based on this, the following can be concluded:

- The baseline air temperature of -15°C safely neutralises the sensor power dissipation after 10 years and EOL fluence.
- Using hotter air or not using air cooling at all ($\geq$ 0°C) leads to some sensors exhibiting thermal runaway behaviour.

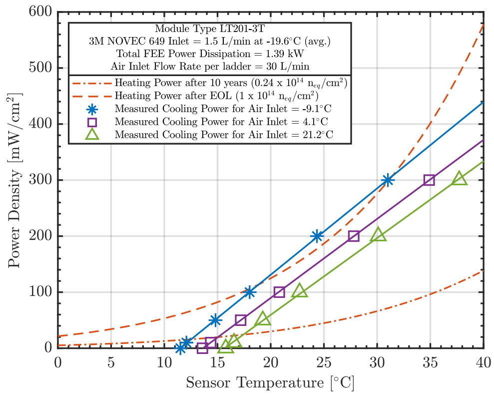

(a) Heating vs Cooling Power

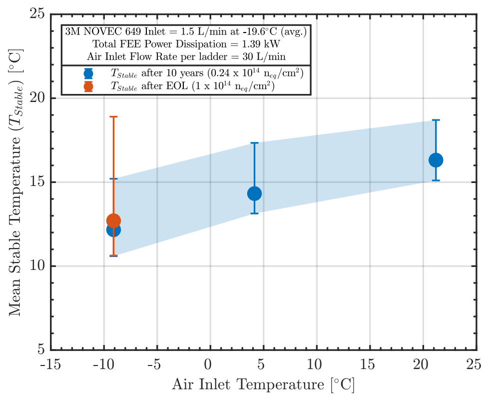

(b) Mean Stable Temp. ($T_{Stable}\ {}^{+Max}_{-Min}$)

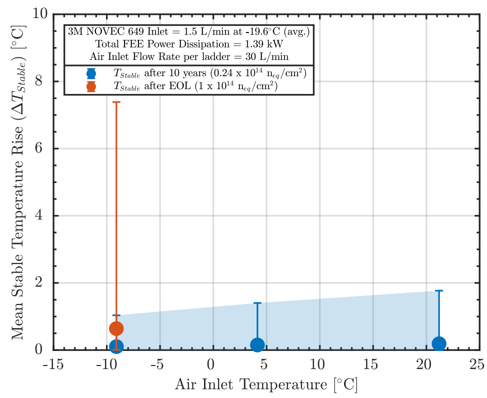

(c) Mean Stable Temp. Rise ($\Delta T_{Stable}\ {}^{+Max}_{-Min}$)

Figure 4.7.: The variation of thermal runaway behaviour with air temperature (set value -15...20°C; inlet value -9...21°C measured at the distribution manifold outside the Thermal Demonstrator's enclosure) for the two fluence scenarios (10 years and EOL). The underlying values are tabulated in Tab. 4.1-4.2 and Fig. F.5-F.8.

4.1.2.3. Dependency on 3M™ NOVEC™ 649 Flow Rate

The dependency of the thermal runaway behaviour for different 3M™ NOVEC™ 649 flow rates per cooling plate (1 ... 2 L/min) has been studied for the two fluence scenarios, i.e., after 10 years and EOL (see Fig. 4.8(a) to see an example of the LT201-3T module). The variation of the resulting mean stable temperature and its rise across the half-station with respect to the inlet flow rate is shown in Fig. 4.8(b)-4.8(c), respectively. Based on this, the following can be concluded:

- The baseline 3M™ NOVEC™ 649 flow rate of 1.5 L/min safely neutralises the sensor power dissipation after 10 years and EOL fluence.
- Lower than baseline flow rate (1 L/min) doesn't lead to stable sensor temperatures at EOL fluence, therefore, isn't recommended.

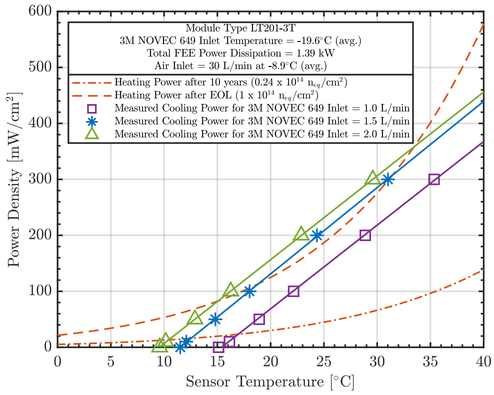

(a) Heating vs Cooling Power

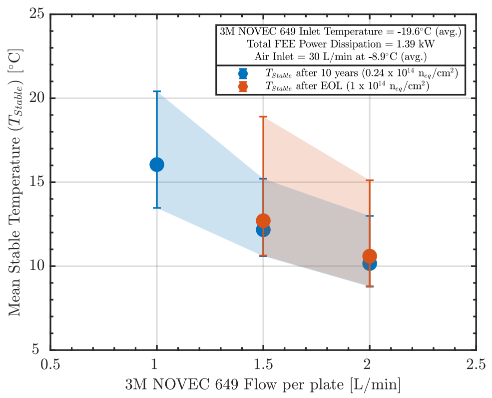

(b) Mean Stable Temp. ($T_{Stable}\ ^{+Max}_{-Min}$)

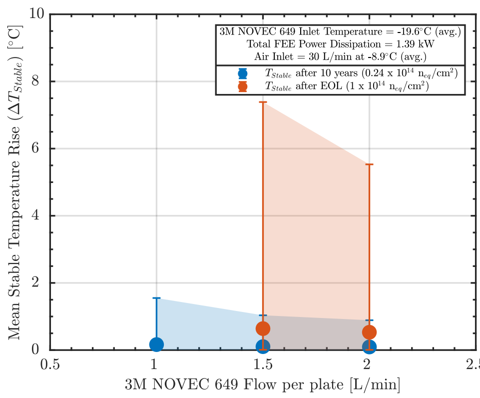

(c) Mean Stable Temp. Rise ($\Delta T_{Stable}\ ^{+Max}_{-Min}$)

Figure 4.8.: The variation of thermal runaway behaviour with 3M™ NOVEC™ 649 flow rate per cooling plate (set value 1 ... 2 L/min; measured at the distribution manifold outside the Thermal Demonstrator's enclosure) for the two fluence scenarios (10 years and EOL). The underlying values are tabulated in Tab. 4.1-4.2 and Fig. F.9-F.12.

4.1.2.4. Dependency on 3M™ NOVEC™ 649 Temperature

The dependency of the thermal runaway behaviour for different 3M™ NOVEC™ 649 temperature (-40 ... -20 °C) has been studied for the two fluence scenarios, i.e., after 10 years and EOL (see Fig. 4.9(a) to see an example of the LT201-3T module). The variation of the resulting mean stable temperature and its rise across the half-station with respect to the inlet temperature is shown in Fig. 4.9(b)-4.9(c), respectively. Based on this, the following can be concluded:

- The baseline 3M™ NOVEC™ 649 temperature of -20°C safely neutralises the sensor power dissipation after 10 years and EOL fluence.
- Lower 3M™ NOVEC™ 649 temperature lowers the stable sensor temperature, thereby increasing the margin from thermal runaway at EOL fluence.

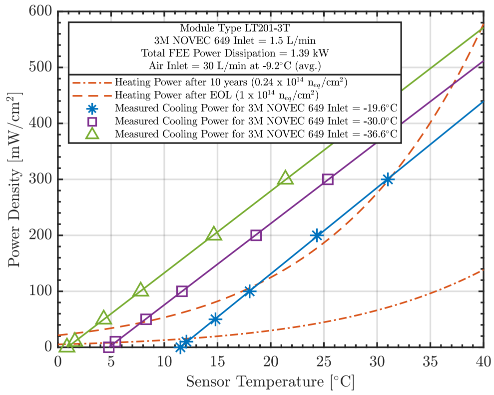

(a) Heating vs Cooling Power

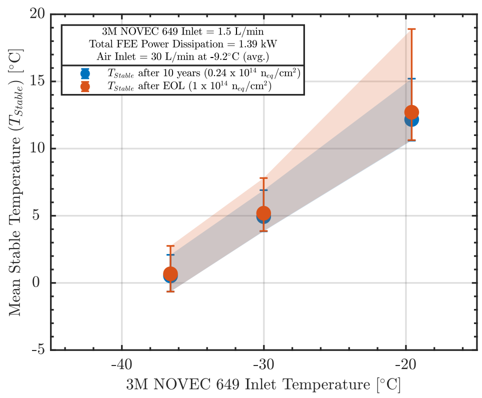

(b) Mean Stable Temp. ($T_{Stable}{}^{+Max}_{-Min}$)

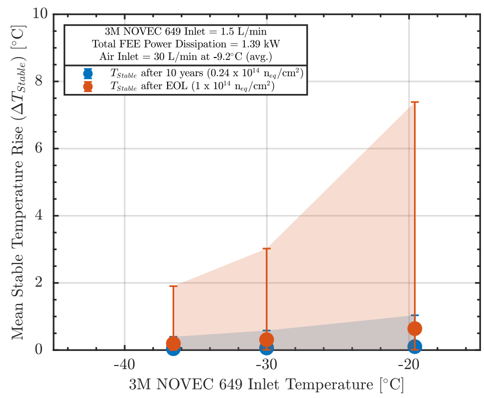

(c) Mean Stable Temp. Rise ($\Delta T_{Stable}{}^{+Max}_{-Min}$)

Figure 4.9.: The variation of thermal runaway behaviour with 3M™ NOVEC™ 649 temperature (set value -40 ... -20°C; inlet value -37...-20°C measured at the manifold outside the Thermal Demonstrator's enclosure) for the two fluence scenarios (10 years and EOL). The underlying values are tabulated in Tab. 4.1-4.2 and Fig. F.13-F.16.

4.1.2.5. Dependency on Side-wall Cooling

The dependency of the thermal runaway behaviour for different side-wall cooling states (ON(-20°C) ... OFF) has been studied for the two fluence scenarios, i.e., after 10 years and EOL (see Fig. 4.10(a) to see an example of the LT201-3T module). The variation of the resulting mean stable temperature and its rise across the half-station with respect to the side-wall cooling states is shown in Fig. 4.10(b)-4.10(c), respectively. Based on this, the following can be concluded:

- The baseline side-wall cooling state (ON at -20°C) safely neutralises the sensor power dissipation after 10 years and EOL fluence.
- Switching the side-wall cooling off results doesn't result in stable operating temperatures at EOL fluence, hence it should be always on.

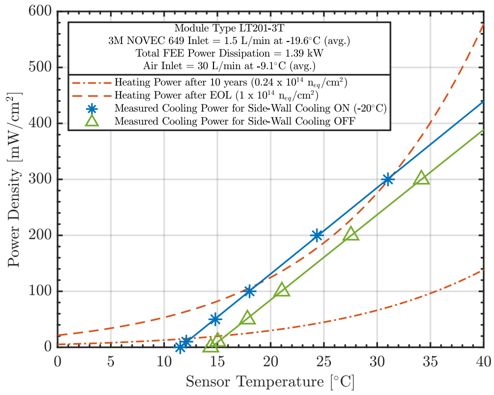

(a) Heating vs Cooling Power

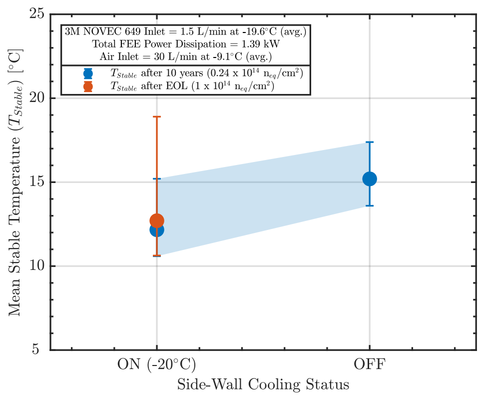

(b) Mean Stable Temp. ($T_{Stable}\,{}^{+Max}_{-Min}$)

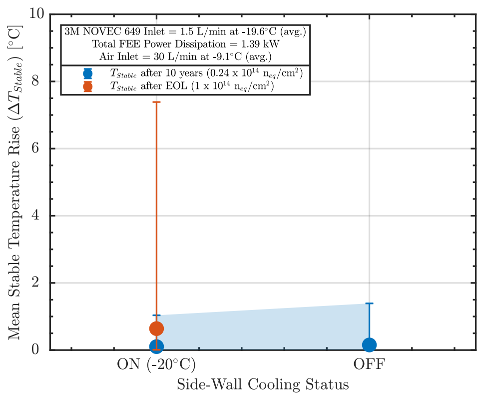

(c) Mean Stable Temp. Rise ($\Delta T_{Stable}\,{}^{+Max}_{-Min}$)

Figure 4.10.: The variation of thermal runaway behaviour for different side-wall cooling states (ON(-20°C) ... OFF; set at a separate chiller outside the Thermal Demonstrator's enclosure) for the two fluence scenarios (10 years and EOL). The underlying values are tabulated in Tab. 4.1-4.2 and Fig. F.17-F.20.

4.1.2.6. Dependency on FEE Power Dissipation

The dependency of the thermal runaway behaviour for different FEB power dissipation (see App. E.2 for different cases) has been studied for the two fluence scenarios, i.e., after 10 years and EOL (see Fig. 4.11(a) to see an example of the LT201-3T module). The variation of the resulting mean stable temperature and its rise across the half-station with respect to the FEB power is shown in Fig. 4.11(b)-4.11(c), respectively. Based on this, the following can be concluded:

- The baseline FEB power (*Maximum Scenario*; 12.93 W per FEB) is safely neutralised to ensure stable operation after 10 years and EOL fluence.
- All realistic FEB powering scenarios, totaling up to maximum 1.39 kW of power, ensure stable operating temperatures at EOL fluence.

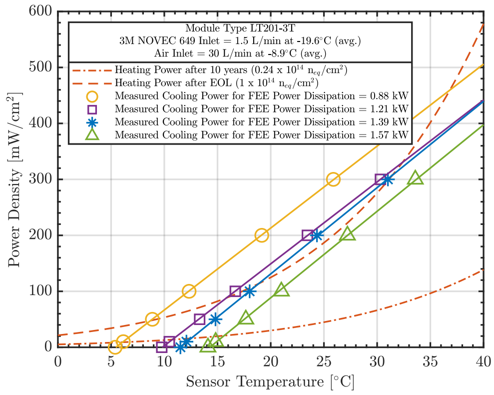

(a) Heating vs Cooling Power

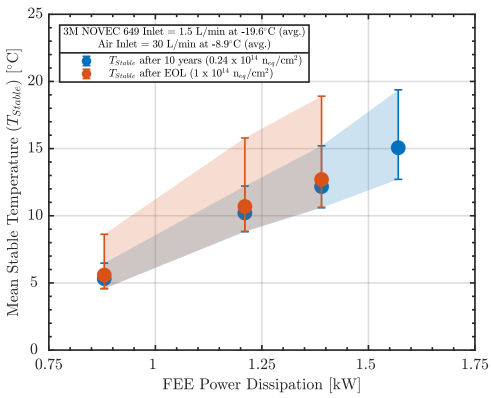

(b) Mean Stable Temp. ($T_{Stable}\ {}^{+Max}_{-Min}$)

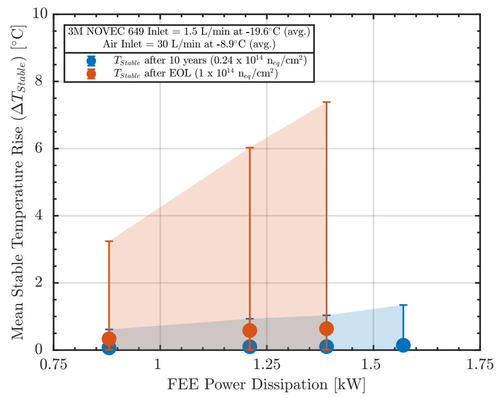

(c) Mean Stable Temp. Rise ($\Delta T_{Stable}\ {}^{+Max}_{-Min}$)

Figure 4.11.: The variation of thermal runaway behaviour with FEB power dissipation (per FEB values ranging from 8.63 ... 14.22 W and total values ranging from 0.88 ... 1.57 kW) for the two fluence scenarios (10 years and EOL). The underlying values are tabulated in Tab. 4.1-4.2 and Fig. F.21-F.24.

4.1.3. Beam Shutdown Scenario

CBM and its comprising subsystems, particularly the STS, are designed to operate concurrently with the SIS-100 accelerator for approximately two months each year. However, even during the SIS-100 beam shutdown periods, the STS must be thermally managed to mitigate the effects of accumulated radiation damage. Maintaining the STS sensors at sub-zero temperatures is imperative to prevent the reverse annealing of the full depletion voltage ($\approx -10°$C) (see Tab. 1.1 for the underlying time constants). This section delves into potential operational scenarios during the SIS-100 beam shutdown that could lead to sub-zero sensor temperatures, considering various operational parameters:

Air Cooling (Sensors and Environment): Cold and dry air cooling is the primary method employed to regulate sensor temperature and maintain a sufficiently low dew point within the thermal enclosure. It remains active at baseline values (30 L/min for sensor cooling per ladder and 60 L/min for environment cooling) at the coldest available set-point of -15°C.

3M™ NOVEC™ 649 Cooling: Electronics cooling is foreseen to be deactivated to prevent "freezing" of electronics during shutdown. However, its contribution to lowering the enclosure's ambient temperature is considered at OFF and between -20°C (baseline) to -40°C, with a flow rate of 1.5 L/min per cooling plate.

Side-Wall Cooling: This method is consistently activated to enhance thermal insulation and reduce the enclosure's ambient temperature. The operational range of -20°C (baseline) to -40°C is considered.

FEB Power Dissipation: Although electronics are powered down during shutdowns, brief activations may occur for cosmic and alignment runs. Hence, the impact is assessed both when switched off and on (baseline; *Maximum Scenario* with 12.93 W power dissipation per FEB and 1.39 kW in total).

The interplay between aforementioned parameters is documented in Tab. 4.3, alongside the mean sensor temperature across the entire half-station (see also Fig. 4.12). Analysis reveals that achieving sub-zero sensor temperatures ($\approx -10°$C) necessitates activating electronics cooling (scenario #4 ...#6), which significantly contributes to lowering the enclosure's ambient temperature. The impact of electronics cooling is most visible when comparing scenario #2 and #4, where the electronics cooling is deactivated for the former and activated at -20°C for the latter, resulting in the mean sensor temperature ($T_{mean}\,{}^{+Max}_{-Min}$) of $7.5^{+1.0}_{-0.9}$ and $-7.5^{+1.5}_{-2.1}$, respectively. Relying solely on air cooling methods proves insufficient to maintain the required temperature and counteract excessive heat ingress into the Thermal Demonstrator's enclosure from the laboratory. Addressing this challenge will involve implementing a better thermally isolated enclosure, reducing inlet air temperature, and increasing inlet air flow rate.

Scenario Number	Coolant Input Parameters						Total FEE Power Dissipation [kW]	Mean Sensor Temperature $\left(T_{avg}\ {}^{Max}_{Min}\right)$ [°C]
	Air (per ladder)		3M™ NOVEC™ 649 (per cooling plate)		Environmental Cooling			
	$\dot{V}_{Air}$ [L/min]	T_{Air} [°C]	$\dot{V}_{Novec}$ [L/min]	T_{Novec} [°C]	Air Flow Rate [L/min]	Side Wall Cooling Bath Temp. [°C]		
				(A) Baseline Scenario				
#1	30	-15 (-9.1)	1.5	-20 (-19.6)	60	-20	1.39	$12.1^{+3.1}_{-1.5}$
				(B) Without Electronics Cooling				
#2	30	-15 (-9.1)	OFF	OFF	60	-20	OFF	$7.5^{+1.0}_{-0.9}$
#3	30	-15 (-9.0)	OFF	OFF	60	-30	OFF	$6.7^{+1.2}_{-1.0}$
				(C) With Electronics Cooling				
#4	30	-15 (-9.1)	1.5	-20 (-19.5)	60	-20	OFF	$-7.5^{+1.5}_{-2.1}$
#5	30	-15 (-9.3)	1.5	-30 (-29.1)	60	-30	OFF	$-13.4^{+2.0}_{-3.0}$
#6	30	-15 (-9.4)	1.5	-40 (-36.7)	60	-40 ($\lessapprox$ -30)	OFF	$-17.8^{+2.4}_{-3.5}$

Table 4.3.: Dependency of the mean sensor temperature across the half-station ($T_{mean}\ {}^{+Max}_{-Min}$) on various operational parameters possible during the SIS-100 beam shutdown (i.e., sensor powering is switched off). The underlying half-station temperature distributions are shown in Fig. F.25. Coolant temperatures outside brackets represent set values at cooling plants, while those within brackets indicate measured values at distribution manifolds outside the Thermal Demonstrator's enclosure.

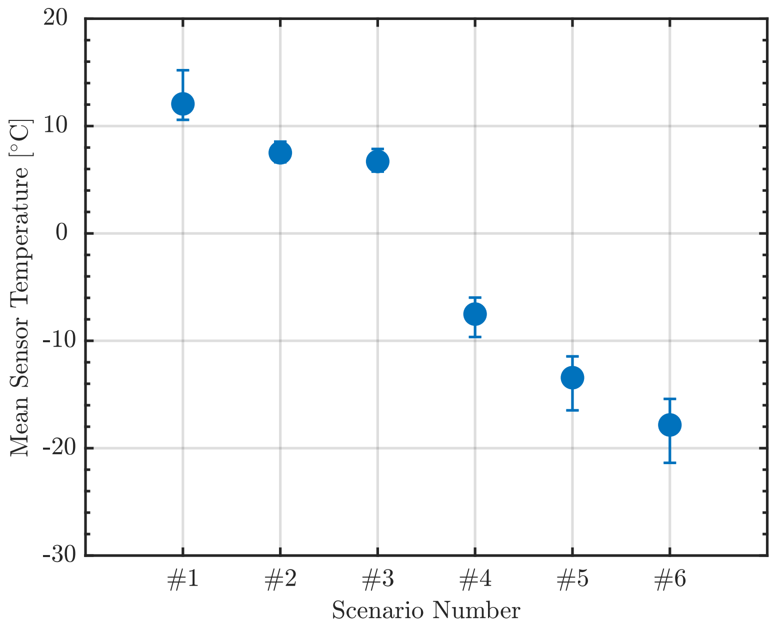

Figure 4.12.: The variation of mean sensor temperature ($T_{mean}\ {}^{+Max}_{-Min}$) across the half-station for several SIS-100 beam shutdown scenarios described in Tab. 4.3. The underlying half-station temperature distributions are shown in Fig. F.25.

4.2. Front-End Electronics Cooling

The peripherally-located electronics contribute the most to the power footprint of the STS ($\approx$ 40 kW in $\approx$ 3.5 m^3 detector enclosure volume). It's imperative that this power dissipation is effectively neutralised to minimise any residual heat transfer between the electronics and silicon sensors. This is especially crucial for the high-irradiated innermost silicon sensors around the beampipe as they are located only 25 ... 50 cm away (see Fig. 4.13) from the electronics, and failure to do so would increase the silicon sensors' temperatures, thus minimising their margin from the thermal runaway. Therefore, electronics are targeted to have a comparable temperature to non-irradiated silicon sensors ($\approx$+10°C). The effect of the front-end electronics (FEE) cooling and the underlying parameters on the thermal runaway behaviour, i.e., with silicon sensors dissipating radiation-induced power, has been studied with the STS Thermal Demonstrator and described in detail in Sec. 4.1.2.3, 4.1.2.4 and 4.1.2.6.

Consequently, the effectiveness of the FEE cooling and its ability to effectively neutralise the electronics' power dissipation primarily depends on the thermal impedance of the entire thermal path from the heat-producing ASICs to the

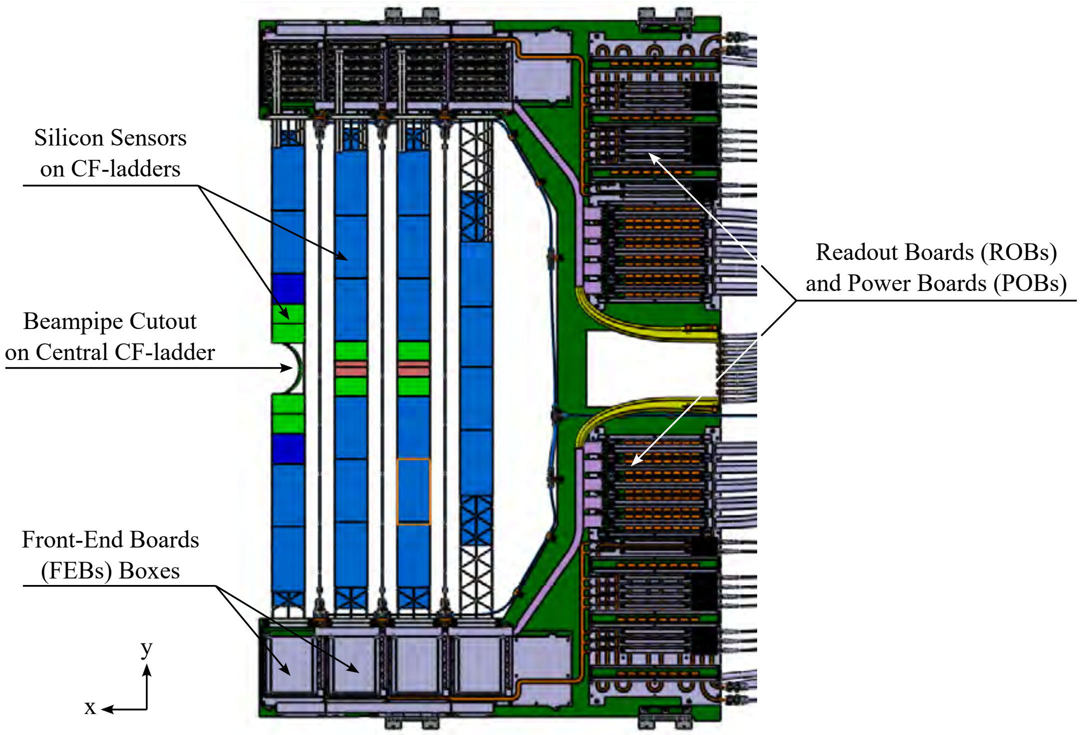

Figure 4.13.: CAD rendering (front-view) of an assembled STS C-frame, also known as half-unit. The silicon sensors are mechanically held by light-weight carbon fibre ladders and the electronics (front-end, readout and power boards) along with its cooling are placed outside the physics aperture (figure from O. Vasylyev (GSI Darmstadt)).

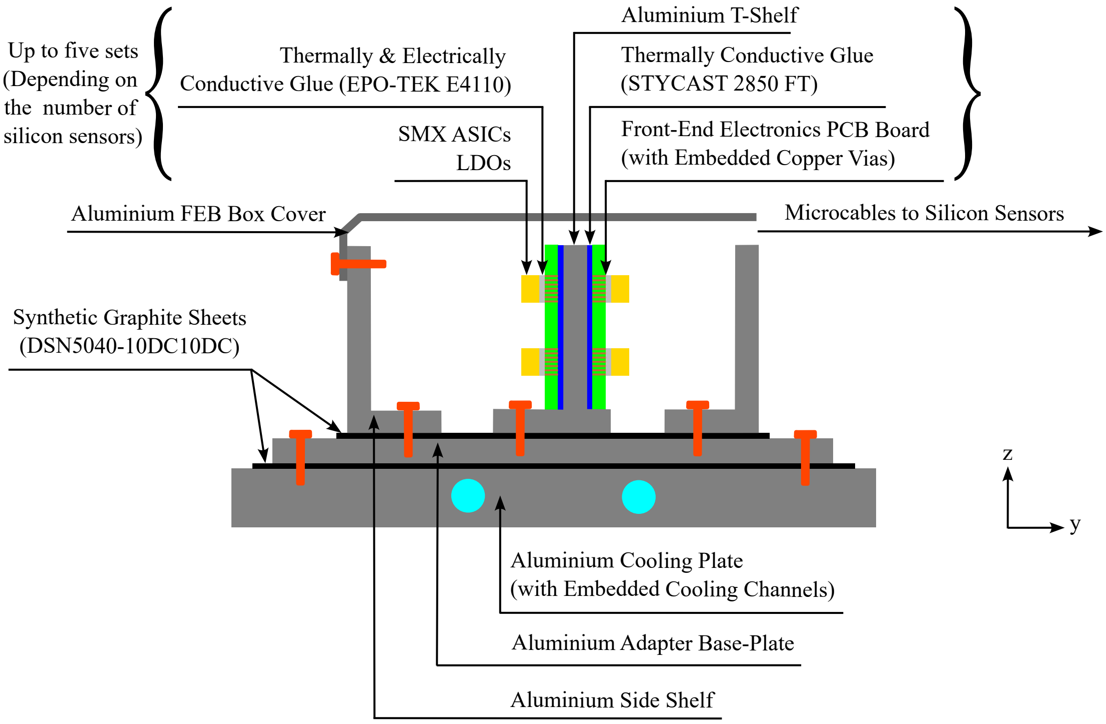

Figure 4.14.: Illustration of the FEB box thermal path. Please note that this only corresponds to one silicon sensor and up to five assembled T-shelves can be comprised in a FEB box. Drawings are not to scale.

heat sink. Key factors affecting this thermal path include the thermal interface materials, copper vias in the PCB, the thickness of the aluminium T-shelf, and the cooling channels in the electronics cooling plate. All FEE boards (FEBs) for a given half-ladder, containing up to five silicon sensors, are stacked in a FEB box enclosed in an aluminium cover to prevent unwanted heat transfer to the sensors. Further details on the FEB box structure are in Sec. 2.2.1 and Fig. 4.14. The Thermal Demonstrator comprises 50 silicon sensor dummies mounted across two thermally active C-frames and six ladders, with 12 FEB boxes on four FEB cooling plates (three per plate), totaling 100 dummy FEBs. Each dummy FEB has three 1-wire temperature sensors (Maxim Integrated DS18B20 (1-wire® readout)) on the ASIC and LDO meanders (see Sec. 3.2 for dummy FEB design and App. E.2 for their powering details). This setup allows for extensive temperature distribution mapping over all the FEBs and evaluate their cooling performance.

In this section, the FEE cooling chain's effectiveness is assessed based on its capacity to neutralise FEE power dissipation and achieve temperatures comparable to the silicon sensors in the *Baseline Operational Scenario*. Furthermore, the interaction between the FEE and silicon sensor temperature is studied by varying the FEE cooling operational parameter, namely the 3M™ NOVEC™ 649 flow rate, temperature and FEE power dissipation.

4.2.1. Baseline Operational Scenario

The FEE cooling baseline operational parameters are dictated by the components' survival properties under prolonged conditions. These factors, which overlap with the sensor thermal runaway analysis in Sec. 4.1.1, are summarised below.

3M™ NOVEC™ 649 Temperature = -20°C: The baseline coolant temperature of -20°C is chosen as thermal cycling studies established a minimum operational limit of -25°C for 10-year FEB operation.

3M™ NOVEC™ 649 Flow Rate = 1.5 L/min: The nominal flow rate for the STS-FEB cooling plates is 3 L/min to maintain flow velocity below the erosional limit of 3 m/s. Since the FEB boxes in the Thermal Demonstrator occupy one side of the cooling plates, the baseline flow rate is set at 1.5 L/min.

Power Dissipation per FEB = 12.93 W: The worst-case scenario foresees FEB power dissipation of 12.93 W, resulting in a total FEE power dissipation of 1.39 kW for the Thermal Demonstrator.

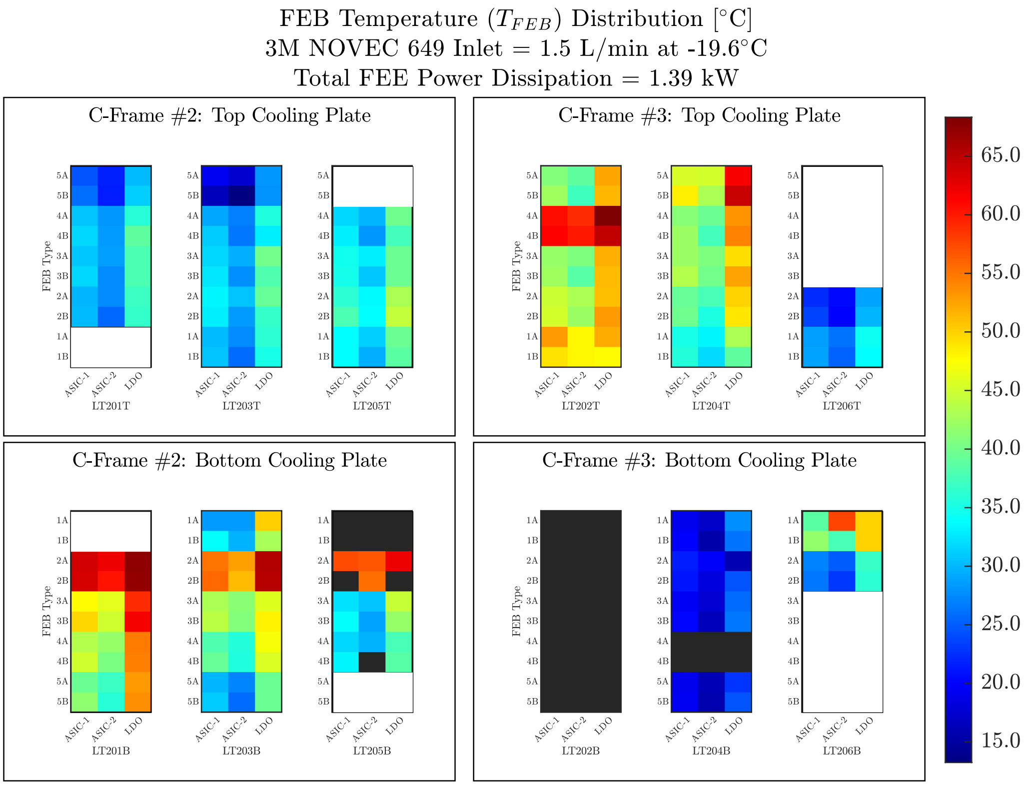

Figure 4.15.: FEE temperature distribution over the two thermally active C-frames under baseline operation parameters. Values are shown for the two ASIC and LDO rows on individual FEBs, grouped by FEB boxes and cooling plates. White bins indicate locations without silicon sensors (beampipe opening and peripheral locations), and black bins indicate FEBs with faulty temperature readout.

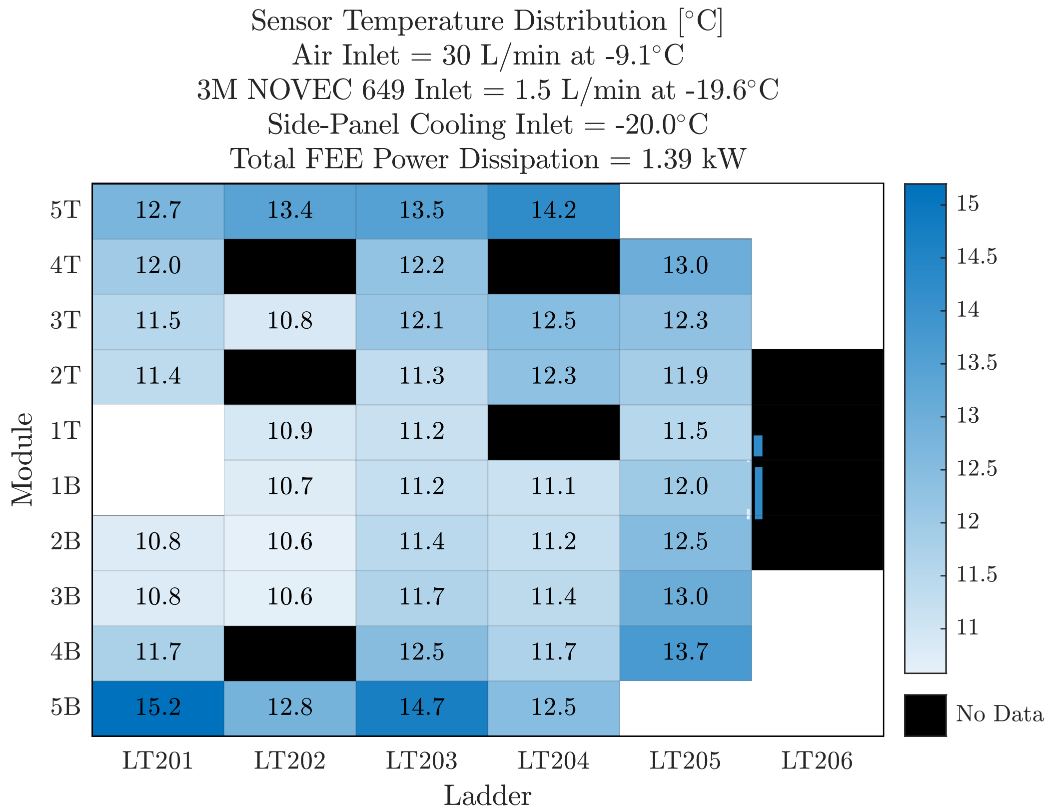

Figure 4.16.: Sensor temperature distribution across the thermally active half-station for the baseline FEE operational scenario when the silicon sensors are powered off, i.e., equivalent to unirradiated scenario. The innermost area in all figures (LT201-1T/B) represents the beam pipe opening, whereas the black bins comprise sensors which are either physically broken or have faulty Pt-100 sensor.

For the aforementioned baseline operational scenario, the temperature distributed was mapped for all FEBs as shown in Fig. 4.15. Based on these measurements, the following conclusions can be drawn:

- The FEB temperatures ($T_{FEE}{}^{+Max}_{-Min} = 37.1^{+31.3}_{-23.8}$°C; see Fig. 4.15) throughout are higher than silicon sensor temperatures (unirradiated; $T_{Sensor}{}^{+Max}_{-Min} = 12.1^{+3.1}_{-1.5}$°C; see Fig. 4.16). This indicates an imperfect thermal coupling between the heat-producing ASICs/LDOs and the heat sink.
- Temperature inhomogeneity is observed among the FEB boxes on each plate. On average, the FEB boxes on C-Frame #2: Top Cooling Plate ($31.8^{+12.5}_{-18.6}$°C) and C-Frame #3: Bottom Cooling Plate ($29.0^{+28.7}_{-13.5}$°C) are cooler than those on C-Frame #2: Bottom Cooling Plate ($44.8^{+22.6}_{-18.8}$°C) and C-Frame #3: Top Cooling Plate ($40.0^{+28.3}_{-20.1}$°C). This discrepancy highlights inconsistent application of the pressure-sensitive graphite sheet thermal interface material. The Thermal Demonstrator comprised only FEB Type-A thermal dummies, while the final STS includes two mirrored FEB types,

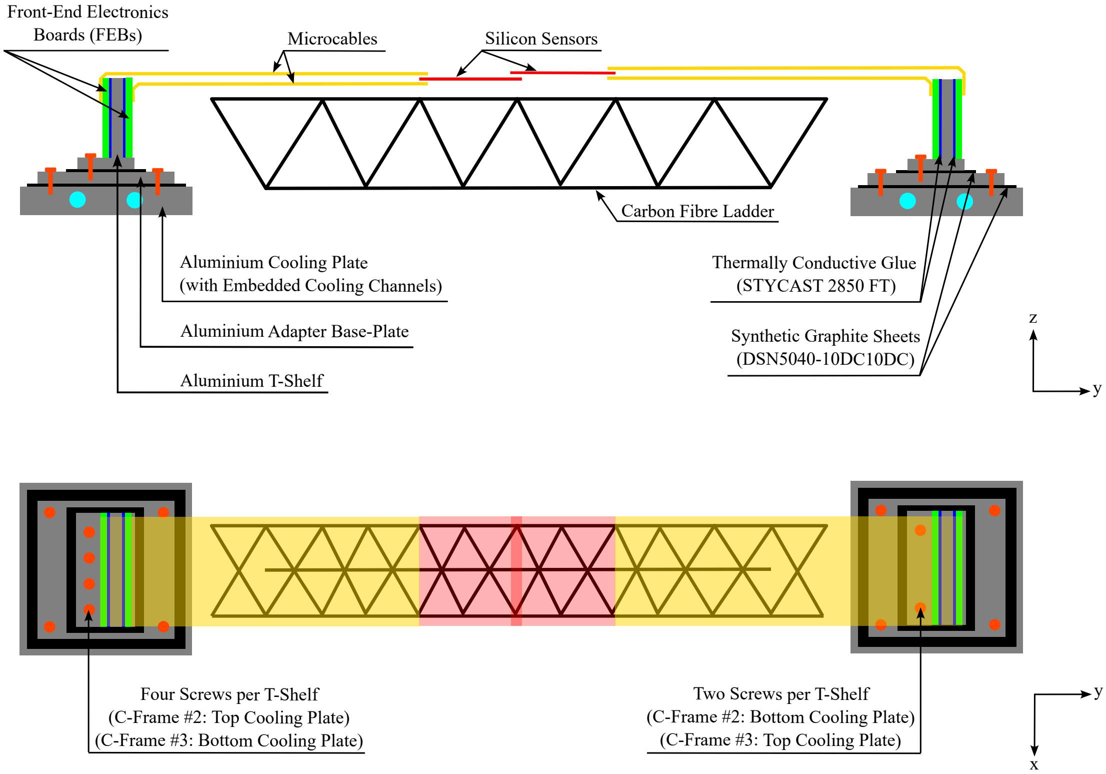

Figure 4.17.: Illustrations showing the ladder and FEB box assembly process for the STS Thermal Demonstrator. The top figure presents a side view, and the bottom figure shows a top view of the process. Drawings are not to scale.

Type-A and Type-B. This configuration facilitates easier integration of microcables onto the overlying SMX ASICs and allows proper screwing of the assembled T-shelf to the heat sink (see the FEB box on the left in Fig. 4.17). However, in the Thermal Demonstrator, T-shelves on one of the FEB boxes were covered by microcables, preventing proper screwing to the heat sink (see the FEB box on the right in Fig. 4.17). Consequently, the properly screwed FEB boxes had better coupling with the heat sink and exhibited lower temperatures, whereas the improperly screwed boxes showed higher temperatures.

- Despite the inefficient thermal coupling within the FEE thermal path and the resulting higher FEE temperatures, the sensor temperatures remain largely unaffected as they are consistently cooler than the FEE (see Fig. 4.18). Therefore, the aluminium cover of the FEB box (see Fig. 4.14) largely shields the silicon sensors from much higher FEE temperatures.

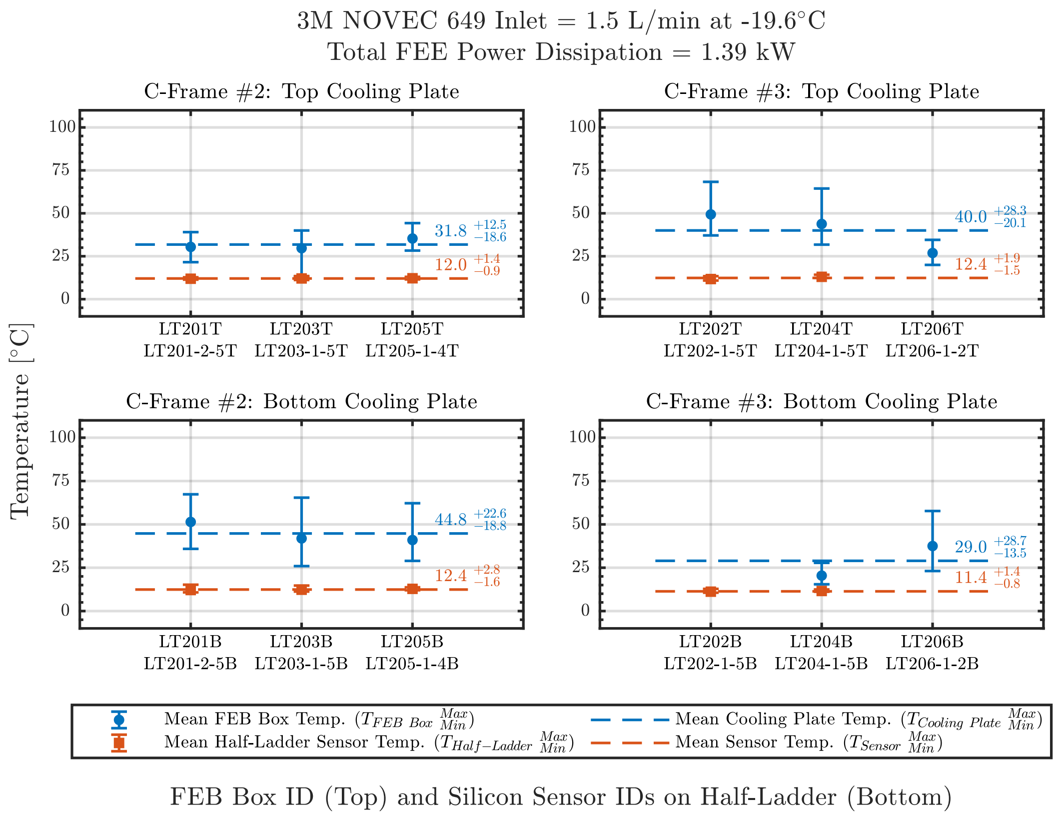

Figure 4.18.: Mean temperature variation of all FEB boxes (blue circle markers) and their corresponding sensors on the half-ladder (orange square markers) for the baseline operation parameters (see Sec. 4.2.1 for the parameters' details). Values are grouped based on the four cooling plates of the two thermally active C-frames. The dashed lines represent the mean temperatures of the cooling plates (blue) and sensors (orange).

4.2.2. Exploring Margins and Dependencies

The FEE cooling performance and its coupling with the silicon sensors was further evaluated by exploring its dependency with the FEE operational parameters relative to the baseline operational scenario (introduced in Sec. 4.2.1). This coupling becomes especially crucial to quantify how the inefficient FEE cooling, which exhibits much higher temperatures than silicon sensors, affect the silicon sensors. This coupling is quantified in terms of:

(i) Mean temperature of the FEE ($T_{FEE}{}^{+Max}_{-Min}$) and silicon sensors ($T_{Silicon}{}^{+Max}_{-Min}$) for a given set of operational parameters.

(ii) Rate of change of $T_{FEE}{}^{+Max}_{-Min}$ and $T_{Silicon}{}^{+Max}_{-Min}$ for the range of considered parameters.

The FEE operational parameters and their range studied are listed below. Concurrently, baseline parameters for the silicon sensor cooling were used for all the sub-scenarios, i.e., air flow rate per inner ladder of 30 L/min and inlet set temperature of -15 °C (see Fig. 4.1.1). Furthermore, the side-wall cooling temperature was set equal to the 3M™ NOVEC™ 649 temperature. Measurements are reported when silicon sensors are powered off, i.e., equivalent to unirradiated scenario.

- *3M™ NOVEC™ 649 flow rate*: 1 to 2 L/min
- *3M™ NOVEC™ 649 temperature*: -40 to -20 °C
- *FEE power dissipation*: 8.63 to 14.22 W per FEB (total 0.88 to 1.57 kW)

Tab. 4.4 summarises the dependency of the FEE cooling performance evaluated in terms of $T_{FEE}{}^{+Max}_{-Min}$, $T_{Silicon}{}^{+Max}_{-Min}$ and their respective rate of change with respect to the baseline parameters. Further details about these dependencies are provided in the following Sec. 4.2.2.1-4.2.2.3. Note that the underlying FEE and sensor temperature distributions for individual flow rates are shown in Figs. G.1, G.2-G.3, and Figs. H.1(a), H.2(a)-H.3(a), respectively. Moreover, comparisons between each FEB box and corresponding sensors on half-ladder for individual flow rates are shown in Figs. H.1(b), H.2(b)-H.3(b), with their collective variation shown in Fig. H.4).

3M™ NOVEC™ 649 Input Parameters (per cooling plate)		Total FEE Power Dissipation [kW]	Pressure Drop [bar]	Extracted Cooling Performance			
				Front-End Electronics		Silicon Sensors	
$\dot{V}_{Novec}$ [L/min]	T_{Novec} [°C]			$T_{FEE}{}^{+Max}_{-Min}$ [°C]	Rate of Change [K/unit]	$T_{Silicon}{}^{+Max}_{-Min}$ [°C]	Rate of Change [K/unit]
(A) Baseline Scenario							
1.5	-20 (-19.6)	1.39	0.73	$37.1^{+31.3}_{-23.8}$	—	$12.1^{+3.1}_{-1.5}$	—
(B) Dependency on 3M™ NOVEC™ 649 Flow Rate							
1.0	-20 (-18.9)	1.39	0.29	$45.1^{+34.4}_{-24.3}$	-8.3	$15.9^{+4.5}_{-2.7}$	-5.8
1.5	-20 (-19.6)		0.73	$37.1^{+31.3}_{-23.8}$		$12.1^{+3.1}_{-1.5}$	
2.0	-20 (-20.4)		1.26	$36.8^{+48.4}_{-26.4}$		$10.1^{+2.9}_{-1.3}$	
(C) Dependency on 3M™ NOVEC™ 649 Temperature							
1.5	-20 (-19.6)	1.39	0.73	$37.1^{+31.3}_{-23.8}$	1.0	$12.1^{+3.1}_{-1.5}$	0.7
	-30 (-30.0)		0.67	$26.6^{+31.5}_{-23.1}$		$4.9^{+2.0}_{-1.1}$	
	-40 (-36.6)		0.67	$20.0^{+32.0}_{-22.6}$		$0.5^{+1.6}_{-1.1}$	
(D) Dependency on FEE Power Dissipation							
1.5	-20 (-19.5)	0.88	0.59	$18.1^{+22.1}_{-14.8}$	38.9	$5.3^{+1.2}_{-0.7}$	13.8
	-20 (-19.5)	1.21	0.63	$31.2^{+30.2}_{-20.6}$		$10.1^{+2.1}_{-1.3}$	
	-20 (-19.6)	1.39	0.73	$37.1^{+31.3}_{-23.8}$		$12.1^{+3.1}_{-1.5}$	
	-20 (-19.6)	1.57	0.59	$45.3^{+37.5}_{-26.9}$		$14.9^{+4.5}_{-2.6}$	

Table 4.4.: Summary showing the dependencies of the mean FEE temperature ($T_{FEE}{}^{+Max}_{-Min}$) and mean silicon sensor temperature ($T_{Silicon}{}^{+Max}_{-Min}$) on the variation of various FEE operational parameters (respective values highlighted in yellow; see text for more details). The silicon sensors are powered off to simulate an unirradiated scenario. The coolant temperature values outside brackets are the set values at the respective cooling plants, whereas the values within brackets are the measured values at the distribution manifolds outside the Thermal Demonstrator's enclosure.

4.2.2.1. Dependency on 3M™ NOVEC™ 649 Flow Rate

The impact of different 3M™ NOVEC™ 649 flow rates (1 ... 2 L/min per cooling plate) on FEE cooling performance was studied, focusing on its effect on silicon sensor temperatures (powered off, simulating an unirradiated scenario, and air-cooled under baseline conditions). The variation of the resulting mean FEE ($T_{FEE}{}^{+Max}_{-Min}$) and silicon sensor ($T_{Silicon}{}^{+Max}_{-Min}$) across the thermally active half-station is shown in Fig. 4.19. Based on this, the following can be concluded:

- The FEE temperature change (-8.3 K·min/L) is sharper compared to the silicon sensors (-5.8 K·min/L), indicating that FEE cooling is more strongly coupled to the 3M™ NOVEC™ 649 flow rate.
- At higher flow rates, the temperature difference between the FEE and silicon sensors decreases, suggesting improved thermal efficiency due to the enhanced cooling capacity of 3M™ NOVEC™ 649.
- The large temperature difference between the mean FEE and silicon sensors throughout the studied FEB power dissipation range suggests that the two elements are only weakly correlated with each other, thus the silicon sensors are largely shielded from the warmer FEE temperatures.

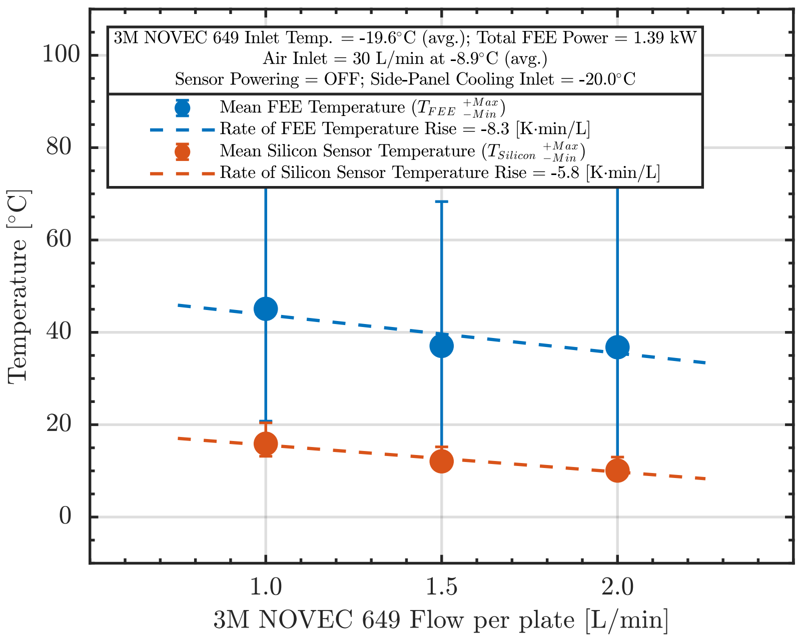

Figure 4.19.: Variation of mean FEE ($T_{FEE}{}^{+Max}_{-Min}$; blue markers) and silicon sensor ($T_{Silicon}{}^{+Max}_{-Min}$; orange markers) temperatures with 3M™ NOVEC™ 649 flow rate per cooling plate (set value 1 ... 2 L/min; measured at the distribution manifold outside the Thermal Demonstrator's enclosure). Dotted lines are the respective linear fits indicating the rate of temperature change. Underlying values are in Tab. 4.4.

4.2.2.2. Dependency on 3M™ NOVEC™ 649 Temperature

The impact of different 3M™ NOVEC™ 649 inlet temperature (-40 ... -20 °C) on FEE cooling performance was studied, focusing on its effect on silicon sensor temperatures (powered off, simulating an unirradiated scenario, and air-cooled under baseline conditions). The variation of the resulting mean FEE ($T_{FEE}{}^{+Max}_{-Min}$) and silicon sensor ($T_{Silicon}{}^{+Max}_{-Min}$) across the thermally active half-station is shown in Fig. 4.20. Based on this, the following can be concluded:

- The FEE temperature change (1 K/K) is sharper compared to the silicon sensors (0.7 K/K), indicating that FEE cooling is more strongly coupled to the 3M™ NOVEC™ 649 flow rate.
- At lower inlet temperatures, the temperature difference between the FEE and silicon sensors decreases, suggesting improved thermal efficiency due to the enhanced cooling capacity of 3M™ NOVEC™ 649.
- The large temperature difference between the mean FEE and silicon sensors throughout the studied FEB power dissipation range suggests that the two elements are only weakly correlated with each other, thus the silicon sensors are largely shielded from the warmer FEE temperatures.

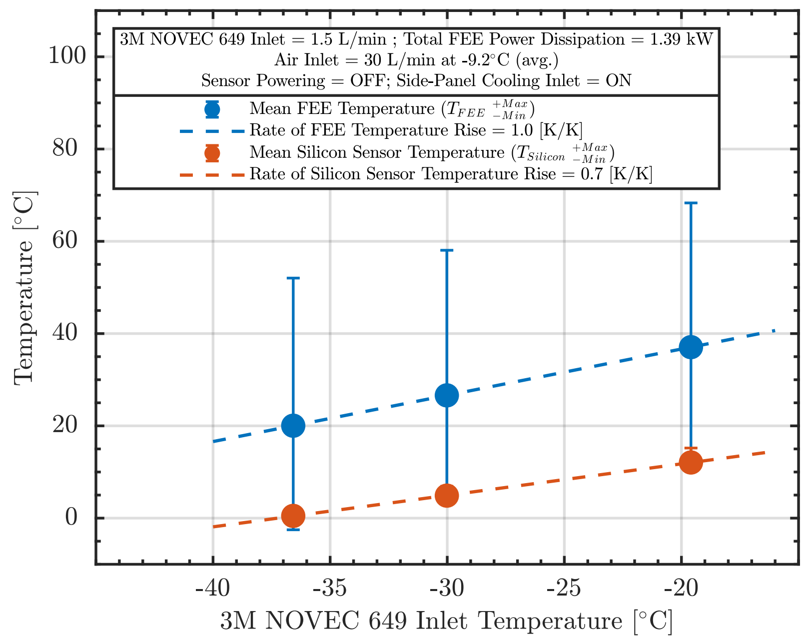

Figure 4.20.: Variation of mean FEE ($T_{FEE}{}^{+Max}_{-Min}$; blue markers) and silicon sensor ($T_{Silicon}{}^{+Max}_{-Min}$; orange markers) temperatures with 3M™ NOVEC™ 649 inlet temperature (set value -40 ... -20 °C; measured at the distribution manifold outside the Thermal Demonstrator's enclosure). Dotted lines are the respective linear fits indicating the rate of temperature change. Underlying values are in Tab. 4.4.

4.2.2.3. Dependency on FEE Power Dissipation

The impact of different FEB power dissipation (see App. E.2 for different cases) on FEE cooling performance was studied, focusing on its effect on silicon sensor temperatures (powered off, simulating an unirradiated scenario, and air-cooled under baseline conditions). The variation of the resulting mean FEE ($T_{FEE}{}^{+Max}_{-Min}$) and silicon sensor ($T_{Silicon}{}^{+Max}_{-Min}$) across the thermally active half-station is shown in Fig. 4.21. Based on this, the following can be concluded:

- The FEE temperature change (38.9 K/kW) is sharper compared to the silicon sensors (13.8 K/kW), indicating that FEE cooling is more strongly coupled to the FEB power dissipation.
- At lower FEB power dissipation, the temperature difference between the FEE and silicon sensors decreases, suggesting improved thermal efficiency of the FEE cooling circuit.
- The large temperature difference between the mean FEE and silicon sensors throughout the studied FEB power dissipation range suggests that the two elements are only weakly correlated with each other, thus the silicon sensors are largely shielded from the warmer FEE temperatures.

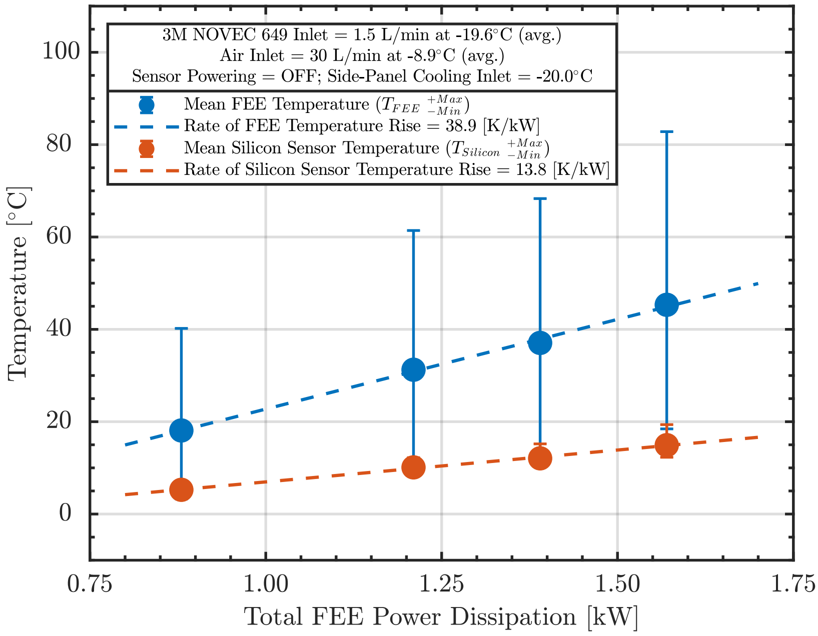

Figure 4.21.: Variation of mean FEE ($T_{FEE}{}^{+Max}_{-Min}$; blue markers) and silicon sensor ($T_{Silicon}{}^{+Max}_{-Min}$; orange markers) temperatures with FEB power dissipation (per FEB values ranging from 8.63 ... 14.22 W and total values ranging from 0.88 ... 1.57 kW). Dotted lines are the respective linear fits indicating the rate of temperature change. Underlying values are in Tab. 4.4.

5. Extrapolation to CBM-STS

The STS Thermal Demonstrator was envisaged as a test bench to not only deduce the operating parameters for STS cooling, but also to check the suitability of prototype and pre-production detector components and their integration methods in STS-like boundary conditions. This chapter aims to summarise the contributions of the STS Thermal Demonstrator in context of the ongoing CBM-STS detector production and assembly. As of the writing of this thesis, the STS has started the series production of modules in fall 2023, finished detailed detector designing in early 2024, and targets to procure the mechanical components for system integration in 2024-25. This schedules the STS installation readiness into the CBM experimental hall in 2026 and eventual data-taking with high-intensity heavy-ion beams with SIS-100 in 2028-29 [234].

5.1. Cooling Elements

(a) Silicon Sensor Cooling: As concluded from the results with the Thermal Demonstrator (see Sec. 4.1.2.1), the use of perforated carbon-fibre tubes is imperative as active silicon sensor cooling elements for the most irradiated silicon sensors around the beam pipe to inhibit their thermal runaway till the end-of-lifetime operation. Therefore, their design and mechanics, as implemented in the Thermal Demonstrator (see Sec. 3.1.1) have been successfully implemented in the CAD design of the final STS (see Fig. 5.1). This already provides a preliminary, yet concrete idea about the integration feasibility of these concepts on higher and more complex mechanical structures.

(b) Front-End Electronics Cooling: The cooling plates, manufactured with Friction-Stir Welding technology, were successfully tested with the STS Thermal Demonstrator both thermally (see Sec. 2.2.2.2 for CFD simulations and Sec. 4.2 for experimental results) and mechanically (see Sec. 3.1.2 for pressure and bulging tests). Based on findings and industrial collaboration with Cool Tec[1], various versions of similar cooling plates have been designed and implemented in the final STS CAD drawings for FEE cooling. This includes the arrangement of metal-to-metal seal connectors to align with their respective distribution manifold. Due to variations in the number of sensors and electronics across different detector stations, two major variants of the FEB cooling blocks are required. *FEB Cooling Block 3* is designed to accommodate a maximum of six FEB boxes (three per side)

1. Cool Tec Electronic GmbH, Germany, `www.cooltec.de`

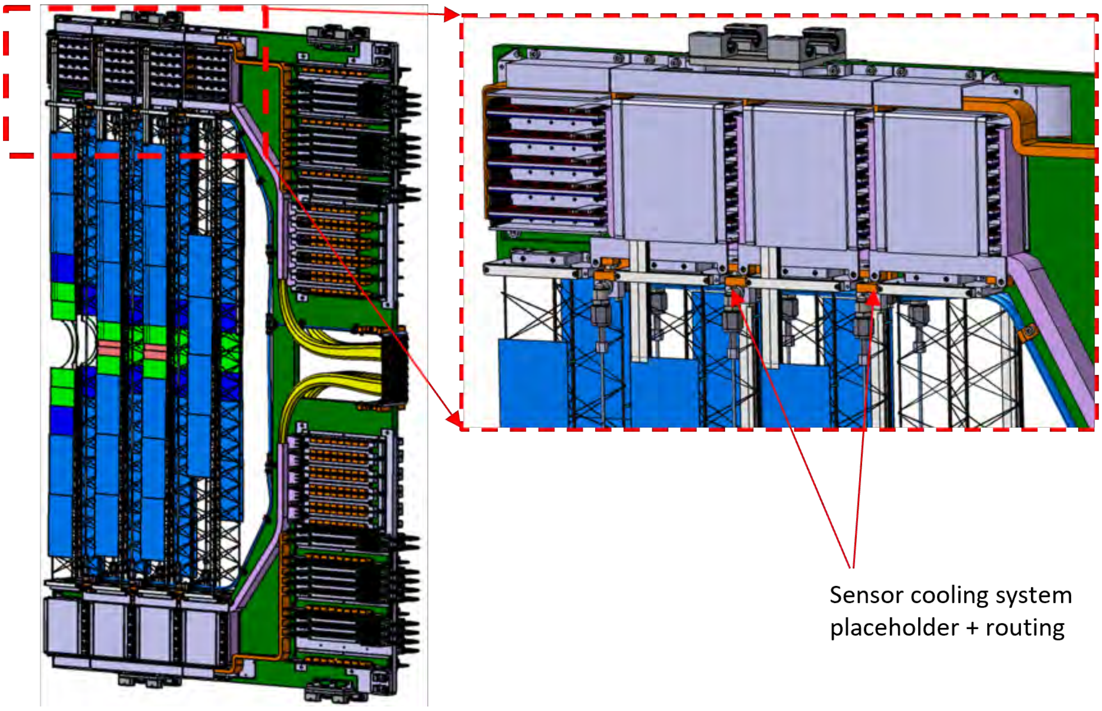

Figure 5.1.: CAD rendering of the most densely assembled C-frame with all cooling and cabling services. The call-out on the right shows a zoomed-in view of the sensor cooling implementation on this critical C-frame (figure from O. Vasylyev (GSI, Darmstadt)).

and *FEB Cooling Block 4* caters to a maximum of eight FEB Boxes (four per side). Given the vertical symmetry of the detector, each FEB cooling block has to be mirrored. Based on these specifications, final series production of the FEB cooling plates, including detailed CFD simulations, has been tendered to Cool Tec (see Fig. 5.2 for the proposed design).

(c) Read-Out and Power Board Electronics Cooling: The R&D for bi-phase CO_2 and its press-fitted cooling plates were not pursued further in favour of 3M™ NOVEC™ 649 and friction-stir welded cooling plates for FEE cooling. Despite that, the R&D and industrial collaborations with Cool Tec for the press-fitted cooling plates were used to design the ROB-POB cooling plates with 3M™ NOVEC™ 649. The cooling plates manufactured with press-fitted cooling channels were deemed to provide sufficient cooling for ROB-POB cooling because of their relaxed cooling requirements since their power density is roughly half of that of FEE cooling. Although the number of ROBs and POBs vary for every STS station, only one ROB-POB cooling plate variant was designed to accommodate the varying requirements. Given the vertical symmetry of the detector, the ROB-POB cooling plate has to be mirrored. Based on these specifications, final series production of the ROB-POB cooling plates, including detailed CFD simulations, has been tendered to Cool Tec (see Fig. 5.3 for the proposed design).

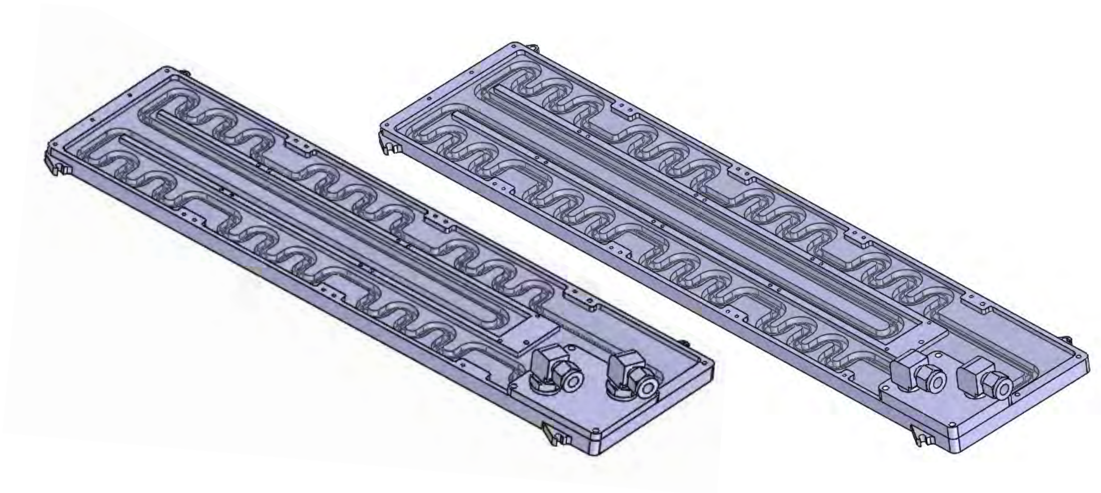

Figure 5.2.: CAD rendering of different versions of FEB Cooling Blocks for the final STS, as proposed by Cool Tec. The transparency of the cover plate is adjusted to see the underlying channels in the base plate. The left design is for the type *FEB Cooling Block 3*, while the right design is for the type *FEB Cooling Block 4* (figure from O. Vasylyev (GSI Darmstadt) and Cool Tec GmbH).

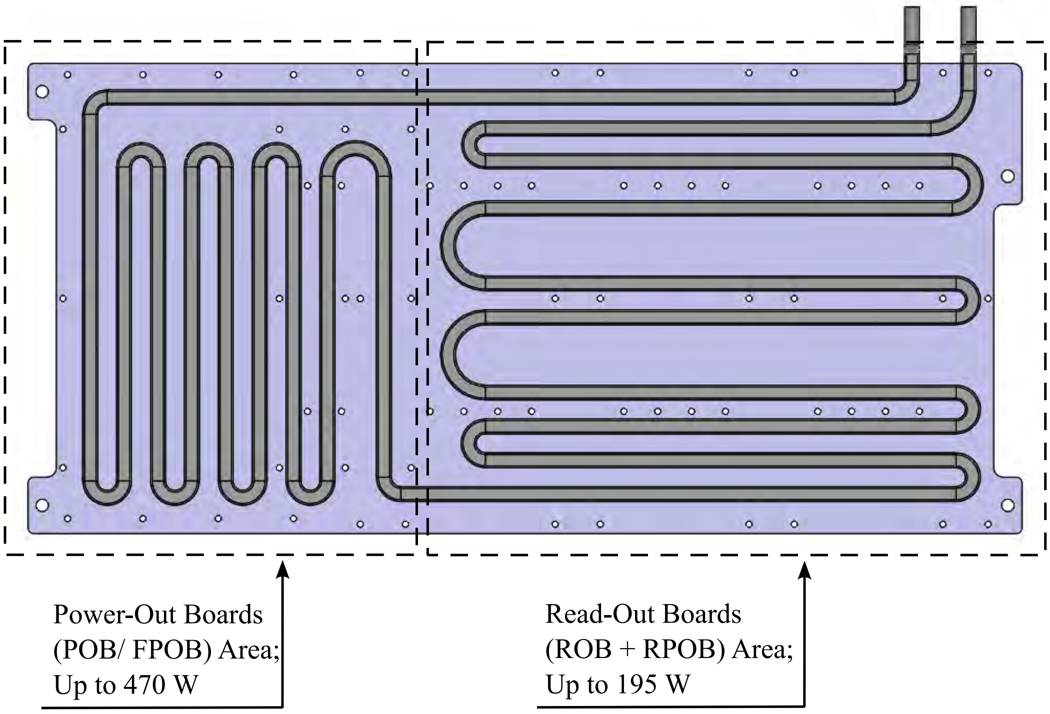

Figure 5.3.: CAD rendering of the ROB-POB Cooling Block for the final STS, as proposed by Cool Tec. The press-fitted pipe is made of steel, while the base plate is made of aluminium (figure from O. Vasylyev (GSI Darmstadt) and Cool Tec GmbH).

5.2. STS Module Assembly

The thermal interface between the FEBs and T-shelf is thermally critical due the high temperature rise across this interface (see Sec. 2.2.1 and Fig. 2.23), while its mechanically critical because of the fragile handling nature of the module. The thermal dummy modules assembled for the Thermal Demonstrator (see Sec. 3.2.3) represented the first opportunity to test the application procedure of the respective thermal interface material (STYCAST 2850FT/Catalyst 23LV). These experiences were further used and refined to finalise the gluing procedure and design the underlying jigs for assembling the final STS modules (see Fig. 5.4). At the time of writing, more than 160 modules (about 18% of the total) have been assembled based on this procedure [234]. More information about the selection, characterisation and application of the chosen glue is available in [190, 192].

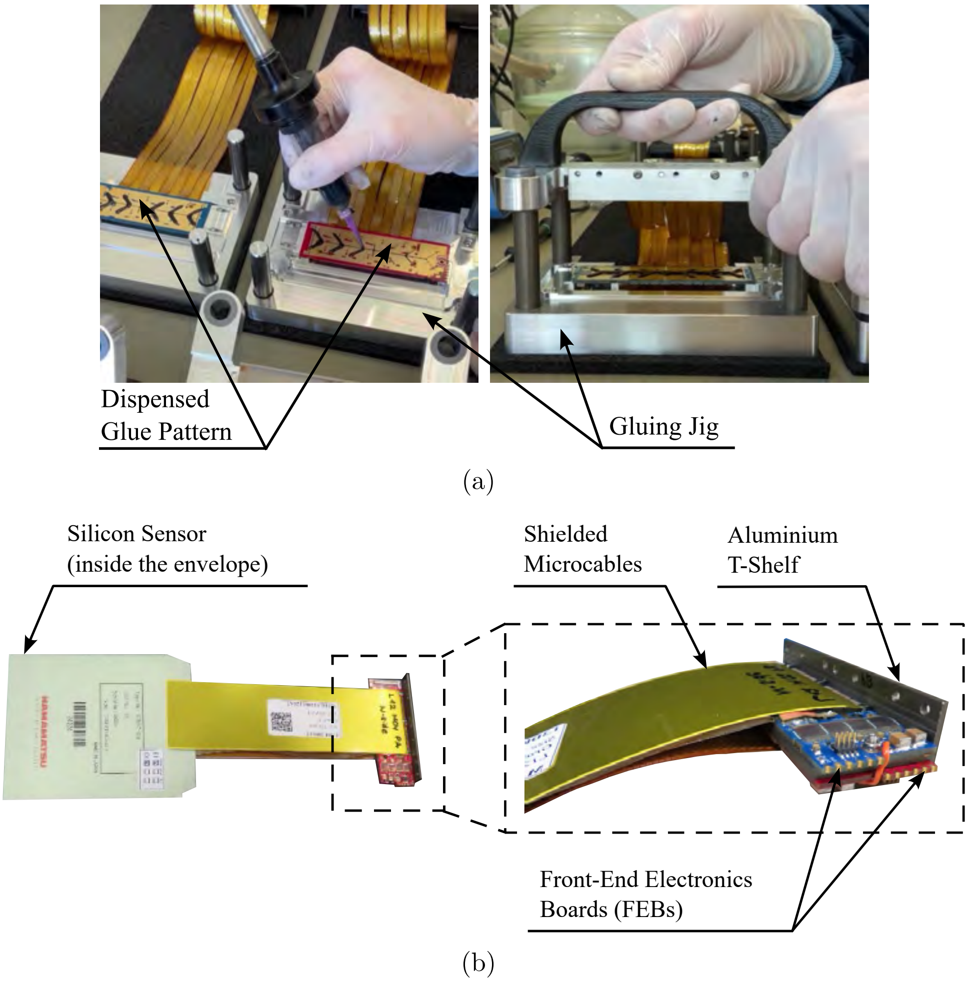

Figure 5.4.: (a) Gluing procedure with the final STS modules (figures from O. Bertini (GSI Darmstadt)). (b) Resulting thermal interface on the first-of-series modules (figures from C.J. Schmidt (GSI Darmstadt)).

5.3. Thermal Enclosure and Services

The STS thermal enclosure is complex due to the threefold requirements on thermal insulation, electromagnetic isolation, and mechanical stability (see Sec. 3.3.1 for requirements and concept). The STS Thermal Demonstrator's enclosure provided solutions to the thermal aspects under realistic mechanical boundary conditions. This specifically included the production feasibility of CF-foam sandwich panels, featuring AIREX® R82.60, in collaboration with the industrial partner on this project - CarbonVision[2]. Moreover, the low humidity observed within the STS Thermal Demonstrator's enclosure (dew point <-45°C) also validated the near-hermetic nature of the integration concept of the panels (see Sec. 3.3.2) and feedthroughs for cables and (Roxtec EzEntry™ cable entry seals[3] for cables and custom-designed feedthroughs for 3M™ NOVEC™ 649; see Sec. 3.3.3). Based on these experiences, the STS thermal enclosure has been detailed in the CAD drawings Fig. 5.5. Furthermore, the final production of panels, including the respective mechanical simulations, have been tendered to CarbonVision.

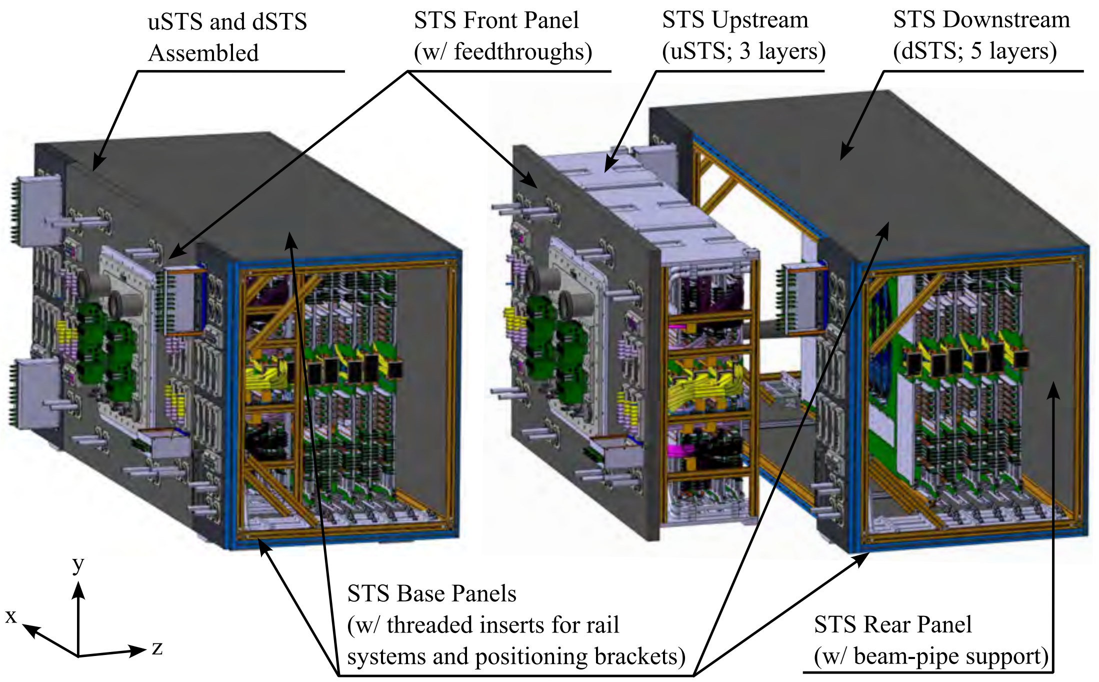

Figure 5.5.: CAD renderings of the STS thermal enclosure: assembled (left) and separated (right). The side walls and cables are hidden for clarity (figures from O. Vasylyev (GSI Darmstadt)).

2. CarbonVision GmbH, Germany - www.carbonvision.de
3. Roxtec EzEntry™ - www.roxtec.com/en/products/solutions/roxtec-ezentry

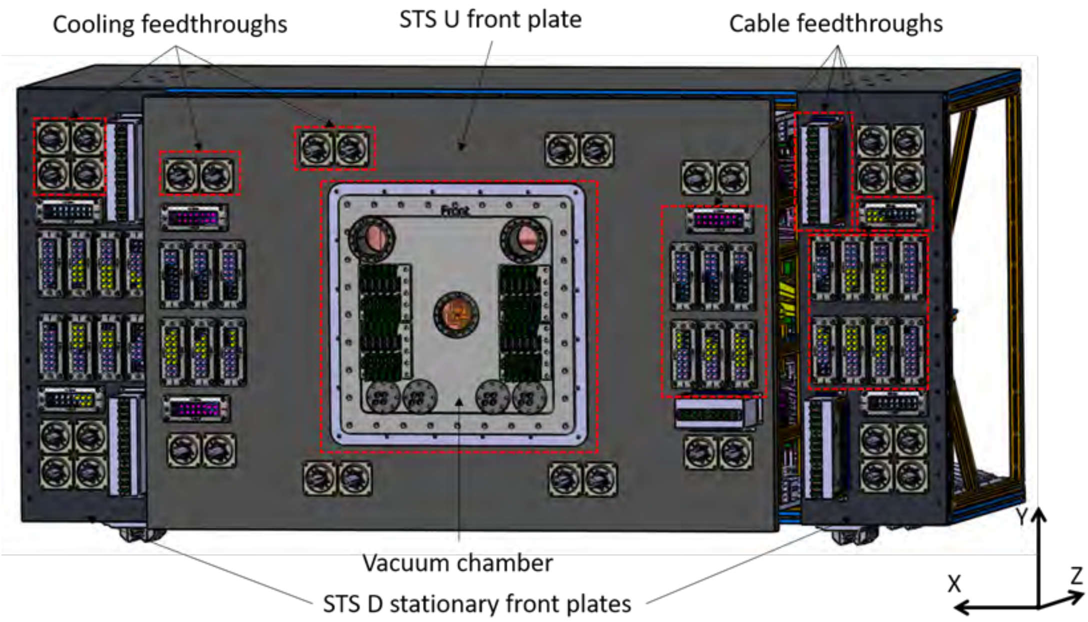

Figure 5.6.: CAD rendering of the front panel of the STS thermal enclosure with all comprising feedthroughs (figure from O. Vasylyev (GSI Darmstadt)).

5.4. Environmental Monitoring

The STS Thermal Demonstrator used temperature (see Sec. 3.4.1) and humidity sensors (see Sec. 3.4.2) to obtain operational experience with these sensing elements and their respective readout. This allows for these learnings to be extrapolated to final STS operation. Commercial digital sensors like DS18B20 temperature and IST HYT-221 humidity sensor are foreseen to be used as a reference during the commissioning phase. Their use for the entirety of the STS's lifetime is limited due to their susceptibility to radiation and magnetic field. During the STS operation, the baseline option for temperature sensing are the Pt-100 temperature sensors and temperature sensing fibre-optic arrays. Moreover, the humidity monitoring will be provided by the sniffing-tube system and hygrometer-type fibre-optics sensors. The Thermal Demonstrator has provided information about their long-distance integration and handling issues, such as bending, for the final STS. It's worth mentioning that all these sensors have been individually characterised with the final EPICS-based Detector Control System (DCS) software in [228, 229].

5.5. Cooling Plants

(a) Silicon Sensor Cooling: The final STS air drying and cooling plant aims to draw from the experiences of the pilot AHS for the Thermal Demonstrator and from the currently operational ventilation system of the ALICE ITS2 [235]. A preliminary proposal made by our industrial partner[4] utilises adsorption dehumidifier (desiccant wheel) together with built-in direct expansion cooling system to supply dry and cold air with -38°C dew point and -20°C, respectively.

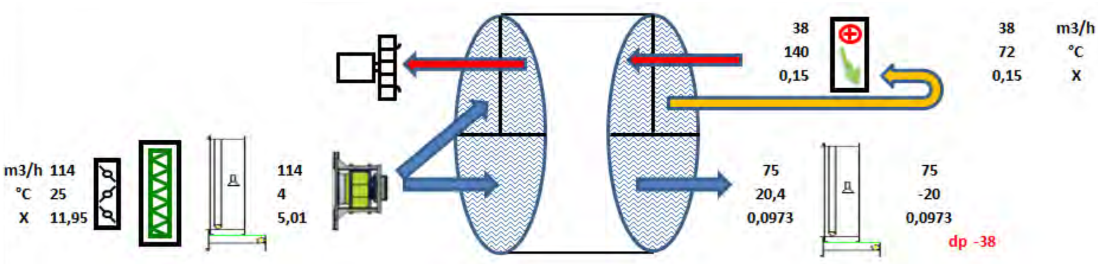

Figure 5.7.: Process flow diagram of the Air Handling System for the final STS. Call-out columns are labelled as the flowrate, air temperature and moisture content, respectively (figure from SAMP S.p.A.).

(b) Electronics Cooling: Experiences from the pilot cooling plant inform the design of a larger 50 kW cooling plant for the final STS (see Fig. 5.8 and Tab. 5.1). The secondary loop with 3M™ NOVEC™ 649 is cooled by CO_2 refrigeration system and comprises similar components, such as the centrifugal pump, accumulator and expansion tank, filter-dryer, and balancing heater. Notably, circulation pumps are positioned in the CBM experimental hall (*E10 level*) to reduce static pressure within the STS, while other cooling plant components are located on the *E30 level*, 10 meters above.

Parameter	Value
Refrigerant - Primary Loop	CO_2 (R744)
Refrigerant - Secondary Loop	3M™ NOVEC™ 649
Cooling Capacity - Nominal (+20% margin)	50 kW
Cooling Capacity - Partial (+20% margin)	23 kW
Coolant Temperature - Nominal Outlet (-2.5 K margin)	-22.5°C
Coolant Temperature - Nominal Inlet (+2.5 K margin)	-11.5°C
Flow Rate (+10% margin)	20 m^3/h
Pressure Difference (+20% margin)	2.7 bar
Static Pressure (Secondary Loop) - Standby Mode	0.9 bar
Static Pressure (Secondary Loop) - Operation	0.2 bar
Electric Power Range - Balancing Heater	50 kW

Table 5.1.: Basic specifications of the 3M™ NOVEC™ 649 final cooling plant [177].

4. SAMP S.p.A. - `www.samp-spa.com`

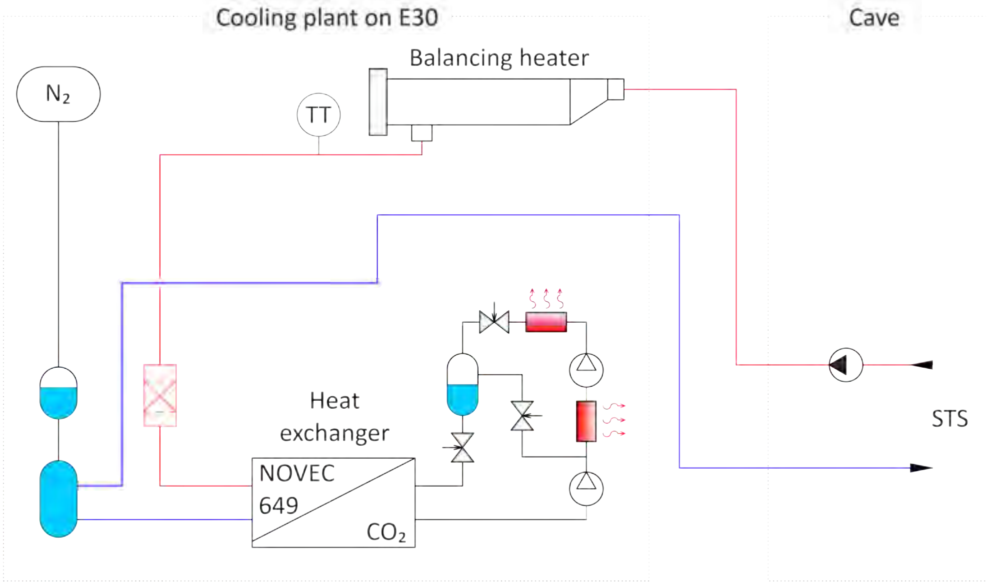

(a)

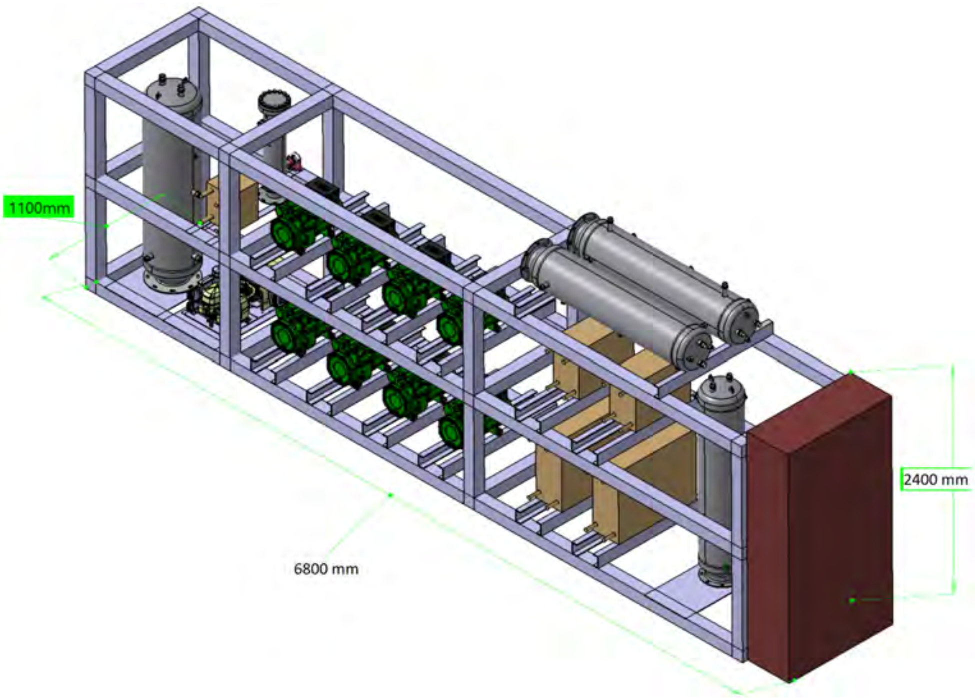

(b)

Figure 5.8.: (a) Process flow diagram of the 3M™ NOVEC™ 649 final cooling plant. The centrifugal pump is located in a different part of the CBM building, inside the experiment cave to minimise the static pressure within the STS detector. (b) CAD rendering of the 3M™ NOVEC™ 649 final cooling plant (figures from [177]).

6. Conclusions

This thesis focusses on the critical challenge of thermal management of the Silicon Tracking System (STS) of the Compressed Baryonic Matter (CBM) experiment at the Facility for Antiproton and Ion Research (FAIR). The cooling requirements are especially unique, as STS silicon sensors require cooling with a minimal material budget to negate adverse radiation effects (up to $10^{14}n_{eq}(1\text{ MeV})/\text{cm}^2$), while the front-end electronics located peripherally outside the STS's physics acceptance dissipate up to 40 kW of power within a 3.5 m^3 detector volume. Therefore, a stable sensor operating temperature of $\approx 10°\text{C}$ must be maintained for an optimal signal-to-noise ratio (S/N $\gtrsim$ 10) and to avoid reverse annealing (full depletion voltage $V_{dep} < 500$ V), while inhibiting thermal runaway and neutralising the electronics' power dissipation. The subsequent paragraphs summarise the key findings and provide potential future research directions.

6.1. Summary of Key Findings

The CBM-STS operating temperature was inferred based on the irradiation behaviour of STS prototype silicon sensors and modules, using the *Hamburg Model* by considering parameters like full-depletion voltage, leakage current, and signal-to-noise ratio. To fulfil these requirements, the cooling concept of the CBM-STS was developed through a multipronged approach, including theoretical calculations using well-established semi-empirical correlations and commercially available numerical simulation tools. Based on this, an extensive experimental campaign was conducted to verify these concepts by building a thermal prototype – *CBM-STS Thermal Demonstrator* – using prototype and pre-production STS components under realistic operating and mechanical boundary conditions. Collectively, this resulted in an innovative cooling concept of *Liquid Assisted Air Cooling*, and has established collaborations with industrial partners to accelerate the transition of the CBM-STS towards detector production. The specific conclusions are as follows.

Multi-Parameter Determination of the CBM-STS Sensor Temperature Requirement

The operating temperature of the CBM-STS sensors was estimated by calculating the temperature and fluence dependence of the STS electrical operating parameters. This involved developing a calculation framework that combined models describing the sensor leakage current, sensor full depletion voltage, and module noise performance. These models were derived previously from extensive experimental studies using prototype and pre-production components. As a result of this framework, it was found that the STS sensors could be operated at temperatures as high as +10°C at the end-of-lifetime fluence of $10^{14}n_{eq}(1\ \text{MeV})/\text{cm}^2$, while still fulfil the criteria to obtain $S/N \gtrsim 10$ and $V_{dep} < 500$ V. This marked a significant improvement in the STS sensor operating conditions, which were initially estimated to be around $\lesssim -5$°C.

Development of the CBM-STS Cooling Concept via Calculations and Simulations

Silicon Sensors - Air Cooling: As the CBM-STS is designed as a forward spectrometer, most non-ionising radiation and resulting sensor power dissipation are concentrated on the innermost silicon sensors of every tracking layer/station ($\Delta x = \Delta y \leq \pm$ 10 cm). Therefore, the innermost sensors are cooled by forced air convection via impinging jets from custom-designed perforated carbon-fibre tubes, while the peripheral sensors are cooled by natural convection. This hybrid solution is not only technically feasible, but also minimises the additional material budget within the STS's physics acceptance. The underlying design and operating conditions were first theoretically calculated by using semi-empirical correlations. The thermal performance of these solutions was further studied by using the Computational Fluid Dynamics (CFD) simulations package from SolidWorks® for specific ladder types to address certain worst-case scenarios. Although some discrepancies were observed between calculations and simulations, collectively it was inferred that the air temperature of $\lesssim$ 0°C (and flow rate rate of 20 ...40 L/min for the ladders cooled with perforated tubes) is sufficient to prevent sensors' thermal runaway throughout the STS operational lifetime.

Front-End Electronics (FEE) - Liquid Cooling: The FEE cooling is designed to minimise the temperature gradient and heat transfer between the innermost silicon sensors and the FEE, located peripherally only 25 ... 50 cm away, keeping the maximum FEE temperature at $\approx$ 10°C. The FEE boards (FEBs) are enclosed within a modular yet thermally conductive FEB box, designed to minimise thermal impedance from the heat-dissipating read-out ASICs and LDO regulators to the underlying heat sink. The thermal performance of the FEB box was studied using thermal Finite Element Analysis (FEA) in SolidWorks®. The heat sink is manufactured using friction-stir welding technology to enhance heat transfer between the fluidic channels and the mono-phase liquid 3M™ NOVEC™ 649 ($C_6F_{12}O$) at −30°C. This coolant offers great advantages in terms of wide operating temperature range, radiation resistance, a sufficiently high heat transfer coefficient, simpler design and commercial manufacturability, and low carbon footprint. Realistic temperature distributions across the heat sink surface were evaluated by using the CFD package from SolidWorks®. Note that biphase CO_2

was the initial choice for the FEE coolant for which novel simulation tool was developed. Therein, empirical correlations solved in MATLAB® were coupled with thermal FEA in SolidWorks® to estimate two-phase flow boiling heat-transfer and temperature distribution over the entire cooling plate. However, mono-phase 3M™ NOVEC™ 649 was eventually chosen as the primary choice of coolant due to its easier implementation compared to the high-pressure and complex bi-phase systems. This thesis presents a systematic comparison between bi-phase CO_2 and mono-phase 3M™NOVEC™649 in their respective cooling plates technologies and refrigeration cycles, using numerical simulations under comparable boundary conditions.

Experimental Verification of the CBM-STS Cooling Concept with the Thermal Demonstrator

Experimental Setup - CBM-STS Thermal Demonstrator: This setup was designed to verify the cooling concepts under realistic boundary conditions, and was commissioned at the GSI Helmholtz Centre for Heavy Ion Research in Darmstadt. It comprised prototype sensor and FEE cooling elements, and 50 silicon sensor modules distributed across a thermally "active" half-station to mimic the heat production of both silicon sensors and FEBs. The setup was housed in a carbon fiber-foam sandwich-based thermal enclosure, providing sufficient thermal insulation while validating the near-hermetic nature of the integration concept of the comprising panels and feedthroughs. Furthermore, a granular temperature and humidity distribution across the enclosure's volume was monitored using various sensors, including commercially available digital sensors, Pt-100 temperature sensors, sniffing-tube systems, and custom-made fibre-optics hygrometer sensors. The cooling requirements for both silicon sensor and FEE were met by the respective custom-designed pilot cooling plants. The Air Handling System (AHS) supplied cold and dry air to the Thermal Demonstrator, while the FEE were cooled by mono-phase liquid 3M™ NOVEC™ 649 (in the secondary loop) cooled by bi-phase CO_2 (in the primary loop). The underlying readout and data-acquisition system was based on LabVIEW, involving various devices and readout hardware sourced from Arduino and National Instruments™.

Measurements and Results: A series of experiments with the CBM-STS Thermal Demonstrator systematically evaluated the cooling of both silicon sensors and front-end electronics. The silicon sensor cooling concept was assessed on its ability to prevent thermal runaway after accumulated fluences corresponding to 10 years (0.24×10^{14}n$_{eq}$(1 MeV)/cm^2) and end-of-lifetime (1×10^{14}n$_{eq}$(1 MeV)/cm^2) detector operation, while neutralising the maximum FEE power dissipation of 12.93 W per FEB (totalling ≈1.4 kW for the entire setup). The baseline operational parameters (−20 °C 3M™ Novec™ 649 temperature and 30 L/min air flow rate) were derived from numerical simulations and further adjusted to address adverse cooling effects, such as silicon sensor vibration due to air flow and thermal stress on FEB wire-bonds due to coolant temperature and FEB power cycling. Additionally, the interaction between the silicon sensors and the front-end electronics was studied. Stable sensor temperatures (T_{Stable}) of 12.6 °C and 18.9 °C are observed for the hottest sensor dummy for power dissipation corresponding to the 10 years and end-of-lifetime operating scenarios, respectively, while maintaining sufficient margins from thermal runaway. Overall, it can be seen that $T_{Sensor} \approx 10\,°C$ can be maintained after 10 years of operation with the baseline parameters, while the 3M$^{\text{TM}}$ Novec$^{\text{TM}}$ 649 inlet temperature can be lowered to obtain $T_{Sensor} \leq 10°C$ for longer detector operation up to end-of-lifetime fluence. Comprehensive studies were also conducted to understand the dependencies of the CBM-STS cooling concept on various operational parameters, providing a holistic understanding. As a result, these experiments helped verify the baseline operational parameters and the underlying margins essential for long-term, reliable operation of the CBM-STS.

Accelerating the Transition of the CBM-STS from Concept to Production Stage

The insights gained from the CBM-STS Thermal Demonstrator have been pivotal in determining the operating parameters for STS cooling and in shaping component choices and integration processes for the final STS, resulting in a detailed detector design in early 2024. This includes the tendering of the FEE cooling elements and thermal enclosure panels to the same companies as those for the Thermal Demonstrator. Moreover, the thermal dummy modules assembled for the Thermal Demonstrator provided the first opportunity to test the application procedure of the critical thermal interface material between the FEBs and T-shelves. These experiences were crucial for finalising the gluing procedure, which has since been used for the assembly of more than 160 modules (about 18% of the total) since fall 2023. Furthermore,the lessons learned from the pilot cooling plants have been essential in drafting the specifications for the final STS cooling plants. Collectively, this has resulted in the timely procurement of mechanical components for system integration in 2024-25, with the STS installation expected to be ready for the CBM experimental hall in 2026.

6.2. Outlook on Potential Future R&D

Although the CBM-STS cooling concept has been thoroughly developed, experimentally verified, and successfully translated into production-ready solutions, there remain several potential future directions where further R&D can be carried out to better understand and optimise the CBM-STS cooling. Some of them are highlighted as follows:

Numerical simulations for silicon sensor cooling: In this work, a notable disagreement was observed between CFD simulations and calculations for silicon sensors cooled by forced convection, while there was agreement for those cooled by natural convection. To address this discrepancy, a careful validation of CFD models with experimental data, along with accurate geometry modelling and mesh refining is needed. This effort has already been initiated by performing more elaborate set of CFD simulations using OpenFOAM®. They aim to perform conjugate heat transfer simulations between silicon sensors and front-end electronics to consider all complex interactions by utilising GSI's high performing computing (HPC) facility – GSI VIRGO Cluster.

Long-term alternative to 3M™ NOVEC™ 649: Despite the fact that 3M™ NOVEC™ 649 has a global warming potential (GWP) of 1, i.e., it contributes to global warming at the same rate as an equivalent mass of CO_2, 3M will discontinue its manufacturing, along with its entire portfolio of per- and polyfluoroalkyl substance (PFAS) substances (also known as *Forever Chemicals*). This situation makes 3M™ NOVEC™ 649 increasingly difficult to obtain due to higher than usual costs and longer wait times. Although this problem could be temporarily mitigated by procuring equivalent alternatives from the market as the patent ended on 19.07.2020, the European Chemicals Agency (ECHA) has proposed to heavily restrict PFAS usage in February 2023 due to their toxicity and environmental persistence. In light of this, the CBM-STS team has opted for a two-way strategy: (i) procuring an equivalent to 3M™ NOVEC™ 649 from alternative suppliers while applying for an exemption from ECHA, and (ii) exploring the use of water-ethylene glycol mixture as an alternative to 3M™ NOVEC™ 649. The latter has been initiated by tendering the FEE cooling plates compatible with both 3M™ NOVEC™ 649 and water-ethylene glycol mixture (50% v/v), while using the same friction-stir welded technology used in the Thermal Demonstrator. This can be further investigated by experimentally comparing the cooling performance of these two coolants. Moreover, based on these studies, the technical specifications of the FEE cooling plant for the final STS can be modified to allow the use of water-ethylene glycol mixture as a drop-in replacement of 3M™ NOVEC™ 649.

Appendix A.

STS's FLUKA Non-Ionising Fluence Distribution

The canonical end-of-lifetime of STS-type silicon sensors is assumed to occur at an accumulated fluence greater than $10^{14} n_{eq}(1 \text{ MeV})/\text{cm}^2$. This has been verified as a lower limit for the operation of the sensors in a series of irradiation campaigns [170–172]. Based on FLUKA calculations, this fluence is expected to be accumulated during 10 years of CBM operation [35] (see Fig. A.1). However, this is a gross overestimate of the accumulated fluence, as the corresponding interaction rates, colliding systems and beam energies are an upper limit.

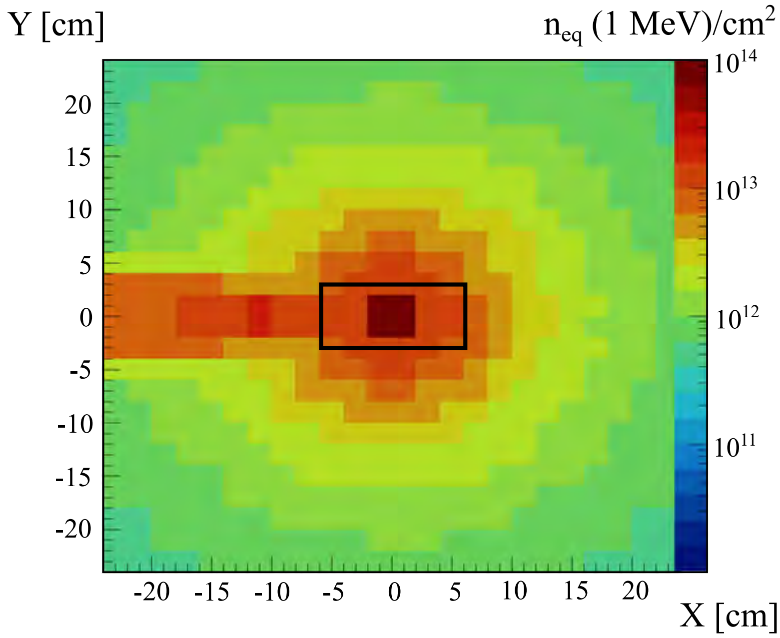

Figure A.1.: FLUKA simulations showing the fluence distribution for the first STS station located 30 cm downstream from the target. Calculations are for a 1-year running scenario (2 month/year) with maximum beam intensity (10^9 Au-ions/s on a 1% Au-target) and maximum beam energy (12A GeV). Please note that the black rectangle represents the beam opening and the highest on-sensor value corresponds to $\approx 1\times10^{14} n_{eq}(1 \text{ MeV})/\text{cm}^2$ (figure from [174]).

Year	CBM Setup	Colliding System	Beam Energies [A GeV]	Days on Target	Number of Events	Remarks
0	Electron-Hadron	Au + Au	2, 4, 6, 8, 10, 12	60 (total)		Commissioning
		Ag + Ag	2, 4, 6, 8, 10, 12			Commissioning
		C + C	2, 4, 6, 8, 10, 12			Commissioning
1	Electron-Hadron	Au + Au	2, 4, 6, 8, 10, 12	30 (5 each)	2×10^{10} each	EB + minBias
		C + C	2, 4, 6, 8, 10, 12	18 (3 each)	4×10^{10} each	minBias
		p + Be	3, 4, 8, 29	12 (3 each)	2×10^{11} each	minBias
2	Muon	Au + Au	2, 4, 6, 8, 10, 12	30 (5 each)	2×10^{11} each	minBias
		C + C	2, 4, 6, 8, 10, 12	18 (3 each)	4×10^{11} each	minBias
		p + Be	3, 4, 8, 29	12 (3 each)	2×10^{12} each	minBias
3	Hadron	Au + Au	2, 4, 6, 8, 10, 12	12 (2 each)	4×10^{11} each	EB + Selector(s)
	Hadron	C + C	2, 4, 6, 8, 10, 12	6 (1 each)	8×10^{11} each	
	HADES	Ag + Ag	2, 4	28 (14 each)	1×10^{10} each	
	Electron-Hadron	Ag + Ag	2, 4	8 (4 each)	2×10^{10} each	minBias

Table A.1.: CBM running scenario for the first three years. Table compiled by N. Herrmann (U. Heidelberg). Different CBM setups/configurations are tabulated in Tab. A.2.

CBM Setup	Detector Sub-Systems							
	BMON	MVD	STS	MuCh	RICH	TRD	TOF	FSD
Electron-Hadron	✓	✓	✓		✓	✓	✓	✓
Muon	✓		✓	✓		✓	✓	✓
Hadron	✓		✓		✓	✓	✓	

Table A.2.: CBM setups and the corresponding underlying detector sub-systems [236].

Colliding System	Beam Energies [A GeV]	Beam Intensity [ions/s]					
		Electron-Hardon		Muon		Hadron	
		Baseline	Max	Baseline	Max	Baseline	Max
Au + Au	2 ... 12	5×10^6	1×10^8	5×10^7	1×10^9	1×10^8	1×10^9
C + C	2 ... 12	1×10^7	1×10^8	1×10^8	1×10^9	1×10^9	1×10^9
Ag + Ag	2 ... 4	5×10^6	1×10^8				
p + Be	3 ... 29	1×10^8	1×10^{10}	1×10^9	1×10^{11}		

Table A.3.: Maximum beam intensities for different running scenarios, including colliding systems, collision energies and experimental setups (see Tab. A.2). "Baseline" corresponds to CBM run scenario for the first three years (see Tab. A.1), where "Max" corresponds to the maximum achievable interaction rate. Table compiled from [174].

A more realistic baseline scenario is based on the current CBM running scenario for the first three years of operation for various CBM setups/configuration (see Tab. A.1 and A.2). Based on this, Tab. A.3 shows the number of events is converted to the required beam intensity by assuming a 1% target for the baseline (see Fig. A.2(a)) and maximum achievable interaction rate scenario (see Fig. A.2(b)). This gives the fluence for the innermost sensors after three years to be $0.01\times10^{14}n_{eq}(1\ \mathrm{MeV})/\mathrm{cm}^2$ and $0.1\times10^{14}n_{eq}(1\ \mathrm{MeV})/\mathrm{cm}^2$, respectively.

Therefore, the fluence accumulated over 10 years of operation is calculated by considering the baseline scenario for the first three years and the maximum interaction scenario for subsequent seven years. Cumulatively, this adds to an accumulated fluence of $0.24\times10^{14}n_{eq}(1\ \mathrm{MeV})/\mathrm{cm}^2$ for 10 years of CBM operation. So, the end-of-lifetime fluence of $10^{14}n_{eq}(1\ \mathrm{MeV})/\mathrm{cm}^2$ will be reached only after 40 years of operation. It is worth noting that this this margin would further increase because the maximum rate is likely to be an upper limit as the SIS-100 spill structure will most likely allow to operate at a rate lower by a factor of two [237].

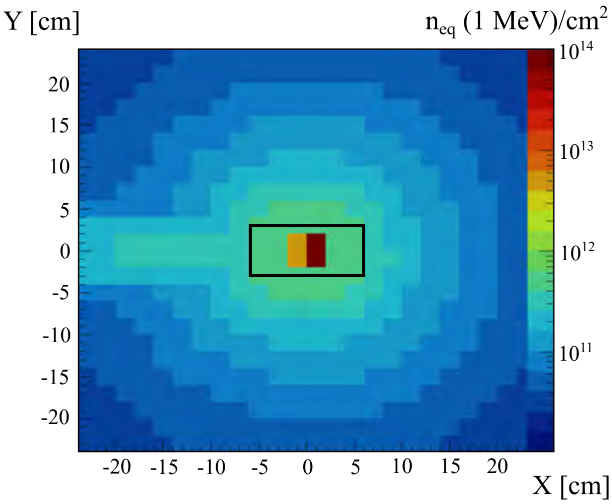

(a) Baseline Beam Intensity

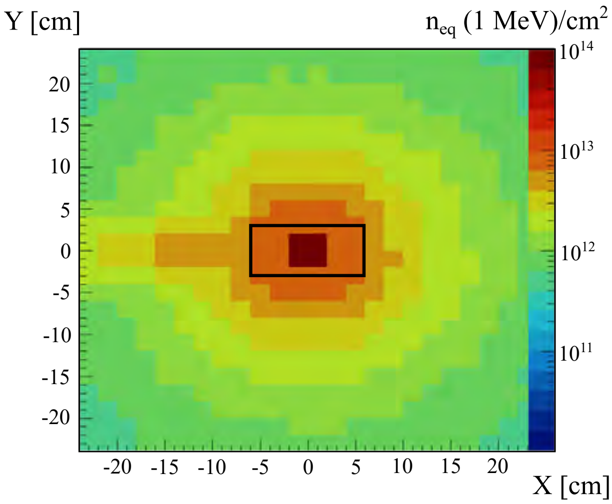

(b) Maximum Beam Intensity

Figure A.2.: FLUKA simulations showing the fluence distribution for the first STS station located 30 cm downstream from the target. Calculations are for the 3-year running scenario foreseen for CBM comprising several beam energies, projectile-target combinations, and detector configurations at (a) baseline, and (b) highest beam intensities. See Tab. A.3 for underlying beam intensities. Please note that the black rectangle represents the beam opening (figure from [174]).

Appendix B.

STS Module's Signal and Noise Behaviour

Signal-to-Noise ratio (S/N) $\geq$ 10 must be maintained for STS to provide its designed track reconstruction efficiency and momentum resolution [175]. The primary contributors to both signal and noise for STS detector modules has been extensively studied experimentally, and are described in subsequent sections.

B.1. Charge Collection Efficiency of STS Sensor

STS irradiation campaign 2018-19 was dedicated to an extensive study of the Charge Collection Efficiency (CCE) of prototype STS sensors with protons at the Irradiation Center Karlsruhe. Based on this study, it was concluded that the signal deposited in the silicon bulk can be recovered ($\gtrsim$ 95%) for up to end-of-lifetime fluence ($1{\times}10^{14}$n$_{eq}$(1 MeV)/cm^2) by raising the sensor bias voltage to 500 V (see Fig. B.1), hence not representing any concern [171, 172].

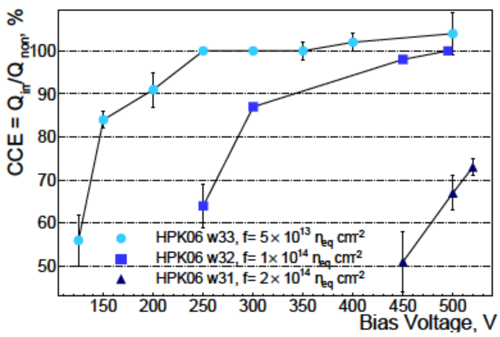

(a) HPK sensors 62 × 42 mm^2 p-side

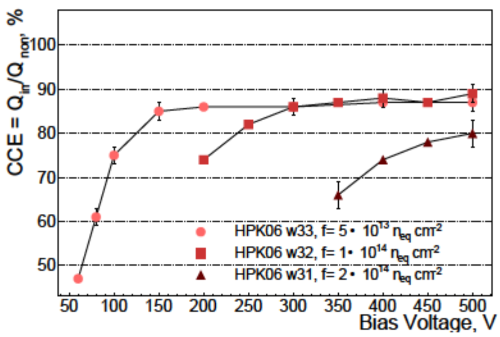

(b) HPK sensors 62 × 42 mm^2 n-side

Figure B.1.: Variation of Charge Collection Efficiency (CCE) with bias voltage for (a) p-side, and (b) n-side of differently irradiated Hamamatsu Photonics (HPK) sensors (62 × 42 mm^2) (figures from [171, 172]). Similar behaviour was also observed for other sensor dimensions and vendors (CiS Forschungsinstitut für Mikrosensorik GmbH) too.

B.2. Noise of STS Module

The noise generated by the silicon sensor module has been investigated through experimental studies and analytical modeling [238, 239]. Effort has been to understand and control the noise sources from all of module's components, namely silicon sensor, ASIC and interconnecting cable. The primary factors contributing to module's noise are the thermal noise associated with the resistive structures, the shot noise resulting from the leakage current in the detector, and the intrinsic noise of the charge-sensitive amplifier. The equivalent circuit for modelling is illustrated in Fig. B.2 and details about the experimental characterisation are in [159, 238].

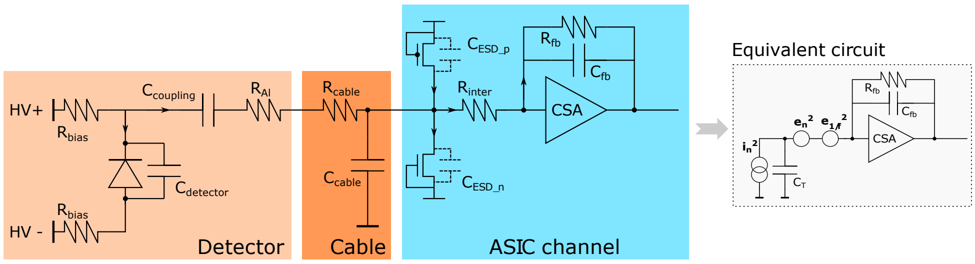

Figure B.2.: Simplified model of the noise sources in STS module (figure from [238]).

The general formulation for the Equivalent Noise Charge (ENC) is provided in terms of three distinct noise sources: current noise (ENC_i), voltage noise (ENC_e), and 1/f noise ($ENC_{1/f}$), further outlined in Eq. B.1. The typical values of the associated parameters for STS modules are tabulated in Tab. B.1.

$$ENC^2 = ENC_i^2 + ENC_e^2 + ENC_{1/f}^2 \tag{B.1a}$$

$$ENC^2 = \left(i_n^2 F_i T_s\right) + \left(e_n^2 F_v \frac{C_T^2}{T_s}\right) + \left(F_{vf} A_f C_T^2\right) \tag{B.1b}$$

$$\text{where, parallel current noise, } i_n^2 = \frac{4k_B T}{R_{bias}} + \frac{4k_B T}{R_{fb}} + 2eI_{leakage} + 2eI_{ESD_n} + 2eI_{ESD_p} \tag{B.1c}$$

$$\text{series voltage noise, } e_n^2 = 4k_B T R_{Al} + 4k_B T R_{cable} + 4k_B T R_{inter} + \frac{\alpha\gamma}{g_m} \tag{B.1d}$$

$$\text{total capacitance, } C_T = C_{sensor} + C_{microcable} \tag{B.1e}$$

The described analytical estimation of noise allows one to estimate the noise behaviour within ±20% of the experimental measurements (see Fig. B.3).

Parameter	Typical Value
Biasing Resistor, R_{bias}	1 MΩ
Feedback Resistor (n-side), R_{fb_n}	12 MΩ
Feedback Resistor (p-side), R_{fb_p}	22 MΩ
Sensor Leakage Current (20°C; non-irradiated sensor), $I_{leakage}$	4 nA
ESD Current (n/p-side), $I_{ESD_{n/p}}$	1 nA
Resistance of Aluminium Traces, R_{Al}	10.5 MΩ/cm
Resistance of Microcables, R_{cable}	0.6 MΩ/cm
Interstrip Resistance, R_{inter}	12.7 MΩ
CSA Properties, α, γ, g_m	0.5, 1, 0.044 A/V
Capacitance of Sensor, C_{sensor}	1.02 pF/cm
Capacitance of Microcables, C_{cable}	0.38 pF/cm
Shaping Characteristic Time, T_s	90 ns
CR-(RC)^2 Shaper Properties, F_i, F_v, F_{vf}	0.64, 0.85, 3.41
Flicker Noise Constant, A_f	9.4×10^{-12} C^2/F^2

Table B.1.: Parameters of the contributors to noise components along with their typical values (values from [239], as communicated by A. R. Rodriguez (GSI, Darmstadt)).

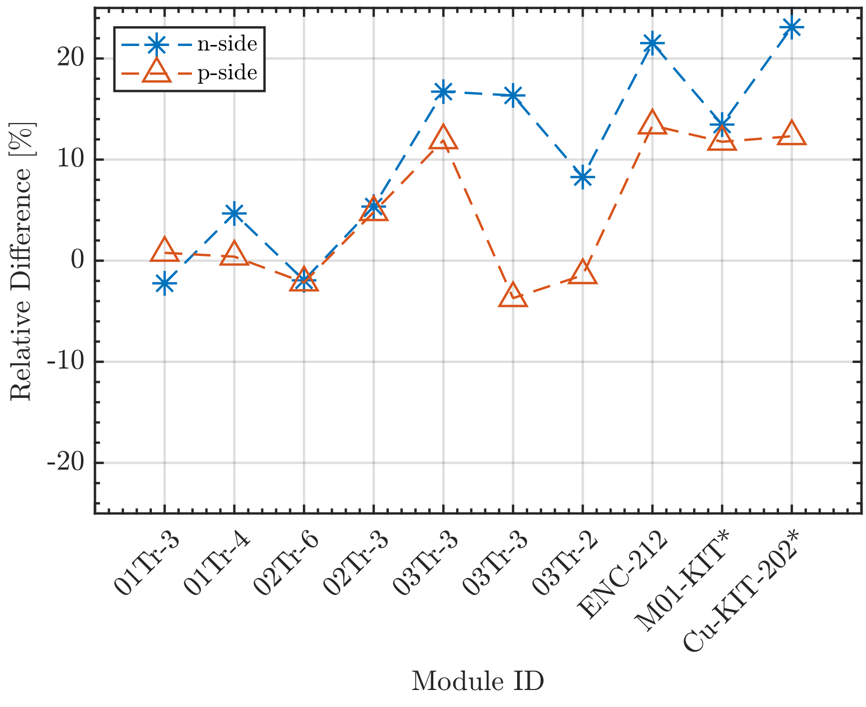

Figure B.3.: Relative difference between the simplified ENC model (see Fig. B.2) and measurements (with reference to measurements) for the various modules produced (figure from [239], as communicated by A. R. Rodriguez (GSI, Darmstadt)).

Appendix C.

STS Sensor's Full Depletion Voltage Evolution

The evolution of the full depletion voltage (V_{dep}) for STS miniature sensors has been experimentally studied [170] to parameterise the annealing time constants using the "Hamburg Model" [39] (also briefly introduced in Sec. 1.1.1) (see Fig. C.1). The underlying damage contributions are heavily time and temperature dependent (see Eq. 1.2), and are detailed in Eq. C.1. The deduced parameters from the fit are tabulated in Tab. C.1.

$$\text{Stable Damage } \Delta N_C = \eta N_d \left(1 - e^{-c\Phi}\right) + g_c \phi \tag{C.1a}$$

$$\text{Annealing Term } \Delta N_A = g_A \Phi e^{-t/\tau_A};\ \frac{1}{\tau_A} = k_{0A} e^{-E_A/kT} \tag{C.1b}$$

$$\text{Reverse Annealing Term } \Delta N_Y = g_Y \Phi \left(1 - \frac{1}{1 + t/\tau_Y}\right);\ \frac{1}{\tau_Y} = k_{0Y} e^{-E_Y/kT} \tag{C.1c}$$

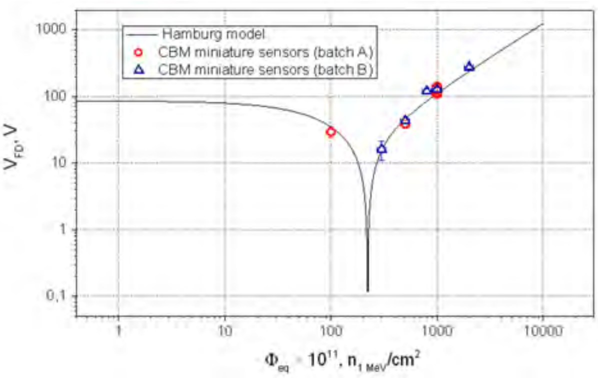

(a)

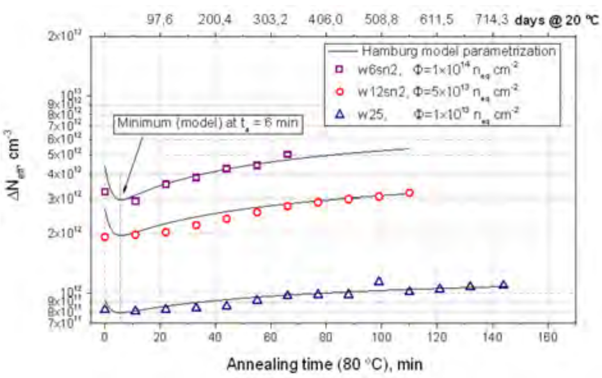

(b)

Figure C.1.: (a) Fluence dependence of full depletion voltage, and (b) time dependence of change of effective doping concentration at various fluences, for smaller STS-type prototype sensors (2014-15 irradiation campaign; figures from [170]).

Parameter	Typical Value
Initial Doping Concentration, N_d	1.34×10^{12} cm^{-3}
Sensor Thickness, d	320 µm
Fraction of Initial Donor Removal, η	0.8
Initial Donor Removal Constant, c	8.2×10^{-14} cm^{-1}
Acceptor Creation Prefactor, g_c	1.9×10^{-2} cm^{-1}
Annealing Term Prefactor, g_A	1.81×10^{-2} cm^{-1}
Annealing Time Constant Prefactor, k_{0A}	2.4×10^{13} s^{-1}
Activation Energy, E_A	1.09 eV
Reverse Annealing Term Prefactor, g_Y	5.16×10^{-2} cm^{-1}
Reverse Annealing Time Constant Prefactor, k_{0Y}	7.4×10^{14} s^{-1}
Activation Energy, E_Y	1.31 eV

Table C.1.: STS sensor properties and Hamburg Model parameters extracted for STS miniature sensors (2014-15 irradiation campaign; values from [170]).

Appendix D.

STS Sensor's Leakage Current at End-of-Lifetime

The leakage current, and thereby power dissipation behaviour of STS sensors at their end-of-lifetime fluence is estimated by stitching together estimates from the Hamburg Model and previous irradiation campaigns with smaller STS-type prototype sensors from 2014-15 and 2018-19, respectively. All estimates were found to be consistent with each other and result in sensor power dissipation values of maximum 53.4 mW/cm^2 at +10°C at 10^{14}n$_{eq}$(1 MeV)/cm^2.

D.1. Hamburg Model Expectations

The damages in the lattice structure of the silicon bulk by non-ionising fluence and their influence on sensor's performance are described by the "Hamburg Model" [39] (also briefly introduced in Sec. 1.1.1). This leads to temperature-dependent changes in sensor's global properties within rising fluence, such as its Leakage Current ($I_{Leakage}$), as shown in Eq. 1.1. Assuming the highest damage coefficient (α) of 7 $\times 10^{17}$ A/cm, for a 320 µm thick sensor irradiated at Φ_{eq} of 1×10^{14}n$_{eq}$(1 MeV)/cm^2, the leakage current and power surface density is approximately 224 µA/cm^2 and 112 mW/cm^2, respectively at +20°C and 500 V[1]. This corresponds to power dissipation of less than 7 mW/cm^2 at -10°C.

D.2. STS Irradiation Campaign 2014-15

Irradiation studies with neutrons were performed at the Jozef Stefan Institute in Ljubljana, Slovenia, with reactor neutrons from the TRIGA type nuclear reactor. Prototype sensors (1.2 × 1.2 cm^2; 290 µm thick) from CiS were fabricated with the same wafers as the CBM05 prototype sensors. Properties of the irradiated sensors along with their IDs are summarised in Tab. D.1. Additionally, the leakage

1. In Eq. 1.1a, the initial leakage current of the sensor plays a negligible role as the post-irradiation leakage current is completely driven by the factor ($\alpha \cdot \Phi_{eq} \cdot d$). Nevertheless, based on the electrical inspection of 1200 STS sensors, the pre-irradiation leakage at +20°C and 500 V is less than 0.04 µA/cm^2.

current variation with bias voltage of these irradiated sensors at -5°C is shown in Fig. D.1. Further details of this irradiation campaign along with measurement details are mentioned in [170]. Given that the end-of-lifetime fluence expected for STS sensors is $1{\times}10^{14}$n$_{eq}$(1 MeV)/cm^2, the prototype sensors *w1sn2* and *w2sn1* are considered (see sensors highlighted in yellow in Tab. D.1). Therefore, the corresponding leakage current measured at -5°C and 500 V is approximately 20 µA (see Fig. D.1). This corresponds to the leakage current and power surface density of approximately 14 µA/cm^2 and 7 mW/cm^2, respectively at -5°C and 500 V.

Acronym	Vendor	Thickness [µm]	Size [cm^2]	Full Depletion Voltage [V]	Strip Pitch [µm]	Fluence [n$_{eq}$(1 MeV)/cm^2]
Irradiated batch A: smaller STS-type prototype sensors irradiated with neutrons						
w06				85		0
w1sn5				88		3×10^{13}
w2sn5				82		3×10^{13}
w2sn3				82		5×10^{13}
w8sn2				83		5×10^{13}
w7sn1	CiS	290	1.2×1.2	85	50	8×10^{13}
w7sn4				80		8×10^{13}
w1sn2				90		1×10^{14}
w2sn1				85		1×10^{14}
w2sn2				85		2×10^{14}
w8sn1				80		2×10^{14}

Table D.1.: Properties of smaller STS-type prototype CiS sensors studied for neutron irradiation during 2014-15. The considered sensors are highlighted in yellow (table from [170]).

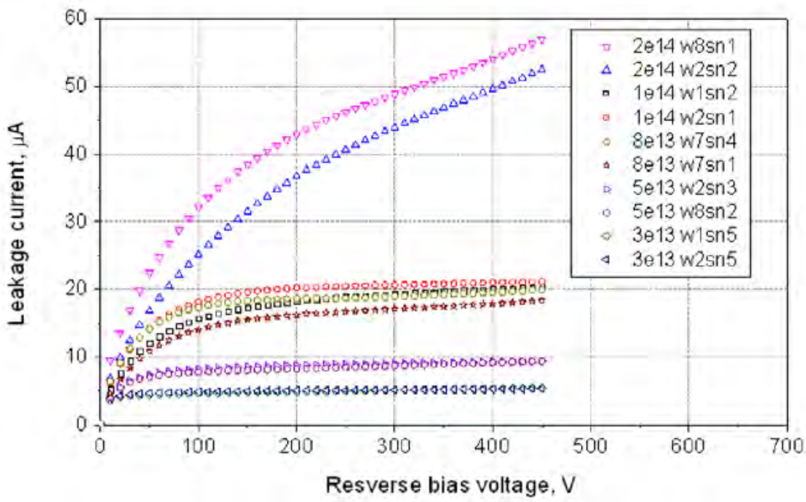

Figure D.1.: Leakage current variation with reverse bias voltage of the irradiated CBM05 prototype sensors (batch A) measured at -5°C (figure from [170]).

D.3. STS Irradiation Campaign 2018-19

Sensor Size [cm^2]	Vendor and Generation	Batch Number	Wafer Number	Fluence [n_{eq}(1 MeV)/cm^2]	Leakage Current at 500V [µA/cm^2]	Operation Voltage [V]
6.2 × 6.2	CiS 06	350191	09	0	0.253	150
			03	1×10^{14}	5.7	350
			08	1×10^{14}	14.3	350
			01	2×10^{14}	8.7	500
			10	2×10^{14}	9.7	500
	HPK 06	S10938-4440	72	0	0.012	150
			65	1×10^{14}	12.7	400
			71	1×10^{14}	10.2	400
			59	2×10^{14}	20.1	500
			79	2×10^{14}	14.1	500
6.2 × 4.2	CiS 08	351135	05	0	0.124	150
		351135	02	1×10^{13}	1.7	150
		351139	01	1×10^{13}	1.9	150
		351135	11	5×10^{13}	11.8	300
		351135	06	1×10^{14}	16.2	350
		351139	08	2×10^{14}	22.7	500
	HPK 06	S10938-5552	84	0	0.006	150
			33	5×10^{13}	7.0	300
			32	1×10^{14}	15.4	400
			31	2×10^{14}	28.2	500
6.2 × 2.2	CiS 07	350714	22-3	5×10^{13}	8.0	300
			23-1	5×10^{13}	9.6	300
			21-3	1×10^{14}	24.2	350
			23-2	1×10^{14}	12.4	350
			17-3	2×10^{14}	29.5	500
			23-3	2×10^{14}	29.1	500
	HPK 06	S10938-4723	06	5×10^{13}	4.7	300
			04	5×10^{13}	5.1	300
			08	1×10^{14}	11.4	400
			01	1×10^{14}	54.2	400
			02	2×10^{14}	25.1	500
			05	2×10^{14}	22.7	500

Table D.2.: Properties of the prototype sensors studied for proton irradiation during 2018-19. The considered sensors are highlighted in yellow (table from [171]).

An extensive irradiation campaign with realistic sensor dimensions (6.2 × 2.2 cm^2, 6.2 × 4.2 cm^2 and 6.2 × 6.2 cm^2) fabricated by CiS and HPK were carried out with protons at the Irradiation Center Karlsruhe. The properties of the irradiated sensors along with their IDs and leakage current properties at -10°C are summarised in Tab. D.2[2]. Further details of this irradiation campaign along with measurement details are mentioned in [171, 172]. Please note that the sensors considered for power dissipation estimates are the ones which will be comprised in the final STS, i.e., HPK-type irradiated at the end-of-lifetime flu-

2. The temperatures for the resulting plots quoted in [171,172] are +20°C, but this is in fact -10°C. Therefore, all plots, figures and data from [171,172] should be referenced at +20°C.

ence of $1\times10^{14}n_{eq}(1\ \text{MeV})/\text{cm}^2$ (see sensors highlighted in yellow in Tab. D.2)[3]. Therefore, the corresponding leakage current and power surface density measured at -10°C and 500 V[4] is between 10...16 µA/cm^2 and 5...8 mW/cm^2.

D.4. Summary and Conclusion

All estimates for STS sensor's end-of-lifetime behaviour, as introduced in previous sub-sections, are collectively plotted in Fig. D.2 by using Eq. 1.1b. They are represented as the variation of power density with sensor temperature, with the underlying values at -10°C and +20°C also summarised in Tab. D.3.

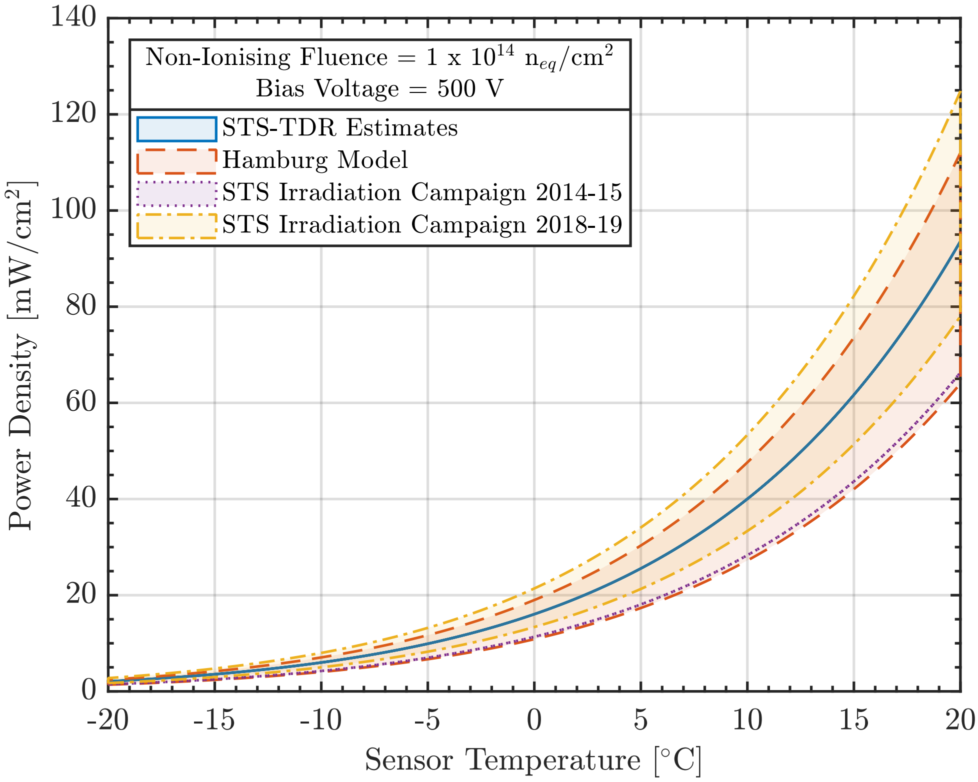

Figure D.2.: Variation of sensor power density with temperature at the end-of-lifetime conditions for different estimates.

Therefore, all estimates, both theoretical and experimental, are coherent with each other and STS sensors are foreseen to dissipate a maximum of 53.4 mW/cm^2

3. CBM06HPK2-w1 isn't considered here because it was mechanically damaged during the measurements.
4. Although the measurements for the considered sensors were conducted at 400 V, it's assumed that the leakage current at 400 V and 500 V is the same as the leakage current is expected to plateau after full-depletion.

Sensor Power Dissipation [mW/cm^2] Non-Ionising Fluence = 10^{14}n$_{eq}$(1 MeV)/cm^2 and Bias Voltage = 500V		
	-10°C	+20°C
STS-Technical Design Report	6.00	93.62
Hamburg Model	4.04 ... 7.06	64.02 ... 112.02
STS Irradiation Campaign 2014-15	4.24	66.32
STS Irradiation Campaign 2018-19	5.00 ... 8.00	78.01 ... 124.82

Table D.3.: Sensor power dissipation at end-of-lifetime conditions for different estimates at different sensor temperatures.

at +10°C at end-of-lifetime fluence of 1×10^{14}n$_{eq}$(1 MeV)/cm^2.

Appendix E.

Thermal Demonstrator Powering

E.1. Silicon Sensor Powering

The thermally active half-station of the Thermal Demonstrator is powered proportional to the non-ionising dose distribution of STS Station-1 (left-half) and appropriately sized silicon sensors (see Fig. E.1(a)-E.1(b))[1]. Accordingly, the silicon power resistors, as described in Sec. 3.2, are distributed to mimic the sensor power dissipation (see Fig. E.1(c)). It's worth mentioning that the resistance values of the produced silicon sensors are consistently higher than theoretically expected values[2] due to production issues. Therefore, the experimentally measured resistance values are used as a reference for the powering scheme. Moreover, given the limited number of power supply channels available to power the silicon power resistors, several resistors were connected in series based on the comparable power dissipation and sizes (see Fig. E.1(d) and Tab.E.1).

Reference Power Density [mW/cm^2] (for LT201-2T/B, 3T/B)	Input Voltage (per channel) at Power Supplies [V]							
	Ch #1	Ch #2	Ch #3	Ch #4	Ch #5	Ch #6	Ch #7	Ch #8
5	2.420	2.366	0.505	1.426	4.135	3.518	0.518	0.399
10	3.423	3.346	0.714	2.017	5.847	4.975	0.733	0.564
25	5.412	5.291	1.130	3.189	9.245	7.867	1.158	0.892
50	7.653	7.482	1.598	4.510	13.075	11.125	1.638	1.262
100	10.824	10.581	2.259	6.378	18.491	15.733	2.317	1.784
150	13.256	12.959	2.767	7.812	22.646	19.269	2.837	2.185
200	15.307	14.964	3.195	9.020	26.150	22.250	3.276	2.523
300	18.747	18.327	3.913	11.047	32.027	27.251	4.013	3.090

Table E.1.: Set voltage per power supply channel for various power densities. The power density values corresponds to the highest irradiated sensors (innermost sensors on the central ladder LT201; LT201-2T/B, 3T/B). The underlying sensors per channel are connected in series (see Fig. E.1(d)). Moreover, sense wires are used between the power supplies and the distribution blocks on the C-frames to compensate for the voltage drop along the way.

1. As the ladder LT205 doesn't exist in STS_v21b, the overlaying fluence distribution for LT205 is that of LT204 (see Tab. 3.3).
2. Theoretically expected resistance values based on 180 nm thick Inconel layer - 6.2×2.2 cm^2: 17.22 Ω; 6.2×4.2 cm^2: 9.02 Ω; 6.2×6.2 cm^2: 6.11 Ω

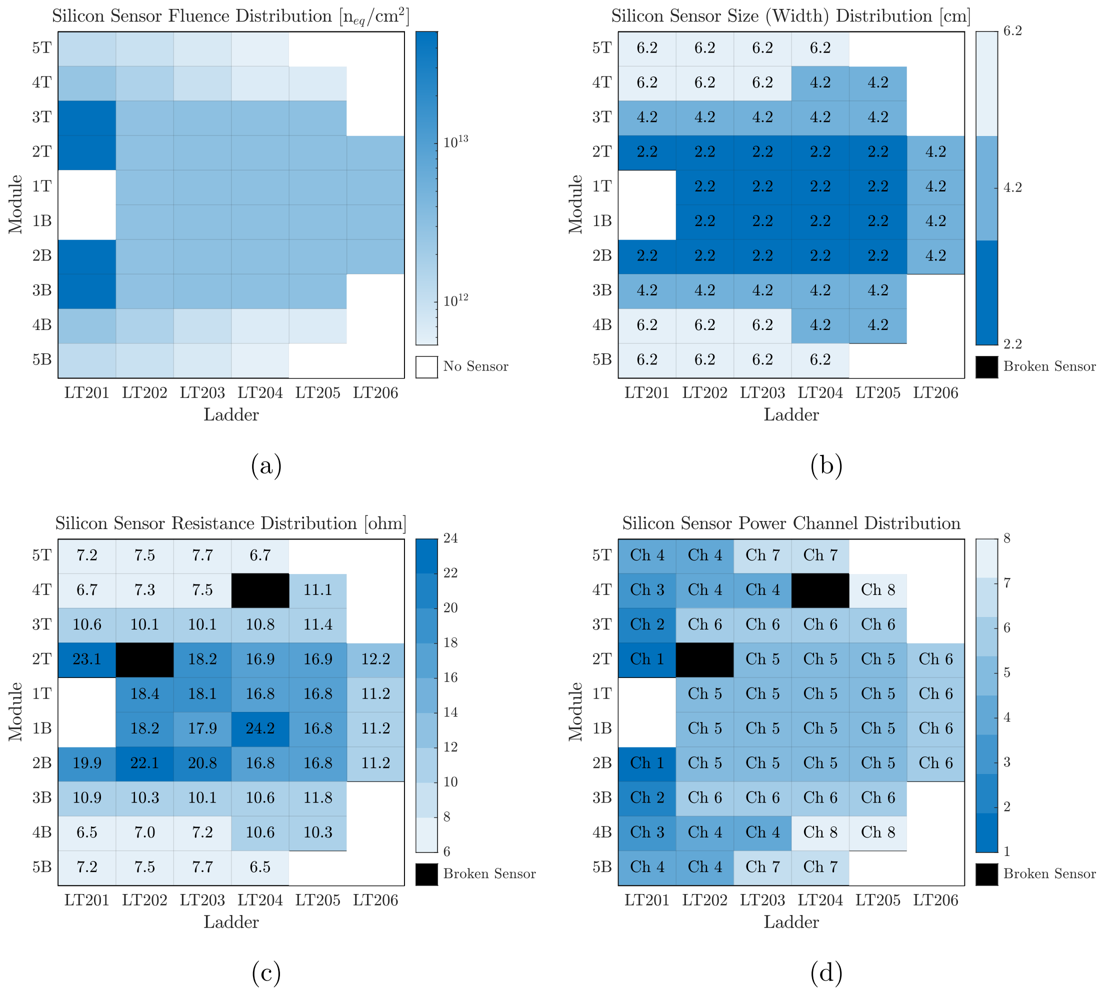

Figure E.1.: (a) Non-Ionising Dose distribution, based on STS geometry version STS_v21b for 11*A*GeV Au+Au at 10 MHz after 1 month of irradiation (values from O. Bertini (GSI Darmstadt)). (b) The sensor size distribution for the Thermal Demonstrator. (c) Measured resistance of the silicon power resistors and their distribution across the Thermal Demonstrator. (d) Power supply channel distribution for all silicon power resistors. Multiple sensors for a given channel are connected in series. The innermost area in all figures (LT201-1T/B) represents the beampipe opening, whereas the black bins comprise sensors which were broken during the setup integration.

E.2. Front-End Electronics Powering

The active half-layer of the Thermal Demonstrator comprises 100 thermally realistic dummies of the STS front-end electronics boards (FEBs) complementing the 50 dummy silicon sensors. The ASICs and LDOs of the thermal dummy FEBs can be powered separately to match the power dissipation foreseen for the real STS FEBs in different operational scenarios (see Tab. E.2-E.3). The respective ASIC and LDO lines are powered separately for individual cooling plates with the underlying FEBs connected in parallel by using commercial distribution blocks (totalling to eight power supply channels; see Fig. E.4). Moreover, sense wires are used between the power supplies and the distribution blocks on the C-frames to compensate for the intermediate voltage drop along the way.

STS-FEB Powering - Input Currents and Efficiencies						
Supply Lines	Minimum Scenario		Typical Scenario		Maximum Scenario	
	Input Current [A]	FEAST Efficiency [-]	Input Current [A]	FEAST Efficiency [-]	Input Current [A]	FEAST Efficiency [-]
FEB 1.2V	1.40	0.82	2.60	0.82	3.20	0.79
FEB 1.8V	2.00	0.82	2.20	0.83	2.40	0.83
ROB 1.5V	2.67	0.73	2.67	0.73	2.67	0.73
ROB 2.5V	0.34	0.82	0.34	0.82	0.34	0.82

STS-FEB Power Dissipation [W]			
Dissipating Lines	Minimum Scenario	Typical Scenario	Maximum Scenario
ASICs 1.2V	1.68	3.12	3.84
ASICs 1.8V	3.60	3.96	4.32
ASICs Total	5.28	7.08	8.16
LDOs	3.35	4.34	4.77
FEB Total	8.63	11.42	12.93

Table E.2.: Top: The input currents of the front-end (FEB) and readout board (ROB) supply lines, and efficiencies of the DC-DC converter (FEAST) for the three operational scenarios planned for powering the final STS FEBs. The *Minimum Scenario* represents the lowest FEB currents and highest FEB-FEAST efficiencies, while vice versa is true for *Maximum Scenario*. Bottom: Expected power dissipation values with the aforementioned input values for both ASICs (1.2V analog and 1.8V digital circuit) and LDOs (values from J. Lehnert (GSI Darmstadt); updated as of 29.06.2023).

Dissipating Lines	Minimum Scenario		Typical Scenario		Maximum Scenario		Maximum Scenario with 10% addition	
	Voltage [V]	Current [A]	Voltage [V]	Current [A]	Voltage [V]	Current [A]	Voltage [V]	Current [A]
ASICs (3.65 Ω)	4.329	1.2	5.013	1.4	5.382	1.5	5.645	1.6
LDOs (0.9 Ω)	1.707	2.0	1.943	2.2	2.037	2.3	2.137	2.5

Table E.3.: The input voltage and current values for all ASICs and LDOs of the thermal dummy FEBs (see Sec. 3.2) for the foreseen operational scenarios (see Tab. E.2). Moreover, further values are quoted for an unrealistic scenario with 10% higher power dissipation than the *Maximum Scenario*.

Power Supply Channel ID	Number of FEBs	Minimum Scenario		Typical Scenario	
		Measured Voltage [V]	Input Current [A]	Measured Voltage [V]	Input Current [A]
CF-2T ASIC	26	4.297	31.7	5.200	36.7
CF-2T LDO	26	1.875	51.0	2.239	58.1
CF-2B ASIC	25	4.250	30.5	5.189	35.3
CF-2B LDO	26	2.057	51.0	2.445	58.1
CF-3B ASIC	24	3.849	29.3	4.676	33.9
CF-3B LDO	24	1.887	47.1	2.263	53.6
CF-3T ASIC	24	4.016	29.3	4.835	33.9
CF-3T LDO	24	1.915	47.1	2.279	53.6
Total Power Dissipation (Expected) [W]		857.72		1134.92	
Total Power Dissipation (Measured) [W]		875.70		1211.96	
Cable Power Dissipation [W]		17.98		77.04	

Power Supply Channel ID	Number of FEBs	Maximum Scenario		Maximum Scenario with 10% addition	
		Measured Voltage [V]	Input Current [A]	Measured Voltage [V]	Input Current [A]
CF-2T ASIC	26	5.697	39.4	6.104	41.3
CF-2T LDO	26	2.391	60.9	2.597	63.9
CF-2B ASIC	25	5.715	37.9	6.138	39.8
CF-2B LDO	26	2.515	60.9	2.752	63.9
CF-3B ASIC	24	5.208	36.4	5.569	38.2
CF-3B LDO	24	2.441	56.2	2.607	58.9
CF-3T ASIC	24	5.284	36.4	5.664	38.2
CF-3T LDO	24	2.333	56.2	2.604	58.9
Total Power Dissipation (Expected) [W]		1284.84		1413.32	
Total Power Dissipation (Measured) [W]		1389.91		1573.71	
Cable Power Dissipation [W]		105.07		160.39	

Table E.4.: The voltage and current values to power the thermal dummy FEBs for a given power supply channel (all connected in series). The power supplies are operated in a constant current mode, while the voltage values are measured at the power supplies. The power dissipation difference between the expected and measured values at the power supply is quoted as the cable power dissipation on the C-frames (voltage drop in the remaining circuit is compensated by using sense wires between the power supplies and the distribution blocks on the C-frames). The values are quoted for all four operational scenarios introduced in Tab. E.3.

Appendix F.

Silicon Sensor Temperature Distributions

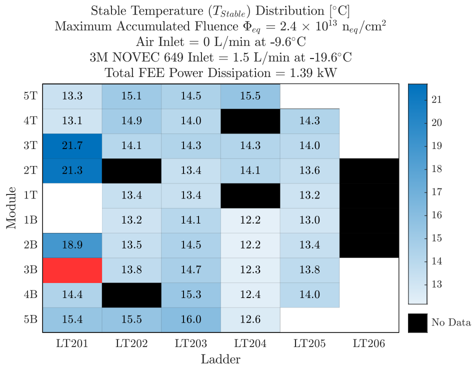

(a) Air Flow Rate = 0 L/min

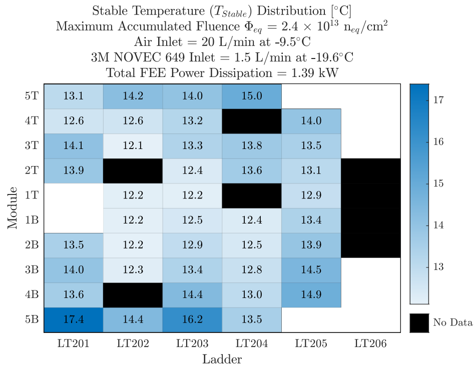

(b) Air Flow Rate = 20 L/min

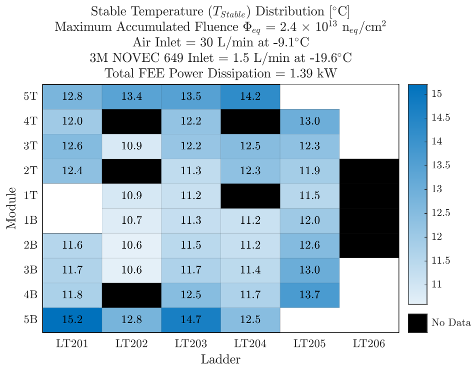

(c) Air Flow Rate = 30 L/min

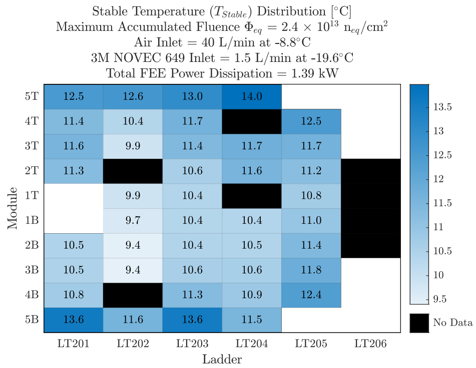

(d) Air Flow Rate = 40 L/min

Figure F.1.: Dependency on Air Flow Rate: Stable Temperature (T_{Stable}) distributions across the thermally active half-station for various air flow rates per ladder (0 ... 40 L/min) after an accumulated fluence of $0.24\times10^{14}n_{eq}(1\ \mathrm{MeV})/cm^2$ for 10 years of CBM operation. The baseline air flow rate is 30 L/min. The innermost area in all figures (LT201-1T/B) represents the beampipe opening, whereas the black bins comprise sensors which are either physically broken or have faulty Pt-100 sensor. The red bins comprise sensors where no T_{Stable} was achieved, i.e., the sensors are in thermal runaway.

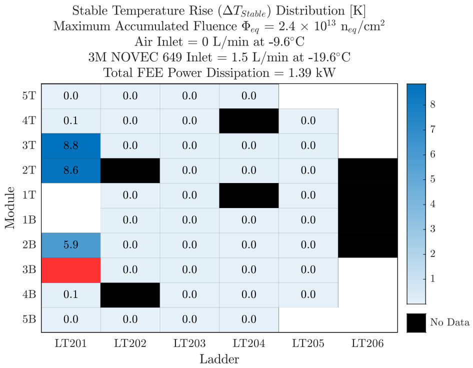

(a) Air Flow Rate = 0 L/min

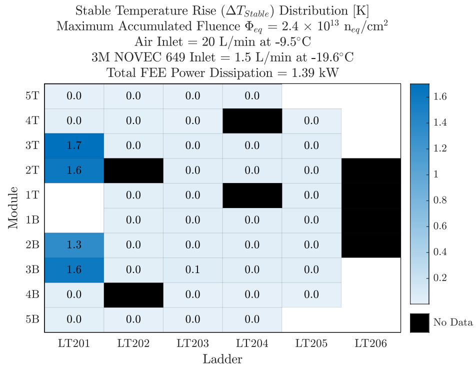

(b) Air Flow Rate = 20 L/min

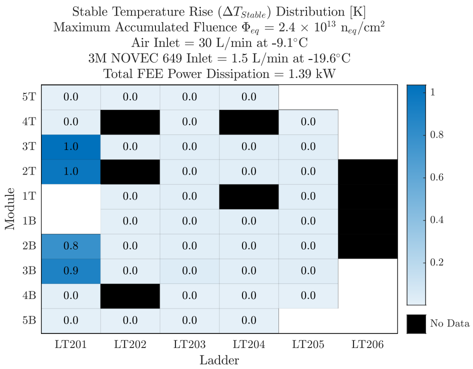

(c) Air Flow Rate = 30 L/min

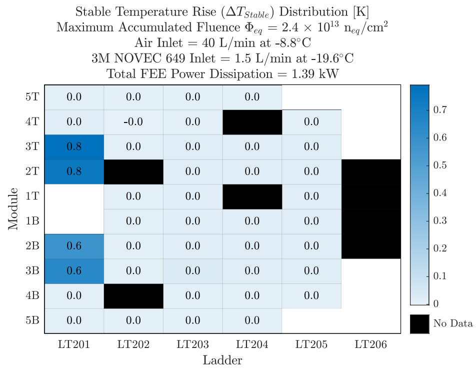

(d) Air Flow Rate = 40 L/min

Figure F.2.: Dependency on Air Flow Rate: Distributions showing the rise of Stable Temperature (ΔT_{Stable}) across the thermally active half-station for various air flow rates per ladder (0 ... 40 L/min) after an accumulated fluence of $0.24 \times 10^{14} n_{eq}(1\ \text{MeV})/cm^2$ for 10 years of CBM operation. The baseline air flow rate is 30 L/min. The innermost area in all figures (LT201-1T/B) represents the beampipe opening, whereas the black bins comprise sensors which are either physically broken or have faulty Pt-100 sensor. The red bins comprise sensors where no T_{Stable} was achieved, i.e., the sensors are in thermal runaway.

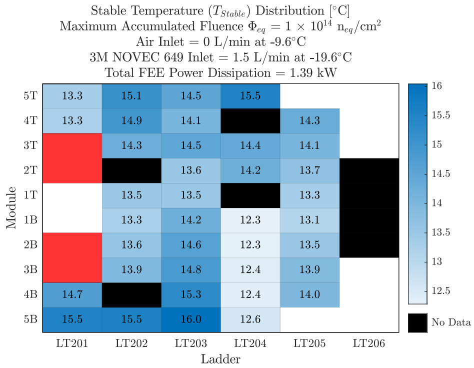

(a) Air Flow Rate = 0 L/min

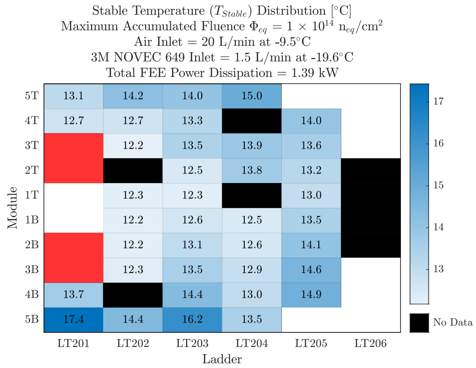

(b) Air Flow Rate = 20 L/min

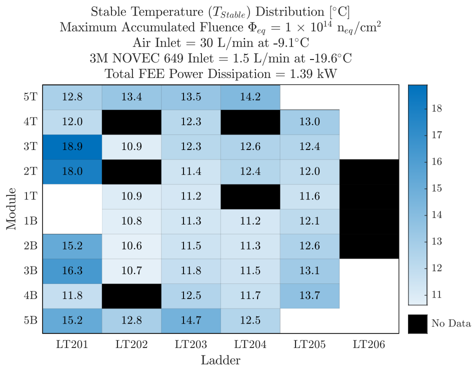

(c) Air Flow Rate = 30 L/min

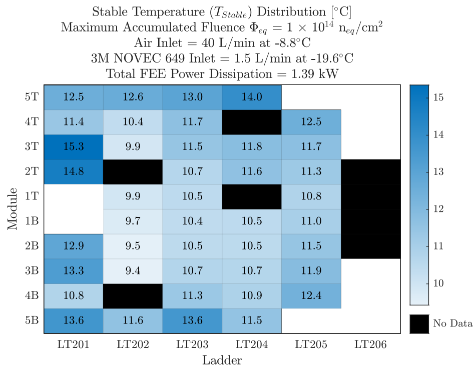

(d) Air Flow Rate = 40 L/min

Figure F.3.: Dependency on Air Flow Rate: Stable Temperature (T_{Stable}) distributions across the thermally active half-station for various air flow rates per ladder (0 ... 40 L/min) after the end-of-lifetime fluence of $1 \times 10^{14} n_{eq}(1\text{ MeV})/cm^2$ which will be reached only after 40 years of CBM operation. The baseline air flow rate is 30 L/min. The innermost area in all figures (LT201-1T/B) represents the beampipe opening, whereas the black bins comprise sensors which are either physically broken or have faulty Pt-100 sensor. The red bins comprise sensors where no T_{Stable} was achieved, i.e., the sensors are in thermal runaway.

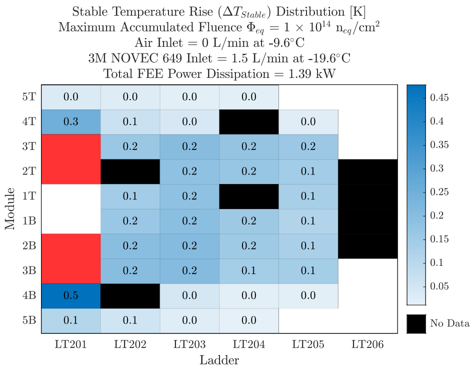

(a) Air Flow Rate = 0 L/min

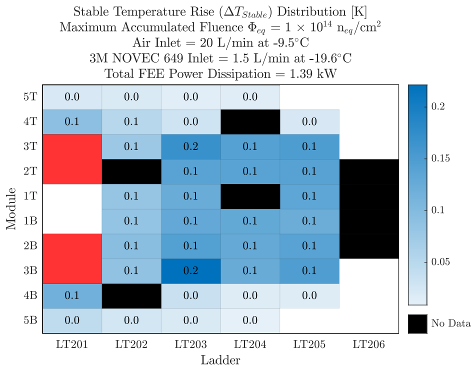

(b) Air Flow Rate = 20 L/min

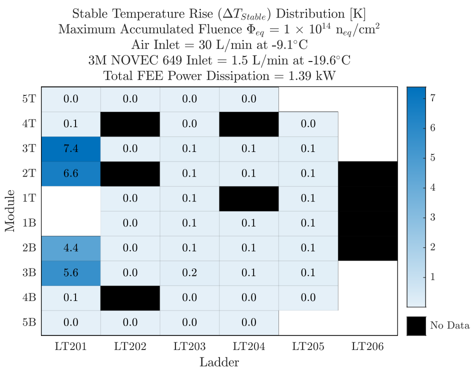

(c) Air Flow Rate = 30 L/min

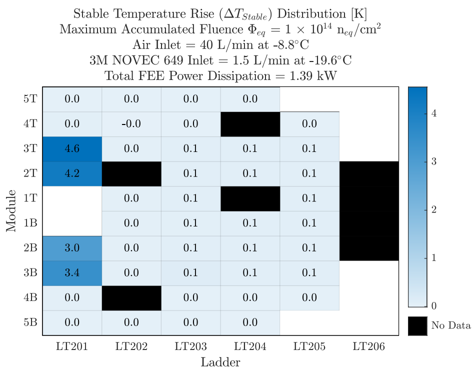

(d) Air Flow Rate = 40 L/min

Figure F.4.: Dependency on Air Flow Rate: Distributions showing the rise of Stable Temperature (ΔT_{Stable}) across the thermally active half-station for various air flow rates per ladder (0 ... 40 L/min) after the end-of-lifetime fluence of $1 \times 10^{14} n_{eq}(1\ \mathrm{MeV})/cm^2$ which will be reached only after 40 years of CBM operation. The baseline air flow rate is 30 L/min. The innermost area in all figures (LT201-1T/B) represents the beampipe opening, whereas the black bins comprise sensors which are either physically broken or have faulty Pt-100 sensor. The red bins comprise sensors where no T_{Stable} was achieved, i.e., the sensors are in thermal runaway.

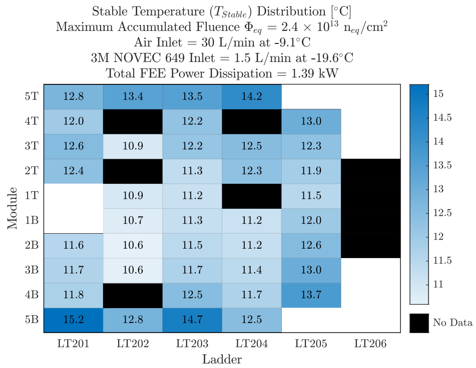

(a) Air Set Temperature = -15°C

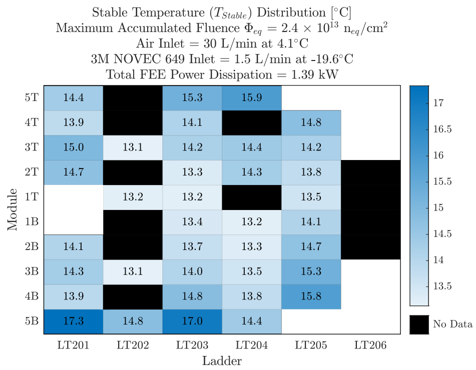

(b) Air Set Temperature = 0°C

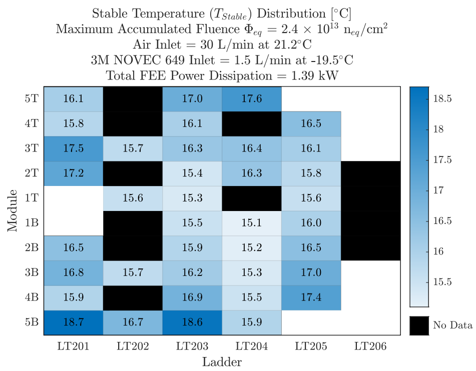

(c) Air Set Temperature = +20°C

Figure F.5.: Dependency on Air Set Temperature: Stable Temperature (T_{Stable}) distributions across the thermally active half-station for various air set temperatures (-15 ... +20°C; baseline = -15°C) after an accumulated fluence of $0.24 \times 10^{14} n_{eq}(1\ \text{MeV})/cm^2$ for 10 years of CBM operation. The innermost area in all figures (LT201-1T/B) represents the beampipe opening, whereas the black bins comprise sensors which are either physically broken or have faulty Pt-100 sensor. The red bins comprise sensors where no T_{Stable} was achieved, i.e., the sensors are in thermal runaway.

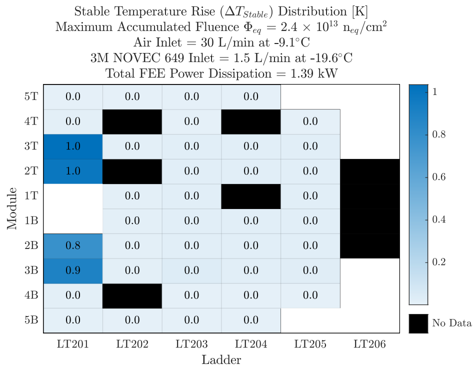

(a) Air Set Temperature = -15°C

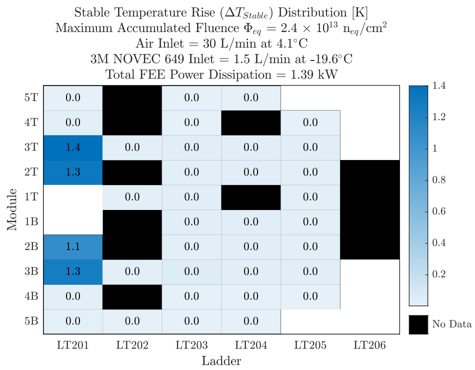

(b) Air Set Temperature = 0°C

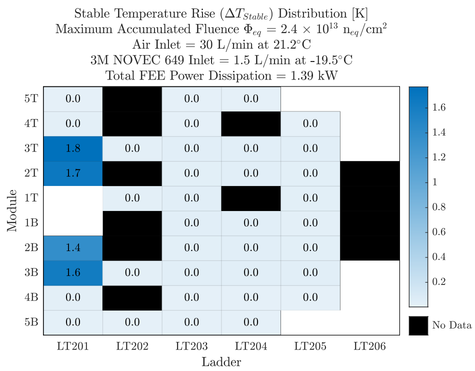

(c) Air Set Temperature = +20°C

Figure F.6.: Dependency on Air Set Temperature: Distributions showing the rise of Stable Temperature (ΔT_{Stable}) across the thermally active half-station for various air set temperatures (-15 ... +20°C; baseline = -15°C) after an accumulated fluence of $0.24{\times}10^{14}$n$_{eq}$(1 MeV)/cm^2 for 10 years of CBM operation. The innermost area in all figures (LT201-1T/B) represents the beampipe opening, whereas the black bins comprise sensors which are either physically broken or have faulty Pt-100 sensor. The red bins comprise sensors where no T_{Stable} was achieved, i.e., the sensors are in thermal runaway.

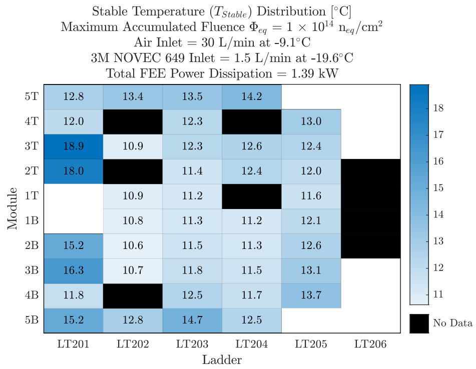

(a) Air Set Temperature = -15°C

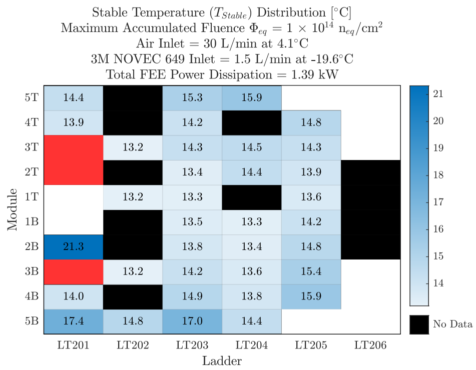

(b) Air Set Temperature = 0°C

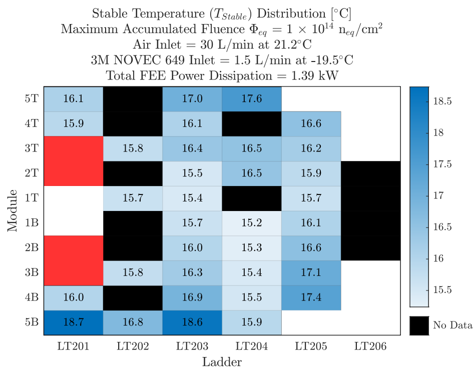

(c) Air Set Temperature = +20°C

Figure F.7.: Dependency on Air Set Temperature: Stable Temperature (T_{Stable}) distributions across the thermally active half-station for various air set temperatures (-15 ... +20°C; baseline = -15°C) after the end-of-lifetime fluence of $1 \times 10^{14} n_{eq}(1\ \text{MeV})/\text{cm}^2$ which will be reached only after 40 years of CBM operation. The innermost area in all figures (LT201-1T/B) represents the beampipe opening, whereas the black bins comprise sensors which are either physically broken or have faulty Pt-100 sensor. The red bins comprise sensors where no T_{Stable} was achieved, i.e., the sensors are in thermal runaway.

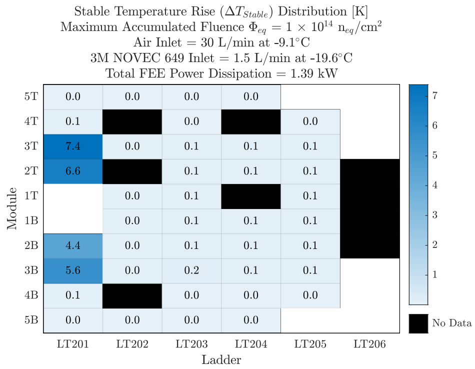

(a) Air Set Temperature = -15°C

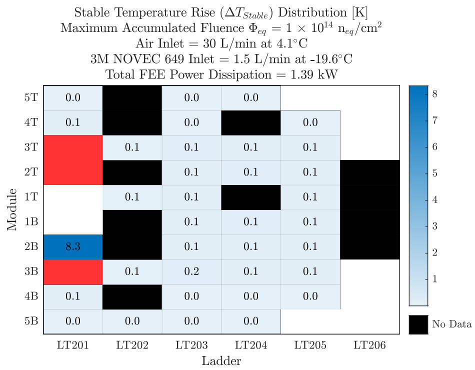

(b) Air Set Temperature = 0°C

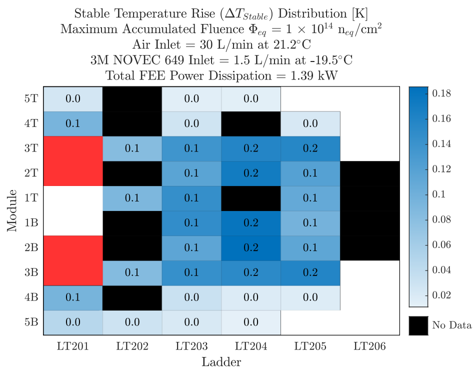

(c) Air Set Temperature = +20°C

Figure F.8.: Dependency on Air Set Temperature: Distributions showing the rise of Stable Temperature (ΔT_{Stable}) across the thermally active half-station for various air set temperatures (-15 ... +20°C; baseline = -15°C) after the end-of-lifetime fluence of $1 \times 10^{14} n_{eq}(1\ \text{MeV})/\text{cm}^2$ which will be reached only after 40 years of CBM operation. The innermost area in all figures (LT201-1T/B) represents the beampipe opening, whereas the black bins comprise sensors which are either physically broken or have faulty Pt-100 sensor. The red bins comprise sensors where no T_{Stable} was achieved, i.e., the sensors are in thermal runaway.

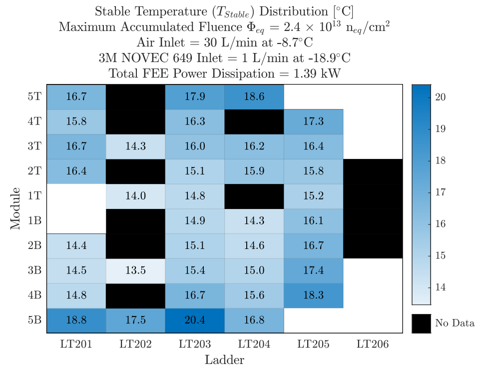

(a) 3M™ NOVEC™ 649 Flow Rate = 1.0 L/min

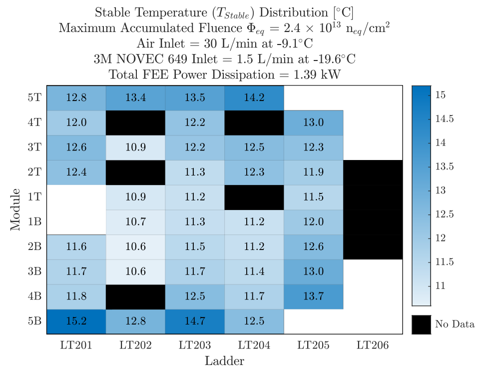

(b) 3M™ NOVEC™ 649 Flow Rate = 1.5 L/min

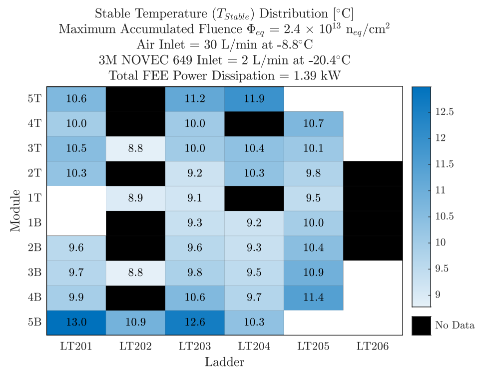

(c) 3M™ NOVEC™ 649 Flow Rate = 2.0 L/min

Figure F.9.: Dependency on 3M™ NOVEC™ 649 Flow Rate: Stable Temperature (T_{Stable}) distributions across the thermally active half-station for various 3M™ NOVEC™ 649 flow rates per cooling plate (1.0 ... 2.0 L/min; baseline = 1.5 L/min) after an accumulated fluence of $0.24 \times 10^{14} n_{eq}(1\ \text{MeV})/cm^2$ for 10 years of CBM operation. The innermost area in all figures (LT201-1T/B) represents the beampipe opening, whereas the black bins comprise sensors which are either physically broken or have faulty Pt-100 sensor. The red bins comprise sensors where no T_{Stable} was achieved, i.e., the sensors are in thermal runaway.

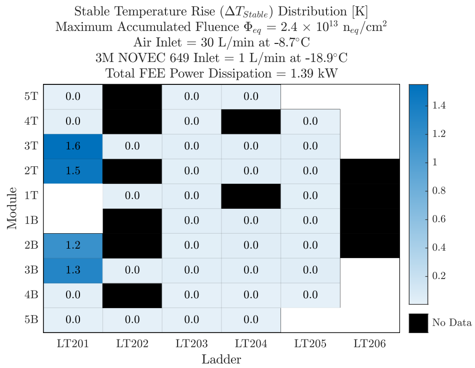

(a) 3M™ NOVEC™ 649 Flow Rate = 1.0 L/min

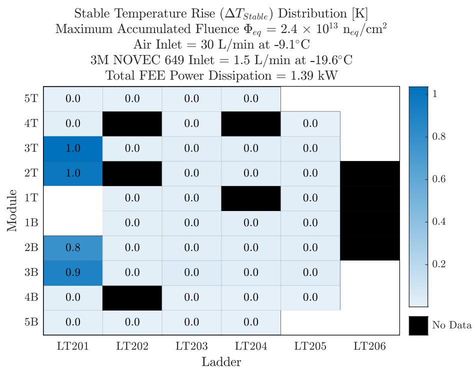

(b) 3M™ NOVEC™ 649 Flow Rate = 1.5 L/min

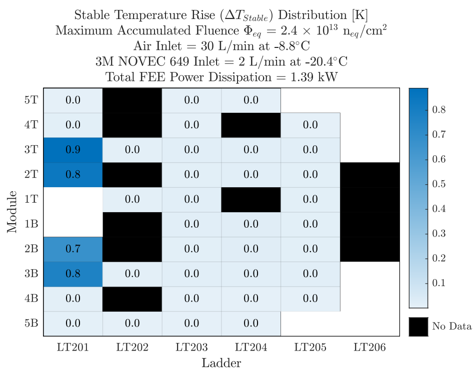

(c) 3M™ NOVEC™ 649 Flow Rate = 2.0 L/min

Figure F.10.: Dependency on 3M™ NOVEC™ 649 Flow Rate: Distributions showing the rise of Stable Temperature (ΔT_{Stable}) across the thermally active half-station for various 3M™ NOVEC™ 649 flow rates per cooling plate (1.0 ... 2.0 L/min; baseline = 1.5 L/min) after an accumulated fluence of $0.24 \times 10^{14} n_{eq}(1\ \mathrm{MeV})/cm^2$ for 10 years of CBM operation. The innermost area in all figures (LT201-1T/B) represents the beampipe opening, whereas the black bins comprise sensors which are either physically broken or have faulty Pt-100 sensor. The red bins comprise sensors where no T_{Stable} was achieved, i.e., the sensors are in thermal runaway.

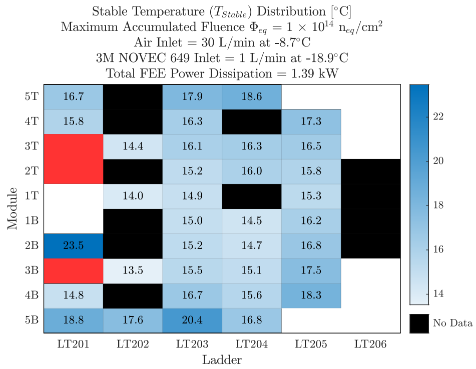

(a) 3M™ NOVEC™ 649 Flow Rate = 1.0 L/min

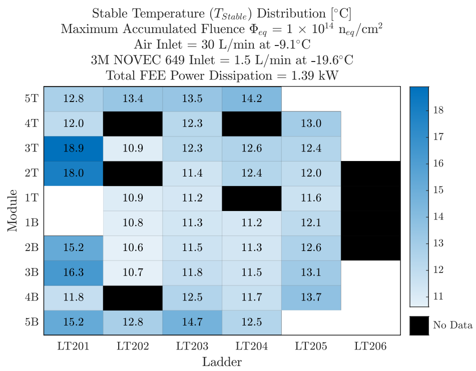

(b) 3M™ NOVEC™ 649 Flow Rate = 1.5 L/min

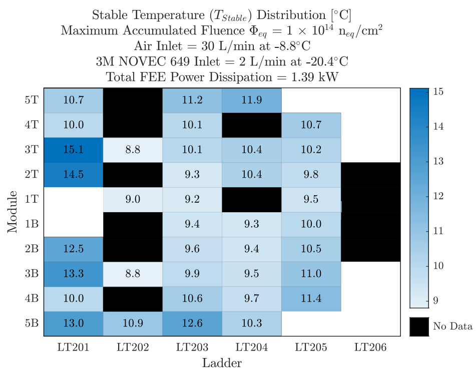

(c) 3M™ NOVEC™ 649 Flow Rate = 2.0 L/min

Figure F.11.: Dependency on 3M™ NOVEC™ 649 Flow Rate: Stable Temperature (T_{Stable}) distributions across the thermally active half-station for various 3M™ NOVEC™ 649 flow rates per cooling plate (1.0 ... 2.0 L/min; baseline = 1.5 L/min) after the end-of-lifetime fluence of 1 × $10^{14}$$n_{eq}$(1 MeV)/cm^2 which will be reached only after 40 years of CBM operation. The innermost area in all figures (LT201-1T/B) represents the beampipe opening, whereas the black bins comprise sensors which are either physically broken or have faulty Pt-100 sensor. The red bins comprise sensors where no T_{Stable} was achieved, i.e., the sensors are in thermal runaway.

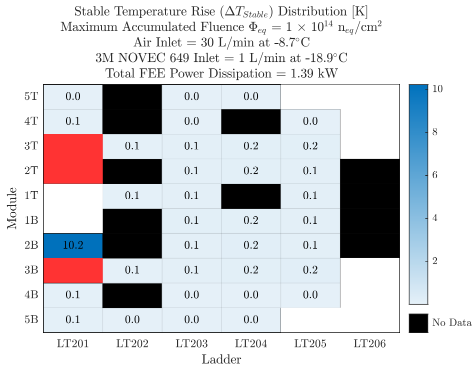

(a) 3M™ NOVEC™ 649 Flow Rate = 1.0 L/min

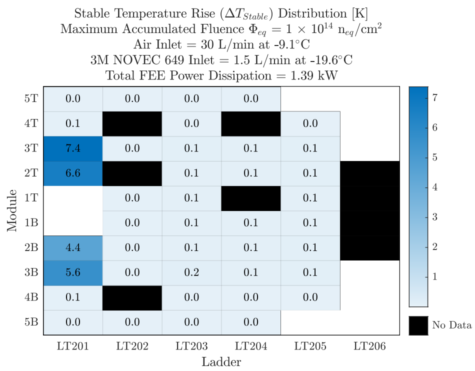

(b) 3M™ NOVEC™ 649 Flow Rate = 1.5 L/min

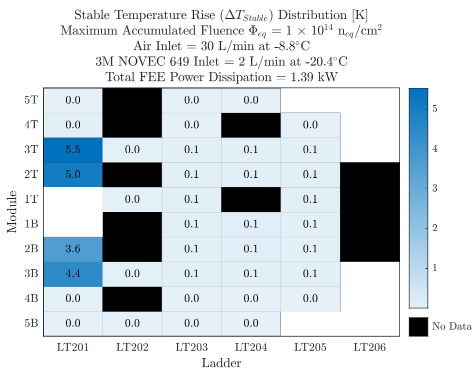

(c) 3M™ NOVEC™ 649 Flow Rate = 2.0 L/min

Figure F.12.: Dependency on 3M™ NOVEC™ 649 Flow Rate: Distributions showing the rise of Stable Temperature (ΔT_{Stable}) across the thermally active half-station for various 3M™ NOVEC™ 649 flow rates per cooling plate (1.0 ... 2.0 L/min; baseline = 1.5 L/min) after the end-of-lifetime fluence of $10^{14} n_{eq}(1\ \text{MeV})/\text{cm}^2$ which will be reached only after 40 years of CBM operation. The innermost area in all figures (LT201-1T/B) represents the beampipe opening, whereas the black bins comprise sensors which are either physically broken or have faulty Pt-100 sensor. The red bins comprise sensors where no T_{Stable} was achieved, i.e., the sensors are in thermal runaway.

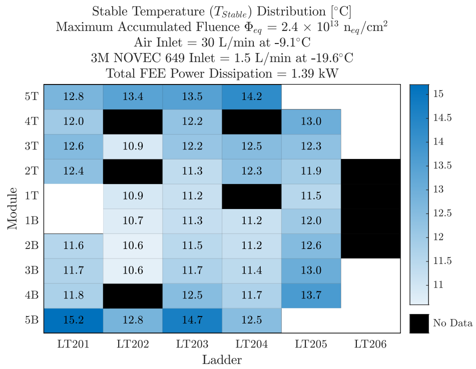

(a) 3M™ NOVEC™ 649 Set Temperature = -20°C

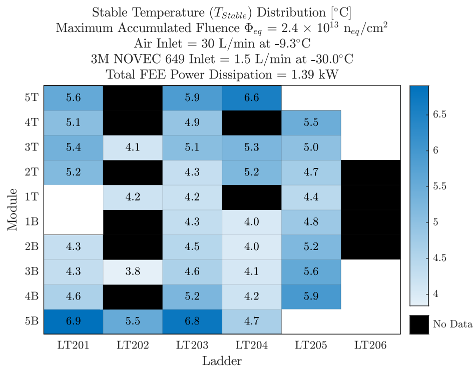

(b) 3M™ NOVEC™ 649 Set Temperature = -30°C

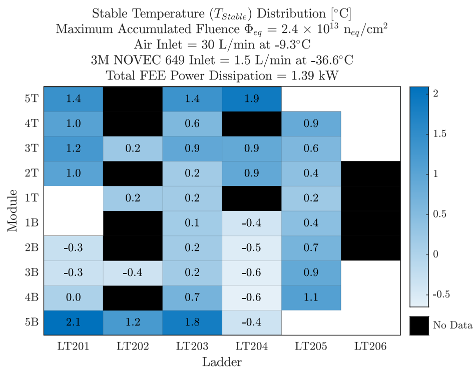

(c) 3M™ NOVEC™ 649 Set Temperature = -40°C

Figure F.13.: Dependency on 3M™ NOVEC™ 649 Set Temperature: Stable Temperature (T_{Stable}) distributions across the thermally active half-station for various 3M™ NOVEC™ 649 set temperatures (-20 ... 40°C; baseline = -20°C) after an accumulated fluence of $0.24{\times}10^{14}n_{eq}(1\ \mathrm{MeV})/cm^2$ for 10 years of CBM operation. The innermost area in all figures (LT201-1T/B) represents the beampipe opening, whereas the black bins comprise sensors which are either physically broken or have faulty Pt-100 sensor. The red bins comprise sensors where no T_{Stable} was achieved, i.e., the sensors are in thermal runaway.

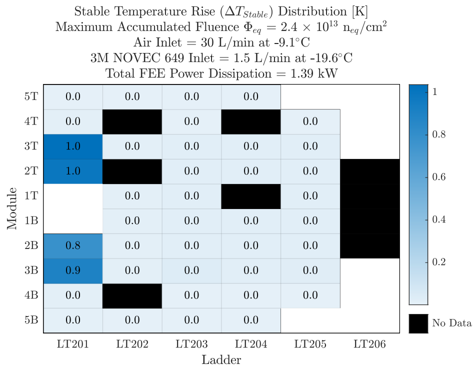

(a) 3M™ NOVEC™ 649 Set Temperature = -20°C

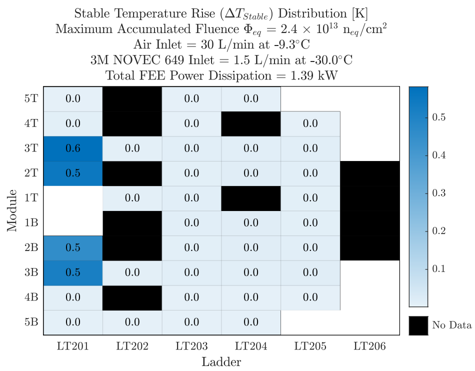

(b) 3M™ NOVEC™ 649 Set Temperature = -30°C

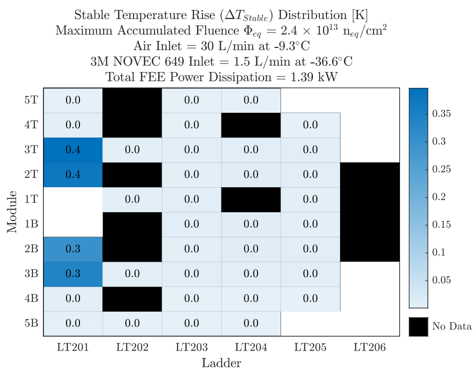

(c) 3M™ NOVEC™ 649 Set Temperature = -40°C

Figure F.14.: Dependency on 3M™ NOVEC™ 649 Set Temperature: Distributions showing the rise of Stable Temperature (ΔT_{Stable}) across the thermally active half-station for various 3M™ NOVEC™ 649 set temperatures (-20 ... 40°C; baseline = -20°C) after an accumulated fluence of $0.24 \times 10^{14} n_{eq}(1\ \text{MeV})/\text{cm}^2$ for 10 years of CBM operation. The innermost area in all figures (LT201-1T/B) represents the beampipe opening, whereas the black bins comprise sensors which are either physically broken or have faulty Pt-100 sensor. The red bins comprise sensors where no T_{Stable} was achieved, i.e., the sensors are in thermal runaway.

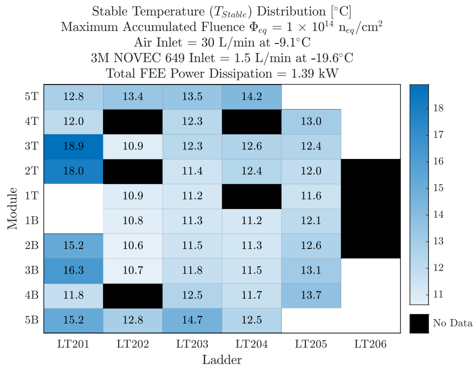

(a) 3M™ NOVEC™ 649 Set Temperature = -20°C

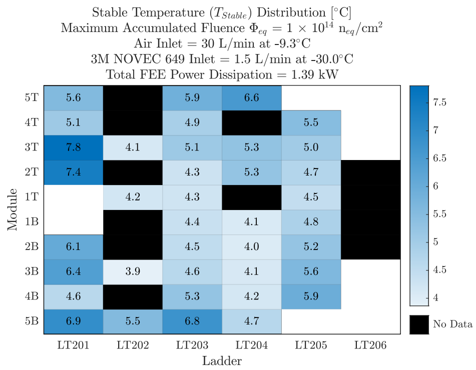

(b) 3M™ NOVEC™ 649 Set Temperature = -30°C

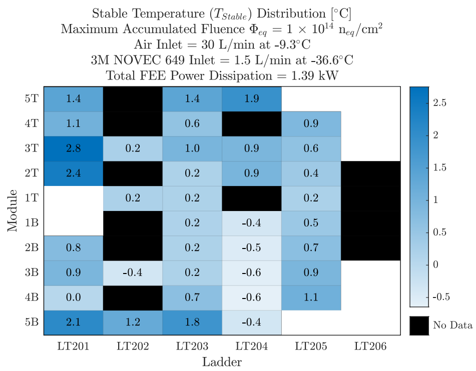

(c) 3M™ NOVEC™ 649 Set Temperature = -40°C

Figure F.15.: Dependency on 3M™ NOVEC™ 649 Set Temperature: Stable Temperature (T_{Stable}) distributions across the thermally active half-station for various 3M™ NOVEC™ 649 set temperatures (-20 ... 40°C; baseline = -20°C) after the end-of-lifetime fluence of $1 \times 10^{14} n_{eq}(1\ \text{MeV})/\text{cm}^2$ which will be reached only after 40 years of CBM operation. The innermost area in all figures (LT201-1T/B) represents the beampipe opening, whereas the black bins comprise sensors which are either physically broken or have faulty Pt-100 sensor. The red bins comprise sensors where no T_{Stable} was achieved, i.e., the sensors are in thermal runaway.

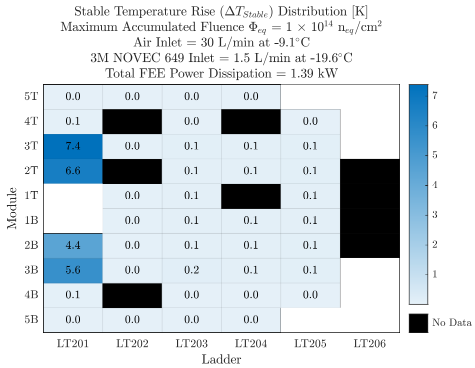

(a) 3M™ NOVEC™ 649 Set Temperature = -20°C

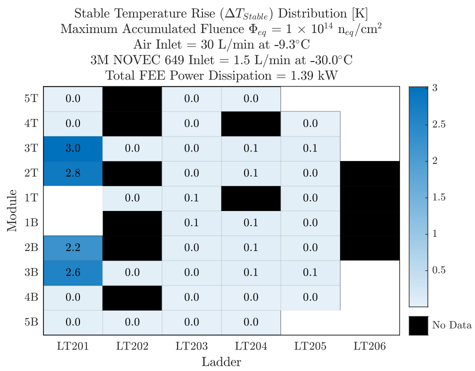

(b) 3M™ NOVEC™ 649 Set Temperature = -30°C

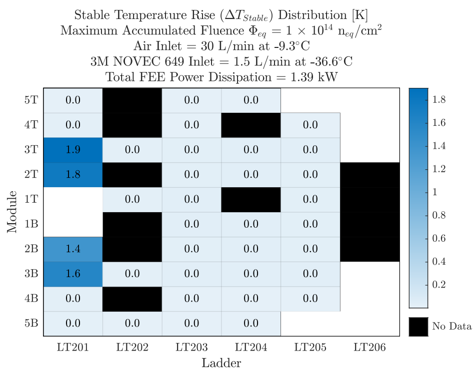

(c) 3M™ NOVEC™ 649 Set Temperature = -40°C

Figure F.16.: Dependency on 3M™ NOVEC™ 649 Set Temperature: Distributions showing the rise of Stable Temperature (ΔT_{Stable}) across the thermally active half-station for various 3M™ NOVEC™ 649 set temperatures (-20 ... 40°C; baseline = -20°C) after the end-of-lifetime fluence of 1 × 10^{14}n$_{eq}$(1 MeV)/cm^2 which will be reached only after 40 years of CBM operation. The innermost area in all figures (LT201-1T/B) represents the beampipe opening, whereas the black bins comprise sensors which are either physically broken or have faulty Pt-100 sensor. The red bins comprise sensors where no T_{Stable} was achieved, i.e., the sensors are in thermal runaway.

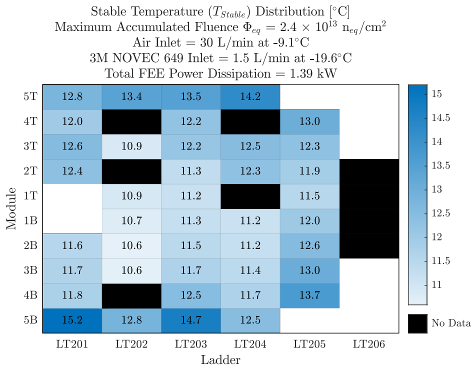

(a) Side-Wall Cooling = ON (-20°C); Sensor Air Cooling = ON (-15°C)

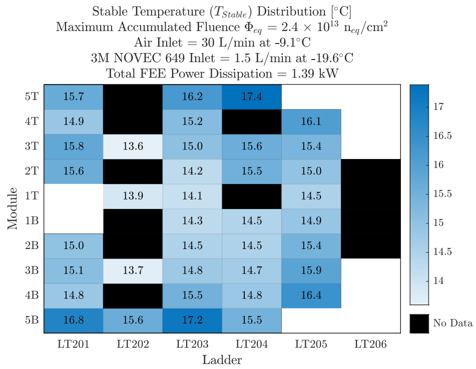

(b) Side-Wall Cooling = OFF; Sensor Air Cooling = ON (-15°C)

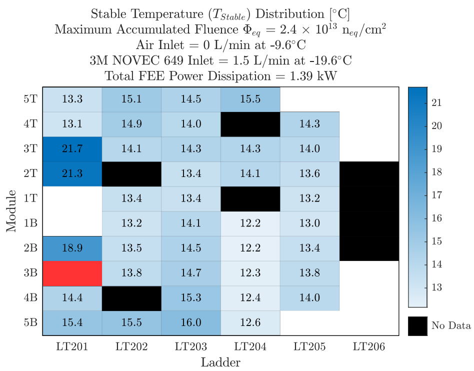

(c) Side-Wall Cooling = ON (-20°C); Sensor Air Cooling = OFF

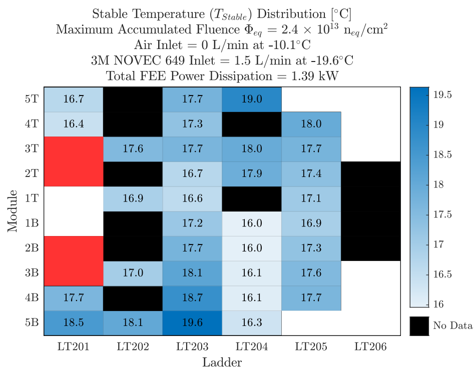

(d) Side-Wall Cooling = OFF; Sensor Air Cooling = OFF

Figure F.17.: Dependency on Side-Wall Cooling: Stable Temperature (T_{Stable}) distributions across the thermally active half-station for various settings of side-wall cooling (ON ... OFF) along with sensor air cooling (ON ... OFF) after an accumulated fluence of $0.24{\times}10^{14} n_{eq}(1\ \text{MeV})/cm^2$ for 10 years of CBM operation. The baseline setting for side-wall cooling is ON at -20°C and for sensor air cooling is ON at -15°C. The innermost area in all figures (LT201-1T/B) represents the beampipe opening, whereas the black bins comprise sensors which are either physically broken or have faulty Pt-100 sensor. The red bins comprise sensors where no T_{Stable} was achieved, i.e., the sensors are in thermal runaway.

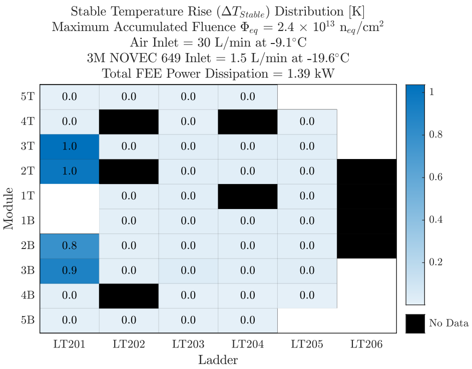

(a) Side-Wall Cooling = ON (-20°C); Sensor Air Cooling = ON (-15°C)

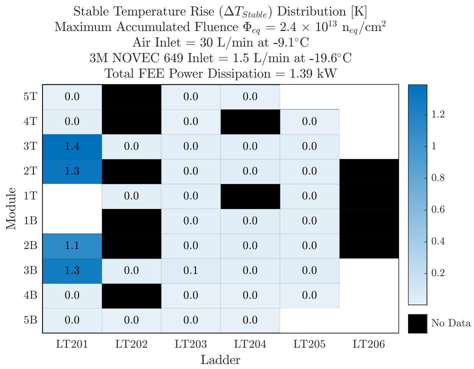

(b) Side-Wall Cooling = OFF; Sensor Air Cooling = ON (-15°C)

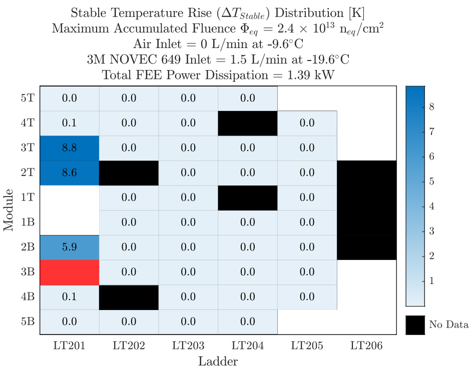

(c) Side-Wall Cooling = ON (-20°C); Sensor Air Cooling = OFF

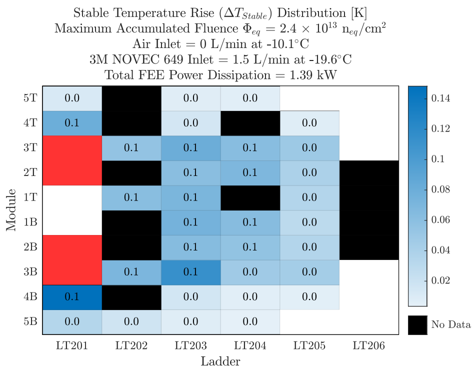

(d) Side-Wall Cooling = OFF; Sensor Air Cooling = OFF

Figure F.18.: Dependency on Side-Wall Cooling: Distributions showing the rise of Stable Temperature (ΔT_{Stable}) across the thermally active half-station for various settings of side-wall cooling (ON ... OFF) along with sensor air cooling (ON ... OFF) after an accumulated fluence of $0.24{\times}10^{14}n_{eq}(1\text{ MeV})/cm^2$ for 10 years of CBM operation. The baseline setting for side-wall cooling is ON at -20°C and for sensor air cooling is ON at -15°C. The innermost area in all figures (LT201-1T/B) represents the beampipe opening, whereas the black bins comprise sensors which are either physically broken or have faulty Pt-100 sensor. The red bins comprise sensors where no T_{Stable} was achieved, i.e., the sensors are in thermal runaway.

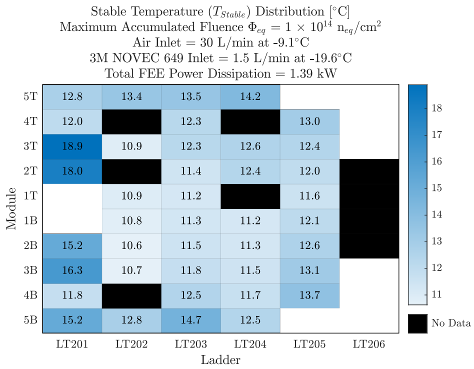

(a) Side-Wall Cooling = ON (-20°C); Sensor Air Cooling = ON (-15°C)

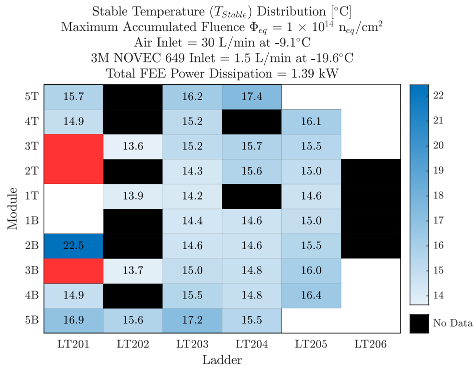

(b) Side-Wall Cooling = OFF; Sensor Air Cooling = ON (-15°C)

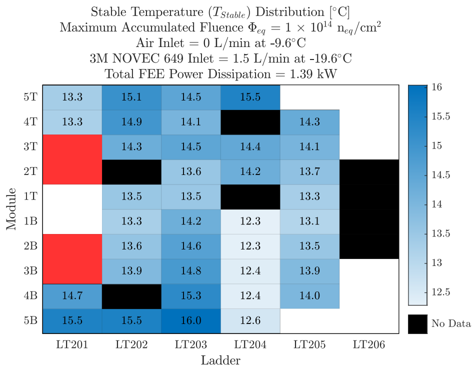

(c) Side-Wall Cooling = ON (-20°C); Sensor Air Cooling = OFF

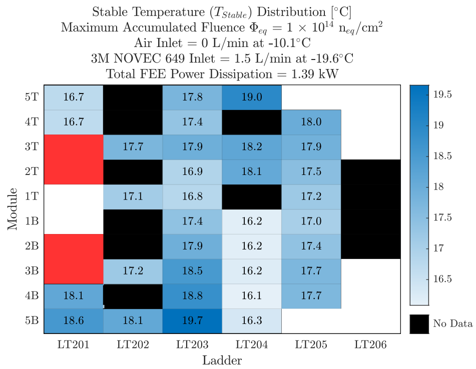

(d) Side-Wall Cooling = OFF; Sensor Air Cooling = OFF

Figure F.19.: Dependency on Side-Wall Cooling: Stable Temperature (T_{Stable}) distributions across the thermally active half-station for various settings of side-wall cooling (ON ... OFF) along with sensor air cooling (ON ... OFF) after the end-of-lifetime fluence of $1 \times 10^{14} n_{eq}(1 \text{ MeV})/cm^2$ which will be reached only after 40 years of CBM operation. The baseline setting for side-wall cooling is ON at -20°C and for sensor air cooling is ON at -15°C. The innermost area in all figures (LT201-1T/B) represents the beampipe opening, whereas the black bins comprise sensors which are either physically broken or have faulty Pt-100 sensor. The red bins comprise sensors where no T_{Stable} was achieved, i.e., the sensors are in thermal runaway.

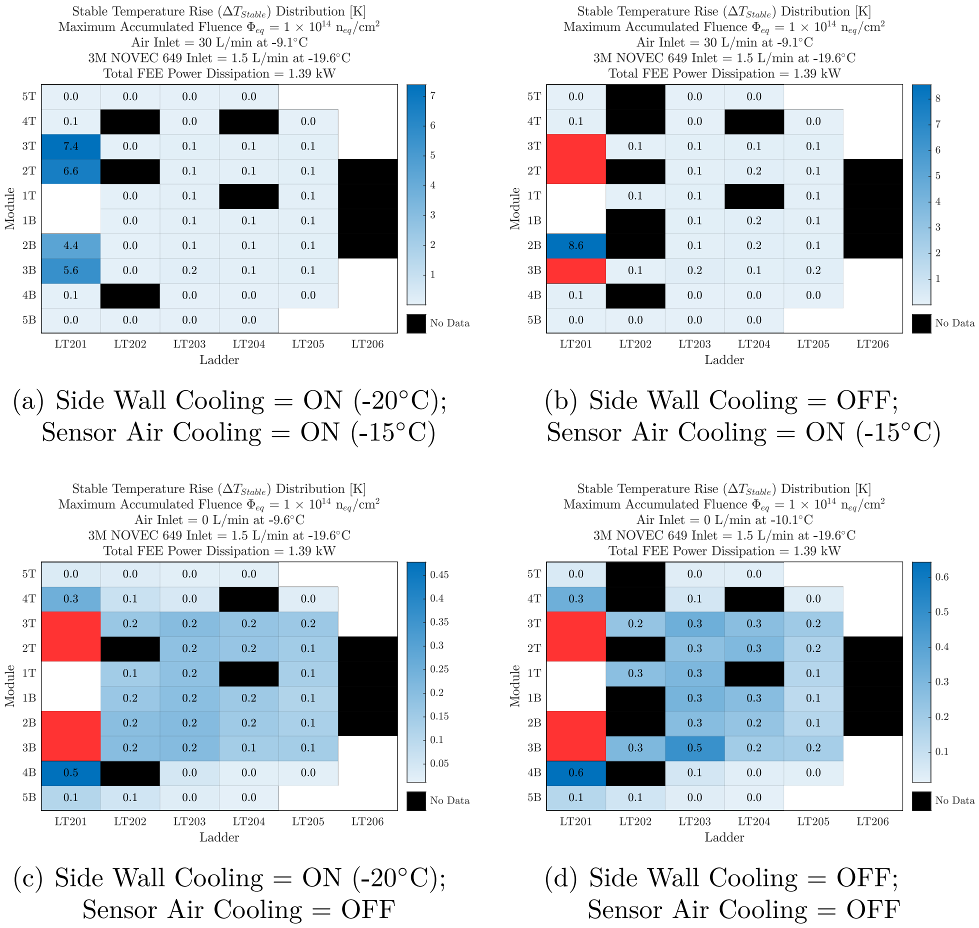

(a) Side Wall Cooling = ON (-20°C); Sensor Air Cooling = ON (-15°C)

(b) Side Wall Cooling = OFF; Sensor Air Cooling = ON (-15°C)

(c) Side Wall Cooling = ON (-20°C); Sensor Air Cooling = OFF

(d) Side Wall Cooling = OFF; Sensor Air Cooling = OFF

Figure F.20.: Dependency on Side-Wall Cooling: Distributions showing the rise of Stable Temperature (ΔT_{Stable}) across the thermally active half-station for various settings of side-wall cooling (ON ... OFF) along with sensor air cooling (ON ... OFF) after the end-of-lifetime fluence of $1 \times 10^{14} n_{eq}(1\ \text{MeV})/cm^2$ which will be reached only after 40 years of CBM operation. The baseline setting for side-wall cooling is ON at -20°C and for sensor air cooling is ON at -15°C. The innermost area in all figures (LT201-1T/B) represents the beampipe opening, whereas the black bins comprise sensors which are either physically broken or have faulty Pt-100 sensor. The red bins comprise sensors where no T_{Stable} was achieved, i.e., the sensors are in thermal runaway.

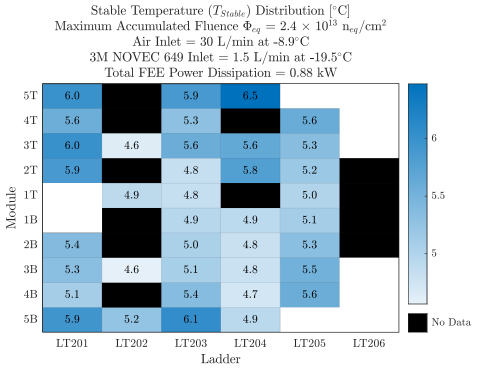

(a) Power Dissipation per FEB = 8.63 W; Minimum Scenario

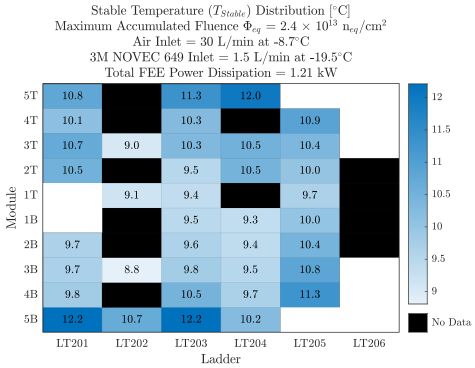

(b) Power Dissipation per FEB = 11.42 W; Typical Scenario

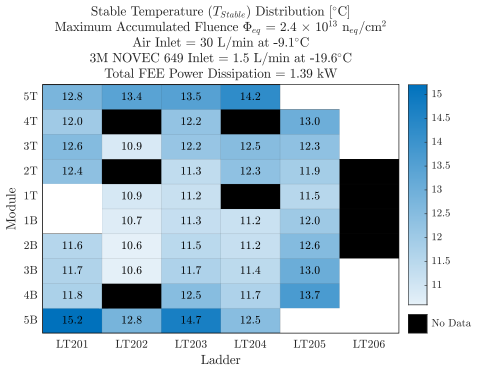

(c) Power Dissipation per FEB = 12.93 W; Maximum Scenario

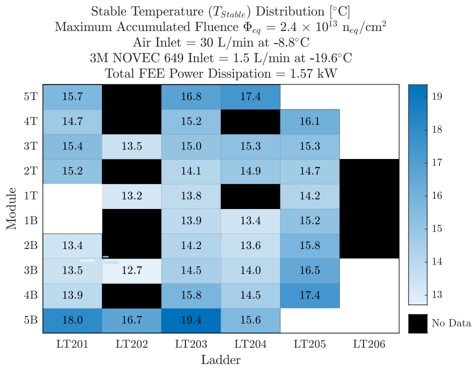

(d) Power Dissipation per FEB = 14.22 W; Maximum Scenario with 10% addition

Figure F.21.: Dependency on FEE Power Dissipation: Stable Temperature (T_{Stable}) distributions across the thermally active half-station for various power dissipation per FEB (8.63 ... 14.22 W) after an accumulated fluence of $0.24{\times}10^{14}n_{eq}(1\ \text{MeV})/\text{cm}^2$ for 10 years of CBM operation. The baseline power dissipation per FEB is the maximum foreseen scenario, i.e., 12.93 W (see App. E.2 for more details about the FEB power dissipation scenarios). The innermost area in all figures (LT201-1T/B) represents the beampipe opening, whereas the black bins comprise sensors which are either physically broken or have faulty Pt-100 sensor. The red bins comprise sensors where no T_{Stable} was achieved, i.e., the sensors are in thermal runaway.

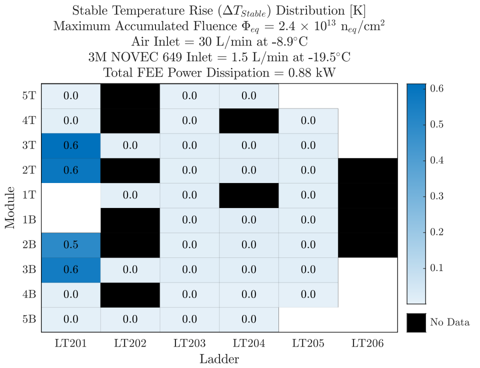

(a) Power Dissipation per FEB = 8.63 W; Minimum Scenario

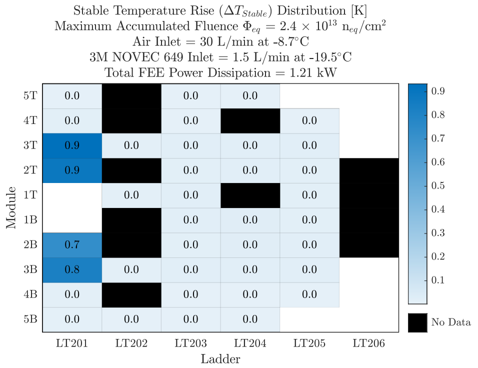

(b) Power Dissipation per FEB = 11.42 W; Typical Scenario

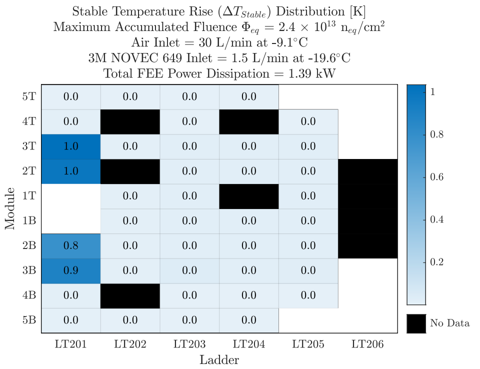

(c) Power Dissipation per FEB = 12.93 W; Maximum Scenario

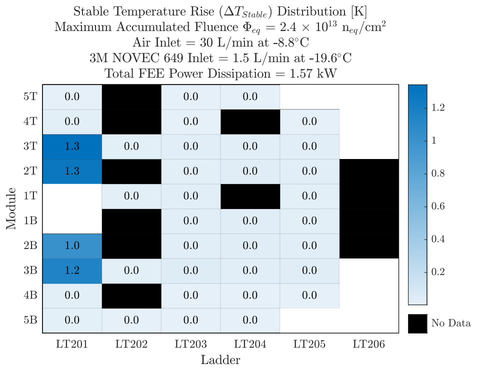

(d) Power Dissipation per FEB = 14.22 W; Maximum Scenario with 10% addition

Figure F.22.: Dependency on FEE Power Dissipation: Distributions showing the rise of Stable Temperature (ΔT_{Stable}) across the thermally active half-station for various power dissipation per FEB (8.63 ... 14.22 W) after an accumulated fluence of $0.24 \times 10^{14} n_{eq}(1\ \text{MeV})/cm^2$ for 10 years of CBM operation. The baseline power dissipation per FEB is the maximum foreseen scenario, i.e., 12.93 W (see App. E.2 for more details about the FEB power dissipation scenarios). The innermost area in all figures (LT201-1T/B) represents the beampipe opening, whereas the black bins comprise sensors which are either physically broken or have faulty Pt-100 sensor. The red bins comprise sensors where no T_{Stable} was achieved, i.e., the sensors are in thermal runaway.

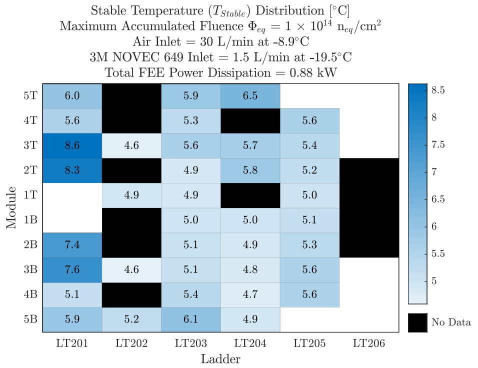

(a) Power Dissipation per FEB = 8.63 W; Minimum Scenario

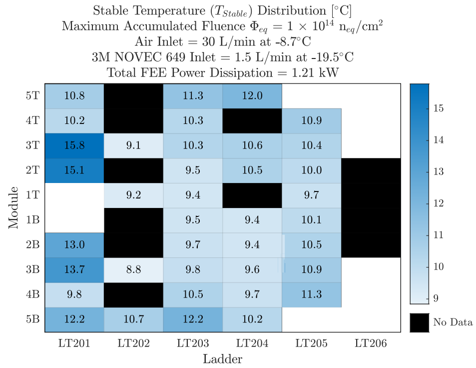

(b) Power Dissipation per FEB = 11.42 W; Typical Scenario

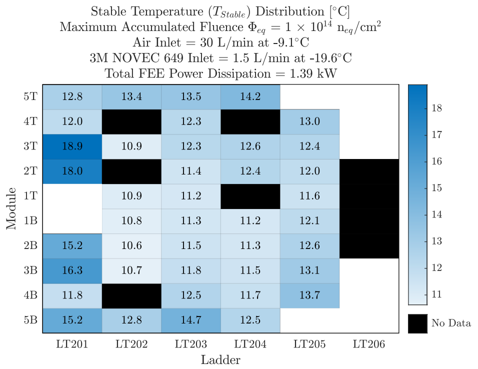

(c) Power Dissipation per FEB = 12.93 W; Maximum Scenario

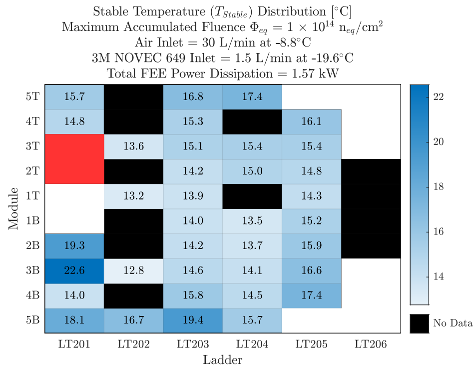

(d) Power Dissipation per FEB = 14.22 W; Maximum Scenario with 10% addition

Figure F.23.: Dependency on FEE Power Dissipation: Stable Temperature (T_{Stable}) distributions across the thermally active half-station for various power dissipation per FEB (8.63 ... 14.22 W) after the end-of-lifetime fluence of $1 \times 10^{14} n_{eq}(1\ \text{MeV})/\text{cm}^2$ which will be reached only after 40 years of CBM operation. The baseline power dissipation per FEB is the maximum foreseen scenario, i.e., 12.93 W (see App. E.2 for more details about the FEB power dissipation scenarios). The innermost area in all figures (LT201-1T/B) represents the beampipe opening, whereas the black bins comprise sensors which are either physically broken or have faulty Pt-100 sensor. The red bins comprise sensors where no T_{Stable} was achieved, i.e., the sensors are in thermal runaway.

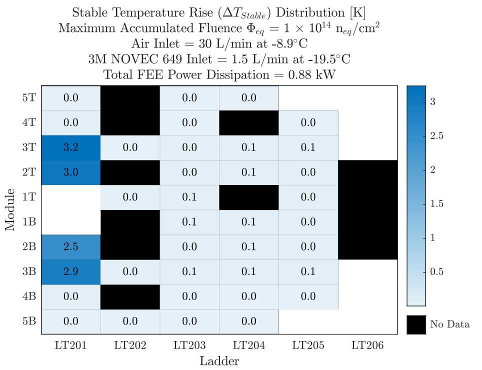

(a) Power Dissipation per FEB = 8.63 W; Minimum Scenario

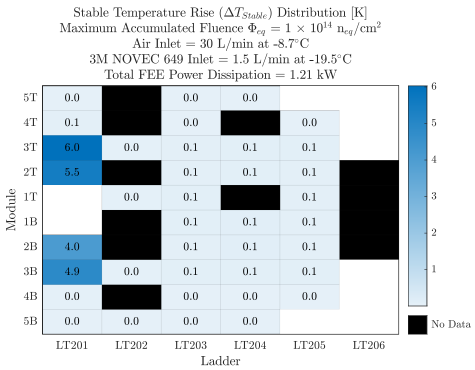

(b) Power Dissipation per FEB = 11.42 W; Typical Scenario

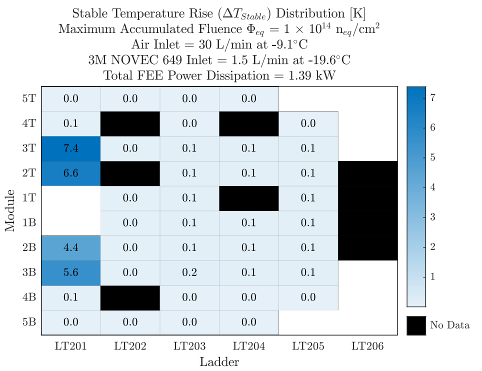

(c) Power Dissipation per FEB = 12.93 W; Maximum Scenario

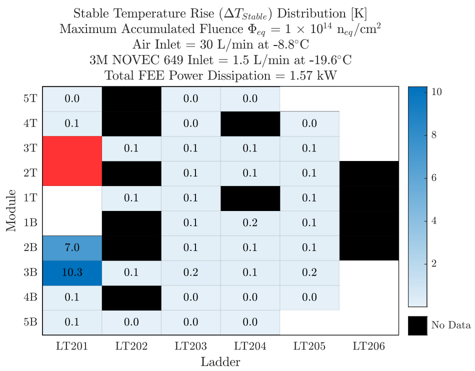

(d) Power Dissipation per FEB = 14.22 W; Maximum Scenario with 10% addition

Figure F.24.: Dependency on FEE Power Dissipation: Distributions showing the rise of Stable Temperature (ΔT_{Stable}) across the thermally active half-station for various power dissipation per FEB (8.63 ... 14.22 W) after the end-of-lifetime fluence of $1 \times 10^{14} n_{eq}(1\ \text{MeV})/\text{cm}^2$ which will be reached only after 40 years of CBM operation. The baseline power dissipation per FEB is the maximum foreseen scenario, i.e., 12.93 W (see App. E.2 for more details about the FEB power dissipation scenarios). The innermost area in all figures (LT201-1T/B) represents the beampipe opening, whereas the black bins comprise sensors which are either physically broken or have faulty Pt-100 sensor. The red bins comprise sensors where no T_{Stable} was achieved, i.e., the sensors are in thermal runaway.

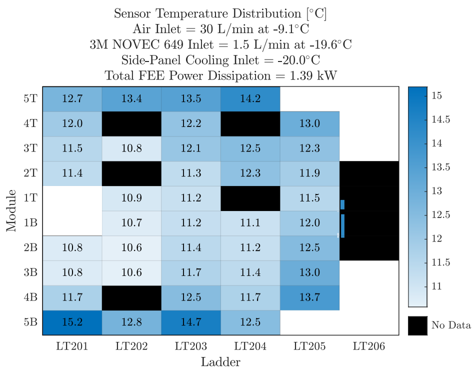

(a) Scenario No: 1

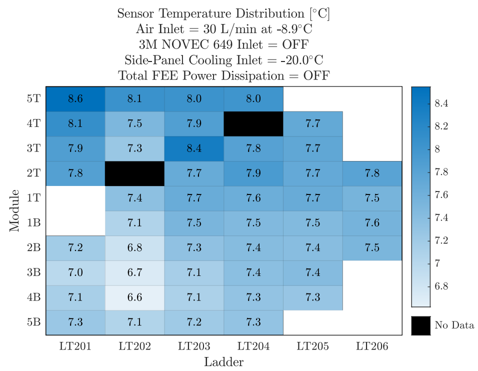

(b) Scenario No: 2

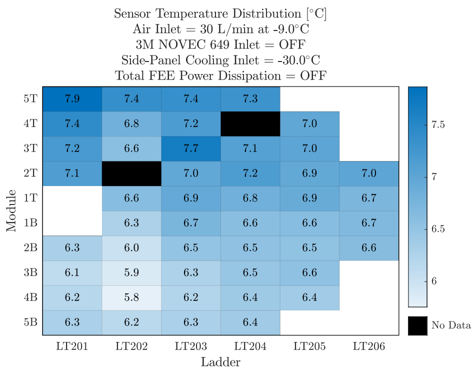

(c) Scenario No: 3

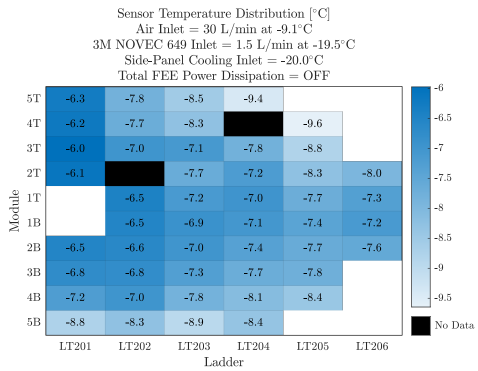

(d) Scenario No: 4

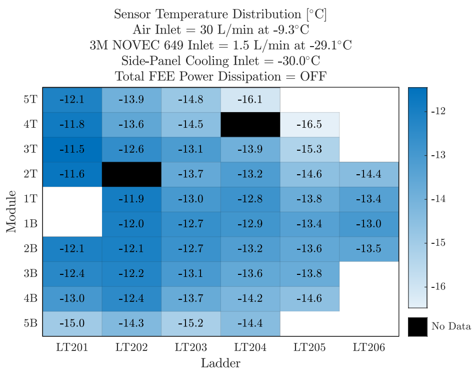

(e) Scenario No: 5

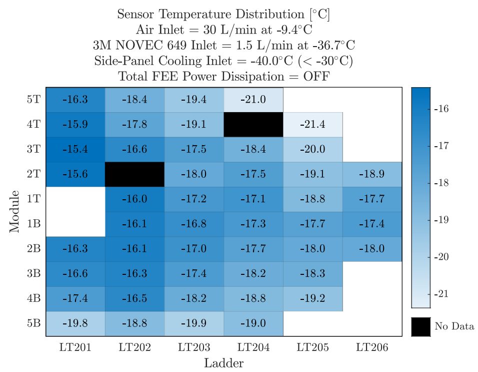

(f) Scenario No: 6

Figure F.25.: Beam Shutdown Scenarios: Sensor temperature distributions across the thermally active half-station for various operating parameter scenarios during beam shutdown (i.e., sensor powering is switched off; see Sec. 4.1.3 for further details about the scenarios). The innermost area in all figures (LT201-1T/B) represents the beampipe opening, whereas the black bins comprise sensors which are either physically broken or have faulty Pt-100 sensor.

Appendix G.

Front-End Electronics Temperature Distributions

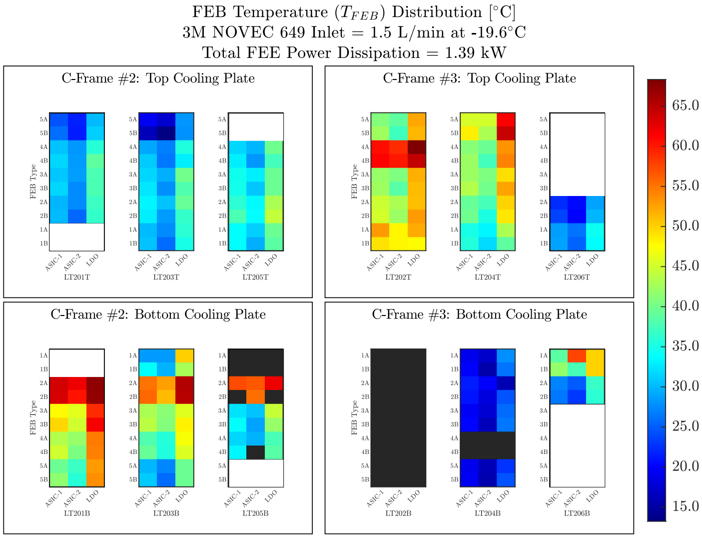

(a) C-Frame Distribution of Mean FEE Temperature (T_{FEE})

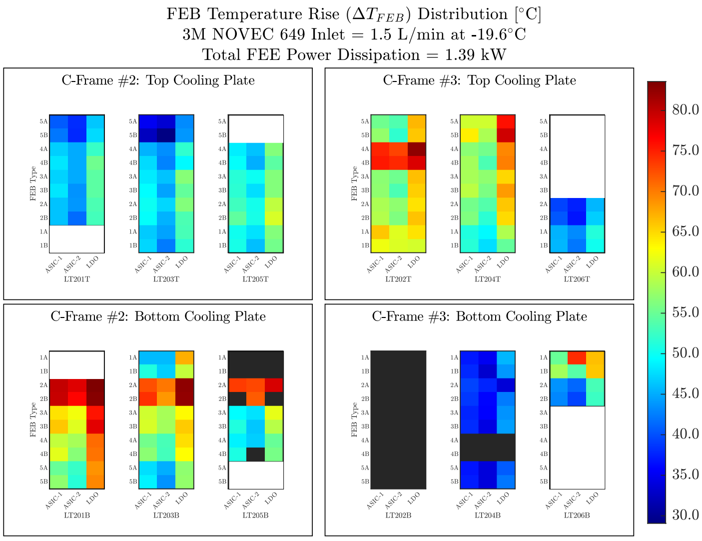

(b) C-Frame Distribution of the Rise of Mean FEE Temperature (ΔT_{FEE})

Figure G.1.: Baseline Scenario: FEE temperature distribution over the two thermally active C-frames for the baseline operation parameters (see Sec. 4.2.1 for the parameters' details). The values are shown for the two ASIC and LDO rows on individual FEBs subsequently grouped together as FEB boxes and cooling plates. The top figure shows the mean FEE temperature in its powered on state (T_{FEE}) and the bottom figure shows the mean rise with reference to its powered off state (ΔT_{FEE}). The white bins represent locations without silicon sensors (beampipe opening and peripheral locations), whereas the black bins comprise represent locations which have faulty DS18B20 temperature readout.

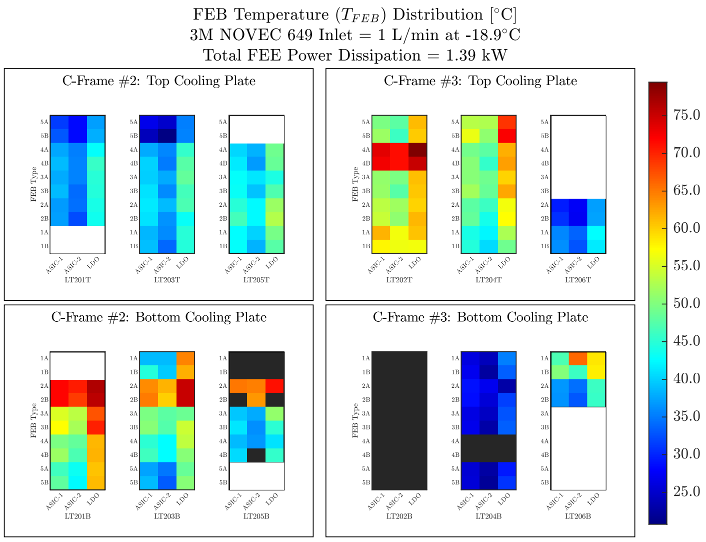

(a) C-Frame Distribution of Mean FEE Temperature (T_{FEE})

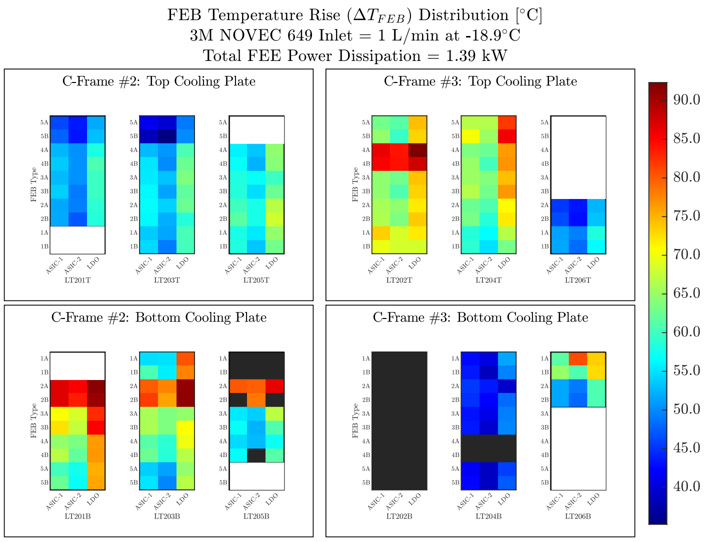

(b) C-Frame Distribution of the Rise of Mean FEE Temperature (ΔT_{FEE})

Figure G.2.: Dependency on 3M™ NOVEC™ 649 Flow Rate (1 L/min): FEE temperature distribution over the two thermally active C-frames for the 3M™ NOVEC™ 649 Flow Rate of 1 L/min (see Sec. 4.2.2.1 for the parameters' details; baseline = 1.5 L/min). The values are shown for the two ASIC and LDO rows on individual FEBs subsequently grouped together as FEB boxes and cooling plates. The top figure shows the mean FEE temperature in its powered on state (T_{FEE}) and the bottom figure shows the mean rise with reference to its powered off state (ΔT_{FEE}). The white bins represent locations without silicon sensors (beampipe opening and peripheral locations), whereas the black bins comprise represent locations which have faulty DS18B20 temperature readout.

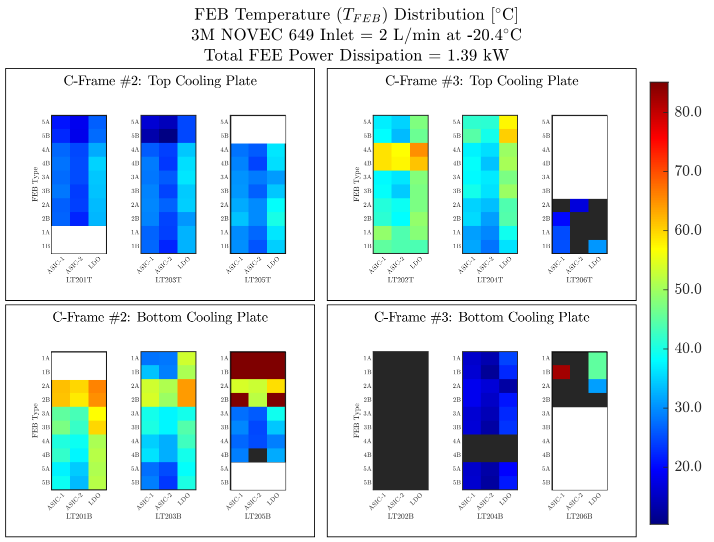

(a) C-Frame Distribution of Mean FEE Temperature (T_{FEE})

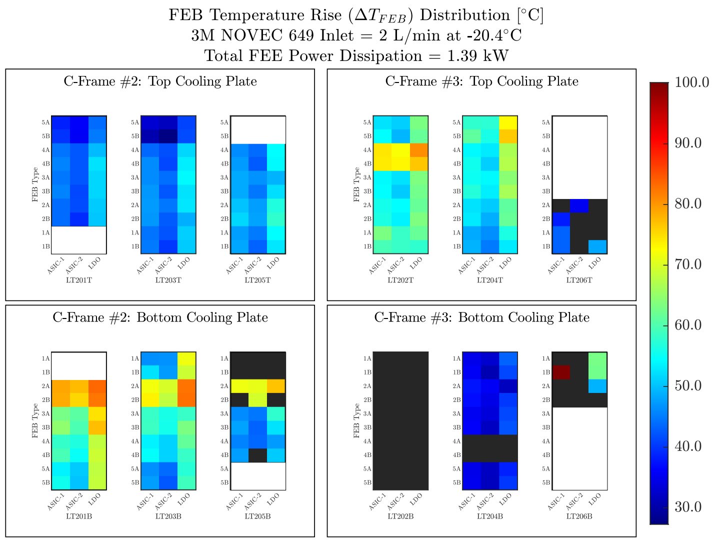

(b) C-Frame Distribution of the Rise of Mean FEE Temperature (ΔT_{FEE})

Figure G.3.: Dependency on 3M™ NOVEC™ 649 Flow Rate (2 L/min): FEE temperature distribution over the two thermally active C-frames for the 3M™ NOVEC™ 649 Flow Rate of 2 L/min (see Sec. 4.2.2.1 for the parameters' details; baseline = 1.5 L/min). The values are shown for the two ASIC and LDO rows on individual FEBs subsequently grouped together as FEB boxes and cooling plates. The top figure shows the mean FEE temperature in its powered on state (T_{FEE}) and the bottom figure shows the mean rise with reference to its powered off state (ΔT_{FEE}). The white bins represent locations without silicon sensors (beampipe opening and peripheral locations), whereas the black bins comprise represent locations which have faulty DS18B20 temperature readout.

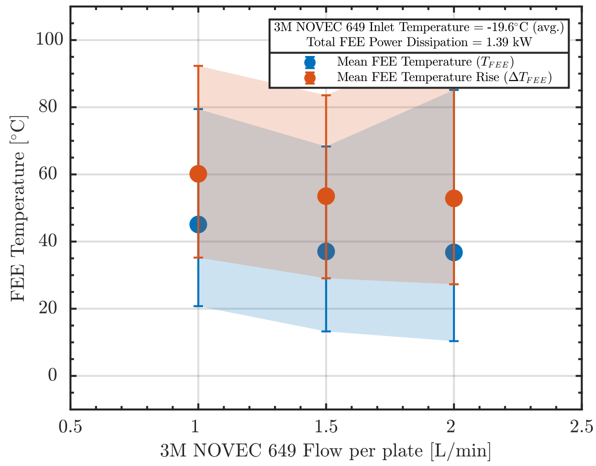

(a)

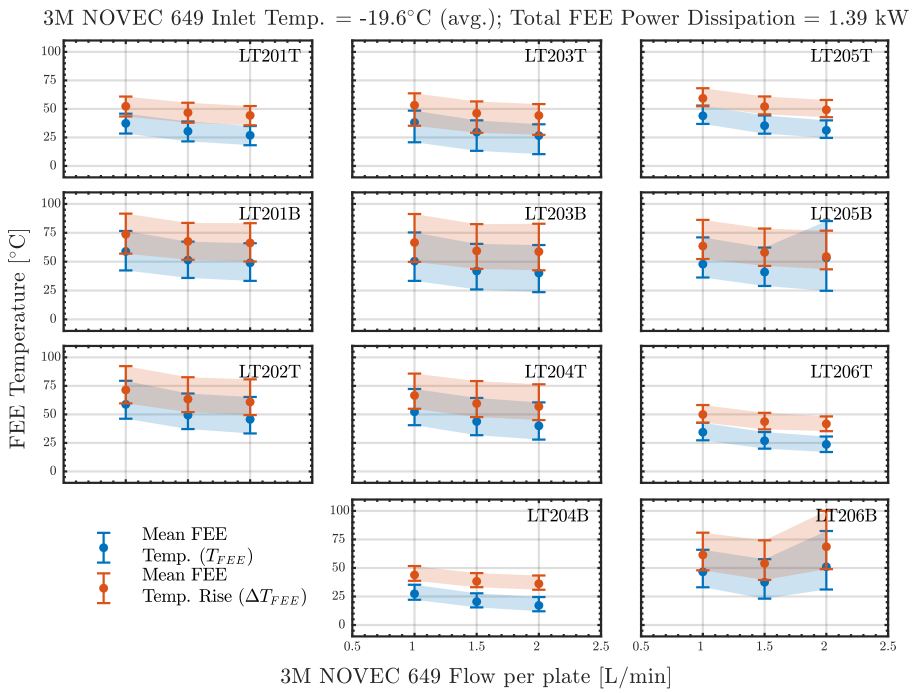

(b)

Figure G.4.: The variation of the FEE temperature with 3M™ NOVEC™ 649 flow rate per cooling plate (set value 1 ... 2 L/min; measured at the distribution manifold outside the Thermal Demonstrator's enclosure). The mean FEE temperature in its powered on state (T_{FEE}) is shown in blue and its mean rise with reference to its powered off state (ΔT_{FEE}) is shown in orange. The top figure is for all FEBs, while the bottom multi-figure panel is for the comprising eleven FEB boxes. Note that measurements from FEB box # LT202B is not shown due to faulty readout. The underlying values are tabulated in Tab. 4.4 and Fig. G.1, G.2-G.3.

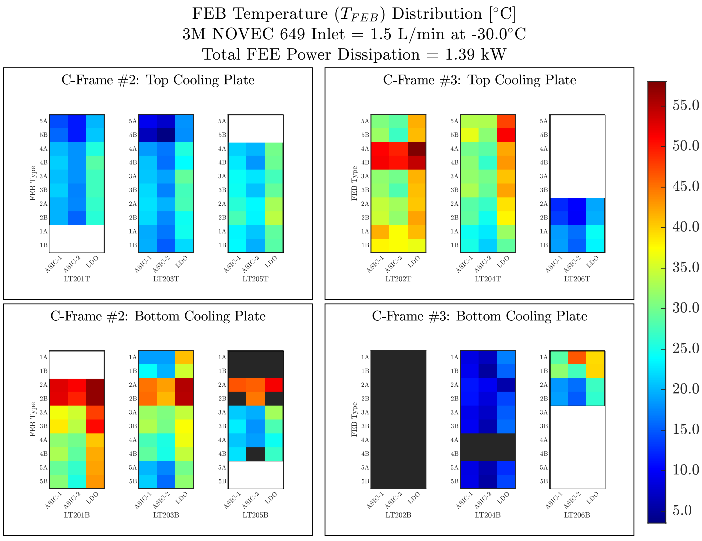

(a) C-Frame Distribution of Mean FEE Temperature (T_{FEE})

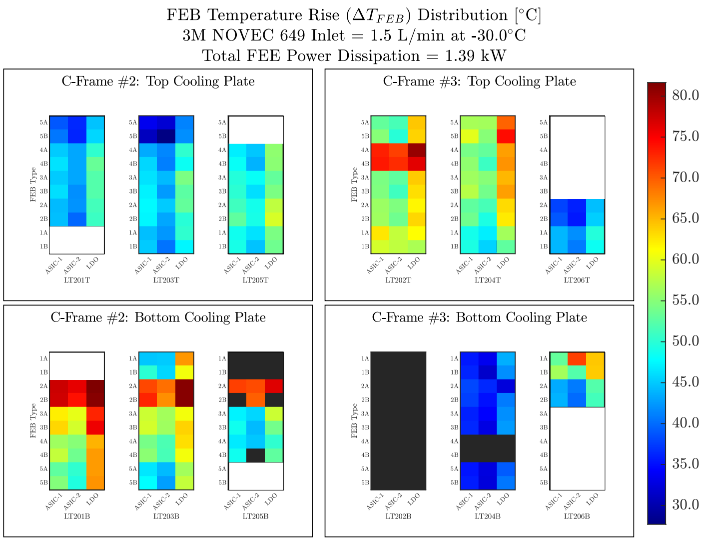

(b) C-Frame Distribution of the Rise of Mean FEE Temperature (ΔT_{FEE})

Figure G.5.: Dependency on 3M™ NOVEC™ 649 Set Temperature (-30°C): FEE temperature distribution over the two thermally active C-frames for the 3M™ NOVEC™ 649 set temperature of -30°C (see Sec. 4.2.2.2 for the parameters' details; baseline = -20°C). The values are shown for the two ASIC and LDO rows on individual FEBs subsequently grouped together as FEB boxes and cooling plates. The top figure shows the mean FEE temperature in its powered on state (T_{FEE}) and the bottom figure shows the mean rise with reference to its powered off state (ΔT_{FEE}). The white bins represent locations without silicon sensors (beampipe opening and peripheral locations), whereas the black bins comprise represent locations which have faulty DS18B20 temperature readout.

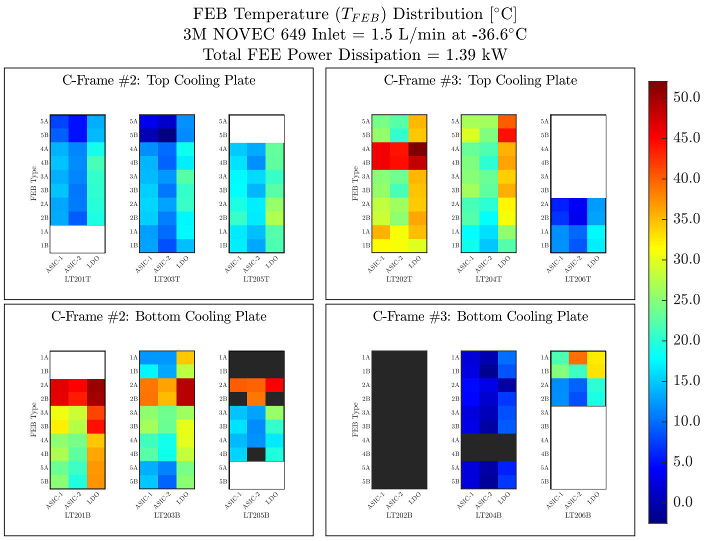

(a) C-Frame Distribution of Mean FEE Temperature (T_{FEE})

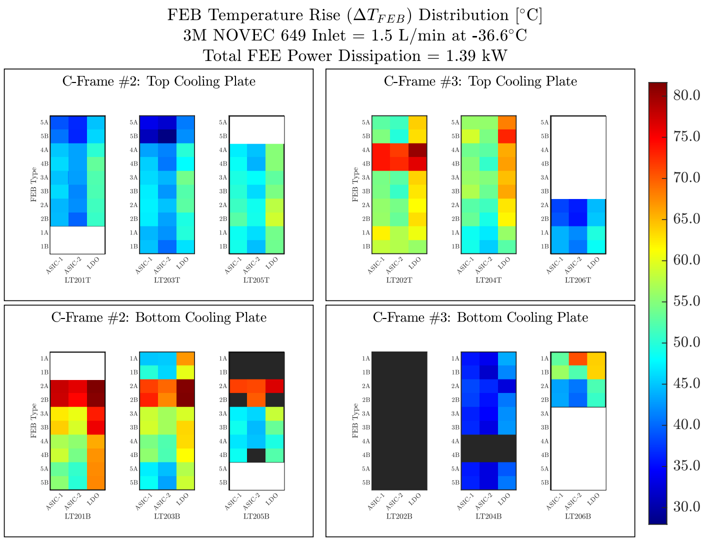

(b) C-Frame Distribution of the Rise of Mean FEE Temperature (ΔT_{FEE})

Figure G.6.: Dependency on 3M™ NOVEC™ 649 Set Temperature (-40°C): FEE temperature distribution over the two thermally active C-frames for the 3M™ NOVEC™ 649 set temperature of -40°C (see Sec. 4.2.2.2 for the parameters' details; baseline = -20°C). The values are shown for the two ASIC and LDO rows on individual FEBs subsequently grouped together as FEB boxes and cooling plates. The top figure shows the mean FEE temperature in its powered on state (T_{FEE}) and the bottom figure shows the mean rise with reference to its powered off state (ΔT_{FEE}). The white bins represent locations without silicon sensors (beampipe opening and peripheral locations), whereas the black bins comprise represent locations which have faulty DS18B20 temperature readout.

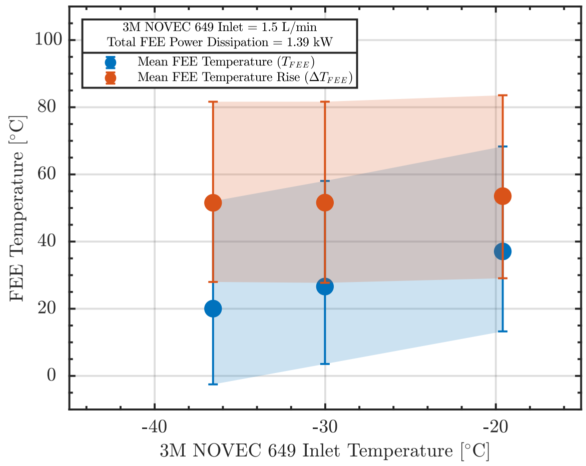

(a)

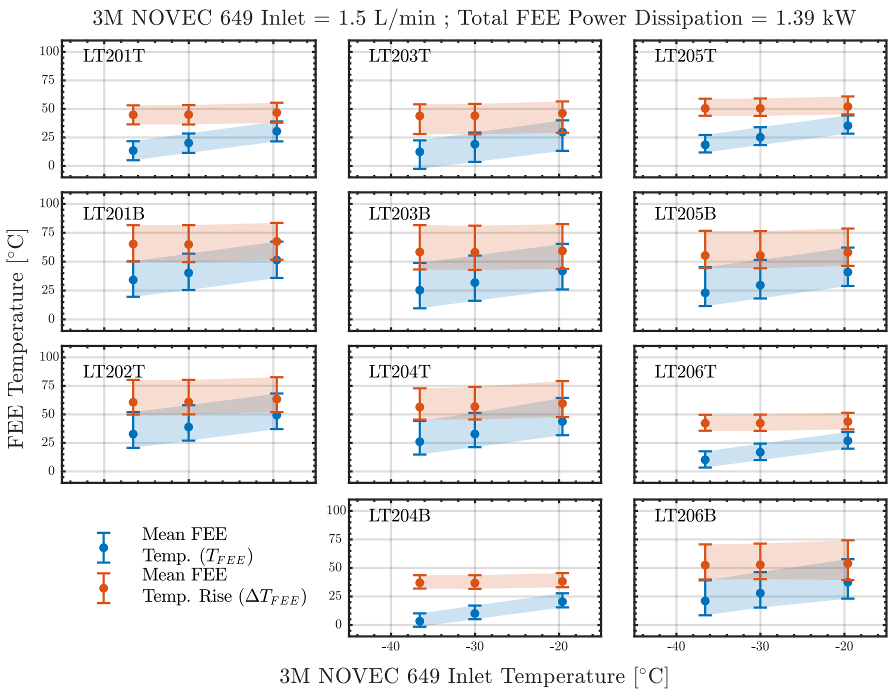

(b)

Figure G.7.: The variation of the FEE temperature with 3M™ NOVEC™ 649 temperature (set value -20 ... 40°C; inlet value -20...-37°C measured at the manifold outside the Thermal Demonstrator's enclosure). The mean FEE temperature in its powered on state (T_{FEE}) is shown in blue and its mean rise with reference to its powered off state (ΔT_{FEE}) is shown in orange. The top figure is for all FEBs, while the bottom multi-figure panel is for the comprising eleven FEB boxes. Note that measurements from FEB box # LT202B is not shown due to faulty readout. The underlying values are tabulated in Tab. 4.4 and Fig. G.1, G.5-G.6.

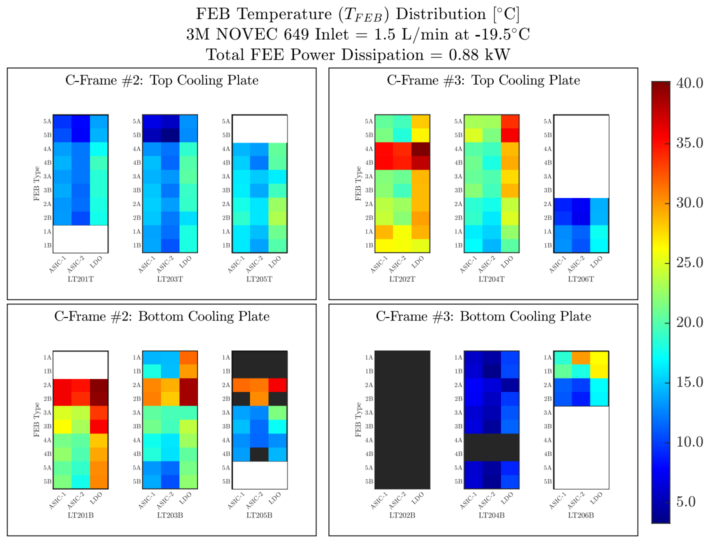

(a) C-Frame Distribution of Mean FEE Temperature (T_{FEE})

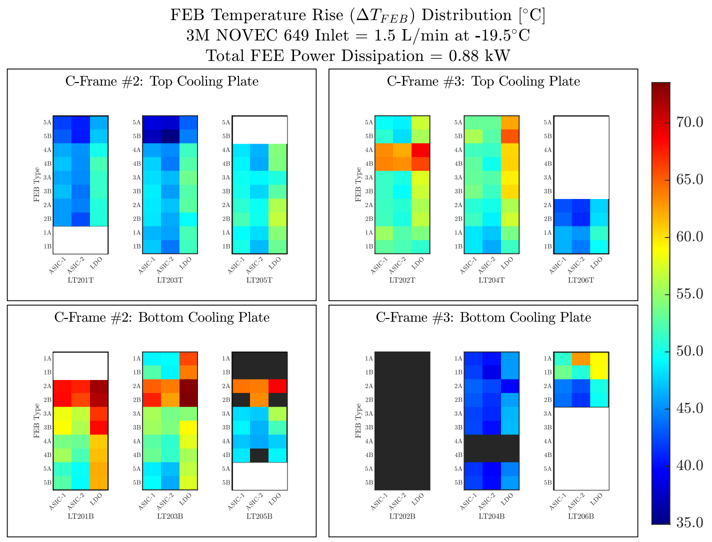

(b) C-Frame Distribution of the Rise of Mean FEE Temperature (ΔT_{FEE})

Figure G.8.: Dependency on FEE Power Dissipation (8.63 W per FEB; Minimum Scenario): FEE temperature distribution over the two thermally active C-frames for the power dissipation per FEB of 8.63 W (see Sec. 4.2.2.3 and App. E.2 for the parameters' details; baseline = Maximum Scenario with 12.93 W per FEB). The values are shown for the two ASIC and LDO rows on individual FEBs subsequently grouped together as FEB boxes and cooling plates. The top figure shows the mean FEE temperature in its powered on state (T_{FEE}) and the bottom figure shows the mean rise with reference to its powered off state (ΔT_{FEE}). The white bins represent locations without silicon sensors (beampipe opening and peripheral locations), whereas the black bins comprise represent locations which have faulty DS18B20 temperature readout.

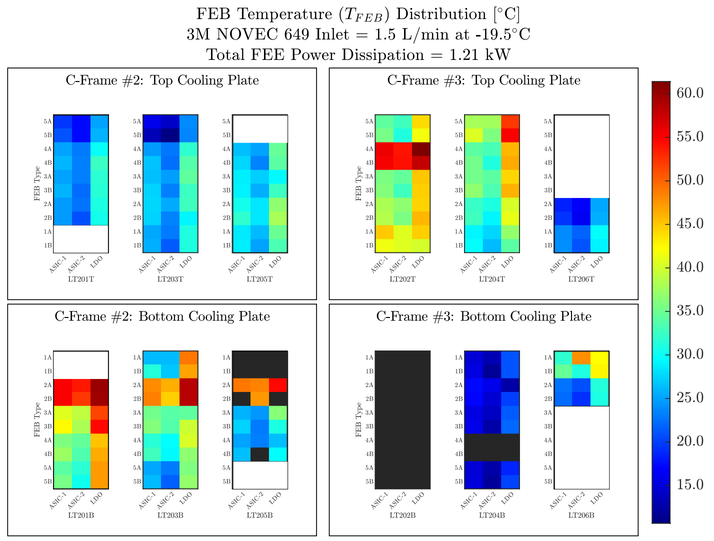

(a) C-Frame Distribution of Mean FEE Temperature (T_{FEE})

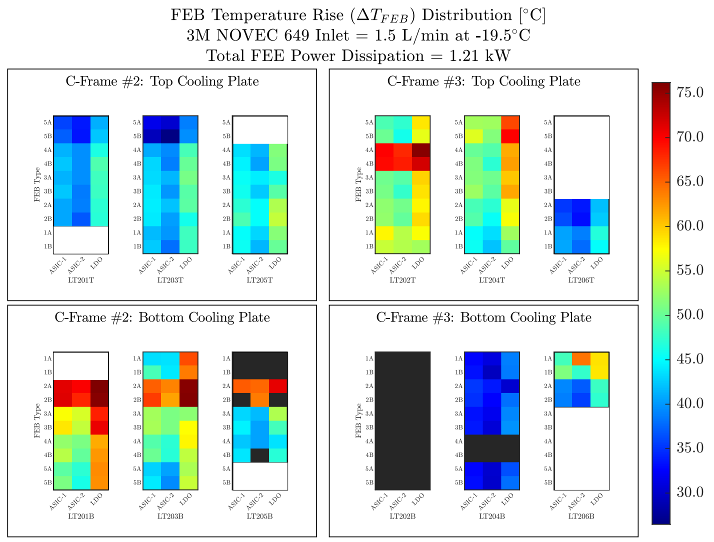

(b) C-Frame Distribution of the Rise of Mean FEE Temperature (ΔT_{FEE})

Figure G.9.: Dependency on FEE Power Dissipation (11.42 W per FEB; Typical Scenario): FEE temperature distribution over the two thermally active C-frames for the power dissipation per FEB of 11.42 W (see Sec. 4.2.2.3 and App. E.2 for the parameters' details; baseline = Maximum Scenario with 12.93 W per FEB). The values are shown for the two ASIC and LDO rows on individual FEBs subsequently grouped together as FEB boxes and cooling plates. The top figure shows the mean FEE temperature in its powered on state (T_{FEE}) and the bottom figure shows the mean rise with reference to its powered off state (ΔT_{FEE}). The white bins represent locations without silicon sensors (beampipe opening and peripheral locations), whereas the black bins comprise represent locations which have faulty DS18B20 temperature readout.

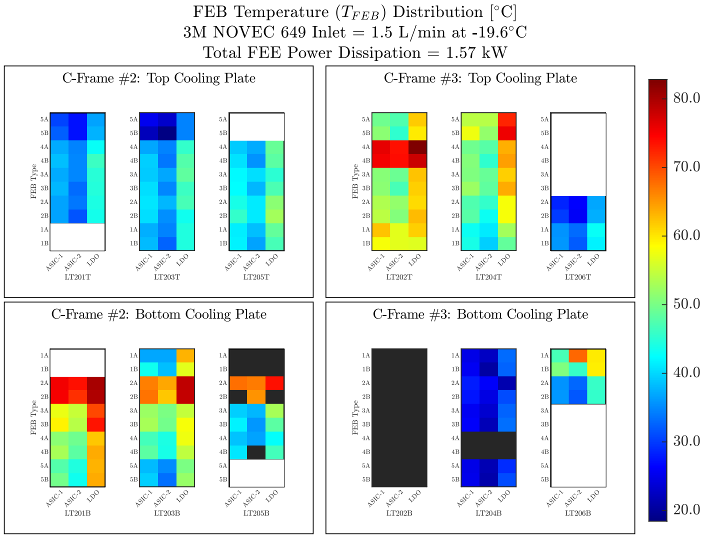

(a) C-Frame Distribution of Mean FEE Temperature (T_{FEE})

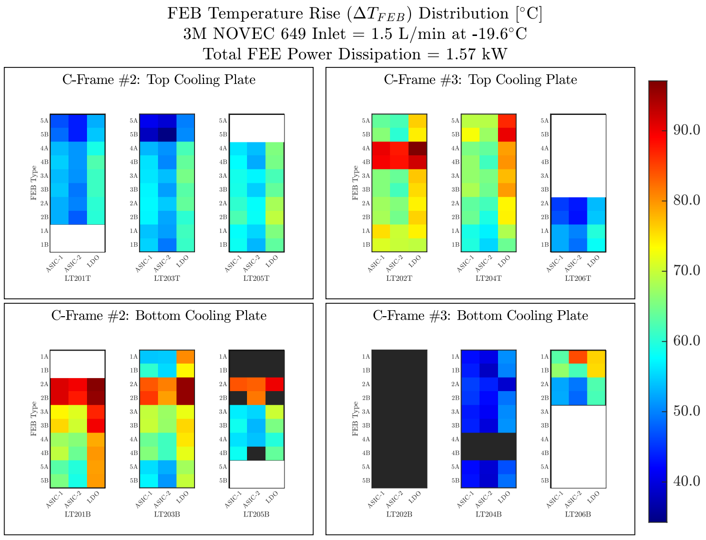

(b) C-Frame Distribution of the Rise of Mean FEE Temperature (ΔT_{FEE})

Figure G.10.: Dependency on FEE Power Dissipation (14.22 W per FEB; Maximum Scenario with 10% addition): FEE temperature distribution over the two thermally active C-frames for the power dissipation per FEB of 14.22 W (see Sec. 4.2.2.3 and App. E.2 for the parameters' details; baseline = Maximum Scenario with 12.93 W per FEB). The values are shown for the two ASIC and LDO rows on individual FEBs subsequently grouped together as FEB boxes and cooling plates. The top figure shows the mean FEE temperature in its powered on state (T_{FEE}) and the bottom figure shows the mean rise with reference to its powered off state (ΔT_{FEE}). The white bins represent locations without silicon sensors (beampipe opening and peripheral locations), whereas the black bins comprise represent locations which have faulty DS18B20 temperature readout.

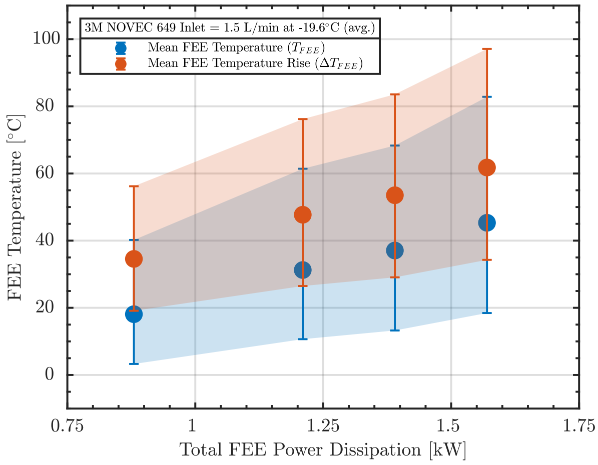

(a)

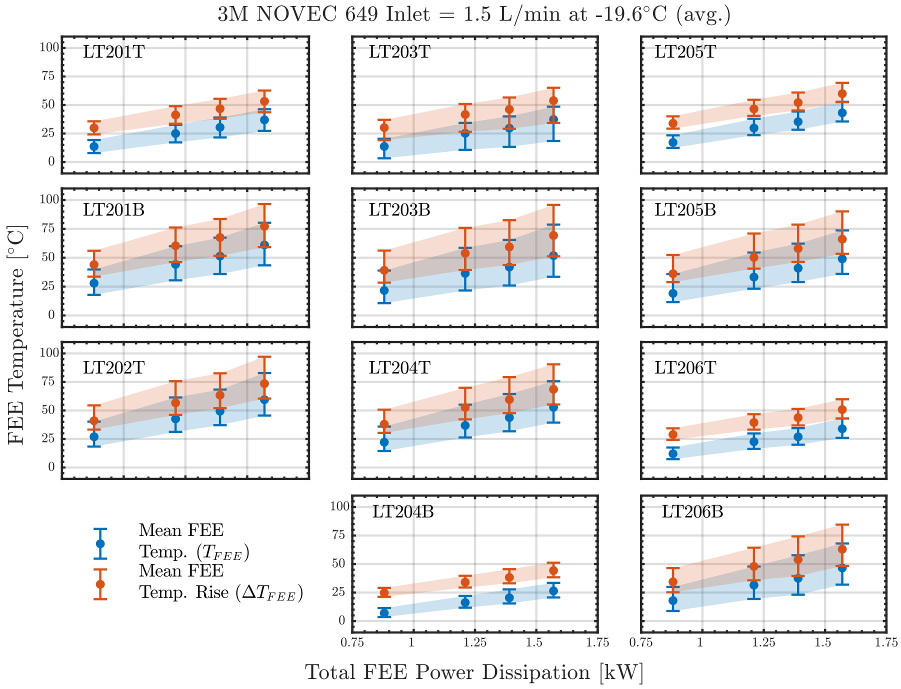

(b)

Figure G.11.: The variation of the FEE temperature with FEB power dissipation (per FEB values ranging from 8.63 ... 14.22 W and total values ranging from 0.88 ... 1.57 kW). The mean FEE temperature in its powered on state (T_{FEE}) is shown in blue and its mean rise with reference to its powered off state (ΔT_{FEE}) is shown in orange. The top figure is for all FEBs, while the bottom multi-figure panel is for the comprising eleven FEB boxes. Note that measurements from FEB box # LT202B is not shown due to faulty readout. The underlying values are tabulated in Tab. 4.4 and Fig. G.1, G.8-G.10.

Appendix H.

Interplay between Silicon Sensor and Front-End Electronics Temperature Distributions

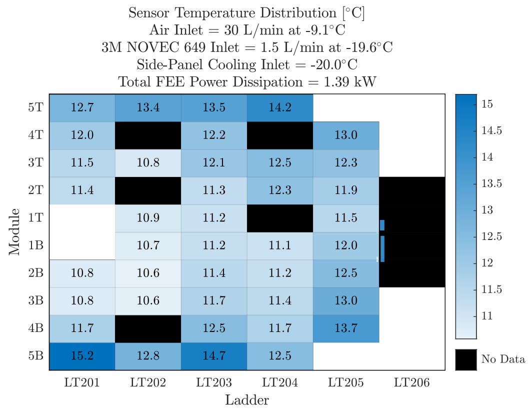

(a)

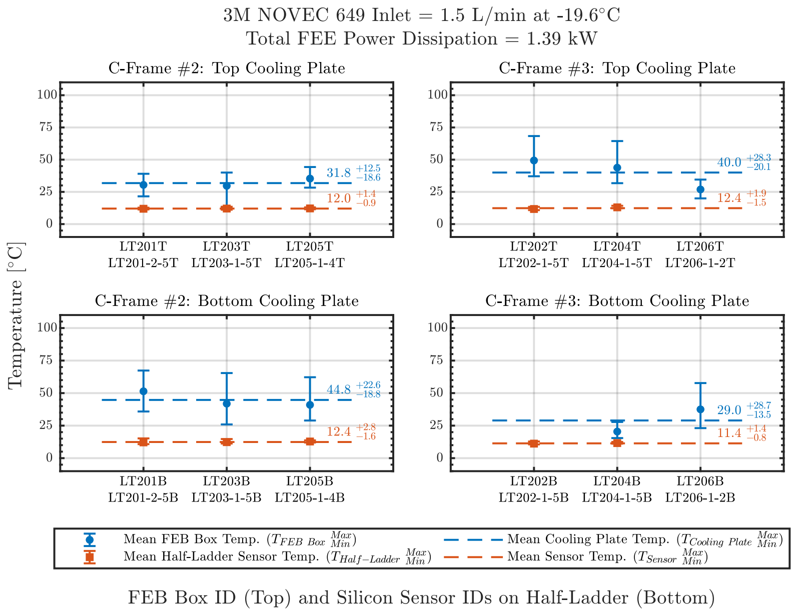

(b)

Figure H.1.: Baseline Scenario: (a) Sensor temperature distribution across the thermally active half-station for the baseline operational scenario when the silicon sensors are powered off, i.e., equivalent to unirradiated scenario (see Sec. 4.1.1 for the parameters' details). The innermost area in all figures (LT201-1T/B) represents the beam pipe opening, whereas the black bins comprise sensors which are either physically broken or have faulty Pt-100 sensor. (b) Mean temperature variation of all FEB boxes (blue circle markers) and their corresponding sensors on the half-ladder (orange square markers) for the baseline operation parameters (see Sec. 4.2.1 for the parameters' details). Values are grouped based on the four cooling plates of the two thermally active C-frames. The dashed lines represent the mean temperatures of the cooling plates (blue) and sensors (orange).

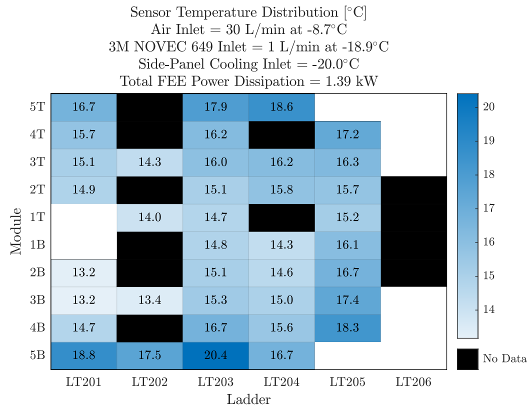

(a)

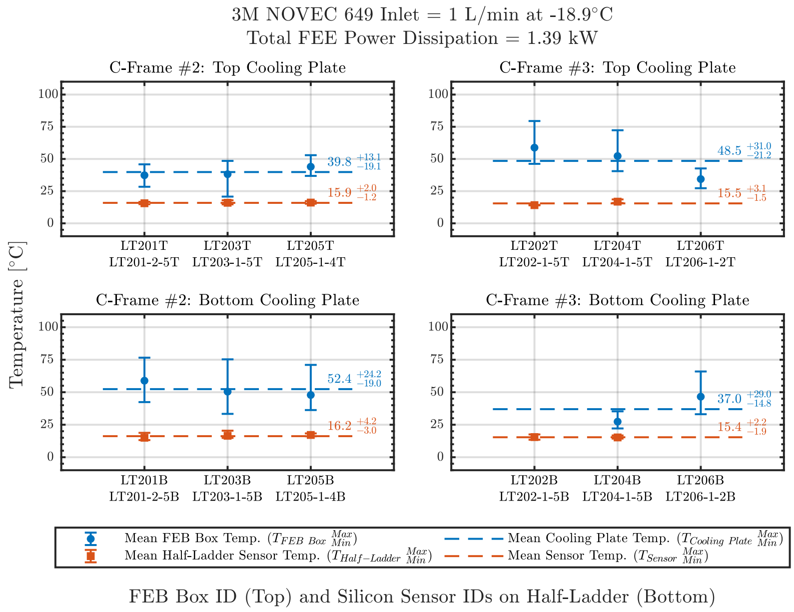

(b)

Figure H.2.: Dependency on 3M™ NOVEC™ 649 Flow Rate (1 L/min): (a) Sensor temperature distribution across the thermally active half-station for 3M™ NOVEC™ 649 Flow Rate of 1 L/min when the silicon sensors are powered off, i.e., equivalent to unirradiated scenario (see Sec. 4.1.1 for the parameters' details; baseline = 1.5 L/min). The innermost area in all figures (LT201-1T/B) represents the beam pipe opening, whereas the black bins comprise sensors which are either physically broken or have faulty Pt-100 sensor. (b) Mean temperature variation of all FEB boxes (blue circle markers) and their corresponding sensors on the half-ladder (orange square markers) for 3M™ NOVEC™ 649 Flow Rate of 1 L/min (see Sec. 4.2.1 for the parameters' details; baseline = 1.5 L/min). Values are grouped based on the four cooling plates of the two thermally active C-frames. The dashed lines represent the mean temperatures of the cooling plates (blue) and sensors (orange).

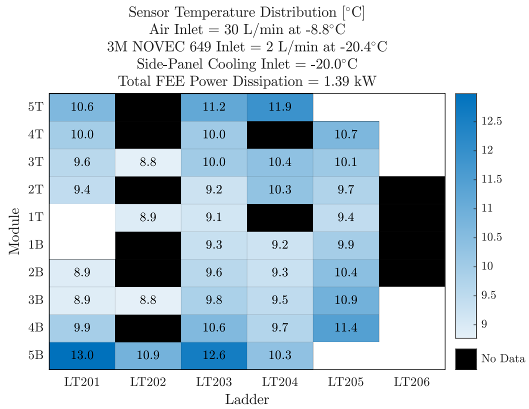

(a)

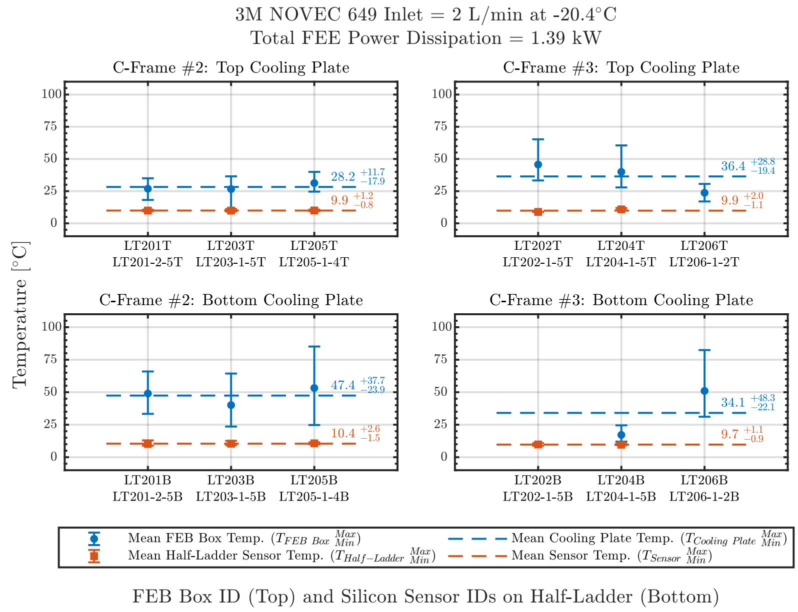

(b)

Figure H.3.: Dependency on 3M™ NOVEC™ 649 Flow Rate (2 L/min): (a) Sensor temperature distribution across the thermally active half-station for 3M™ NOVEC™ 649 Flow Rate of 2 L/min when the silicon sensors are powered off, i.e., equivalent to unirradiated scenario (see Sec. 4.1.1 for the parameters' details; baseline = 1.5 L/min). The innermost area in all figures (LT201-1T/B) represents the beam pipe opening, whereas the black bins comprise sensors which are either physically broken or have faulty Pt-100 sensor. (b) Mean temperature variation of all FEB boxes (blue circle markers) and their corresponding sensors on the half-ladder (orange square markers) for 3M™ NOVEC™ 649 Flow Rate of 2 L/min (see Sec. 4.2.1 for the parameters' details; baseline = 1.5 L/min). Values are grouped based on the four cooling plates of the two thermally active C-frames. The dashed lines represent the mean temperatures of the cooling plates (blue) and sensors (orange).

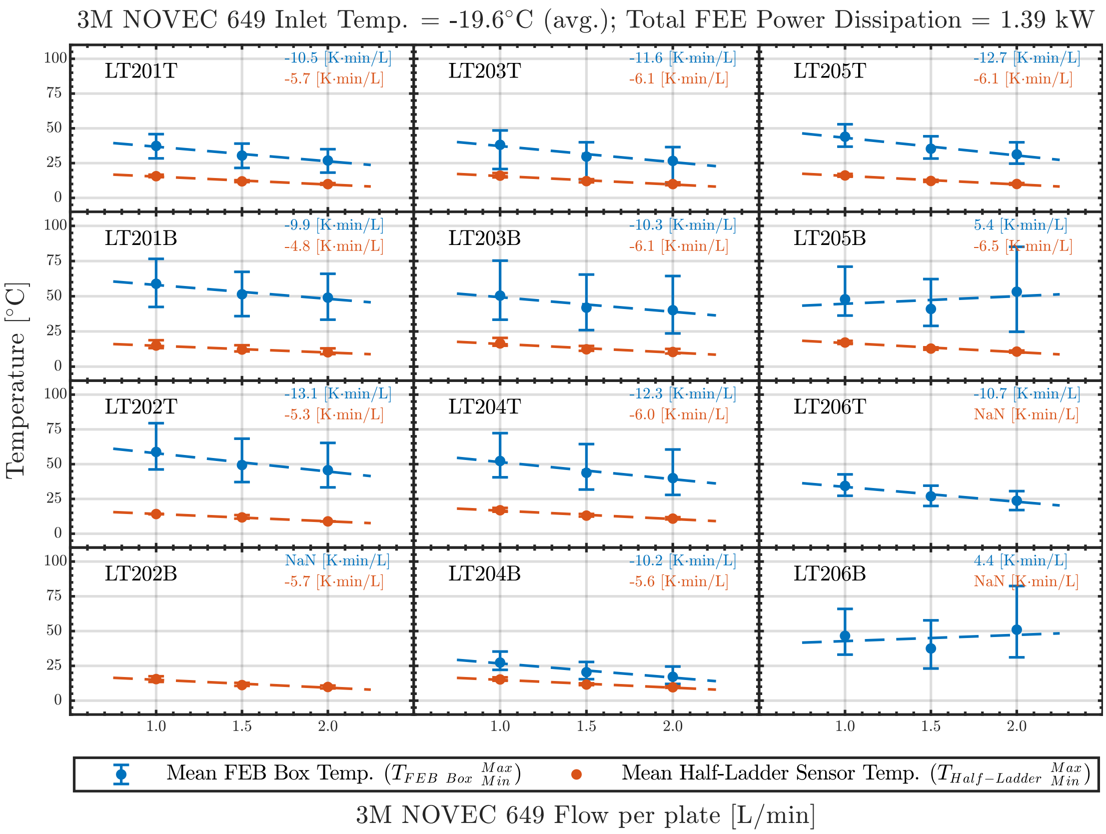

Figure H.4.: Dependency on 3M™ NOVEC™ 649 Flow Rate: Variation of mean FEE ($T_{FEE}{}^{+Max}_{-Min}$) and silicon sensor temperature ($T_{Silicon}{}^{+Max}_{-Min}$) with 3M™ NOVEC™ 649 flow rate per cooling plate for all FEB boxes (blue markers) and their corresponding sensors on the half-ladder (orange markers). The flow rate variation is for set value of 1 ... 2 L/min (measured at the distribution manifold outside the Thermal Demonstrator's enclosure). Dotted lines are the respective linear fits indicating the rate of temperature change with the slope values mentioned on the top right of every panel. Temperature distributions for individual cases are in Fig. H.2-H.3. The silicon sensor temperatures for LT206T and LT206B, and the FEE temperatures for LT202B are missing measurements due to either physically broken or faulty temperature readout. See Sec. 4.2.2.1 for the average variation across the entire thermally active half-station.

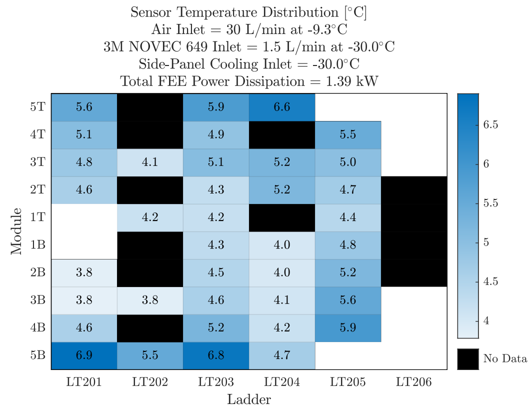

(a)

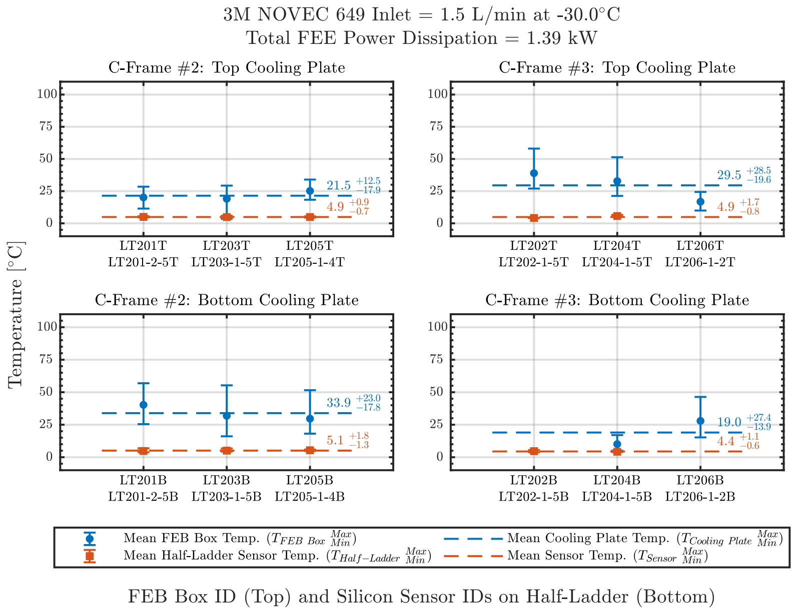

(b)

Figure H.5.: Dependency on 3M™ NOVEC™ 649 Set Temperature (-30°C): (a) Sensor temperature distribution across the thermally active half-station for 3M™ NOVEC™ 649 set temperature of -30°C when the silicon sensors are powered off, i.e., equivalent to unirradiated scenario (see Sec. 4.1.1 for the parameters' details; baseline = -20°C). The innermost area in all figures (LT201-1T/B) represents the beam pipe opening, whereas the black bins comprise sensors which are either physically broken or have faulty Pt-100 sensor. (b) Mean temperature variation of all FEB boxes (blue circle markers) and their corresponding sensors on the half-ladder (orange square markers) for 3M™ NOVEC™ 649 set temperature of -30°C (see Sec. 4.2.1 for the parameters' details; baseline = -20°C). Values are grouped based on the four cooling plates of the two thermally active C-frames. The dashed lines represent the mean temperatures of the cooling plates (blue) and sensors (orange).

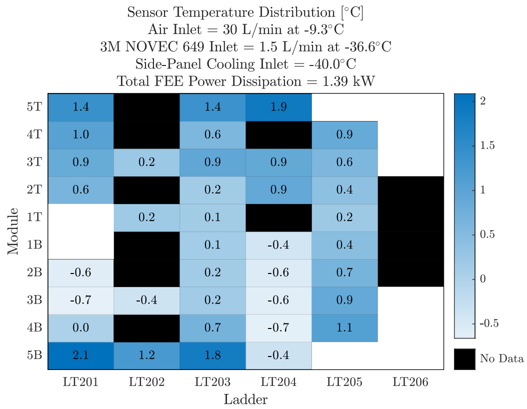

(a)

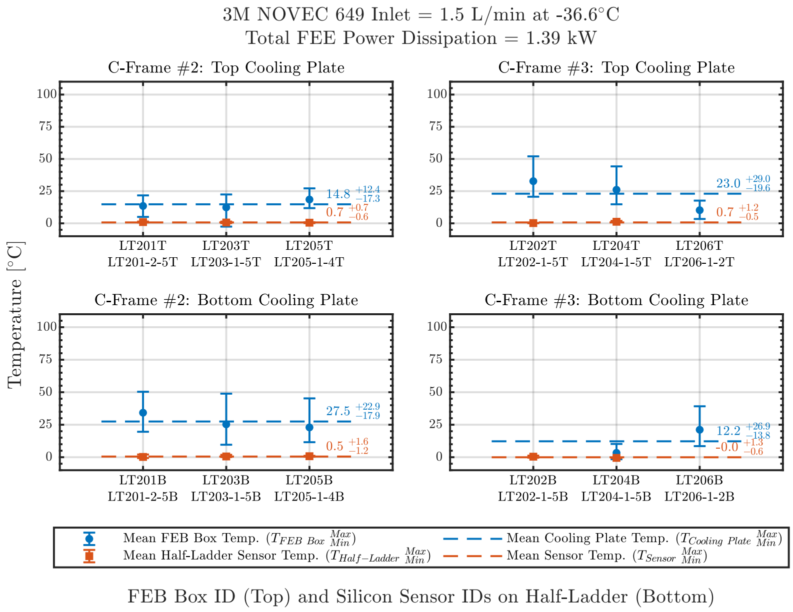

(b)

Figure H.6.: Dependency on 3M™ NOVEC™ 649 Set Temperature (-40°C): (a) Sensor temperature distribution across the thermally active half-station for 3M™ NOVEC™ 649 set temperature of -40°C when the silicon sensors are powered off, i.e., equivalent to unirradiated scenario (see Sec. 4.1.1 for the parameters' details; baseline = -20°C). The innermost area in all figures (LT201-1T/B) represents the beam pipe opening, whereas the black bins comprise sensors which are either physically broken or have faulty Pt-100 sensor. (b) Mean temperature variation of all FEB boxes (blue circle markers) and their corresponding sensors on the half-ladder (orange square markers) for 3M™ NOVEC™ 649 set temperature of -30°C (see Sec. 4.2.1 for the parameters' details; baseline = -20°C). Values are grouped based on the four cooling plates of the two thermally active C-frames. The dashed lines represent the mean temperatures of the cooling plates (blue) and sensors (orange).

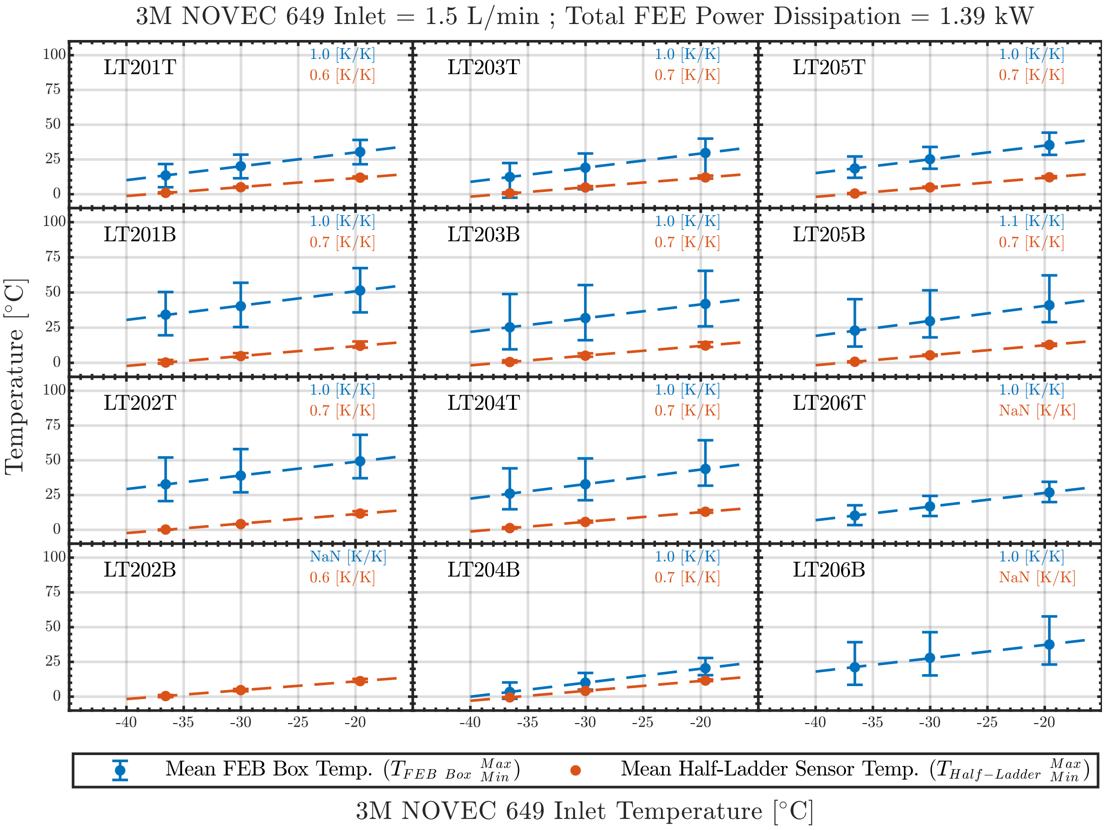

Figure H.7.: Dependency on 3M™ NOVEC™ 649 Set Temperature: Variation of mean FEE ($T_{FEE}{}^{+Max}_{-Min}$) and silicon sensor temperature ($T_{Silicon}{}^{+Max}_{-Min}$) with 3M™ NOVEC™ 649 set temperature for all FEB boxes (blue markers) and their corresponding sensors on the half-ladder (orange markers). The inlet temperature variation is for set value of -40 ... -20°C (measured at the distribution manifold outside the Thermal Demonstrator's enclosure). Dotted lines are the respective linear fits indicating the rate of temperature change with the slope values mentioned on the top right of every panel. Temperature distributions for individual cases are in Fig. H.5-H.6. The silicon sensor temperatures for LT206T and LT206B, and the FEE temperatures for LT202B are missing measurements due to either physically broken or faulty temperature readout. See Sec. 4.2.2.1 for the average variation across the entire thermally active half-station.

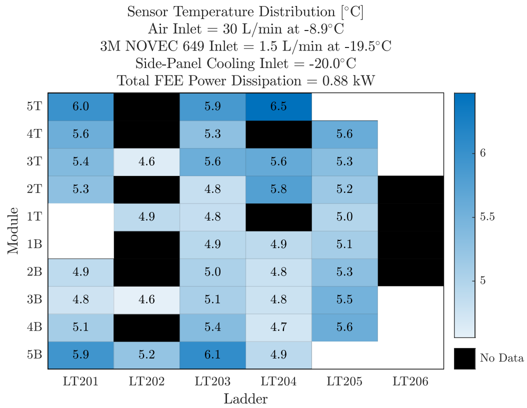

(a)

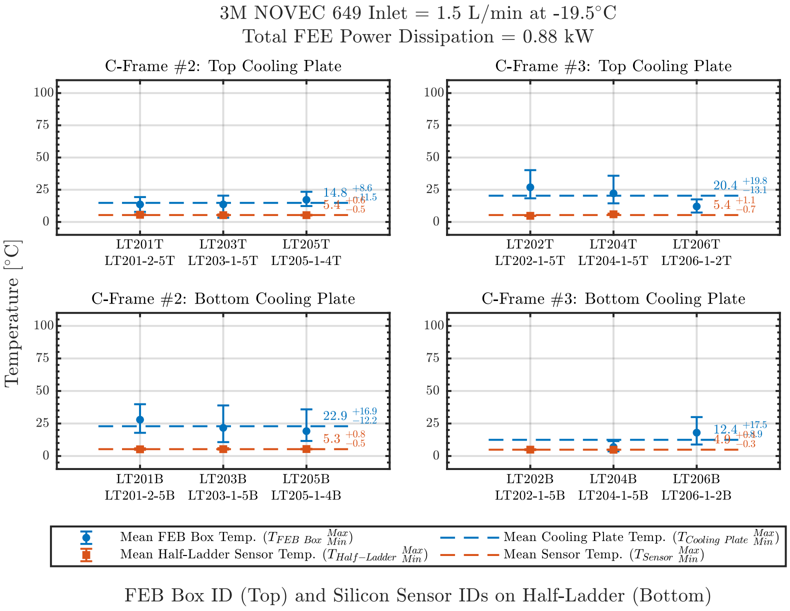

(b)

Figure H.8.: Dependency on FEE Power Dissipation (8.63 W per FEB; Minimum Scenario): (a) Sensor temperature distribution across the thermally active half-station for the power dissipation per FEB of 8.63 W when the silicon sensors are powered off, i.e., equivalent to unirradiated scenario (see Sec. 4.1.1 and App. E.2 for the parameters' details; baseline = Maximum Scenario with 12.93 W per FEB). The innermost area in all figures (LT201-1T/B) represents the beam pipe opening, whereas the black bins comprise sensors which are either physically broken or have faulty Pt-100 sensor. (b) Mean temperature variation of all FEB boxes (blue circle markers) and their corresponding sensors on the half-ladder (orange square markers) for the power dissipation per FEB of 8.63 W (see Sec. 4.1.1 and App. E.2 for the parameters' details; baseline = Maximum Scenario with 12.93 W per FEB). Values are grouped based on the four cooling plates of the two thermally active C-frames. The dashed lines represent the mean temperatures of the cooling plates (blue) and sensors (orange).

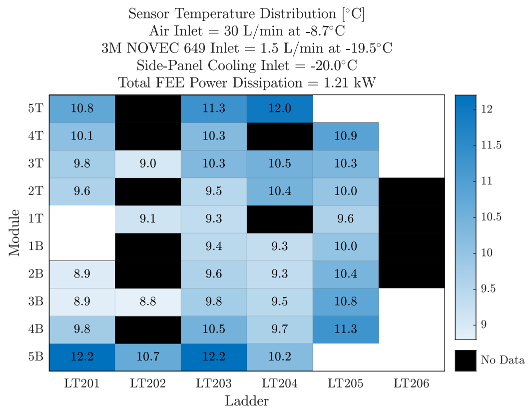

(a)

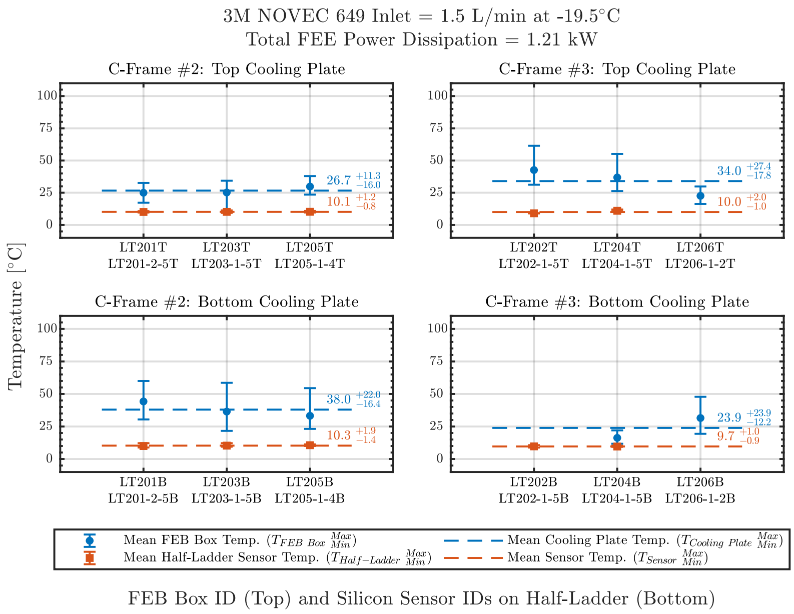

(b)

Figure H.9.: Dependency on FEE Power Dissipation (11.42 W per FEB; Typical Scenario): (a) Sensor temperature distribution across the thermally active half-station for the power dissipation per FEB of 11.42 W when the silicon sensors are powered off, i.e., equivalent to unirradiated scenario (see Sec. 4.1.1 and App. E.2 for the parameters' details; baseline = Maximum Scenario with 12.93 W per FEB). The innermost area in all figures (LT201-1T/B) represents the beam pipe opening, whereas the black bins comprise sensors which are either physically broken or have faulty Pt-100 sensor. (b) Mean temperature variation of all FEB boxes (blue circle markers) and their corresponding sensors on the half-ladder (orange square markers) for the power dissipation per FEB of 11.42 W (see Sec. 4.1.1 and App. E.2 for the parameters' details; baseline = Maximum Scenario with 12.93 W per FEB). Values are grouped based on the four cooling plates of the two thermally active C-frames. The dashed lines represent the mean temperatures of the cooling plates (blue) and sensors (orange).

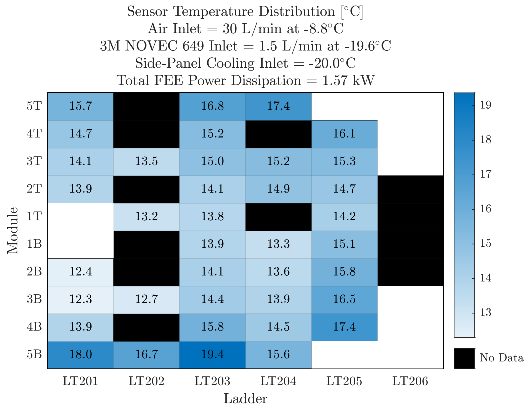

(a)

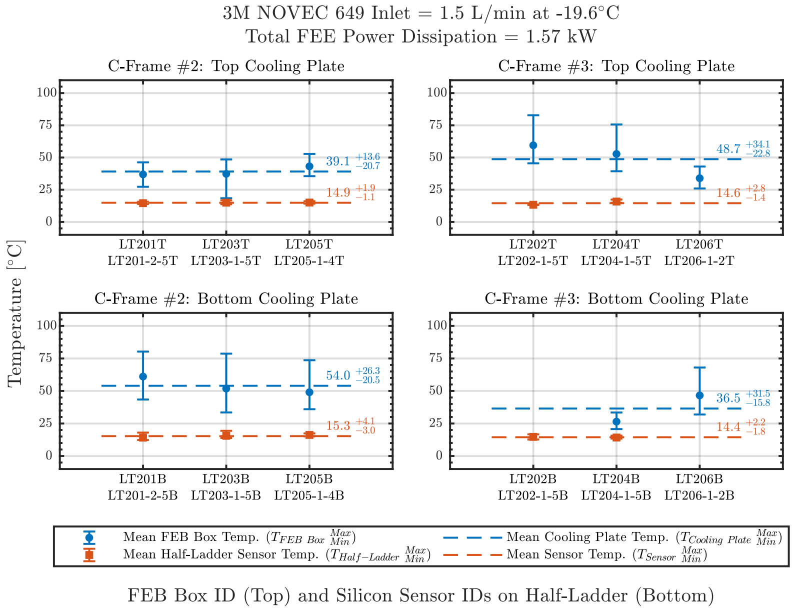

(b)

Figure H.10.: Dependency on FEE Power Dissipation (14.22 W per FEB; Maximum + 10%): (a) Sensor temperature distribution across the thermally active half-station for the power dissipation per FEB of 14.22 W when the silicon sensors are powered off, i.e., equivalent to unirradiated scenario (see Sec. 4.1.1 and App. E.2 for the parameters' details; baseline = Maximum Scenario with 12.93 W per FEB). The innermost area in all figures (LT201-1T/B) represents the beam pipe opening, whereas the black bins comprise sensors which are either physically broken or have faulty Pt-100 sensor. (b) Mean temperature variation of all FEB boxes (blue circle markers) and their corresponding sensors on the half-ladder (orange square markers) for the power dissipation per FEB of 14.22 W (see Sec. 4.1.1 and App. E.2 for the parameters' details; baseline = Maximum Scenario with 12.93 W per FEB). Values are grouped based on the four cooling plates of the two thermally active C-frames. The dashed lines represent the mean temperatures of the cooling plates (blue) and sensors (orange).

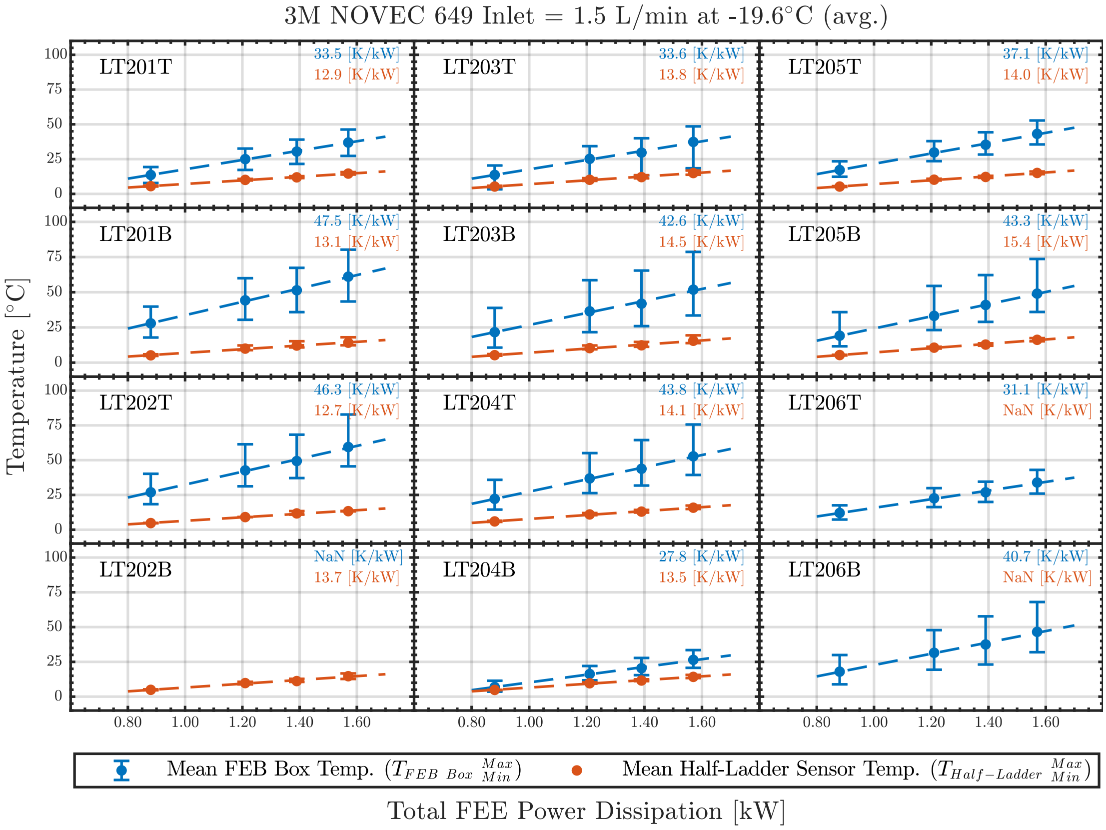

Figure H.11.: Dependency on FEE Power Dissipation: Variation of mean FEE ($T_{FEE}{}^{+Max}_{-Min}$) and silicon sensor temperature ($T_{Silicon}{}^{+Max}_{-Min}$) with FEE power dissipation for all FEB boxes (blue markers) and their corresponding sensors on the half-ladder (orange markers). The FEE power dissipation is for set value of 8.63 ... 14.22 W per FEB (total 0.88 ... 1.57 kW) (see App. E.2 for the parameters' details). Dotted lines are the respective linear fits indicating the rate of temperature change with the slope values mentioned on the top right of every panel. Temperature distributions for individual cases are in Fig. H.8-H.10. The silicon sensor temperatures for LT206T and LT206B, and the FEE temperatures for LT202B are missing measurements due to either physically broken or faulty temperature readout. See Sec. 4.2.2.1 for the average variation across the entire thermally active half-station.

Bibliography

[1] T. Ferbel. *Experimental Techniques in High Energy Physics*, volume 64. Addison-Wesley, Calif., 1987.

[2] W. R. Leo. *Techniques for Nuclear and Particle Physics Experiments.* Springer, 1994.

[3] K. Kleinknecht. *Detectors for Particle Radiation.* Cambridge University Press, 1998.

[4] H.-G. Moser. Silicon detector systems in high energy physics. *Prog. Part. Nucl. Phys.*, 63:186–237, 2009.

[5] G. Knoll. *Radiation Detection and Measurement (4th ed.).* John Wiley, Hoboken, NJ, 2010.

[6] C. Leroy and P.-G. Rancoita. *Principles of Radiation Interaction in Matter and Detection.* World Scientific, Singapore, 2011.

[7] C. Grupen and I. Buvat, editors. *Handbook of Particle Detection and Imaging, Vol. 1 and Vol. 2.* Springer Berlin, Heidelberg, 2012.

[8] H. Kolanoski and N. Wermes. *Particle Detectors.* Oxford University Press, 6 2020.

[9] C. Grupen and B. Schwartz. *Particle Detectors (2nd Edition).* Cambridge Monographs on Particle Physics, Nuclear Physics and Cosmology. Cambridge University Press, 7 2023.

[10] G. Lutz. *Semiconductor Radiation Detectors: Device Physics.* Springer, New York, 1999.

[11] C. Haber. Introductory lectures on tracking detectors. *AIP Conf. Proc.*, 674(1):36–75, 2003.

[12] H. Spieler. *Semiconductor Detector Systems*, volume v.12 of *Semiconductor Science and Technology.* Oxford University Press, Oxford, 2005.

[13] C. Lippmann. Particle identification. *Nucl. Instrum. Meth. A*, 666:148–172, 2012.

[14] F. Hartmann. Silicon tracking detectors in high-energy physics. *Nucl. Instrum. Meth. A*, 666:25–46, 2012.

[15] F. Hartmann. *Evolution of Silicon Sensor Technology in Particle Physics*, volume 275 of *Springer Tracts in Modern Physics*. Springer, 2017.

[16] M. Garcia-Sciveres and N. Wermes. A review of advances in pixel detectors for experiments with high rate and radiation. *Rept. Prog. Phys.*, 81(6):066101, 2018.

[17] I. Panasenko. *Development of Electrical Quality Assurance Procedures and Methods for the Silicon Tracking System of the CBM Experiment*. PhD thesis, Eberhard Karls University of Tuebingen, 3 2023.

[18] A. Tumasyan et al. A portrait of the Higgs boson by the CMS experiment ten years after the discovery. *Nature*, 607(7917):60–68, 2022.

[19] A. S. Schwarz. Heavy flavor physics at colliders with silicon strip vertex detectors. *Phys. Rept.*, 238:1–133, 1994.

[20] R. Barate et al. Study of B_s^0 oscillations and lifetime using fully reconstructed D_s - decays. *Eur. Phys. J. C*, 4:367–385, 1998.

[21] R. Barate et al. Search for B_s^0 oscillations using inclusive lepton events. *Eur. Phys. J. C*, 7:553–569, 1999.

[22] P. Abreu et al. Measurement of the B_s^0 lifetime and study of $B_s^0 - \bar{B}_s^0$ oscillations using $D_s\ell$ events. *Eur. Phys. J. C*, 16:555, 2000.

[23] S. Abachi et al. Observation of the top quark. *Phys. Rev. Lett.*, 74:2632–2637, 1995.

[24] F. Abe et al. Observation of top quark production in $\bar{p}p$ collisions. *Phys. Rev. Lett.*, 74:2626–2631, 1995.

[25] G. Aad et al. Observation of a new particle in the search for the Standard Model Higgs boson with the ATLAS detector at the LHC. *Phys. Lett. B*, 716:1–29, 2012.

[26] G. Aad et al. A detailed map of Higgs boson interactions by the ATLAS experiment ten years after the discovery. *Nature*, 607(CERN-EP-2022-057):52–59, 2022. [Erratum: Nature 612, E24 (2022)].

[27] S. Chatrchyan et al. Observation of a New Boson at a Mass of 125 GeV with the CMS Experiment at the LHC. *Phys. Lett. B*, 716:30–61, 2012.

[28] D. Dobrigkeit Chinellato. Charm and multi-charm baryon measurements via strangeness tracking with the upgraded ALICE detector. *EPJ Web Conf.*, 259:09004, 2022.

[29] J. Adams et al. Experimental and theoretical challenges in the search for the quark gluon plasma: The STAR Collaboration's critical assessment of the evidence from RHIC collisions. *Nucl. Phys. A*, 757:102–183, 2005.

[30] S. Gupta et al. Scale for the Phase Diagram of Quantum Chromodynamics. *Science*, 332:1525–1528, 2011.

[31] ALICE Collaboration. The ALICE experiment – A journey through QCD. *Submitted to Eur.Phys.J.C*, 11 2022.

[32] T. Ablyazimov et al. Challenges in QCD matter physics –The scientific programme of the Compressed Baryonic Matter experiment at FAIR. *Eur. Phys. J. A*, 53(3):60, 2017.

[33] B. Friman et al., editors. *The CBM Physics Book: Compressed Baryonic Matter in Laboratory Experiments*, volume 814 of *Lecture Notes in Physics*. Springer Berlin, Heidelberg, 2011.

[34] K. Agarwal. The compressed baryonic matter (CBM) experiment at FAIR—physics, status and prospects. *Phys. Scripta*, 98(3):034006, 2023.

[35] J. M. Heuser et al. *Technical Design Report for the CBM Silicon Tracking System (STS)*. GSI, Darmstadt, 2013.

[36] H. R. Schmidt. The silicon tracking system of the CBM experiment at FAIR. *Nucl. Instrum. Meth. A*, 936:630–633, 2019.

[37] ECFA Detector R&D Roadmap Process Group. The 2021 ECFA detector research and development roadmap. Technical report, CERN, Geneva, 2020.

[38] ALICE France. ALICE-France in LHC runs 3+4 and upgrade of the inner tracker, ITS3. Technical report, IN2P3 Scientific Council, 2022.

[39] M. Moll. *Radiation damage in silicon particle detectors: Microscopic defects and macroscopic properties*. PhD thesis, Hamburg U., 1999.

[40] M. Moll. Displacement damage in silicon detectors for high energy physics. *IEEE Trans. Nucl. Sci.*, 65(8):1561–1582, 2018.

[41] G. Kramberger. *Solid State Detectors for High Radiation Environments*, pages 965–1034. Springer International Publishing, Cham, 2020.

[42] A. Chilingarov. Temperature dependence of the current generated in Si bulk. *Journal of Instrumentation*, 8(10):P10003, Oct 2013.

[43] O. Krasel. *Charge collection in irradiated silicon-detectors*. PhD thesis, Dortmund U., 8 2004.

[44] G. Kramberger et al. Effective trapping time of electrons and holes in different silicon materials irradiated with neutrons, protons and pions. *Nucl. Instrum. Meth. A*, 481:297–305, 2002.

[45] A. G. Bates and M. Moll. A comparison between irradiated magnetic Czochralski and float zone silicon detectors using the transient current technique. *Nucl. Instrum. Meth. A*, 555:113–124, 2005.

[46] J. Weber and R. Klingenberg. Free charge carriers trapping properties in neutron-irradiated DOFZ silicon pad detectors. *IEEE Trans. Nucl. Sci.*, 54:2701–2705, 2007.

[47] The URL of the RD48 Collaboration. `http://www.cern.ch/rd48/`.

[48] G. Lindstrom et al. Radiation hard silicon detectors developments by the RD48 (ROSE) Collaboration. *Nucl. Instrum. Meth. A*, 466:308–326, 2001.

[49] G. Lindstrom. Radiation damage in silicon detectors. *Nucl. Instrum. Meth. A*, 512:30–43, 2003.

[50] The URL of the RD50 Collaboration. `http://www.cern.ch/rd50/`.

[51] M. Moll. RD50 Status Report 2009/2010 - Radiation hard semiconductor devices for very high luminosity colliders. Technical Report CERN-LHCC-2012-010, LHCC-SR-004, CERN, Geneva, 2012.

[52] F. Zareef, A. Oblakowska-Mucha, and T. Szumlak. Silicon detectors beyond LHC — RD50 status report. *JINST*, 17(11):C11004, 2022.

[53] V.L. Highland. Some Practical Remarks on Multiple Scattering. *Nucl. Instrum. Meth.*, 129:497, 1975.

[54] G.R. Lynch and O.I. Dahl. Approximations to multiple Coulomb scattering. *Nucl. Instrum. Meth. B*, 58:6–10, 1991.

[55] R. L. Workman et al. Review of Particle Physics. *PTEP*, 2022:083C01, 2022.

[56] R. L. Gluckstern. Uncertainties in track momentum and direction, due to multiple scattering and measurement errors. *Nucl. Instrum. Meth.*, 24:381–389, 1963.

[57] Z. Drasal and W. Riegler. An extension of the Gluckstern formulae for multiple scattering: Analytic expressions for track parameter resolution using optimum weights. *Nucl. Instrum. Meth. A*, 910:127–132, 2018.

[58] C. Joram et al. Extension of the R&D Programme on Technologies for Future Experiments: Proposal for the period 2024-2028. Technical report, CERN EP Department, Geneva, 2023.

[59] The URL of the AIDAinnova WP10: Advanced Mechanics for Tracking and Vertex Detectors. `https://aidainnova.web.cern.ch/wp10`.

[60] P. Petagna, B. Verlaat, and A. Francescon. *Two-Phase Thermal Management of Silicon Detectors for High Energy Physics*, chapter 5, pages 335–412. Encyclopedia of Two-Phase Heat Transfer and Flow III. World Scientific, May 2018.

[61] G. Viehhauser. Thermal management and mechanical structures for silicon detector systems. *JINST*, 10(09):P09001, 2015.

[62] M. Olcese. Mechanics and cooling of pixel detectors. *Nucl. Instrum. Meth. A*, 465:51–59, 2000.

[63] P. Petagna. Past Experiences and Future Trends on Vertex Detector Cooling at LHC. *PoS*, Vertex2013:037, 2013.

[64] C. Gargiulo. Challenges for future tracking detectors mechanics. `https://indico.cern.ch/event/766853/`. CERN Detector Seminar (26.10.2018).

[65] G. D. Hallewell. The “green” use of fluorocarbons in Cherenkov detectors and silicon tracker cooling systems: challenges and opportunities in an unfolding era of alternatives. *Eur. Phys. J. Plus*, 138(12):1141, 2023.

[66] G. D. Hallewell. Unit 5: Cooling and thermal management, in Survey of Instrumentation and Laboratory Techniques (PHYS 524). University of Illinois Urbana-Champaign, Fall 2023.

[67] The URL of the Forum on Tracking Detector Mechanics 2023. `https://indico.cern.ch/event/1228295/`.

[68] H. Ye et al. Thermal mock-up studies of the Belle II vertex detector. *Nucl. Instrum. Meth. A*, 896:82–89, 2018.

[69] H. Ye et al. Commissioning and performance of the Belle II pixel detector. *Nucl. Instrum. Meth. A*, 987:164875, 2021.

[70] K. Arndt et al. Technical design of the phase I Mu3e experiment. *Nucl. Instrum. Meth. A*, 1014:165679, 2021.

[71] T.T. Rudzki et al. Successful cooling of a pixel tracker using gaseous helium: Studies with a mock-up and a detector prototype. *Nucl. Instrum. Meth. A*, 1054:168405, 2023.

[72] E. Anderssen. The STAR PXL detector cooling system. `https://indico.cern.ch/event/469996/contributions/2148211/`. Forum on Tracking Detector Mechanics, 2016.

[73] G. Contin et al. The STAR MAPS-based PiXeL detector. *Nucl. Instrum. Meth. A*, 907:60–80, 2018.

[74] ALICE Collaboration. Expression of Interest for an ALICE ITS Upgrade in LS3. Technical Report ALICE-PUBLIC-2018-013, CERN, Geneva, 2018.

[75] C. Gargiulo. Ultralight air-cooled mechanics for ALICE ITS3. `https://ep-news.web.cern.ch/content/ultralight-air-cooled-mechanics-alice-its3`. CERN-EP Newsletter (23.06.2023).

[76] A. Carballo. Design, thermal, and dynamic stability analyses of the air-cooled ALICE Inner Tracking System 3. `https://indico.cern.ch/event/1228295/contributions/5390941/`. Forum on Tracking Detector Mechanics, 2023.

[77] A.D. Hellenschmidt. *Experimental studies on small diameter carbon dioxide evaporators for optimal Silicon Pixel Detector cooling*. PhD thesis, U. Bonn (main), 2020.

[78] E. W. Lemmon, I. H. Bell, M. L. Huber, and M. O. McLinden. NIST Standard Reference Database 23: Reference Fluid Thermodynamic and Transport Properties-REFPROP, Version 10.0, National Institute of Standards and Technology, 2018.

[79] STAR tracker snares heavy flavours. `https://cerncourier.com/a/star-tracker-snares-heavy-flavours/`. CERN COURIER (25.09.2015).

[80] A. Mapelli. Microfabricated silicon substrates for pixel detectors assembly and thermal management a.k.a. Silicon Microchannel Cooling Plates. *Nucl. Instrum. Meth. A*, 958:162142, 2020.

[81] M Bosteels. Systeme a pression hydrostatique inverse. Technical report, LEP-IM/YN, 1985.

[82] M. Bosteels. LCS: Leakless cooling system: Leakless cooling system for electronic cards and racks, 1994.

[83] P. Bonneau. Leakless Cooling System V.2: Pressure Drop Calculations and Assumptions. `https://detector-cooling.web.cern.ch/coolingsystems/CoolingSystemWeb/LCSv.2calculations.pdf`. Prepared on 22.02.2001.

[84] B Abelev et al. Technical Design Report for the Upgrade of the ALICE Inner Tracking System. *J. Phys. G*, 41:087002, 2014.

[85] M. Gómez Marzoa. *Innovative low-mass cooling systems for the ALICE ITS Upgrade detector at CERN.* PhD thesis, Ecole Polytechnique, Lausanne, 2016.

[86] M. Angeletti and C. Gargiulo. Production, quality assurance and integration of staves mechanics for the new ALICE Inner Tracking System. https://indico.cern.ch/event/775863/contributions/3413647/. Forum on Tracking Detector Mechanics, 2019.

[87] D. Amidei et al. The Silicon Vertex Detector of the Collider Detector at Fermilab. *Nucl. Instrum. Meth. A*, 350:73–130, 1994.

[88] K. Hara et al. CDF Silicon Tracking Detectors, 1988-2011. *Nucl. Instrum. Meth. A*, 699:84–88, 2013.

[89] S. Chatrchyan et al. The CMS Experiment at the CERN LHC. *JINST*, 3:S08004, 2008.

[90] P. Tropea. The CMS Tracker Fluorocarbon Cooling System. https://indico.cern.ch/event/41288/contributions/1871985/. Engineering Forum: experiences from Engineering Engineering Forum: experiences experiences from cooling systems for LHC detectors.

[91] A. Mapelli et al. Microfluidic cooling for detectors and electronics. *JINST*, 7:C01111, 2012.

[92] G. Romagnoli et al. Silicon micro-fluidic cooling for NA62 GTK pixel detectors. *Microelectron. Eng.*, 145:133–137, 2015.

[93] P. Gorbounov et al. NOVEC Fluids Qualification Report. Technical report, CERN, Geneva, 2017.

[94] 3M to Exit PFAS Manufacturing by the End of 2025. https://news.3m.com/2022-12-20-3M-to-Exit-PFAS-Manufacturing-by-the-End-of-2025. 3M Press Release (20.12.2022).

[95] X.Z. Lim. Could the world go PFAS-free? Proposal to ban 'forever chemicals' fuels debate. *Nature*, 620(7972):24–27, 2023.

[96] A. Abdesselam et al. The barrel modules of the ATLAS semiconductor tracker. *Nucl. Instrum. Meth. A*, 568:642–671, 2006.

[97] A. Abdesselam et al. The ATLAS semiconductor tracker end-cap module. *Nucl. Instrum. Meth. A*, 575:353–389, 2007.

[98] A. Augusto Alves, Jr. et al. The LHCb Detector at the LHC. *JINST*, 3:S08005, 2008.

[99] R. Aaij et al. Performance of the LHCb Vertex Locator. *JINST*, 9:P09007, 2014.

[100] M Needham and T Ruf. Estimation of the material budget of the LHCb detector. Technical Report LHCb-2007-025, CERN-LHCb-2007-025, CERN, Geneva, 2007.

[101] B. Abbott et al. Production and Integration of the ATLAS Insertable B-Layer. *JINST*, 13(05):T05008, 2018.

[102] C. Gargiulo. Production, quality assurance and integration of staves mechanics for the new ALICE Inner Tracking System. `https://indico.cern.ch/event/775863/contributions/3413647/`. Forum on Tracking Detector Mechanics, 2019.

[103] W. Poonsawat et al. Stave module design and development of the new ALICE Inner Tracking System. *JINST*, 14(05):P05003, 2019.

[104] ATLAS Collaboration. Technical Design Report for the ATLAS Inner Tracker Pixel Detector. Technical report, CERN, Geneva, 2017.

[105] ATLAS Collaboration. Technical Design Report for the ATLAS Inner Tracker Strip Detector. Technical report, CERN, Geneva, 2017.

[106] P. Barroca. *Modelling of CO_2 cooling of the ATLAS ITk Pixel Detector*. PhD thesis, LPSC, Grenoble, 2019.

[107] G. Aglieri Rinella et al. The NA62 GigaTracKer: a low mass high intensity beam 4D tracker with 65 ps time resolution on tracks. *JINST*, 14:P07010, 2019.

[108] LHCb Collaboration. LHCb VELO Upgrade Technical Design Report. Technical report, CERN, Geneva, 2013.

[109] O.A. de Aguiar Francisco, W Byczynski, et al. Microchannel Cooling for the LHCb VELO Upgrade I. *Nucl. Instrum. Meth. A*, 1039:166874, 2022.

[110] M. Gupta. Calculation of radiation length in materials. Technical report, CERN, Geneva, 2010.

[111] VDI-Gesellschaft Verfahrenstechnik und Chemieingenieurwesen. *VDI heat atlas; 2nd ed.* Landolt-Börnstein. Additional resources. Springer, Berlin, 2010.

[112] P. Charitos. The ALICE ITS upgrade: Pixels for quarks. `https://ep-news.web.cern.ch/content/alice-its-upgrade-pixels-quarks`. CERN-EP Newsletter (19.09.2019).

[113] V. Vacek et al. Perfluorocarbons and their use in Cooling Systems for Semiconductor Particle Detectors. *Fluid Phase Equilib.*, 174:191–201, 2000.

[114] G. D. Hallewell. *Aspects of the use of saturated fluorocarbon fluids in high energy physics*. PhD thesis, Marseille, CPPM, 2011.

[115] D. Attree et al. The evaporative cooling system for the ATLAS inner detector. *JINST*, 3:P07003, 2008.

[116] G. Viehhauser. Evaporative cooling in ATLAS: Present and future. *Nucl. Instrum. Meth. A*, 628:251–255, 2011.

[117] M Battistin et al. The Thermosiphon Cooling System of the ATLAS Experiment at the CERN Large Hadron Collider. *International Journal of Chemical Reactor Engineering*, 13(4):511–521, 2015.

[118] A. Pepato et al. The mechanics and cooling system of the ALICE silicon pixel detector. *Nucl. Instrum. Meth. A*, 565:6–12, 2006.

[119] B. Verlaat. Controlling a 2-phase co2 loop using a 2-phase accumulator. In *International Conference of Refrigeration*. Citeseer, 2007.

[120] B. Verlaat et al. CO-2 cooling for HEP experiments. In *Topical Workshop on Electronics for Particle physics*, pages 328–336, 2008.

[121] CO_2 cooling is getting hot in high-energy physics. `https://cerncourier.com/a/co2-cooling-is-getting-hot-in-high-energy-physics/`. CERN COURIER (31.05.2012).

[122] P. Tropea et al. Design, construction and commissioning of a 15 kW CO_2 evaporative cooling system for particle physics detectors: lessons learnt and perspectives for further development. *PoS*, TIPP2014:223, 2014.

[123] W. Adam et al. The CMS Phase-1 Pixel Detector Upgrade. *JINST*, 16(02):P02027, 2021.

[124] A. Tumasyan and others (CMS Collaboration). The Phase-2 Upgrade of the CMS Tracker. Technical Report CERN-LHCC-2017-009, CMS-TDR-014, CERN-LHCC-2017-009, CMS-TDR-014, CERN, 6 2017.

[125] ATLAS Collaboration. Technical Design Report for the ATLAS Inner Tracker Strip Detector. Technical Report CERN-LHCC-2017-005, ATLAS-TDR-025, CERN, 4 2017.

[126] ATLAS Collaboration. Technical Design Report for the ATLAS Inner Tracker Pixel Detector. Technical Report CERN-LHCC-2017-021, ATLAS-TDR-030, CERN, 2017.

[127] P. Tropea et al. Advancements and plans for the LHC upgrade detector thermal management with CO_2 evaporative cooling. *Nucl. Instrum. Meth. A*, 936:644–645, 2019.

[128] J.-H. Arling et al. Performance study of dual-phase CO2 cooling on the example of the ATLAS ITk strip end-cap detector. *Nucl. Instrum. Meth. A*, 1038:166953, 2022.

[129] L. Zwalinski et al. Progress in new environmental friendly low temperature detector cooling systems development for the ATLAS and CMS experiments. *Nucl. Instrum. Meth. A*, 1047:167688, 2023.

[130] B. Verlaat and P. Petagna. R&D for a colder future in HEP. https://indico.cern.ch/event/775863/contributions/3413707/. Forum on Tracking Detector Mechanics, 2019.

[131] B. Verlaat. Cooling R&D needs for future detectors. https://indico.cern.ch/event/999825/contributions/4251045. ECFA Detector R&D Roadmap Symposium of Task Force 8 Integration, 2021.

[132] L. Contiero *et al.* Krypton, applied as a refrigerant for cooling of silicon detector trackers. https://cds.cern.ch/record/2850803. 15th IIR Gustav Lorentzen Conference on Natural Refrigerants, 2022.

[133] F. Jerve. Advanced experimental analysis of a small-scale prototype with noble gases for the future upgrade of the detector cooling system at CERN. Master's thesis, NTNU, 2023.

[134] B. Verlaat. Cooling beyond -40 C. https://indico.cern.ch/event/1228626/contributions/5238839/. VELO Upgrade II Workshop, 2023.

[135] M. Garcia-Sciveres. ATLAS Experiment Pixel Detector Upgrades. *Proceedings of the DPF-2011 Conference*, 9 2011.

[136] H. Gutbrod. *FAIR baseline technical report - Volume 1 Executive Summary.* GSI, Darmstadt, 2006.

[137] M. Durante et al. All the Fun of the FAIR: Fundamental physics at the Facility for Antiproton and Ion Research. *Phys. Scripta*, 94(3):033001, 2019.

[138] J. Blaurock et al. FAIR completion of construction works, towards commissioning and first science. *JACoW*, IPAC2023:THYD1, 2023.

[139] S. Huth et al. Constraining Neutron-Star Matter with Microscopic and Macroscopic Collisions. *Nature*, 606:276–280, 2022.

[140] E. R. Most et al. Probing neutron-star matter in the lab: Similarities and differences between binary mergers and heavy-ion collisions. *Phys. Rev. D*, 107(4):043034, 2023.

[141] A. Sorensen et al. Dense nuclear matter equation of state from heavy-ion collisions. *Prog. Part. Nucl. Phys.*, 134:104080, 2024.

[142] A. Andronic et al. Decoding the phase structure of QCD via particle production at high energy. *Nature*, 561(7723):321–330, 2018.

[143] L. Adamczyk et al. Bulk Properties of the Medium Produced in Relativistic Heavy-Ion Collisions from the Beam Energy Scan Program. *Phys. Rev. C*, 96(4):044904, 2017.

[144] A. Bazavov et al. Chiral crossover in QCD at zero and non-zero chemical potentials. *Phys. Lett. B*, 795:15–21, 2019.

[145] S. Borsanyi et al. QCD Crossover at Finite Chemical Potential from Lattice Simulations. *Phys. Rev. Lett.*, 125(5):052001, 2020.

[146] J. Pochodzalla et al. Probing the nuclear liquid - gas phase transition. *Phys. Rev. Lett.*, 75:1040–1043, 1995.

[147] F. Gross et al. 50 Years of Quantum Chromodynamics. *Eur. Phys. J. C*, 83:1125, 2023.

[148] D. Hutter et al. CBM First-level Event Selector Input Interface Demonstrator. *J. Phys. Conf. Ser.*, 898(3):032047, 2017.

[149] I. Kisel. Event Topology Reconstruction in the CBM Experiment. *J. Phys. Conf. Ser.*, 1070(1):012015, 2018.

[150] D. Emschermann. The readout system of the CBM experiment. Workshop IX on Streaming Readout, 2021.

[151] A. Rost et al. *Design of beam monitors and T0-counters for CBM*, page 141. CBM Progress Report 2020. GSI, Darmstadt, 2021.

[152] P. Klaus et al. Status of the vertex detector program of the CBM experiment at FAIR. *Nucl. Instrum. Meth. A*, 936:705–706, 2019.

[153] A. Malakhov and A. Shabunov, editors. *Technical Design Report for the CBM Superconducting Dipole Magnet.* GSI, Darmstadt, 2013.

[154] S. Chattopadhyay et al., editors. *Technical Design Report for the CBM : Muon Chambers (MuCh).* GSI, Darmstadt, 2015.

[155] C. Höhne, editor. *Technical Design Report for the CBM Ring Imaging Cherenkov Detector.* GSI, Darmstadt, 2013.

[156] C. Blume et al., editors. *Technical Design Report for the CBM Transition Radiation Detector (TRD).* GSI, Darmstadt, 2018.

[157] N. Herrmann, editor. *Technical Design Report for the CBM Time-of-Flight System (TOF).* GSI, Darmstadt, 2014.

[158] F. Guber and I. Selyuzhenkov, editors. *Technical Design Report for the CBM Projectile Spectator Detector (PSD).* GSI, Darmstadt, 2015.

[159] A. Rodríguez Rodríguez et al. Functional characterization of modules for the Silicon Tracking System of the CBM experiment. *Nucl. Instrum. Meth. A*, 1058:168813, 2024.

[160] Hamamatsu Photonics K.K. `https://www.hamamatsu.com/`. Website (Accessed 01.01.2024).

[161] E. Lavrik. *Development of quality assurance procedures and methods for the CBM Silicon Tracking System.* PhD thesis, U. Tubingen, 2017.

[162] E. Lavrik et al. Optical inspection of the silicon micro-strip sensors for the CBM experiment employing artificial intelligence. *Nucl. Instrum. Meth. A*, 1021:165932, 2022.

[163] M. Shiroya et al. Update on the simulation geometry for the Silicon Tracking System. Technical report, CBM Progress Report 2021, 2022.

[164] K. Kasinski et al. Characterization of the STS/MUCH-XYTER2, a 128-channel time and amplitude measurement IC for gas and silicon microstrip sensors. *Nucl. Instrum. Meth. A*, 908:225–235, 2018.

[165] M. Teklishyn et al. From 3D to 5D tracking: SMX ASIC-based Double-Sided Micro-Strip detectors for comprehensive space, time, and energy measurements. In *Topical Workshop on Electronics for Particle Physics*, 11 2023.

[166] J. M. Heuser et al. Production Readiness Review for the STS Carbon Fiber Ladders. Technical Report CBM-TN-19006, GSI, Darmstadt, 2019.

[167] J. Lehnert et al. GBT based readout in the CBM experiment. *JINST*, 12(02):C02061, 2017.

[168] J. de Cuveland et al., editors. *Technical Design Report for the CBM Online Systems - Part I, DAQ and FLES Entry Stage.* GSI, Darmstadt, 2023.

[169] P. Koczon et al. The powering concept of the Silicon Tracking System for CBM@FAIR. *PoS*, 370:063, 2020.

[170] P. Larionov. *Systematic irradiation studies and Quality Assurance of silicon strip sensors for the CBM Silicon Tracking System.* PhD thesis, Frankfurt U., 2016.

[171] I. Momot. *Characterization and radiation hardness studies of the silicon microstrip sensors for the CBM experiment.* PhD thesis, Frankfurt U., 2019.

[172] I. Momot et al. Evaluation of the sts sensor prototypes irradiated with 23 mev proton beam using relativistic β-electrons. Technical Note CBM-TN-18015, GSI, 2018.

[173] T. T. Böhlen et al. The FLUKA Code: Developments and Challenges for High Energy and Medical Applications. *Nucl. Data Sheets*, 120:211–214, 2014.

[174] A. Senger. Non-ionising energy loss (NIEL) in STS cooling. `https://indico.gsi.de/event/18427/contributions/75188/`. STS Construction Meeting (20.10.2023).

[175] H. Malygina. *Hit reconstruction for the Silicon Tracking System of the CBM experiment.* PhD thesis, Frankfurt U., 2018.

[176] J. Lehnert. STS ROB/POB Cooling Plates: Cooling Power and Device Count. `https://indico.gsi.de/event/17916/contributions/72502/`. STS Cooling Meeting (23.06.2023).

[177] I. Elizarov et al. The final and pilot cooling plant for the sts detector. Technical Note CBM-TN-23003, GSI, 2023.

[178] K. Agarwal et al. Sts sensor's leakage current at their end-of-lifetime. Technical Note CBM-TN-23001, GSI, 2023.

[179] P. Petagna and M. Voss. Local cooling. `https://indico.cern.ch/event/999825/contributions/4251041`. ECFA Detector R&D Roadmap Symposium of Task Force 8 Integration, 2021.

[180] T.L. Bergman, A.S. Lavine, F.P. Incropera, and D.P. DeWitt. *Fundamentals of Heat and Mass Transfer.* Wiley, 2017.

[181] S. W. Churchill and H. Chu. Correlating equations for laminar and turbulent free convection from a vertical plate. *International Journal of Heat and Mass Transfer*, 18(11):1323–1329, 1975.

[182] Y.A. Çengel and R.H. Turner. *Fundamentals of Thermal-fluid Sciences.* McGraw-Hill series in mechanical engineering. McGraw-Hill Companies, 2004.

[183] E. Specht. *Impinging Jet Drying*, chapter 1, pages 1–26. John Wiley & Sons, Ltd, 2014.

[184] V. Tesař. *Impinging Jets*, pages 191–231. Springer Singapore, Singapore, 2015.

[185] H. Martin. Heat and mass transfer between impinging gas jets and solid surfaces. In J. P Hartnett and T. F. Irvine, editors, *Advances in Heat Transfer*, volume 13, pages 1–60. Elsevier, 1977.

[186] N. Zuckerman and N. Lior. Jet impingement heat transfer: Physics, correlations, and numerical modeling. In G. A. Greene et al., editors, *Advances in Heat Transfer*, volume 39, pages 565–631. Elsevier, 2006.

[187] B. Weigand and S. Spring. Multiple jet impingement – a review. *Heat Transfer Research*, 42(2):101–142, 2011.

[188] W. Schabel and H. Martin. *G10 Impinging Jet Flow Heat Transfer*, pages 745–752. Springer Berlin Heidelberg, Berlin, Heidelberg, 2010.

[189] K. Agarwal et al. Conceptual design report of the sts cooling system. Technical Note CBM-TN-18004, GSI, 2018.

[190] S. Mehta et al. CBM Silicon Tracking System integration: from module production to ladder assembly. *PoS*, FAIRness2022:036, 2023.

[191] S. Mehta. Impact of air cooling on mechanical stability of silicon sensors in cbm-sts. `https://indico.cern.ch/event/1228295/contributions/5390888/`. Forum on Tracking Detector Mechanics, 2023.

[192] S. Mehta. *Characterization of ultra light carbon fiber structures for the Silicon Tracking System of the CBM Experiment*. PhD thesis, Eberhard Karls University of Tuebingen, 2024.

[193] S. Ilie et al. Chemical and radiolytical characterization of some perfluorocarbon fluids used as coolants for LHC experiments - Chemical characterization. Technical Report EDMS No. 804849, TS-Note-2006-010, CERN, Geneva, 2006.

[194] S. Ilie et al. Chemical and radiolytical characterization of perfluorocarbon fluids used as coolants for LHC experiments - Radiolysis effects in perfluorohexane fluids. Technical Report EDMS No. 842110, TS-Note-2007-005, CERN, Geneva, 2007.

[195] Regulation (EU) 2021/1119 of the European Parliament and of the Council of 30 June 2021 establishing the framework for achieving climate neutrality and amending Regulations (EC) No 401/2009 and (EU) 2018/1999 ('European Climate Law'). `http://data.europa.eu/eli/reg/2021/1119/oj`. Document 32021R1119.

[196] Regulation (EU) No 517/2014 of the European Parliament and of the Council of 16 April 2014 on fluorinated greenhouse gases and repealing Regulation (EC) No 842/2006. http://data.europa.eu/eli/reg/2014/517/oj. Document 32014R0517.

[197] Regulation (EU) 2024/573 of the European Parliament and of the Council of 7 February 2024 on fluorinated greenhouse gases, amending Directive (EU) 2019/1937 and repealing Regulation (EU) No 517/2014. http://data.europa.eu/eli/reg/2024/573/oj. Document 32024R0573.

[198] Heuser, J. M. STS integration. https://indico.gsi.de/event/10132/contributions/379/. CBM Technical Board Meeting (03.03.2020).

[199] L Friedel. Improved friction pressure drop correlations for horizontal and vertical two-phase pipe flow. In *European two-phase group meeting, Ispra, Italy*, 1979.

[200] S. G. Kandlikar. A General Correlation for Saturated Two-Phase Flow Boiling Heat Transfer Inside Horizontal and Vertical Tubes. *Journal of Heat Transfer*, 112(1):219–228, 02 1990.

[201] J. van Es et al. Ams02 tracker thermal control system overview and spin-off for future spacecraft cooling system developments. Technical report, National Aerospace Laboratory NLR, 2009.

[202] J. Sanchez et al. *TRACI-XL, the test cooling system for the CBM Silicon Tracking System*, volume 2013-1 of *GSI Report*, page 54 p. GSI Helmholtzzentrum für Schwerionenforschung, Darmstadt, 2013.

[203] J. Sanchez et al. *Development of a CO_2 cooling prototype for the CBM Silicon Tracking System*, volume 2014-1 of *GSI Report*, page 37 p. GSI Helmholtzzentrum für Schwerionenforschung, Darmstadt, 2014.

[204] C. Rotth. Industrial Presentation: A CO2 based Bi-Phase Cooling System. https://indico.gsi.de/event/9671/contributions/41668/. CBM-STS Cooling Conceptual Design Review (10.12.2019).

[205] J. Sanchez et al. Technical specifications of the bi-phase co_2 cbm-sts cooling system. Technical Note CBM-TN-18003, GSI, 2015.

[206] Ricardo J. Da Silva Lima and John R. Thome. *Flow Pattern-Based Boiling Heat Transfer and Frictional Pressure Drop Models for Plain Horizontal Tubes*, chapter Chapter 9, pages 355–394. World Scientific, 2015.

[207] Lixin Cheng, Gherhardt Ribatski, Jesús Moreno Quibén, and John R. Thome. New prediction methods for co2 evaporation inside tubes: Part

1 - a two-phase flow pattern map and a flow pattern based phenomenological model for two-phase flow frictional pressure drops. *International Journal of Heat and Mass Transfer*, 51(1-2):111–124, 1 2008.

[208] Lixin Cheng, Gherhardt Ribatski, and John R. Thome. New prediction methods for co2 evaporation inside tubes: Part ii - an updated general flow boiling heat transfer model based on flow patterns. *International Journal of Heat and Mass Transfer*, 51(1-2):125–135, 1 2008.

[209] E. W. Lemmon, I.H. Bell, M. L. Huber, and M. O. McLinden. NIST Standard Reference Database 23: Reference Fluid Thermodynamic and Transport Properties-REFPROP, Version 10.0, National Institute of Standards and Technology, 2018.

[210] B. Verlaat and J. Noite. Design considerations of long length evaporative co_2 cooling lines. In *10th IIR-Gustav Lorentzen Conference on Natural Working Fluids (GL2012). Proceedings. Delft, The Netherlands, June 25-27, 2012*, 2012.

[211] B. Verlaat. Dimensioning of CO2 cooling pipes in detector structures. `https://indico.cern.ch/event/233332/contributions/1546088/`. Forum on Tracking Detector Mechanics, 2013.

[212] Z. Zhang. *Optimization of the thermal performances of the Alpine Pixel Detector*. PhD thesis, Annecy, LAPP, 12 2015.

[213] P. Gorbounov et al. Alternative to liquid perfluorocarbons for detector cooling applications at CERN . Technical report, CERN, Geneva, 2015.

[214] P. Gorbounov et al. 3M Novec 649 as a replacement of C6F14 in liquid cooling systems. Technical report, CERN, Geneva, 2017.

[215] American Petroleum Institute. *Recommended Practice for Design and Installation of Offshore Production Platform Piping Systems*. API Recommended Practice 14E. American Petroleum Institute, Washington, D.C., 4th edition, October 1991.

[216] F. Madani Sani et al. Review of the API RP 14E erosional velocity equation: Origin, applications, misuses, limitations and alternatives. *Wear*, 426-427:620–636, 2019. 22nd International Conference on Wear of Materials.

[217] K. Agarwal and H.R. Schmidt. Simulations and Details of the STS Cooling Concept. `https://indico.gsi.de/event/9671/contributions/41661/`. CBM-STS Cooling Conceptual Design Review, 2019.

[218] E. Lavrik et al. High-precision contactless optical 3D-metrology of silicon sensors. *Nucl. Instrum. Meth. A*, 935:167–172, 2019.

[219] T. Rannersberger (3M Germany). Private Communication, 02.03.2021.

[220] O.C. Lopez and M. Doubek (CERN). Private Communication, 22.05.2019.

[221] E. Petit. Alpine stave mechanical proposal for the atlas pixel upgrade project. `https://indico.cern.ch/event/590227/contributions/2613973/`. Forum on Tracking Detector Mechanics, 2017.

[222] P. Petagna. Thermal enclosures and environmental management. `https://indico.cern.ch/event/41288/`. Engineering Forum: Experiences from Cooling Systems for LHC Detectors (30.10.2008).

[223] A. Abdesselam et al. Engineering for the ATLAS SemiConductor Tracker (SCT) end-cap. *JINST*, 3:P05002, 2008.

[224] A. Abdesselam et al. The integration and engineering of the ATLAS SemiConductor Tracker barrel. *JINST*, 3:P10006, 2008.

[225] R. L. Bates et al. The ATLAS SCT grounding and shielding concept and implementation. *JINST*, 7:P03005, 2012.

[226] K Bosinger, F Lehner, S Steiner, and S StrÃ¤ssle. Design, Construction and Thermal Measurements on a Detector Box for the Inner Tracker of the LHCb Experiment. Technical report, CERN, Geneva, 2002.

[227] M-O Bettler, G Conti, H Voss, N Gauvin (Gueissaz), R Frei, D Esperante-Pereira, J van Hunen, and P Fauland. Assembly of the Inner Tracker Detector Boxes. Technical report, CERN, Geneva, 2007.

[228] M. Bajdel et al. Solutions for humidity and temperature monitoring in the Silicon Tracking System of Compressed Baryonic Matter Experiment: Sensors, Testing and DCS integration. *PoS*, FAIRness2022:003, 2023.

[229] M. Bajdel. *Development of the detector control system and instrumentation for the silicon tracking system in the Compressed Baryonic Matter experiment.* PhD thesis, Goethe U., Frankfurt (main), 2023.

[230] A. Kapic et al. Humidity Sensors for High Energy Physics Applications: A Review. *IEEE Sensors J.*, 20(18):10335–10344, 2020.

[231] I. Elizarov et al. Pilot cooling supply for sts. CBM Progress Report GSI-2023-00384, GSI Darmstadt, 2022.

[232] O. Bertini et al. Basic electrical inspection of silicon microstrip sensors for the STS. CBM Progress Report GSI-2021-00421, CBM-PR-2020, GSI Darmstadt, 2021.

[233] S. Mehta et al. Impact of air cooling on mechanical stability of silicon sensors in cbm-sts. Technical Note CBM-TN-23004, GSI, 2023.

[234] J. M. Heuser. The high count-rate self-triggering Silicon Tracking System of the CBM experiment at FAIR: Design, series assembly, upgrade options. *Nucl. Instrum. Meth. A*, 1066:169620, 2024.

[235] Josa, F. and others. ALICE ITS Detector Ventilation - Renewal of the HVAC system. Technical report, CERN, Geneva, 2015.

[236] N. Herrmann. Status and Perspectives of the CBM experiment at FAIR. *EPJ Web Conf.*, 259:09001, 2022.

[237] V. Friese. Estimate of the cbm computing requirements for operation at sis-100. Technical Note CBM-CN-18001, GSI, 2018.

[238] A. R. Rodríguez. *The CBM Silicon Tracking System front-end electronics : from bare ASIC to detector characterization, commissioning and performance*. PhD thesis, Frankfurt U., 2020.

[239] A. R. Rodríguez. Private Communication, 05 2022.

List of Figures

List of Tables

List of Acronyms

2PACL 2-Phase Accumulator Controlled Loop.

AHS Air Handling System.

ALEPH Apparatus for LEP PHysics.

ALICE A Large Ion Collider Experiment.

ALICE-ITS ALICE Inner Tracking System.

ALICE-ITS2 ALICE Inner Tracking System 2.

ALICE-ITS3 ALICE Inner Tracking System 3.

ALICE-SSD ALICE Silicon Strip Detector.

AMS Alpha Magnetic Spectrometer.

AMS02 TTCS AMS02 Tracker Temperature Control System.

APPA Atomic, Plasma Physics and Applications.

ASIC Application Specific Integrated Circuit.

ATLAS A Toroidal LHC Apparatus.

ATLAS-IBL ATLAS Insertable B-Layer.

ATLAS-ID ATLAS Inner Detector.

Belle II-PXD Belle II Pixel Vertex Detector.

BNL Brookhaven National Laboratory.

CAD Computer-Aided Design.

CBM Compressed Baryonic Matter.

CBM-BMON CBM Beam Monitor and Start.

CBM-FSD CBM Forward Spectator Detector.

CBM-MuCh CBM Muon Chambers.

CBM-MVD CBM Micro Vertex Detector.

CBM-RICH CBM Ring Imaging Cherenkov.

CBM-STS CBM Silicon Tracking System.

CBM-TOF CBM Time-of-Flight.

CBM-TRD CBM Transition Radiation Detector.

CCE Charge Collection Efficiency.

CDF Collider Detector at Fermilab.

CDF SVX-II CDF Silicon Vertex Tracker - II.

CEP Critical End Point.

CERN Conseil Européen pour la Recherche Nucléaire, or European Council for Nuclear Research.

CERN-RD48 Research and development On Silicon for future Experiments (ROSE).

CERN-RD50 Radiation hard semiconductor devices for very high luminosity colliders.

CF Carbon Fibre.

CFD Computational Fluid Dynamics.

CMS Compact Muon Solenoid.

CMS Phase-I SST CMS Phase-I Silicon Strip Tracker.

CMS-ECAL CMS Electromagnetic Calorimeter.

CMS-HCAL CMS Hadronic Calorimeter.

CoBra CO2 BRAnch Calculator.

CTE Coefficient of Thermal Expansion.

DAQ Data Acquisition.

DCS Detector Control System.

DELPHI DEtector with Lepton, Photon and Hadron Identification.

DØ DZero.

EOL End-Of-Lifetime.

EOS Equation of State.

EPDM Ethylene propylene diene monomer.

ePIC Electron-Proton/Ion Collider.

FAIR Facility for Antiproton and Ion Research.

FBG-FOS Fiber Bragg Grating FOS.

FCC-ee Future Circular Collider - Electron-Positron Collisions.

FCC-hh Future Circular Collider - Hadron-Hadron Collisions.

FEA Finite Element Analysis.

FEB FEE Board.

FEE Front-End Electronics.

FLUKA FLUktuierende KAskade, or Fluctuating Cascade.

FOS Fibre-Optics Sensor.

FPOB FEE Power Board.

GBT GigaBit Transceiver.

GRP Glass Reinforced Plastic.

GSI Gesellschaft für Schwerionenforschung - GSI Helmholtz Centre for Heavy Ion Research.

GWP Global Warming Potential.

HADES High Acceptance DiElectron Spectrometer.

HL-LHC High-Luminosity Large Hadron Collider.

HTC Heat Transfer Coefficient.

ISS International Space Station.

LDO Low Dropout Regulator.

LEP Large Electron and Positron.

LHC Large Hadron Collider.

LHCb Large Hadron Collider beauty.

LHCb VELO LHCb VErtex LOcator.

LQCD Lattice QCD.

MIP Minimum Ionising Particle.

MRPC Multi-Gap Resistive Plate Chambers.

MWPC Multi-Wire Proportional Counters.

NA62 North Area 62 Experiment.

NA62 GTK NA62 GigaTracKer.

NIEL Non-Ionising Energy Loss.

NTP Normal Temperature and Pressure.

NUSTAR Nuclear Structure, Astrophysics and Reactions.

PA Polyamide.

PANDA AntiProton Annihilation at Darmstadt.

PC Polycarbonate.

PCB Printed Circuit Board.

PE Polyethylene.

PED Pressure Equipment Directive.

PEEK Polyether ether ketone.

PFAS Per- and Poly-fluoroalkyl.

PFC Per-fluorocarbon.

PMMA Poly(methyl methacrylate).

POB Power Board.

PP Polypropylene.

PTFE Polytetrafluoroethylene.

PUR Polyurethane.

PVC Polyvinyl chloride.

QCD Quantum Chromodynamics.

QGP Quark-Gluon Plasma.

RHIC Relativistic Heavy Ion Collider.

ROB Read-Out Board.

RPOB Read-Out Power Board.

RTD Resistance Temperature Detector.

SIS-100 Schwerionensynchrotron-100.

SIS-18 Schwerionensynchrotron-100.

SMX STS/MuCh X-Y-Time-Energy Read-out.

STAR Solenoidal Tracker at RHIC.

STAR PXL-HFT STAR Heavy Flavor Tracker PIxel Detector.

STP Standard Temperature and Pressure.

TFM Thermal Figure of Merit.

TRACI Transportable Refrigeration Apparatus for CO2 Investigation.

UHMWPE Ultra-High Molecular Weight Polyethylene.

Acknowledgments

The work presented in this thesis is the culmination of efforts by numerous people from both my professional and personal spheres, who have played a significant role at various stages in its completion. Thank you all.

There is no better place to start than thanking Prof. Dr. Hans Rudolf Schmidt, who steered this entire project to completion by providing the ecosystem that enabled me to discover and develop my own scientific process. He achieved this by initially providing structured guidance to facilitating the research by providing all necessary resources to the final stage of us being - dare I say - colleagues and collaborators. Furthermore, he constantly helped me to broaden my scientific horizon by encouraging and supporting me to present at various forums, ranging from chalk-talks within the working group to conferences, on multitude of topics, some even unrelated to my core doctoral research. I must acknowledge his patience and conviction to prioritise the entire training process over the outcome, which is especially challenging given my unusually long term as a doctoral student and all its limitations. All in all - it was pleasure to work with him and it was a pleasure to work for him.

I would also like to thank the entire CBM-STS team for their immense support, especially Dr. Ulrich M. Frankenfeld, Dr. Johann M. Heuser, Dr. Mladen Kiš, Dr. Piotr Koczoń, Dr. Jörg Lehnert, Dr. Anton Lymanets, Dr. Walter F.J. Müller, Dr. Adrian Rodríguez Rodríguez, Dr. Christian J. Schmidt and Dr. Maksym Teklishyn, for hosting the *STS Thermal Demonstrator* project at GSI and providing unconditional infrastructural support of the *GSI Detector* and *STS Laboratory*. Furthermore, the framework of *STS Integration* and *Construction Meetings* was crucial to scrutinise my work in the context of the entire detector subsystem and provide a holistic view on several aspects of detector operation in an open-minded, consistent and constructive manner. Therefore, this instilled a sense of pragmatism which was essential for efficient project implementation.

Given the complex technical nature of this work, I can not overstate the importance of our technical and engineering team, without whom this project would not have materialised from illegible blackboard sketches. I am extremely thankful to Jens Thaufelder whose commitment, expertise and coordination with GSI's workshop facilities was central to this project. I would also like to thank Ilya Elizarov to bringing into operation the pilot cooling plants and necessary service infrastructure. Moreover, the help by Patrick Dahm, Ralf M. Kapell, Peter Kuhl, Ulrich Möller, Frederike Nickels, Holger Risch, Carmen Simons, and O. Vasylyev in designing, ordering, debugging and their understated capability to immediately arrange components was decisive. A special thanks to (soon-to-be-Dr.) Shaifali Mehta for her hands-on support during various stages of setup assembly and operation, Dr. Marcel Bajdel and Dr. Ulrich M. Frankenfeld for providing a reliable DCS and DAQ, and Lady Maryann Collazo Sanchez, Dairon Rodríguez Garces and Mehulkumar Shiroya for urgently operating the setup during my inadvertently long stay in India.

Most of the work presented in this thesis is a direct result of the learnings from numerous presentations at the annual *Forum on Tracking Detector Mechanics*. I would take this opportunity to thank all the organisers of these events for providing a discussion-centric platform, where the community could come together to share their success stories while also honestly sharing their what-not-to-do and it's-a-bad-idea stories.

Although this thesis focuses on my core doctoral research on detector instrumentation, I am indebted to Dr. Arnaud Le Févre, Prof. Dr. Peter Senger, and Prof. Dr. Wolfgang Trautmann, who helped me explore the world of neutron stars and heavy ion collisions. This was made possible by the freedom and encouragement provided by Prof. Dr. Hans Rudolf Schmidt to "distract" myself with this subject from time-to-time. Certainly, this was and continues to be a very productive distraction, and long it may continue.

I also thank all colleagues at the Physikalisches Institut - Universität Tübingen and the CBM Department - GSI for the friendly and collegial atmosphere. Special thanks goes to Gaby Behring, Dr. Olga Bertini, Lady Maryann Collazo Sanchez, Susovan Das, Eduard Friske, Dr. Torsten Hehl, Dr. Benjamin Hess, Prof. Dr. Josef Jochum, Dr. Irakli Keshelashvili, Dr. Shahid Khan, Dr. Viktor Klochkov, Dr. Günter Lang, Prof. Dr. Tobias Lachenmaier, Dr. Evgeny Lavrik, Dr. Oleksii Lubynets, Dr. Osnan Maragoto Rodríguez, Shaifali Mehta, Dr. Ievgeniia Momot, Dr. Iaroslav Panasenko, Dario Ramirez, Dairon Rodríguez Garces, Dr. Ilya Selyuzhenkov, Martin Schmidt, Mehulkumar Shiroya, Dr. Omveer Singh, Prof. Dr. Alberica Toia, Dr. Martin Völkl, Elena Volkova, and Annette Zimbelius.

I would also like to express my immense gratitude to the following people for proof-reading my thesis and all their suggestions: Dr. Johann M. Heuser, Franz A. Matejcek, Shaifali Mehta, Dr. Iaroslav Panasenko, Dario Ramirez, Prof. Dr. Hans Rudolf Schmidt, and Dr. Maksym Teklishyn.

Many thanks to Prof. Dr. Subhasis Chattopadhyay and his entire team at VECC - Kolkata, especially Dr. Rajesh Ganai and Dr. Arindam Roy, for introducing me to the world of detector physics and instrumentation. I am also grateful to my high-school physics teacher, Dr. Gaurav Dubey, who triggered my interest in physics and helped me to develop some "intuition" for the subject.

This work was supported by the BMBF, HGS-HIRe, and Stiftung Giersch for financing my stay and this project in various capacities.

I would also like to acknowledge the timely and professional support of the university's Psychosocial Counseling Service, specifically Dr. Annette Mauch. Academia especially tests the mental resilience of graduate students due to multitude of reasons, with these challenges amplified during the COVID-19 pandemic and its aftermath. Sometimes we lose our balance, and these services are imperative to tackle the resulting mental-health challenges. Therein also comes the crucial support of all my friends and family (fortunately, too many to list) who were always there and brought the much needed equilibrium.

Finally, I neither have enough words nor the courage to express the anchoring role of my mother – Dr. Nisha Agarwal and late father – Mr. Rakesh Agarwal, during this entire work. Since Bollywood tends to have songs and dialogues to summarise most feelings, I borrow one dialogue:

"मेरे पास मां है!",
read as – *Mere Paas Maa Hai!*,
meaning – *I have my mother with me!*